Experimental Investigation of Trailing-Edge Separation

by

Sen Wang

A thesis submitted in partial fulfillment of the requirements for the degree of

Doctor of Philosophy

Department of Mechanical Engineering

University of Alberta

Abstract

Flow separation at the trailing-edge (TE) region of wings, known as trailing-edge separation, is a process where the boundary layer detaches from the wing surface under the effect of an adverse pressure gradient (APG). The phenomenon is known for reducing lift, increasing drag and producing unsteady force fluctuations. It is commonly seen on devices with a thick airfoil profile. Addressing the adverse effects of TE separation is essential for improving aviation safety and prolonging the lifetime of aerial vehicles. It is in the interest of the aerodynamic community to develop strategies to detect and mitigate trailing-edge separation. This process, however, requires an adequate knowledge of the flow field regarding its time-averaged and unsteady characteristics.

In aim to gain deeper insights into TE separation, this study employed an experimental approach to investigate the turbulent separated flow near the TE of a two-dimensional (2D) wing with a NACA 4418 profile. The near-wall topology of the separated flow was characterized by performing full-span planar particle image velocimetry (PIV) measurements. The time-averaged near-wall streamline pattern revealed that a unique cellular structure formed at angle-of-attack of 9.7°. The structure is known as stall cell, featuring an arc-shape separation front that both ends spiral into two counter-rotating foci. The pattern of stall cell was observed to expand with increasing α. Its three-dimensional (3D) topology at angle-of-attack of 9.7° was characterized through a large-scale 3D particle tracking velocimetry (PTV) measurement with the help of a novel helium-filled soap bubble seeding system. The results showed that stall cell had a short height and consisted of two wall-normal counter-rotating vortices, which were normal to the wing surface and extended to the edge of the turbulent separation bubble.

Time-resolved planar PIV measurements were then carried out to investigate the unsteadiness in trailing-edge separation. The Strouhal number St_l of the unsteadiness was computed based on the characteristic length l of the turbulent separation bubble and freestream velocity. Spectral analysis of the velocity field from the streamwise-wall-normal plane showed two ranges of St_l that were energetic. The lower range extended from $St_l = 0.03$ to 0.08, with a spectral peak occurring at $St_l = 0.06$. The higher range was observed within $0.2 < St_l < 0.8$ and

the spectral peak was detected at $St_l = 0.4$. Spectral proper orthogonal decomposition (SPOD) analysis was then performed using velocity data to identify the associated flow motions. It was found that the lower range corresponded to the breathing motion, while the higher range was attributed to the vortex shedding motions. The breathing motion was shown to correlate with the dynamics of shear layers.

Finally, the relation between the breathing motion and wall pressure was investigated using simultaneous wall-pressure and planar PIV measurements. The velocity fields from PIV measurement were later synchronized with wall-pressure data in post-processing. Spatio-temporal cross-correlations between the velocity fields and wall-pressure data demonstrated that the breathing motion was well correlated with the low-frequency wall-pressure fluctuations measured at $0.44l$ upstream and downstream of the mean detachment point. The results indicated that the optimal location for sensing the breathing motion was in the region with low-intermittency flow. To determine the phase relation between the breathing motion and low-frequency wall-pressure fluctuations, SPOD analysis was performed using synchronized velocity fields and wall pressure data. A reduced-order model of velocity fields and wall pressure fluctuations was reconstructed, based on the leading SPOD mode at $St_l = 0.024$. The results revealed that the expansion (or contraction) of separation bubble preceded a decrease (or increase) in wall pressure measured $0.44l$ upstream of mean detachment point by a phase of 0.37π. Conversely, the expansion (or contraction) of separation bubble preceded an increase (or decrease) in wall pressure $0.44l$ downstream of mean detachment point by a phase of 0.34π. The observations align with the fact that TSB expansion occurs when local APG increases, whereas contraction corresponds to a decrease in APG. In summary, the results provide insights into the simultaneous evolution of breathing motion and wall pressure. The findings of this investigation can be utilized in devising strategies for detecting breathing motion and benefiting the future development of active control strategy.

Preface

This thesis is based on the experimental investigation of a turbulent separation bubble near the trailing edge of a NACA 4418 airfoil. All experiments in this work were performed by the author under the supervision of Dr. Sina Ghaemi. All the measurements were carried out in the 2-story, closed-loop, low-speed wind tunnel in the mechanical engineering building at the University of Alberta. The airfoil was designed by Austin Ma (Ma et al., 2020). The wall-pressure measurement technique was developed by Bradley Gibeau (Gibeau & Ghaemi, 2021).

The contents of Chapter 4 and 5 were published in the following papers:

Wang, S., & Ghaemi, S. (2021). Full-span topology of trailing-edge separation at different angles of attack. *AIAA Journal*, 59(12), 5186-5197,

Wang, S., & Ghaemi, S. (2022). Unsteady motions in the turbulent separation bubble of a two-dimensional wing. *Journal of Fluid Mechanics*, *948*, A3,

and were presented in the thesis with the permission of the copyright holder. The analysis and interpretation of the experimental results from Chapters 4 and 5 were conceived by the author under the supervision of Dr. Sina Ghaemi. The results of Chapter 6 were analyzed and interpreted by the author with the assistance of Bradley Gibeau, under the supervision of Dr. Sina Ghaemi. The contents of Chapter 6 were encompassed in the following manuscript, and was submitted for review:

Wang, S., Gibeau, B., & Ghaemi, S. (2022). The Interaction between Turbulent Separation Bubble Breathing and Wall Pressure on a 2D Wing. *Experiments in Fluids* (submitted).

Table of Contents

Chapter 1. Introduction 1

1.1 Motivation 1

1.2 Topology of stall cell 2

1.3 Low-frequency flow motion 3

1.4 Breathing motion detection 4

1.5 Thesis outline 6

Chapter 2. Flow separation on airfoils 8

2.1 Stall type 8

2.2 Trailing-edge separation 10

2.2.1 Stall cell 10

2.2.2 Low-frequency unsteadiness and breathing motion 13

2.2.3 Detecting breathing motion 19

Chapter 3. Experimental methodology 23

3.1 Wind tunnel and airfoil 23

3.2 Particle image velocimetry 25

3.3 Shake-the-box algorithm 27

3.4 Helium-filled soap bubble system 29

3.5 Spectral proper orthogonal decomposition 30

Chapter 4. Topology of trailing-edge separation 32

4.1 Introduction 32

4.2 Experimental setup 34

4.2.1 Planar particle image velocimetry 34

4.2.2 Vortex generators 36

4.2.3 Three-dimensional particle tracking velocimetry 38

4.3 Results and discussion 40

4.3.1 The effect of angle-of-attack on stall cell 40

4.3.2 Three-dimensional characterization of the separation bubble 44

4.3.3 Application of vortex generators 49

4.4 Conclusion 52

Chapter 5. Unsteady motions in trailing-edge separation 53

5.1 Introduction 53
5.2 Experimental setup 55
5.2.1 Planar particle image velocimetry 55
5.2.2 Wall-pressure measurement 57
5.3 Results and discussion 58
5.3.1 Turbulent Separation Bubble 58
5.3.2 Unsteady Motions 69
5.3.3 Temporal and Spatial Scales 71
5.3.4 Energetic Motions 78
5.3.5 The Breathing Motion 82
5.4 Conclusion 87
Chapter 6. The breathing motion in wall pressure 90
6.1 Introduction 90
6.2 Experimental setup 92
6.2.1 Time-resolved planar PIV 92
6.2.2 Wall-pressure measurement 93
6.3 Results and discussion 97
6.3.1 Velocity field 97
6.3.2 Wall pressure 99
6.3.3 Relation between wall pressure and breathing motion 105
6.3.4 A conceptual model 116
6.4 Conclusion 118
Chapter 7. Conclusion 120
7.1 Topology of trailing-edge separation 120
7.2 Unsteady motions in trailing-edge separation 121
7.3 The breathing motion in wall pressure 122
7.4 Recommendation for future work 123
Bibliography 125
Appendices 137
A. Uncertainty analysis 137
A.1. Sources of uncertainty 137
A.2. Uncertainty analysis for Chapter 4 139
A.3. Uncertainty analysis for Chapter 5 141

A.4. Uncertainty analysis for Chapter 6 143
B. MATLAB code 144
B.1. Helmholtz resonance correction 144
B.2. Wiener noise estimation 145
C. SOLIDWORKS drawings 146
C.1. Modified NACA4418 wing 146
C.2. The assembly for wall-pressure measurements 150
C.3. Wall-pressure measurements insert plate (Chapter 5) 151
C.4. Wall-pressure measurements insert plate (Chapter 6) 153

List of Figures

Figure 2.1. A conceptual sketch of three types of stalls (Bak et al., 1999). The copyright holder grants permission for the usage of figure. 9

Figure 2.2. A schematic drawing of TSB in TE separation. 10

Figure 2.3. Oil-flow visualizations of (a) an asymmetric full-span separation, (b) 3D separation with mid-span recirculation, and (c) 3D separation with two SCs (Dell'Orso & Amitay, 2018). The copyright holder grants permission for the usage of figure........................11

Figure 2.4. Oil-flow visualization of a SC pattern that lack spanwise symmetry and deviates from the midspan (Dell'Orso & Amitay, 2018). The copyright holder grants permission for the usage of figure...13

Figure 2.5. A schematic view of turbulent separation bubble formed on a flat plate. 16

Figure 2.6. Contours of the mean streamwise velocity, associated with the leading POD mode (a) minimum temporal coefficients Min($a^1(t)$), (b) near-zero temporal coefficient $a^1(t) \approx 0$, and (c) maximum temporal coefficient Max($a^1(t)$). The contour of $\langle U \rangle = 0$ is represented by the solid white line. The copyright holder grants permission for the usage of figure. 17

Figure 2.7. (a) The result of cross-correlation between the low-pass filtered wall-pressure fluctuations measured at x = 1.65 m and x = 2.30 m and a moving measurement point along the centerline of TSB. (b) A conceptual model of the effect of TSB breathing on pressure mean distribution. The copyright holder grants permission for the usage of figure. 22

Figure 3.1. A schematic view of the wind tunnel with a 2D wing vertically installed in the test section...23

Figure 3.2. Comparison between the original (dashed line) and modified (solid line) NACA 4418 airfoils. 24

Figure 3.3. Experimental arrangement for a PIV setup in a wind tunnel (Raffel et al., 2018). The copyright holder grants permission for the usage of figure. 25

Figure 3.4. Cross-correlation between the sampled window at (m, n) from image 1 and image 2 produces a vector $d(m, n)$ for pixel displacement (Raffel et al., 2018). The copyright holder grants permission for the usage of figure. 26

Figure 3.5. The (a) front, and (b) isometric views of the HFSB system. (c) A photo of the seeding system in operation. 29

Figure 4.1. A schematic of the full-span planar PIV measurements. The stitched FOV is shown in dashed line boxes, and the origin of the coordinate is placed at the center of TE. The free stream flows from left to right. 35

Figure 4.2. The three arrangements of VG pairs used to enforce a symmetric flow around the SC. 37

Figure 4.3. A schematic view of the 3D PTV measurements. The measurement volume at midspan is shown in the dashed line box. 39

Figure 4.4. Streamline pattern over the airfoil at α of (a) 9°, (b) 9.5°, (c) 9.7°, (d) 10°, (e) 10.5° and (f) 11°. 44

Figure 4.5. Visualization of the SC in a x-z plane at $y/s = 4 \times 10^{-3}$, a x-y plane at $z/s = 0.02$ and a y-z plane at $x/c = 0.22$. 46

Figure 4.6. The velocity field in x-z planes at (a) $y/c = 0.0092$, (b) $y/c = 0.012$, and (c) $y/c = 0.018$ 47

Figure 4.7. The velocity field in the y-z plane at (a) $x/c = -0.15$, (b) $x/c = -0.13$, (c) $x/c = -0.12$, and (d) $x/c = -0.11$ 48

Figure 4.8. The 3D streamlines of the SC. The green iso-surface shows $\langle U \rangle / U_\infty = 0$. The blue, white, and red streamlines indicate negative, zero, and positive streamwise velocity (backward-to-forward flow). 48

Figure 4.9. The effect of VG arrangements on the streamlines at α of 9.7°. 51

Figure 5.1. (a) Time-resolved planar PIV in a streamwise-wall-normal plane at the midspan of the wing using three high-speed cameras. The origin of the measurement system (point O) is at the TE of the midspan plane. (b) Time-resolved planar PIV in a wall-parallel plane using two high-speed cameras. 57

Figure 5.2. (a) Instantaneous contours of streamwise velocity and (b) contours of γ in the streamwise-wall-normal measurement plane. (c) Instantaneous contours of the streamwise velocity and (d) contours of γ in the streamwise-spanwise plane located at y/c = 0.004. The detachment and endpoints of the instantaneous TSB are labeled in (a) as points D′ and E′, respectively. 62

Figure 5.3. (a) Contours of $\langle U\rangle/U_\infty$ in the streamwise-wall-normal plane reveal the triangular-shaped TSB. (b) Contours of $\langle V\rangle/U_\infty$ in the streamwise-wall-normal plane with an overlay of mean flow streamlines. (c) The variation of boundary layer thickness, momentum thickness, and the pressure coefficient with streamwise distance. (d) Contours of $\langle U\rangle/U_\infty$ in the streamwise-spanwise plane. In (a) and (d), the black line shows the contour of $\langle U\rangle$ = 0. The detachment and endpoints of the time-averaged TSB are labeled in (a) as points D and E, respectively. 64

Figure 5.4. The contours of (a) $\langle u^2\rangle_c$, (b) $\langle v^2\rangle_c$, and (c) $\langle uv\rangle_c$, normalized by U_∞^2. The velocity components are computed in the curvilinear x_c-y_c coordinate system shown in (a). The contour line shows the boundary of the mean TSB based on $\langle U\rangle$ = 0. 67

Figure 5.5. (a) The contour of $<\omega_z>$ normalized by U_∞/l. The black dashed lines follow the location of peak vorticity, $\langle\omega_z\rangle_{peak}$, along the upper and lower shear layers. (b) The variation of vorticity thickness, δ, for the upper and lower shear layers with respect to x/c. 68

Figure 5.6. Contours of the pre-multiplied PSD of u along (a) y/c = 0.02, (b) the upper shear layer, and (c) the lower shear layer. Note that $St_l = 4.2 \times St_\delta$. 71

Figure 5.7. Instantaneous visualization of spanwise profiles of u/U_∞ as they evolve in time at three streamwise locations of $x/c = -0.25$, -0.15, and -0.05. 73

Figure 5.8. The temporal evolution of streamwise profiles of u/U_∞ over (a) a short duration of $20T$ and (b) a longer duration of $98T$. The data corresponds to the midspan of the wing ($z/c = 0$) from the streamwise-spanwise PIV plane at $y/c = 4 \times 10^{-3}$. 75

Figure 5.9. The (a) spatial and (b) temporal scales of the motions estimated based on two-point correlations of the streamwise velocity fluctuations. The spatial scales, l_i, are normalized using c, and the temporal scale is normalized using T, defined as l/U_∞. 77

Figure 5.10. The correlation functions for five reference points located at $y_0/c = 4 \times 10^{-3}$ and $x_0/c = -0.3$, -0.25, -0.2, -0.15, and -0.05. The most downstream correlation function shows a double-peak pattern. 78

Figure 5.11. The energy spectra of the first 3 SPOD modes are calculated from the streamwise-wall-normal velocity fields. 79

Figure 5.12. The spatial structures of the first SPOD mode from the streamwise-wall-normal plane at $St_l = 0.02$, 0.16, and 0.72. The contour lines represent the forward-flow probability obtained from the ROM following equation 5.2. 80

Figure 5.13. The energy spectra of the first 3 SPOD modes obtained from the streamwise-spanwise velocity fields. 81

Figure 5.14. The spatial structures of the first SPOD mode of the streamwise-spanwise PIV plane at $St_l = 0.02$, 0.04, 0.06, and 0.08. The contour lines represent the forward-flow probability obtained from the ROM following equation 5.2. 82

Figure 5.15. (a) Pre-multiplied PSD of the fluctuations in A, $x_{D'}$, $x_{E'}$, and $y_{M'}$. (b) The coherence functions between A and the three TSB coordinates $x_{D'}$, $x_{E'}$, and $y_{M'}$, and (c) the coherence between $x_{D'}$, $x_{E'}$, and $y_{M'}$. 85

Figure 5.16. Pre-multiplied PSD of streamwise velocity fluctuations at $(x, y) = (0, 3.3c)$ and pre-multiplied PSD of spatially averaged velocity according to equation 5.3. 86

Figure 6.1. (a) A schematic of the experimental setup: a 2D wing is vertically installed in the test section at $\alpha = 9.7°$. The two FOVs in the x-y plane are illustrated by dashed lines and are imaged by two high-speed cameras. The origin of the coordinate O is placed at the spanwise center of TE. (b) The 7 pinholes for wall-pressure measurements are labelled in the enlarged view, with P1 being the most upstream pinhole and P7 being the most downstream one. The pinholes are aligned along the midspan of the wing, evenly spaced between $x/c = -0.300$ to -0.084. 93

Figure 6.2. The cross-section view of the pinhole attachment in the (a) x-y and (b) y-z planes. The pinhole connects the wing surface to a cavity, sealed by the microphone diaphragm. The small diameter of pinhole reduces the spatial-averaging effect in wall-pressure measurements.96

Figure 6.3. The contours of (a) $\langle U\rangle/U_\infty$ and (b) forward-flow probability (γ). The upper and lower shear layers are annotated and the black line shows $\langle U\rangle = 0$ contour. Blue dots represent the pinhole locations in both (a) and (b), indicating P1 to P7 pinholes from left to right. 98

Figure 6.4. The PSD of u/U_∞ along $y/c = 0.011$ line. Blue dots indicate the pinhole locations, representing P1 to P7 from left to right. The largest unsteadiness is associated with the breathing motion with a peak at $St_l = 0.03$ and $x/c = -0.11$, overlapping with the front edge of the TSB. . 99

Figure 6.5. The PSD of p/q_∞ is shown for various streamwise locations along the mid-span. The PSD at P5 shows strong evidence of the breathing motion with a peak at $St_l = 0.05$. The effect of vortex shedding is pronounced downstream of MD with a peak at $St_l = 0.35$. 101

Figure 6.6. The coefficient of wall-pressure fluctuation c_p is plotted against x/c. The solid line corresponds to c_p calculated using p. The dashed lines with diamonds and squares represent c_p calculated using p' and p'', respectively. The former one is low-pass filtered p at $St_l < 0.16$, and is associated with the breathing motion. The latter one is the rms of band-pass filtered p within $0.16 < St_l < 0.7$ and is due to the vortex shedding motions. 103

Figure 6.7 Temporal cross-correlation between (a) p' (St_l < 0.16), and (b) p'' (0.16 < St_l < 0.70) measured at various pinholes with the measurement wall-pressure at P4........................105

Figure 6.8 The cross-correlation between (u, v) and p' measured at x/c = −0.300 (P1). The time trace of R_{sum} is displayed in (a), with the bands of Δt that include the local peaks marked as T1 and T2. The correlation contours corresponding to the maxima of R^+_{sum} in T1 and T2 are depicted in (b) and (d), respectively. The correlations contours corresponding to the minima of R^-_{sum} in T1 and T2 are presented in (c) and (e), respectively. 110

Figure 6.9 The cross-correlation between (u, v) and p' at x/c = −0.084 (P7). The time trace of R_{sum} is displayed in (a), with the bands of Δt that include the local peaks marked as T1 and T2. The correlation contours corresponding to the minima of R^+_{sum} in T1 and T2 are depicted in (b) and (d), respectively. The correlations contours corresponding to the maxima of R^-_{sum} in T1 and T2 are presented in (c) and (e), respectively...111

Figure 6.10 The energy spectra of the dominant SPOD modes. The leading SPOD mode at St_l represents the breathing motion. The energy spectra of the dominant SPOD modes. The leading SPOD mode at St_l = 0.024 represents the breathing motion. 113

Figure 6.11 (a) The spatial organization of the first SPOD mode at Stl = 0.024. The locations of P1 and P7 are labeled with blue and green dots, respectively. (b) The temporal evolution of A and usum are plotted with respect to θ. The evolutions of (c) pP1ROM and (d) pP7ROM in θ are plotted along with A..116

Figure 6.12 A conceptual model of the relation between wall-pressure field and breathing motion. A mean TSB in the TE section of a wing (grey) is presented in a green contour. The x-axis aligns with the wing surface, representing the streamwise flow direction. An expanding TSB is shown in (a), which increases the local APG. A contracting TSB that reduces the local APG is presented in (b)..117

Figure A.1. Statistical convergence plots for (a) U and (b) W at α = 11°, near x/c = −0.16 and z/c = 0..139

Figure A.2. Statistical convergence plots for (a) U (b) V, and (b) W at α = 9.7°, near $x/c \approx -0.15$, $y/c \approx 4\times 10^{-3}$ and $z/c \approx 0.02$. 140

Figure A.3. Statistical convergence plots for (a) U and (b) V, near $x/c \approx -0.20$ and $y/c \approx 0.01$. 141

Figure A.4. Statistical convergence plots for (a) U and (b) W, near $x/c \approx -0.20$ and $z/c \approx 0$. 142

Figure A.5. Statistical convergence plots for differential pressure dP measurements. 142

Figure A.6. Statistical convergence plots for (a) U and (b) V, near $x/c \approx -0.20$ and $y/c \approx 0.01$. 143

Chapter 1. Introduction

1.1 Motivation

Trailing-edge (TE) separation is the departure of the turbulent boundary layer (TBL) from the wing surface near the TE of a wing. In TE separation, a turbulent separation bubble (TSB) is formed between the shear layers emerging from the suction and pressure surfaces. TE separation is commonly seen on the wings of wind turbines and transport aircraft with a thick airfoil profile. It can adversely affect the performance of aerodynamic devices by reducing lift and introducing extra drag and unsteady force fluctuations.

In the wind energy industry, increasing lift production is a primary objective in wind blade design. A large rotor blade is more favorable since the size of the rotor is proportional to the lift production, i.e., power output (Manwell et al., 2010). Thick airfoils are frequently employed to enhance structural strength (Lago et al., 2013; Fischer et al., 2014; Gao et al., 2015), while their efficiency in lift production is limited by TE separation. Aerial vehicles also prefer large amounts of lift during takeoff and landing. The deployment of TE flaps allows the aircraft to generate large lifts due to their lift-enhancing characteristics (Zaccai et al., 2016). However, the performance of these high-lift devices, e.g., lift-to-drag ratio, is adversely affected by TE separation.

Moreover, unsteady force fluctuation on airfoils draws great interest in the aeronautical communities since it is critical to the lifetime of aerial vehicles and the safety of aviation. A series of experimental studies on various airfoils conducted by Broeren & Bragg (1998, 1999) revealed that the unsteadiness in TE separation can produce lift fluctuations that are similar to the ones generated by leading-edge separation. In addition, Broeren & Bragg (1998, 1999) showed that lift fluctuation is amplified when TE separation merges with leading-edge separation, and violent force fluctuation can be observed at pre-stall angles-of-attack (α). These examples show that TE separation control is crucial, and an adequate understanding of TE separation is required to develop an effective control strategy. Investigating the dynamics of TE separation through simple measurements can benefit the wind energy and aviation industries.

Hence, it is discernible that the potential solution falls into the category of separation control: postponing or suppressing the detachment of boundary layer (BL) to mitigate the separation zone. The recent development of the active flow control strategy shows the potential of effectively controlling the flow separation with fewer adverse effects than the passive devices, e.g., the drag penalty of vortex generators (Cattafesta III & Sheplak, 2011). For an active flow control strategy, the efficiency of flow control depends on how effectively the disturbance generated by the actuator interacts with the flow. This often demands a profound comprehension of the flow field. For example, identifying the approximate region requiring control necessitates a scrutiny of the time-averaged flow topology. Additionally, the formulation of a real-time control strategy is reliant on the successful detection of the undesired flow phenomenon. In the context of an unsteady flow phenomenon, it is imperative to investigate its source of unsteadiness and assess its influence on the signal outputted by a detector, e.g., wall-pressure sensor.

A comprehensive literature review has been undertaken concerning the aforementioned topics. The documented research has provided substantial background information on the topics such as the mean topology of TE separation and the associated unsteady force fluctuation. Nevertheless, the recognition of numerous research gaps indicates that there is room for further improvement in understanding TE separation; necessary knowledge is also missing in devising a successful detection strategy aimed at unsteady fluctuation. To provide the reader with a concise overview, a summary of the identified research gaps is presented in the following sections, along with the objectives and formulated approaches employed in this investigation.

1.2 Topology of stall cell

Regarding the mean topology of TE separation on thick airfoil, early studies have revealed that the separation zone exhibits a cellular pattern, through oil-flow (Weihs & Katz, 1983) and tufts (Yon & Katz, 1998) visualizations. The pattern is referred to as a stall cell (SC), and contradictory observations have been noted regarding its formation and behavior with increasing angle-of-attack (Boiko et al., 1996; Manolesos & Voutsinas, 2014b; Dell'Orso & Amitay, 2018). It was also observed that the vortex structures within SC, produced using similar flow setup, exhibit variation in response to controlled perturbation (Dell'Orso et al., 2016b; Dell'Orso & Amitay, 2018). The inconsistent observations of SC pattern in response to varying setup configurations indicate that the influence of varying flow conditions on SC requires further investigation. The lack of three-dimensional (3D) investigation on SC topology suggested that some observations may be constrained by the flow measurement technique. Furthermore, numerous studies reported that the SC pattern produced in their investigations were asymmetric in the spanwise direction (Weihs & Katz; 1983), which brings challenges in comparing the results of SC from different studies. Further investigation is needed to solve this issue. Note that more details regarding the background information of SC are provided in Section 2.2.1. In this investigation, the following approaches were adopted with the aim of addressing these issues to the best extent possible. First of all, full-span velocity fields were characterized at different angles-of-attack to gain deeper insights into the response of SC under various conditions. Additionally, the study delved into the 3D topology of SC to uncover the full picture of vortex structures in a SC. Leveraging the advantage of full-span measurements, the corner flow formed at the spanwise ends of wing could be characterized. The investigation therefore explored the possibility of employing vortex generators to mitigate the effect of corner flow on the symmetry of SC, offering insights into the source of asymmetry.

1.3 Low-frequency flow motion

Moving to the unsteady parts of TE separation, a review of turbulent separation bubble (TSB) in TE separation indicates that limited investigations were carried out to investigate the flow motion associated with the low-frequency force fluctuation. However, a broad look at the investigations of TSBs shows that the low-frequency flow motion can also be found in investigations of geometry-induced (Eaton, 1980; Casto, 1981; Eaton & Johnston, 1982; Kiya & Sasaki, 1983; Cherry et al., 1984; Castro & Haque 1987; Pearson et al., 2013) and pressured-induced TSB on flat plate (Patrick, 1987; Na & Moin 1998; Weiss et al., 2015; Mohammed-Taifour & Weiss, 2016; Eich & Kähler, 2020; Wu et al., 2020). Based on these investigations, the low-frequency force fluctuation is ascribed to the breathing motion, characterized by the large-scale expansion/contraction of the TSB. Hypotheses have also been proposed regarding the source unsteadiness of the breathing motion. However, a noticeable difference in flow configuration between TSB formed on airfoil and TSB formed in other flow configurations: the TSB on TE separation is confined by two shear layers and wing surface, while the TSBs formed in other configurations are bounded by a single shear layer and wall. This raises concern about whether the low-frequency flow motion in TE separation behaves similarly as the breathing motion observed in the aforementioned studies. Furthermore, it is uncertain whether the hypotheses from those studies are applicable to the TSB of interest in this investigation. More details on the low-frequency unsteadiness and breathing motion can be found in Section 2.2.2. The concerns mentioned above were addressed in this investigation by investigating the low-frequency unsteadiness in the velocity fields. Spectral analyses were performed to characterize the corresponding frequency range and to make comparison with literature. Furthermore, the energetic flow motions in the velocity fields were identified through modal decomposition analysis and was compared with the documented breathing motion. The results confirmed that the spatial variation of TSB in TE separation exhibited a different pattern compared to the document breathing motion induced on flat plate. The source unsteadiness responsible for the breathing motion was then probed through a coherence function between the TSB size and unsteadiness in the velocity fields, and hypothesis was proposed based on the current results.

1.4 Breathing motion detection

In the end, the relation between wall pressure and breathing motion has to be explored to develop a detection algorithm for the breathing motion. A brief survey of the literature indicates that only a few studies have investigated the relation between low-frequency wall pressure and velocity fields. A recent experimental investigation on pressured-induced TSB from Mohammed-Taifour & Weiss (2021) proposed a conceptual model to describe the impact of breathing motion on wall pressure: a contraction motion induces a reduction in wall pressure at the edge of TSB, while an increase in the TSB. Their discoveries significantly enhanced the understanding of the relation between breathing motion and wall pressure. Nevertheless, some crucial information for devising a strategy to detect breathing motion is still lacking. For instance, the optimal location for installing a sensor, and the phase relation between breathing motion and its manifestation in wall pressure. In particular, the actuation timing will heavily rely on the latter relation. More background information regarding the pressure-velocity relation is provided in Section 2.2.3. In this thesis, these two issues are addressed by conducting simultaneous wall-pressure and velocity measurements. The pressure-velocity relation in low-frequency range is explored. The derived relation can be used to predict the breathing of TSB. The outcomes of this thesis have the potential to enhance the understanding of the mean topology of SC and can be beneficial in designing a strategy for detecting breathing motion in the future.

1.5 Thesis outline

The current investigation is broken into three projects to establish a coherent understanding of trailing-edge separation. The topics of time-averaged topology, unsteady motions and their impact on wall pressure are progressively investigated. The sequential progression of these projects unfolds as follows: project 1 initiates the investigation by characterizing the time-averaged two- and three-dimensional topologies of trailing-edge separation. Subsequently, project 2 explores the unsteady behavior of the turbulent separation bubble. Finally, project 3 investigates the impact of the low-frequency unsteady motions on wall pressure. This thesis is paper-based, and the organization of the thesis is outlined below:

- Chapter 2 introduces the background information on flow separation on airfoils. The present study mainly focuses on the turbulent separation bubble in trailing-edge separation. This chapter is, therefore, further expanded regarding the trailing-edge separation, which includes literature reviews on the unique cellular structure — stall cell, unsteady behavior, and the corresponding impact on wall pressure.
- Chapter 3 provides information on the experimental methodologies employed in this study. It includes the details of the wind tunnel, two-dimensional wing, particle image velocimetry, Shake-the-box algorithm, novel helium-filled soap bubble system, and spectral proper orthogonal decomposition.
- Chapter 4 (project 1) presents the published results of the near-wall topology of trailing-edge separated flow at pre-stall angles-of-attack. The effect of varying the angle-of-attack on the development of stall cells is discussed. The three-dimensional topology of the stall cell is characterized. In addition, the possibility of employing vortex generators to address the asymmetry in stall cell patterns is explored. The results enhance the understanding of trailing-edge separation with a turbulent boundary layer.
- Chapter 5 (project 2) is based on the published results regarding the unsteadiness in the trailing-edge separation. Spectral analysis is performed to characterize the unsteadiness in the turbulent separation bubble and the shear layers surrounding it. Hypothesis regarding the source of unsteadiness responsible for the low-frequency flow motion in trailing-edge separation is discussed.

- Chapter 6 (project 3) is derived from a manuscript that has been submitted. The chapter demonstrates the relation between the breathing motion and wall-pressure fluctuations in trailing-edge separation. The optimal location to sense the breathing motion using wall pressure is assessed. Moreover, the phase relation between the two is investigated. The results can be utilized to develop a detection strategy for real-time identification of the breathing motion.

Chapter 2. Flow separation on airfoils

This chapter provides background information on separated flow on airfoils, commencing with fundamentals on different types of stalls and their corresponding separations (Section 2.1). As the primary focus of this thesis is on TE separation, the literature review is further expanded further on this topic (Section 2.2), covering its time-averaged flow topology and unsteady characteristics. Towards the end of this chapter, a brief review of the relation between wall pressure and the energetic motion in TE separation is also provided.

2.1 Stall type

Flow separation on airfoils is known as a root cause of airfoil stalls at low speeds. During the process, the forward-moving boundary layer departs from the wing surface, forming a separation zone that grows in size as α increases. This usually leads to a disruption of the pressure distribution on the wing surface and will adversely impact the aerodynamic performance of aerial vehicles, e.g., loss of lift and increase in drag. The phenomenon also exhibits unsteady features, which instigate stall flutter (Zaman et al. 1989) that can potentially damage aerial vehicles. Based on the time-averaged characteristics of flow, the aerodynamic stall is categorized into three types: leading-edge (LE) stall, thin-airfoil stall, and TE stall (Jones, 1933; McCullough & Gault, 1951; Broeren & Bragg, 1998; Bak et al., 1999). A conceptual illustration of three types of stalls is presented in Figure 2.1, depicting the relation between lift coefficient and α.

The first type of stall is LE stall, where separation occurs near the LE of an airfoil (Broeren & Bragg, 1998). It is commonly seen on airfoils with a moderate thickness (Bak et al., 1999). Prior to the stall, a small laminar separation bubble formed near the LE. With increasing α, the separated flow fails to reattach and leads to "bursting" at the stall α (Ward, 1963). This results in a dramatic decrease in lift force as illustrated in Figure 2.1 (Tuck, 1991; Bak et al., 1999). Here, the stall α corresponds to maximum steady lift.

The second type, thin-airfoil stall, is relevant to the first one since the flow separation occurs close to the LE (Broeren & Bragg, 1998). This type of stall is typically encountered on airfoils with sharp LE and low-thickness airfoils with rounded LE (Bak et al., 1999). As a thin airfoil approaches the stall α, a laminar separation bubble forms near its LE. The reattachment point gradually moves downstream with further increase in α. The reattachment process ensures that the airfoil does not experience in a catastrophic loss of lift during stall as depicted in Figure 2.1 (Bak et al., 1999).

The third type of stall is TE stall, where flow separation happens at the aft section of a wing (Broeren & Bragg, 1998) and is mostly seen on wings with thick airfoil profiles (Bak et al., 1999). TE stall differs significantly from the two types of stalls introduced above, as the separation happens at a location farther downstream. TE separation is triggered by an adverse pressure gradient (APG) developed along the wing surface. The forward-moving boundary layer departs from the wing surface and forms a separation bubble with an intermittent detachment point. The detachment point progressively moves upstream as α increases. Similar to thin-airfoil stall, TE stall does not exhibit a dramatic reduction of lift at α beyond the stall angle.

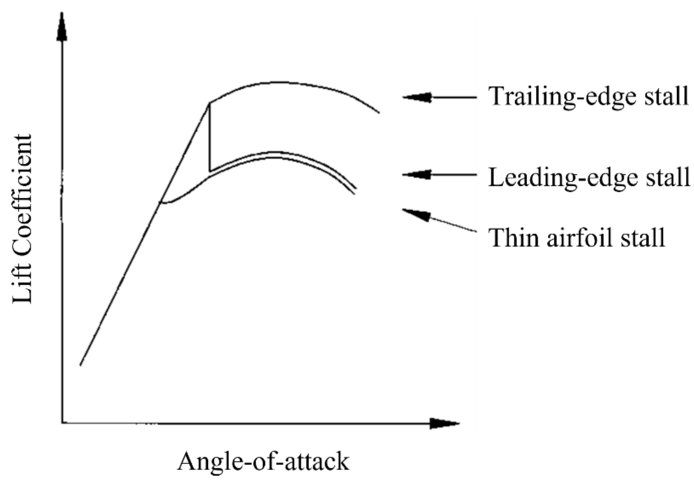

Figure 2.1. A conceptual sketch of three types of stalls (Bak et al., 1999). The copyright holder grants permission for the usage of figure.

2.2 Trailing-edge separation

As previously introduced, TE separation is induced by an APG, resulting from the mild curvature of an airfoil. This pressure gradient reduces the streamwise momentum of the forward-moving TBL on the suction side of the wing, causing the TBL to separate from the wing surface. An illustration of TE separation is provided in Figure 2.2, where two shear layers, namely upper and lower shear layers emerge from the suction and pressure sides of the airfoil, respectively. The blue contour represents a triangular-shaped mean TSB, and the red dots indicate its vertices. The upstream vertex on the wing surface is annotated as the mean detachment point. The most downstream vertex is the end point of the separation bubble. The last vertex is at the TE, where the separated flow is forced to reattach.

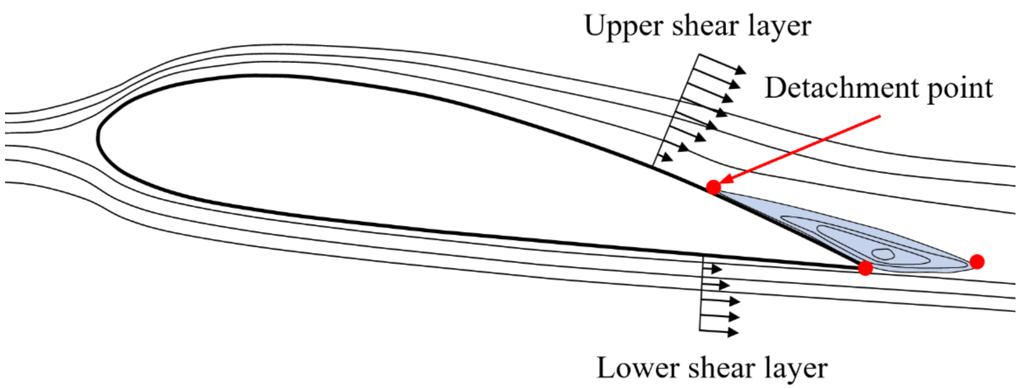

Figure 2.2. A schematic drawing of TSB in TE separation.

2.2.1 Stall cell

In TE separation, the TSB is not a simple two-dimensional (2D) flow that is uniform in the spanwise direction. In most applications, including flow over 2D wings, the separated flow is three-dimensional, and separation occurs along an axis, where the streamlines converge and lift up from the surface. This axis passes through a saddle-type critical point and is known as a separation/detachment line (Tobak & Peake, 1982; Délery, 2013).

The skin-friction patterns obtained from different visualization techniques have often been used to identify different topologies associated with separated flows. An early oil-flow visualization conducted by Moss & Murdin (1971) showed a large mid-span separation zone with two wall-normal counter-rotating vortices on a NACA 0012 airfoil. Using the same visualization technique, Dell'Orso & Amitay (2018) also showed that a 2D wing exhibits different separation patterns including an asymmetric full-span separation, 3D separation with mid-span recirculation, or 3D separation with one or multiple stall cells (SCs). The corresponding oil-flow patterns are demonstrated in Figure 2.3(a), (b), and (c), respectively. In particular, the cellular organization SC has drawn a great amount of attention. Oil-flow (Weihs & Katz, 1983) and tufts (Yon & Katz, 1998) visualizations demonstrated that the SC has an arc-shape separation front that both ends spiral into two counter-rotating foci. The formation of SC is shown to depend on airfoil shape and flow conditions. For example, Broeren & Bragg (2001) did not observe the SC pattern on thin airfoils with leading-edge flow separation. They observed SCs only for thicker airfoils with TE separation. Dell'Orso & Amitay (2018) observed SCs on 2D wings with NACA 0015 profile at moderate to high chord-based Reynolds number (Re_c = 10^5 to 10^6). Moreover, the SC pattern has been observed on wings at both pre-stall α (Boiko et al., 1996; Manolesos & Voutsinas, 2014a; Ma, Gibeau, & Ghaemi, 2020) and post-stall α (Moss & Murdin, 1971; Winkelman & Barlow, 1980; Winkelmann, 1981; Yon & Katz, 1998; Dell'Orso et al., 2016).

(a) (b) (c)

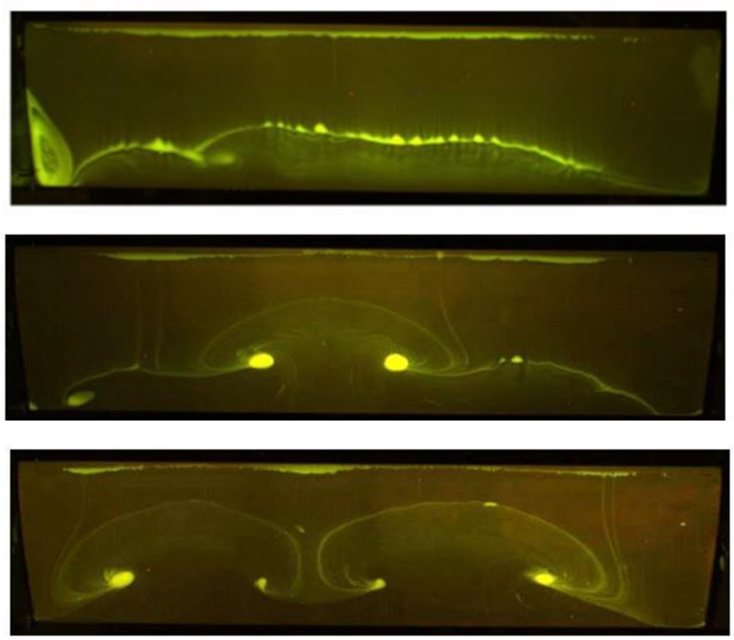

Figure 2.3. Oil-flow visualizations of (a) an asymmetric full-span separation, (b) 3D separation with mid-span recirculation, and (c) 3D separation with two SCs (Dell'Orso & Amitay, 2018). The copyright holder grants permission for the usage of figure.

Several investigations were conducted to investigate the impact of different experimental conditions including on the SC patterns. It was found that both wing aspect ratio (AR), α, and Re_c can influence the SC patterns. For instance, Winkelmann & Barlow (1980) demonstrated that the number of SCs increased when AR increased from 3 to 12 for a Clark Y airfoil at a post-stall α of 18.4° and Re_c of 3.85×10^5. A subsequent investigation from Weihs & Katz (1983) formulated a linear relation between the number of SCs and AR, based on their oil-flow visualization and crow-type instability (Crow, 1970). The relation was also supported by the experimental investigation of SC structures by Yon & Katz (1998) on a post-stall NACA 0015 airfoil at $\alpha = 17°$ and Re_c of 6.2×10^5. They observed that the number of SCs was proportional to AR using tuft visualization. Moreover, the number of SCs observed by the recent investigation of Dell'Orso & Amitay (2018) agreed with the relation proposed by Weihs & Katz (1983).

Unlike the relation between the number of SC and AR, a brief review of the investigations on other experimental conditions (α and Re_c) showed some contradicting observations. Boiko et al. (1996) observed five SCs at $\alpha = 9.1°$, and the number of SC reduced to one large SC covering the full span of the wing as α increased to 18.4°. While α was increasing, it was seen that the cellular structures expanded and merged. In contrast to the observation of Boiko et al. (1996), Dell'Orso & Amitay (2018) reported that with increasing α (15° to 21.5°), the flow pattern developed from an asymmetric full-span separation into a single SC, and eventually into a dual SC pattern. The disagreement in results from Boiko et al. (1996) and Dell'Orso & Amitay (2018) was possibly due to the differences in the airfoil shape. Regarding the effect of Re_c, Dell'Orso & Amitay (2018) showed that at a fixed α of 17°, the flow pattern changed from an asymmetric full-span separation to an asymmetric SC with increasing Re_c from 3.02×10^5 to 4.47×10^5. They also observed a minimum Re_c to have SC formed. This critical Re_c was observed to increase with increasing α. However, this appears to contradict the results of Manolesos & Voutsinas (2014) in which the critical Re_c reduced with increasing α. It is important to note that the experiment of Manolesos & Voutsinas (2014) was conducted at higher Re_c from 5×10^5 to 1.5×10^6, and the wing was at pre-stall α from 6° to 9°. The differences in flow conditions add more complexity to understanding the experimental results from different works.

In the experimental investigations of SC, it was found that most experiments encountered an issue of lacking spanwise symmetry in SC patterns. Previous tuft (Yon & Katz, 1998), and oil-flow visualizations (Winkelman & Barlow, 1980; Winkelmann, 1981; Weihs & Katz, 1983; Schewe, 2001; Dell'Orso & Amitay, 2018; Garland et al., 2019) showed that the pattern of multiple SCs is usually asymmetric in the spanwise direction. The size of each SC is inconsistent across the span and the organization is asymmetric. This is also exhibited in separated flows with only one SC, where the centerline of the SC may deviate from the midspan of the wing (Broeren & Bragg, 2001; Manolesos & Voutsinas, 2014a; Ragni & Ferreira, 2016; Dell'Orso & Amitay, 2018). An example of an asymmetric SC that deviated from the midspan is presented in Figure 2.4. It is speculated that the asymmetries are due to factors such as dissimilar corner flows near the spanwise ends of the airfoil, imperfections of the airfoil, and non-uniformity of the freestream flow. The asymmetry in SC patterns of the previous investigations complicates the comparison of experimental results and brings challenges to the repeatability of experiments. To better understand the dynamics of SC under different experimental conditions, it is of interest to identify the source of asymmetry and to produce symmetric SCs.

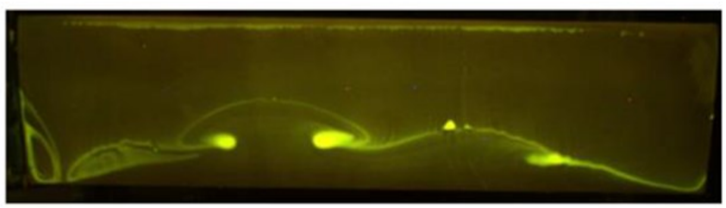

Figure 2.4. Oil-flow visualization of a SC pattern that lack spanwise symmetry and deviates from the midspan (Dell'Orso & Amitay, 2018). The copyright holder grants permission for the usage of figure.

2.2.2 Low-frequency unsteadiness and breathing motion

Numerous studies reported the existence of low-frequency force fluctuations on airfoils with TE separation at α prior to the stall (Carmichael, 1981; Mueller, 1985; Zaman et al., 1987). The fluctuations typically have frequencies much smaller than the vortex shedding frequencies and produce force fluctuations much larger than the ones related to bluff-body shedding (Zaman et al., 1989). However, not many investigations were carried out to probe the physics behind the low-frequency unsteadiness since the aerodynamic communities originally treated it as an inherited nuisance from the experimental setup instead of a hydrodynamic phenomenon (Zaman et al., 1989). It was only until the late 1980s, its hydrodynamic nature was revealed by Zaman et al. (1989) in their experimental investigation of flow past various 2D wings. Zaman et al. (1989)

suggested that the low-frequency force fluctuations are related to the periodic switching between stalled and unstalled states and the fluctuations only take place when a closed separation bubble was formed, e.g., in trailing-edge stall and thin-airfoil stall. It is reasonable to expect that the fluctuations originate from some energetic flow motions associated with the dynamics of the separation bubble.

More insights into the low-frequency force fluctuation were provided by Liu & Xiao (2020) through numerically simulating a TE separated flow over a NACA 0015 airfoil. In their investigation, the lift fluctuations of a NACA 0015 airfoil at near-stall α exhibited high coherence with the low-frequency expansion/contraction of separation zone at a St_h = 0.013. The St_h is very similar to the one reported by Zaman et al. (1989) and Broeren & Bragg (1998) and their results suggested the low-frequency force fluctuation was attributed to the large-scale spatial variation of the separation zone, which is commonly referred to as the "breathing motion" by literature. A recent experimental investigation of TE separated flow on a NACA 4418 wing also demonstrated that the TSB featured a breathing motion with a St_h of 0.05. They attributed this flow motion to the unsteadiness related to vortex shedding process, which had a spatial-averaged frequency on the order of St_h = 0.01.

A survey of the investigations of TSBs shows that the low-frequency flow motions are not limited to pressure-induced separation on airfoils. Apart from the ones related to airfoils, earlier observations of this low-frequency flow motion were reported in investigations of geometry-induced TSBs, where the separation is generated by geometric singularities. Eaton (1980) first reported the backward-facing step generated TSB contains low-frequency flow motions. Similar low-frequency motions were reported in TSBs formed by flat plates mounted perpendicular to the freestream (Castro & Haque, 1987), two- and three-dimensional surface-mounted blocks (Castro, 1981), more investigations on flows with backward- and forward-facing steps (Eaton & Johnston, 1982; Camussi et al., 2008; Pearson et al., 2013), and the leading-edge of blunt plates (Kiya & Sasaki, 1983; Cherry, Hilier, & Latour, 1984). In these cases, the TSBs expanded/contracted through the intermittent behavior of the detachment and reattachment point, depending on the geometry. When scaled by L — a characteristic length of the geometry, e.g., the step height or plate thickness, the Strouhal number St_L of the low-frequency motions was found to range from 0.08 to 0.2, while the vortex shedding process was generally at a higher range of frequencies $St_L = 0.5$ to 1.0 (Trünkle et al., 2016).

In geometry-induced TSBs, the low-frequency expansion/contraction of TSBs is attributed to the flapping motion of detached shear layers (Eaton, 1980). In an experimental investigation of a TSB generated by a backward-facing step, Eaton & Johnston (1982) first hypothesized that the flapping motion is generated due to an instantaneous imbalance of the entrainment and reinjection of fluid between the shear layer and the recirculating zone. The imbalance of fluid exchanging has a frequency much lower than the vortex shedding frequency and is suggested to associate with the modulation, pairing, or interruption of the vortex shedding process (Kiya & Sasaki, 1983; Cherry, Hilier, & Latour, 1984; Driver et al., 1987). A different hypothesis was proposed by Pearson et al. (2013) when considering a TSB of a forward-facing step. Pearson et al. (2013) attributed the flapping motion to the perturbations induced by the upstream TBL. Here, the driving unsteadiness originates from the streamwise-elongated low- and high-velocity motions of the incoming TBLs (Adrian et al., 2000; Hutchins & Marusic, 2007). Pearson et al. (2013) observed that the TSB expanded or contracted simultaneously in both the streamwise and wall-normal directions, which was like the ones observed in TE separation. The flapping of the shear layer modified the overall volume of the TSB, which is known as the “breathing” motion. It is obvious that the mechanisms proposed by Eaton & Johnston (1982) and Pearson et al. (2013) are different due to the difference in flow configuration. The TSB of Eaton & Johnston (1982) was downstream of a backward-facing step, and the spatial variation of the recirculation zone was mainly due to an intermittent reattachment point. In contrast, the TSB of Pearson et al. (2013) was produced upstream of a forward-facing step and featured an intermittent detachment point and stagnation point. These observations suggest that the mechanism responsible for the breathing motion in TSBs is configuration dependent. 1

Note that most of the investigations regarding the low-frequency motions were conducted in fixed-separation flows, where the detachment point of a TSB is tied to the location of the geometric singularity. A better comparison with TE separation should consider pressure-induced TSBs on a flat plate, where the departure of TBL is due to an APG and the detachment point is intermittent on the wall (Wu et al., 2020). For clarification, an example of TSB on a flat plate is demonstrated in Figure 2.5, in which the TSB is presented in blue contour and the detachment and reattachment points are annotated using red dots.

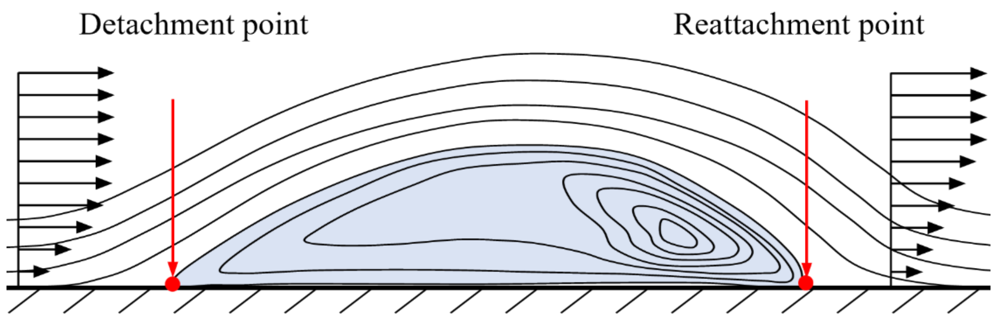

Figure 2.5. A schematic view of turbulent separation bubble formed on a flat plate.

A recent investigation on pressure-induced TSB was performed by Mohammed-Taifour & Weiss (2016) using high-speed planar particle image velocimetry (PIV) measurements. In their experiment, the TSB was induced on a flat plate using an opposing converging-diverging wall. They performed proper orthogonal decomposition (POD) analysis and reconstructed the mean streamwise velocity field $\langle U \rangle$ using the leading POD mode to determine the flow topology associated with the breathing motion. As shown in Figure 2.6, Mohammed-Taifour & Weiss (2016) observed that the TSB undergoes large-scale expansion and contraction (solid white line) from the reconstructed contours of mean streamwise velocity $\langle U \rangle$ corresponding to the maximum (Figure 2.6a), near-zero (Figure 2.6b), and minimum (Figure 2.6c) temporal coefficient $a^1(t)$. From their previous work, they determined the breathing motion has a $St_l \approx 0.01$, while the vortex shedding was at a higher frequency of $St_l \approx 0.35$ (Weiss et al., 2015). Here, St_l is defined based on the characteristic length l of the separation bubble. In contrast, a recent DNS by Wu et al. (2020) showed that a TSB induced only by an APG on a flat plate exhibited low-frequency motions at $St_l = 0.45$, which was 2-3 times smaller than the St of the vortex shedding process. In this numerical investigation, when the TSB was induced using an APG followed by a forward pressure gradient (FPG), the low-frequency fluctuations disappeared. Wu et al. (2020) attributed this behavior to the forced attachment of the shear layer by the imposed FPG. Although the TSB in the work of Wu et al. (2020) was induced by an APG, this flow configuration is still not a true representation of TE separation since the reattachment point is allowed to oscillate. As it is shown in the current investigation, TE separation forms a triangular-shaped TSB that is different from the dome-shaped TSBs that form on flat plates. The first vertex of the triangular-shaped TSB is the intermittent separation point, the second vertex is pinned at the trailing edge, and the third vertex extends into the wake region downstream of the TE. TE separation also has an additional shear layer that forms by the separation of the pressure-side boundary layer at the airfoil TE. This shear layer plays an important role in fluid entrainment and wake dynamics (Cicatelli & Sieverding, 1997; Ozkan, 2021).

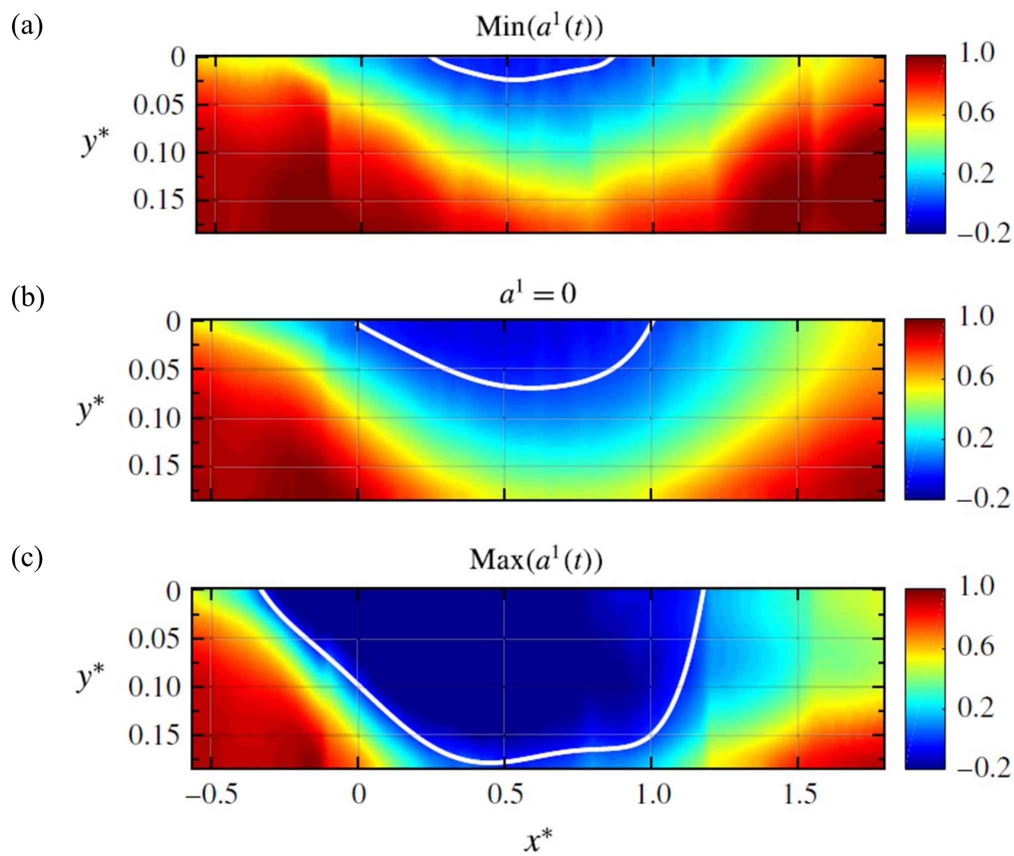

Figure 2.6. Contours of the mean streamwise velocity, associated with the leading POD mode (a) minimum temporal coefficients Min($a^1(t)$), (b) near-zero temporal coefficient $a^1(t) \approx 0$, and (c) maximum temporal coefficient Max($a^1(t)$) (Mohammed-Taifour & Weiss, 2016). The contour of $\langle U \rangle = 0$ is represented by the solid white line. The copyright holder grants permission for the usage of figure.

There are several differences between the observations of Wu et al. (2020) using DNS and the experiments of Weiss et al. (2015) and Mohammed-Taifour & Weiss (2016). First, the low-frequency oscillations in Wu et al. (2020) were at $St_l = 0.45$, while Weiss et al. (2015) observed the low-frequency motions at $St_l = 0.01$. Second, Wu et al., (2020) observed the low-frequency oscillations close to the reattachment location, whereas Weiss et al. (2015) and Mohammed-Taifour & Weiss (2016) detected them near the separation location. Third, Wu et al. (2020) did not observe any low-frequency motion when a suction-blowing boundary condition was used for generating the TSB, which is similar to the APG followed by FPG boundary condition applied by Weiss et al. (2015) and Mohammed-Taifour & Weiss (2016). These apparent contradictions can be explained by noting the differences in the flow conditions between studies. The DNS of Wu et al (2020) was carried out using a TBL at $Re_\theta = 490$, which is quite different than the $Re_\theta = 5{,}000$ TBLs studied by Weiss et al. (2015). At such high Re_θ, the TBL contains large-scale motions that populate the logarithmic and lower wake regions of high-Reynolds-number TBLs (Guala et al., 2006; Hutchins & Marusic 2007). In addition, the APG applied in the work of Wu et al. (2020) produced a TSB with a fixed separation line, which no longer oscillates and contributes to the spatial variation of TSB. The TSB from the work of Mohammed-Taifour & Weiss (2016), have an oscillation detachment point, as indicated by the most upstream Another striking difference is the longer extent of the reattachment region featured by the TSB of Wu et al. (2020). More specifically, the region between forward-flow fractions of $\gamma = 0.2$ and 0.8 extended over a length equal to l in Wu et al. (2020), while this zone was approximately equal to $0.2l$ in the studies of Mohammed-Taifour & Weiss (2016). The longer reattachment length in Wu et al. (2020) was due to the lack of a FPG boundary condition, thus allowing the separated shear layer to gradually attach. Finally, computational limitations may also contribute to the discrepancies. The smallest St_l resolved by Wu et al. (2020) was 0.2, which does not allow inspecting lower frequencies.

The mechanisms that are proposed for the low-frequency fluctuations in pressure-induced TSBs are similar to those suggested for geometry-induced TSBs. Na & Moin (1998a) associated the low-frequency fluctuations with the intermittency of the reattachment point due to large arch-type vortical structures. The latter structures potentially formed from the agglomeration of smaller Kelvin-Helmholtz vortices. Since the arch-type vortices transport fluid in the wall-normal direction, this observation is consistent with the proposed mechanism based on the imbalance between fluid entrainment and reinjection in geometry-induced TSBs. The recent DNS of Wu et al. (2020) also demonstrated large-scale vorticity packets that resulted in intermittent displacements of the reattachment location and flow fluctuations at $St_l = 0.45$. Using dynamic mode decomposition, Wu et al. (2020) observed streamwise-elongated structures that cover the full length of the TSB and break down into large-scale vorticity packets. They suggested that Görtler-type instabilities (Görtler, 1954) amplify the perturbations of the incoming TBL and generate the streamwise-elongated structures. The latter hypothesis also points to the incoming TBL as a source for the low-frequency fluctuations and is supported by several recent numerical studies (Priebe et al., 2016; Pasqiariello, Hickel, & Adams, 2017; Yon et al., 2021).

In a recent experimental investigation, Mohammed-Taifour & Weiss (2021) showed that transient forcing of the incoming TBL using pulsed-jet actuators first influences the separation point and then the reattachment location. They also observed that the time required for the flow to recover from the controlled state was of the same order of magnitude as the timescale of the low-frequency breathing motions. Their findings suggest the breathing motion is a response of the TSB to the upstream perturbations. The perturbations of the upstream flow first affect the separation point and then indirectly affecting the reattachment point through large-scale pressure fluctuations (Mohammed-Taifour & Weiss, 2021). Mohammed-Taifour & Weiss (2021) pointed out that the TSB acts as a low-pass filter, which converts the higher-frequency unsteadiness of the incoming flow to low-frequency flow motion. This process is similar to the spatial-averaging effect of shear layer entrainment observed by Wang & Ghaemi (2022). The additional impact of large-scale motions of the incoming TBL on the separation line was demonstrated by Eich & Kähler (2020). By investigating the TSB of a flat plate, they showed that large high-speed motions within the incoming TBL push the separation location in the downstream direction while large low-speed motions result in an upstream displacement of the separation location.

2.2.3 Detecting breathing motion

As previously mentioned, the breathing motion contributes to the unsteady force fluctuations on a wing. To effectively address this unsteady behaviour, active flow control appears to be a suitable solution that offers advantages of flexible deployment timing and superior adaptability to changes in flow conditions (Gad-el-Hak et al., 2003; Collis, et al., 2004; Widerhold et al., 2010). In active flow control, controlled perturbations are introduced to the flow of interest in a feedforward or feedback loop. The control system needs to be equipped with real-time information of the flow state to ensure its effectiveness. For instance, the state of TSB, i.e., expansion or contraction, should be identified in order to adjust the behavior of actuator. This is often measured through a nonintrusive sensor such as a wall-pressure measurement device (Cattafesta & Sheplak, 2011; Greenblat et al., 2019). The utilization of wall-pressure measurement was also justified by Schubauer & Spangenberg (1960), who demonstrated a clear connection between wall-pressure distribution and flow separation effectiveness.

Once real-time wall pressure is measured, the detection strategy requires a relation between the wall pressure measurements and the state of the breathing motion. Such relation can be obtained by examining the pressure-velocity correlation for various locations of wall-pressure measurement. It can provide information necessary for flow control, such as the optimal location to install the pressure sensor and the appropriate timing to trigger the actuation. A relevant example of the former information is illustrated by Camussi et al. (2008) in an experimental study of geometry-induced TSB. Camussi et al. (2008) demonstrated that large-scale vortex shedding took place at the edge of a forward-facing step, and the advection of vortices over the separation bubble induced significant pressure fluctuations on the wall. The region upstream of the reattachment zone exhibited the strongest pressure-velocity correlation, which suggested it might be the optimal region for detecting the passage of large-scale vortices. Furthermore, an effective timing for actuation can be determined from the velocity-pressure phase relation. The necessity of this relation is demonstrated by Mohammed-Taifour & Weiss (2021) when they attempted to modulate the breathing of a pressure-induced TSB using periodic forcing upstream of the TSB. In their investigation, they employed a calorimetric sensor to track the direction of flow over a duration of time that encompassed the activation of the actuator. By statistically averaging the calorimetric sensor output of each duration over 90 actuation cycles, they obtained the forward-flow probability (γ) as a function of time. Mohammed-Taifour & Weiss (2021) noticed a time delay existed between enabling the actuator and the change in γ. Therefore, the effectiveness of active flow control can only be assured when the phase relation between the breathing motion and wall-pressure signal is accounted for.

A review of investigations on TSBs revealed that only a few studies have investigated the relation between low-frequency wall-pressure fluctuations and the velocity fields. In an experimental investigation of pressure-induced TSB on a flat plate, Mohammed-Taifour & Weiss (2016) performed synchronized wall-pressure and planar PIV measurements along the centerline of the flat plate. Their PIV measurement was carried out in a streamwise-wall-normal plane along with a wall-pressure fluctuation measurement at $0.4l$ upstream of the mean detachment point (MD), which corresponded to the incipient detachment (ID) position with $\gamma = 0.99$ (Simpson, 1989). Proper orthogonal decomposition (POD) was used to obtain a reduced-order model (ROM) of the flow field, which was then used to represent the breathing motion. Their investigation found a strong correlation between the temporal coefficient of the leading POD mode and the wall-pressure fluctuation. Upon inspecting the time traces of the two signals, they proposed that the rise and fall of wall pressure was associated with the expansion and contraction of the TSB, respectively. However, the necessary phase relation between the breathing motion and wall-pressure fluctuation was not investigated in their study and the correlation was only done for the wall-pressure fluctuation measured near ID. Therefore, the phase relation and the optimal location for detecting the breathing motion are still unclear. In a follow-up investigation, Le Floc'h et al. (2020) examined the wall-pressure signature of the breathing motion from a family of TSBs with different sizes. They showed that the amplitude of wall-pressure fluctuation increases with the size of TSB. More details regarding the relation between the breathing motion and wall pressure were provided in a subsequent investigation by Mohammed-Taifour & Weiss (2021). They carried out synchronized wall-pressure measurements at numerous streamwise locations along the centerline of a pressure-induced TSB on a flat plate. Mohammed-Taifour & Weiss (2021) then performed cross-correlation between wall pressure measured at different streamwise locations with respect to reference points outside of mean TSB and the result is shown in Figure 2.7a. They found that wall pressure measured inside and outside of TSB are inversely related. This observation agrees with the results derived from their earlier work (Mohammed-Taifour & Weiss 2016), based on the temporal coefficients of POD modes. They further provided a conceptual model regarding the impact of breathing motion on average wall pressure distribution, which is illustrated in Figure 2.7b. As depicted in Figure 2.7b, Mohammed-Taifour & Weiss (2021) suggested that an expanded TSB corresponding to an increase in wall pressure outside of the mean TSB and a decrease in wall pressure inside the mean TSB. A contracted TSB, however, corresponded to a reduction in wall pressure outside of the mean TSB and a rise in wall pressure inside the mean TSB. These findings greatly improved the understanding of the connection between breathing motion and wall pressure. However, a comprehensive pressure-velocity relation that can identify suitable sensor installation location for wall-pressure measurement and optimal actuation timing is not available yet.

(a)

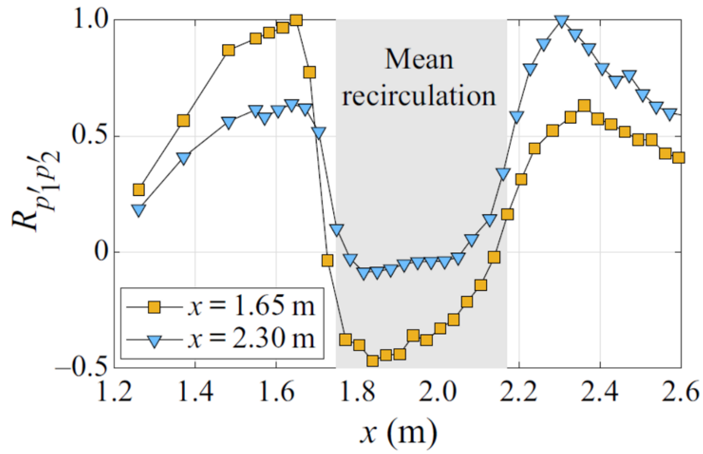

(b)

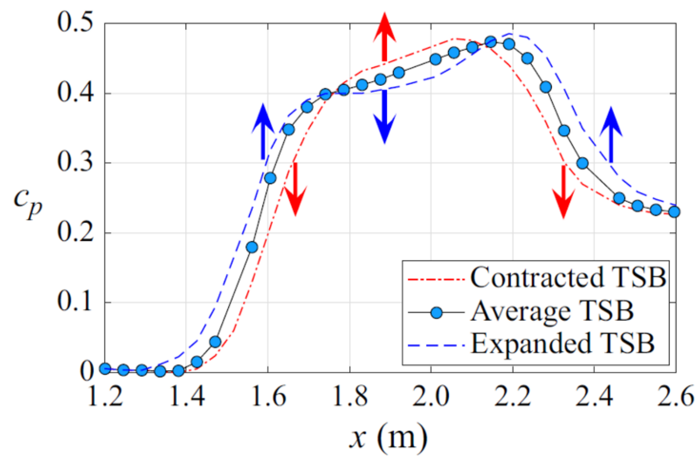

Figure 2.7. (a) The result of cross-correlation between the low-pass filtered wall-pressure fluctuations measured at x = 1.65 m and x = 2.30 m and a moving measurement point along the centerline of TSB (Mohammed-Taifour & Weiss, 2021). (b) A conceptual model of the effect of TSB breathing on pressure mean distribution (Mohammed-Taifour & Weiss, 2021). The copyright holder grants permission for the usage of figure.

Chapter 3. Experimental methodology

This chapter encompasses an overview of the experimental methodologies employed across the projects presented in this thesis. The introduction of flow facility and wing model is detailed in Section 3.1. Since all the experiments conducted in this work consistently utilized PIV technique, the principles of PIV measurements are reviewed in Section 3.2. To characterize the 3D topology of TE separation, state-of-art 3D particle tracking velocimetry (PTV) was employed. Its foundation Shake-the-box (STB) algorithm is thereby introduced in Section 3.3. Additionally, the novel seeding system specifically designed for large-scale 3D PTV measurements is elucidated in Section 3.4. Finally, Section 3.5 introduces the modal decomposition algorithm employed in this thesis to extract energetic flow motions.

3.1 Wind tunnel and airfoil

All the experiments in this investigation were carried out in a large two-story, closed-loop wind tunnel at the University of Alberta. A schematic model of the wind tunnel is illustrated in Figure 3.1a. The wind tunnel nozzle had a contraction ratio of 6.3:1, followed by a test section that is 1.2 m wide and 2.4 m tall. Previous measurements using hotwire anemometry showed that the free stream flow has very low turbulence intensity and non-uniformity in the test section (Gibeau et al., 2020). The flow direction is from left to right as indicated in Figure 3.1a.

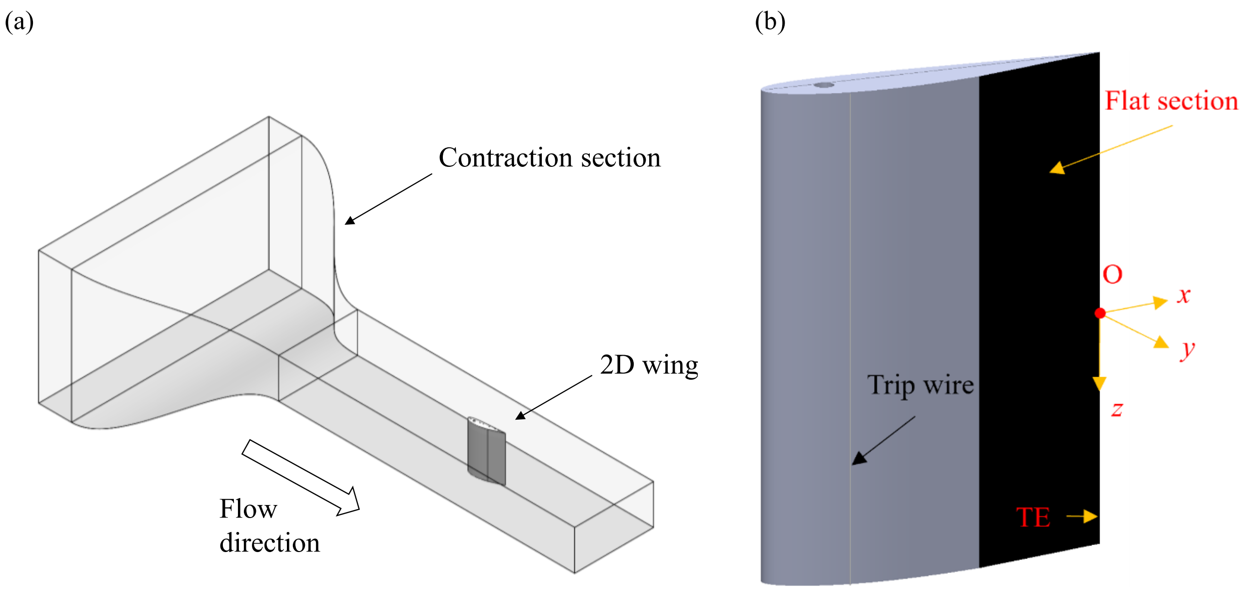

Figure 3.1. A schematic view of the wind tunnel with a 2D wing vertically installed in the test section.

Experiments were conducted on a two-dimensional wing with an AR of 1.2. The wing was mounted vertically within the test section with its spanwise ends mounted flush to the ceiling and floor. The wing featured a NACA 4418 airfoil cross-section and a chord length of c = 975 mm. As shown in Figure 3.1b, a full-span trip wire with a 1-mm diameter was installed at 0.2c downstream of the leading edge to ensure a uniform laminar-to-turbulent transition across the wingspan. The small curvature of the airfoil profile from 0.67c to the TE of the suction side was replaced with a straight line. A side-view comparison between the original NACA 4418 airfoil and the modified one is demonstrated in Figure 3.2. The main difference is highlighted in the enlarged view at TE, where it shows the reduction of the extent of "surface curving". This small modification resulted in a flat section, which is colored in black as seen in Figure 3.1b. This is suitable for wall-parallel PIV measurements. For more details regarding the wing, please refer to Appendix C.1. The origin of the coordinate system, which is illustrated by point O in Figure 3.1b, was placed at the center of TE. The streamwise, wall-normal, and spanwise directions are denoted by x, y, and z, respectively.

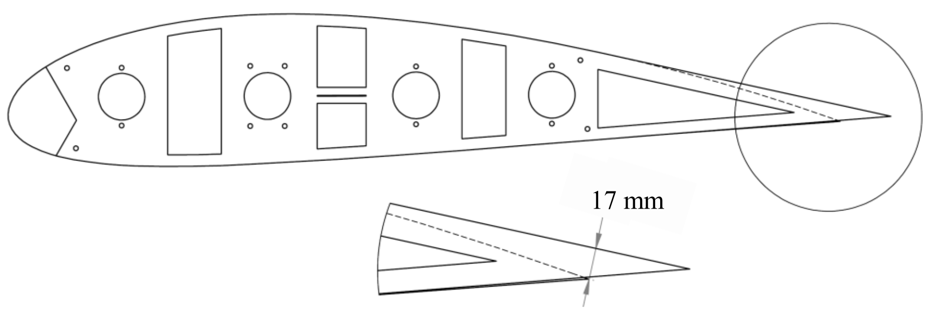

Figure 3.2. Comparison between the original (dashed line) and modified (solid line) NACA 4418 airfoils.

3.2 Particle image velocimetry

In this investigation, the velocity fields in the TE section of wing are obtained through the particle image velocimetry (PIV). The technique was initially developed to address the need for non-intrusive and quantitative measurements of flow fields. The technique was initially developed during the 1980s, and was widely adopted within both the fundamental and industrial research communities by the late 1990s. Since then, the PIV technique experienced rapid advancement, primarily attributed to the leaps in both imaging and computer technologies. Currently, the PIV technique allows for investigating three-dimensional flow fields in a time-resolved manner.

For the sake of brevity, this section only introduces the most basic two-components two-dimensional (2C-2D) PIV setup. The essential components of a 2C-2D PIV setup are detailed in Figure 3.3, which illustrates a schematic view of velocity measurements in a wind tunnel (Raffel et al., 2018). As shown in Figure 3.3, the PIV setup consists of several subsystems, including: seeding, illumination, and recording (Raffel et al., 2018).

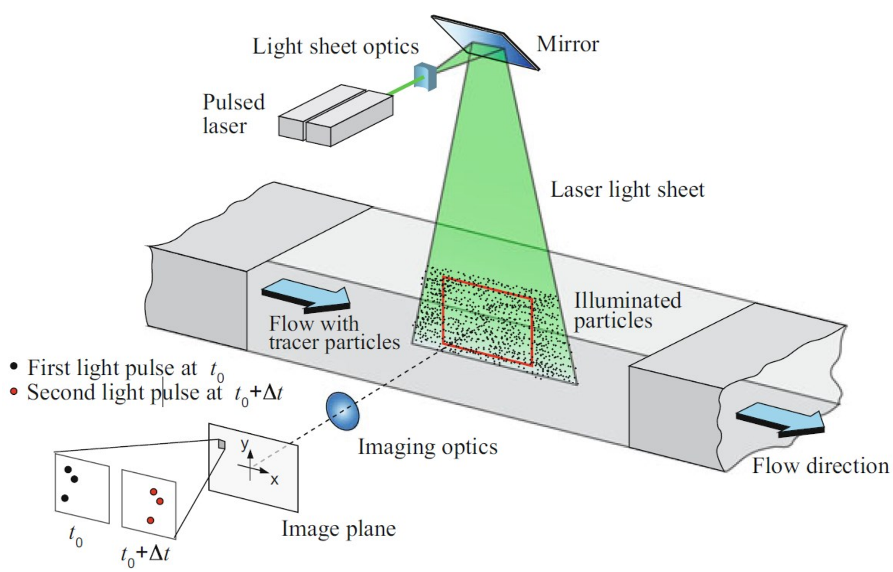

Figure 3.3. Experimental arrangement for a PIV setup in a wind tunnel (Raffel et al., 2018). The copyright holder grants permission for the usage of figure.

During the experiment, seeding particles are added to the flow to trace the flow motion. To ensure that particles can faithfully follow the flow motion, it's important to make careful selection of seeding particles for different fluids. As the seeding particle is subjected to gravitational force, the particle selection should consider the influence of fluid properties, particle diameter and particle density (Raffel et al., 2018). As shown in Figure 3.3, the illumination system consists of a pulsed laser, while emits a laser beam towards the seeded flow. The beam is expanded through a combination of optics to produce a thin light sheet. The seeding particles within the light sheet are illuminated twice with a short time interval Δt, defined by the time delay between laser pulses. The recording system is also presented in Figure 3.3, which captures the position of seeding particles and stores them in 2D images. The recorded images will then be processed through cross-correlation algorithm to determine the particle displacement that corresponds to Δt.

As detailed by Raffel et al., (2018), the principle of cross-correlation for PIV images is explained in Figure 3.4, in which an interrogation window $I(m,n)$ from image 1 at time t_0 is cross-correlated with the interrogation window $I'(m,n)$ from image 2 at $t_0 + \Delta t$. Here, (m, n) represents the position of the window in pixel unit. Cross correlation I with I' provides a correlation peak, in which its position is the vector displacement d corresponds to the window at (m, n).

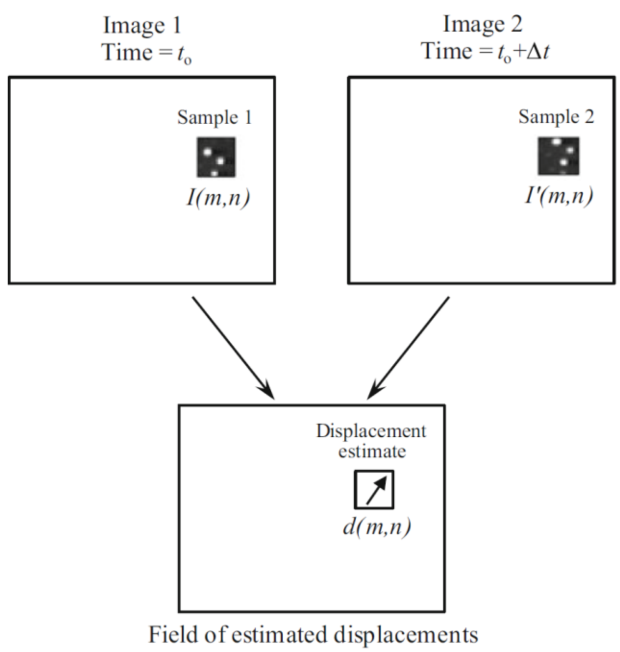

Figure 3.4. Cross-correlation between the sampled window at (m, n) from image 1 and image 2 produces a vector $d(m, n)$ for pixel displacement (Raffel et al., 2018). The copyright holder grants permission for the usage of figure.

3.3 Shake-the-box algorithm

The 3D topology of SC was investigated through large-scale 3D PTV measurements, based on the state-of-art STB algorithm (Schanz et al., 2016). The algorithm enables particle tracking to be performed at a high particle image density, up to 0.05 particles per pixel (ppp), by employing the method of 'Iterative reconstruction of volumetric Particle Distribution' (IPR) (Wieneke, 2013). Another advantage of STB is that it significantly reduces the computational cost compared to tomographic PIV (tomo-PIV) (Schröder et al., 2011). For instance, the number of variables need to be computed is dictated by the number of triangulated particles rather than the total number of voxels in the measurement domain. The procedures for performing STB algorithm are summarized into three phases, as described in the following context (Schanzet al., 2016).

The first phase is referred to as the initialization phase by Schanz et al. (2016). At this stage, no track information is available, and the first task is to identify a sufficient number of particles using the first few images. Schanz et al. (2016) pointed out that the initialization is typically performed over the first 4 time-steps, based on experience. The employment of a predictor is preferred to reduce the number of falsely detected particles. Based on the particle image density, a variety method including IPR, normal triangulation, and tomo-PIV reconstruction, can be used to determine the predictor. The positions of these identified particles are referred to as particle candidates by Schanz et al. (2016). Tracks are derived from these particles, and those that failed the meet the velocity and acceleration thresholds are discarded.

The next phase is the convergence phase, during which the tracks obtained from the previous step are utilized to predict the positions of particles in the following time-step. A Wiener filter is applied for the extrapolation of particle positions. The extrapolated positions are then "shaked" in all directions, followed by image matching techniques (Wieneke, 2013) that aim to minimize the intensity of residual images. The particles are reprojected using a calibrated optical transfer function (Schanz et al., 2012). Tracks related to ghost particles are deleted based on a threshold of particle intensity. Following by the initial shaking, the whole process will be iterated by 5 to 10 times to correct the errors in particle position prediction. To increase the number of tracks, new particles are identified from the residual images. The complexity in the reconstruction is significantly reduced, as the particle image density of residual images is lower due to the removal of previously identified particles. These images will be processed using the procedures introduced above in multiple iterations, until nearly all true particles are tracked (converged phase).

At a converged state, the number of true tracks does not change significantly as the number of particles entering the measurement volume is compensated by those leaving the volume. The triangulation process is limited to the particles that have newly entered the measurement volume The computational efficiency is largely improved as only minor deviations on the prediction need to be corrected. The tracks with particle left the measurement volume are terminated.

3.4 Helium-filled soap bubble system

In large-scale 3D PTV measurements, the laser energy was expanded over a large volume. Hence, it was essential to use large tracers that scatter sufficient light to obtain an adequate signal-to-noise ratio (SNR). For this reason, an in-house seeding system was employed to generate neutrally buoyant helium-filled soap bubbles (HFSB) with a mean diameter of approximately 0.5 mm (Gibeau & Ghaemi, 2018). The nozzles that generated HFSB bubbles were installed on a structure shown in Figure 3.5a and b. The structure had 4 modular ducts with 12 nozzles installed in each duct (a total of 48 nozzles). The nozzles pointed downward and were installed in a staggered pattern on the top plate of the duct. The ducts had a thin wall of 3 mm thickness. The structure had a supporting base with NACA 0012 profiles. The airfoils had a thickness of ~15 mm to reduce the flow blockage and downstream disturbances. The HFSB structure was placed in the settling chamber, upstream of the contraction section. The blockage of the HFSB structure increased the freestream turbulence intensity by approximately 0.1% and increased the non-uniformity of the mean flow by 0.8% (Gibeau et al., 2020). The HFSB system was only employed for the 3D PTV measurements and was removed from the test section during the planar-PIV measurements. A photo of the HFSB in operation is presented in Figure 3.5c. The modular ducts were vertically spaced to seed a rectangular measurement volume.

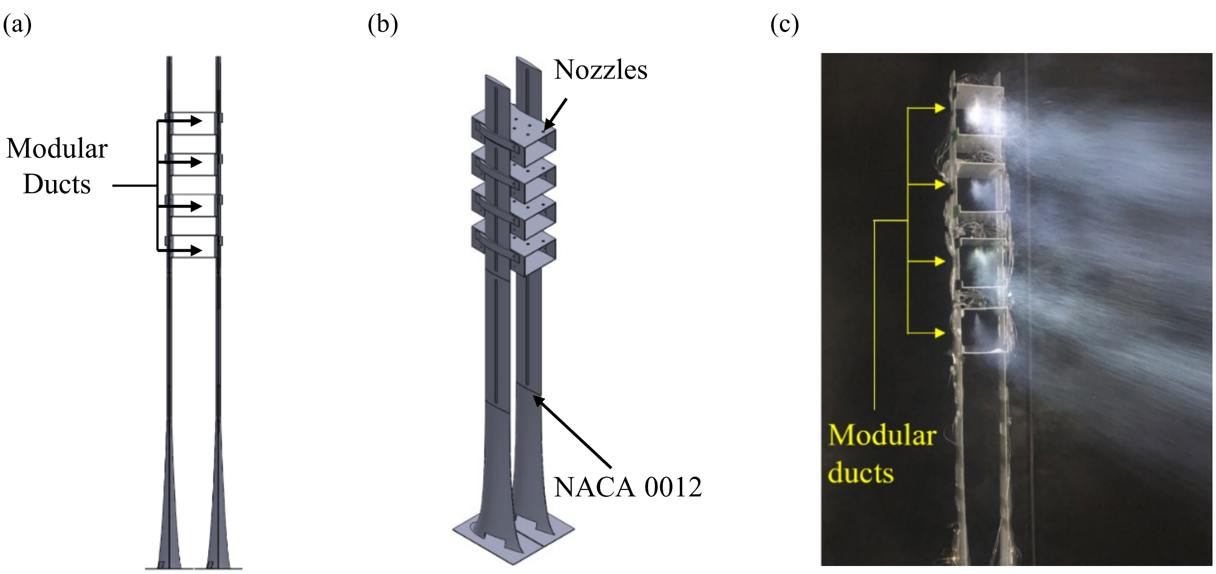

Figure 3.5. The (a) front, and (b) isometric views of the HFSB system. (c) A photo of the seeding system in operation.

3.5 Spectral proper orthogonal decomposition

Modal decomposition analyses have been extensively used in the field of aerodynamics to help extract significant flow features that are physically or temporally coherent. Such techniques can also help to identify flow features that are not easily recognizable through visual inspection and provides a low-order description of higher-order complex flow field (Taira, et al., 2017). In the context of flow field, proper orthogonal decomposition (POD) is one of the most widely adopted technique that being used to extract coherent flow structures (Lumley, 1970). Since its introduction, the dominant form of POD in the literature is space-only POD, which produces a set of spatially coherent modes that are modulated by expansion coefficients (Towne et al., 2018). The method offers the advantages of not requiring time-resolved flow data and is based on Galerkin projection of the Navier-Stokes equations (Aubry et al., 1988; Holmes et al., 1997; Noack et al., 2003). However, it only identifies the flow structures that are coherent in space as the decomposition is performed over the special correlation tensor.

In this investigation, the unsteady flow motions are explored. The identification of such flow motions requires us to determine the energetic flow motions that are both spatially and temporally coherent. The solution is by applying the POD method in a frequency domain. The corresponding method is known as the spectral POD (SPOD), while the conventional space-only POD is sometimes considered as an approximation of SPOD (George, 2017). The flow structures identified by the SPOD method are coherent both spatially and temporally, which is more suitable for identifying coherent structures that are physically meaningful (Towne et al., 2018). Note that the input flow data must be time-resolved to allow the spectral formulations of POD.

As detailed in several works (Schmidt et al., 2018; Schmidt & Colonius, 2020; Nekkanti & Schmidt, 2021), the SPOD computation starts with the construction of a snapshot matrix

$$Q = [q_1, q_2, \dots, q_M], \tag{3.1}$$

in which q is the fluctuating velocity field at one instance and M is the total number of snapshots. In this context, q is a column vector with a length of N, where N is defined by the number of grid points times the number of variables. Segmentation of Q is performed with a 50% overlap (Welch, 1967) to minimize the variance of the spectral estimates. The operation produces a total number of K segments, and each segmented Q is converted to the frequency domain through fast Fourier transform (FFT). The resulted $\hat{Q}$ is presented as,

$$\widehat{Q_K} = [\widehat{q_1}, \widehat{q_2}, \dots, \widehat{q_l}]. \tag{3.2}$$

Here, $\widehat{q_l}$ is a column vector of Fourier coefficients at frequency index l. The vector $\widehat{q_l}$ from each segment is then assembled into

$$\widehat{Q_l} = \left[\widehat{q_l^1}, \widehat{q_l^2}, \dots, \widehat{q_l^K}\right]. \tag{3.3}$$

For each frequency, the cross spectral density (CSD) matrix C_l is computed following (Schmidt & Colonius, 2020)

$$C_l = \frac{1}{K} \widehat{Q_l}^T \widehat{Q_l}. \tag{3.4}$$

For the l-th frequency, eigenvalue decomposition on C_l is performed by solving

$$C_l \Psi_l = \Psi_l \lambda_l. \tag{3.5}$$

The eigenvalues for the SPOD modes at l-th frequency are stored in the diagonal components of λ_l in a descending order. The l-th SPOD mode ϕ_l can be obtained from

$$\phi_l = \widehat{Q_l} \Psi_l. \tag{3.6}$$

In the end, a time-evolving SPOD mode at l-th frequency can be recovered by expanding the SPOD mode over time as $\phi_l e^{\mathrm{i}2\pi f_l t}$ (Nekkanti & Schmidt, 2021). Superimposing the mean flow field with the time-evolving SPOD mode allows to construct a reduced-order model (ROM) of the flow field. For instance, the U-component of the ROM based on the n-th SPOD mode at l-th frequency can be written as

$$U_{\mathrm{ROM}} = \langle U \rangle + \mathrm{Re}\left(\phi_{u,l}^n e^{i2\pi f_l t}\right), \tag{3.7}$$

where Re(…) indicating the real part of the complex number.

Chapter 4. Topology of trailing-edge separation

Chapter 4 serves as the summary of project 1, marking the inception of investigation into trailing-edge separation. In this chapter, the two- and two-dimensional topologies of stall cell are characterized. The effect of varying angle-of-attack on the stall cell pattern is thoroughly examined. Additionally, the exploration delves into the potential use of vortex generators to address the asymmetry issue in the stall cell pattern.

4.1 Introduction

Flow separation near the trailing edge (TE) of an airfoil is a complex flow phenomenon and is commonly seen on thick airfoils. Numerous studies pointed out that a highly 3D flow structure exists in the TE separation, where near-wall streamlines converge into a mushroom-shape separation front and lift up from the wing surface (Tobak & Peake, 1982; Weihs & Katz, 1983; Yon & Katz, 1998; Délery, 2013). It is observed that the separation front spirals into two counter-rotating foci and forms a unique cellular structure. The structure is known as stall cell (SC), and its pattern vary upon the change in flow conditions.

The structure of SC attracted a good amount of attention in the aerodynamic communities due to its unique cellular pattern. In addition, contradicted observations were made which showed a lack of understanding of SC. For instance, regarding how the SC change with respect to α, different observations were reported. A trend of decrease in the number of SC with increasing α was observed in the oil-flow visualizations made by Boiko et al. (1996). In their observations, the size of individual SC expanded and adjacent SCs merged as α increased. This led to a reduction in the number of SC with increasing α. However, the oil-flow visualization from Dell'Orso & Amitay (2018) showed an opposite trend, where a large SC broke into two SCs with increasing α. The reason why the opposite results are present is unclear. It is speculated that the difference in wing geometry is responsible for the contradicted observations. Regarding the aspect ratio (AR) of wing, both Winkelmann & Barlow (1980) and Yon & Katz (1998) suggested that the number of SC is proportional to the AR of a 2D wing. The comparison between experimental results also pointed out installing tip plate can increase the number of SC produced on a wing. Their studies showed that wing tip treatment may play a role in the formation of SC. However, these results are still unable to explain the contradicted merging and splitting process of SC with increasing α. Further investigations of the SC topology at various α are necessary.

Regarding the 3D topology of the SC, numerical and experimental works using stereoscopic PIV measurements were carried out to investigate the vortical structures in SCs (Manolesos & Voutsinas, 2014a; Dell'Orso et al., 2016; Dell'Orso & Amitay, 2018). Contradicted observations were made regarding the existence of the streamwise vortices in the SC. The comparison between the results from Dell'Orso et al. (2016) and Dell'Orso & Amitay were particularly interesting. Both works had similar experimental conditions, except the former one introduced upstream perturbations by installing a zig-zag tape on the wing surface near the leading edge, and no streamwise vortices were seen in the investigation. The latter work, however, captured a pair of counter-rotating streamwise vortices in the SC. The contradiction suggests that the understanding of how the 3D structures were developed is not well understood. More investigations on the 3D topology will benefit the understanding of SC formation.

In addition, the asymmetry issue in the SC pattern was another nuisance when investigating the SC. Numerous studies reported that the observed SC patterns were asymmetric in the spanwise direction (Winkelman & Barlow, 1980; Weihs & Katz, 1983; Yon & Katz, 1998; Broeren & Bragg, 2001; Schewe, 2001; Ragni & Ferreira, 2016; Dell'Orso & Amitay, 2018; Garland et al., 2019). The asymmetry issue is speculated to associate with the spanwise ends flows, which can be modified through different wing tip treatments or be affected by the inherited imperfections in experimental setup. The asymmetry in SC pattern usually makes comparison of results difficult and poses challenges in the repeatability of experiments. Moreover, determining the source of asymmetry could help understand the formation process of SC.

In this work, we aim to improve the understanding of SC by further investigating some contradicted observations from the literatures. The full-span near-wall SC pattern was investigated by conducting planar PIV measurements at various α. The near-wall streamlines across the entire span are plotted for each α to investigate how the topology of separated flow evolves with increasing α. Then, the 3D topology of the SC was characterized through large-scale 3D PTV measurements. In the end, the possibility of using vortex generators (VGs) to suppress the asymmetry issue in the SC was explored.

4.2 Experimental setup

In project 1, the time-averaged topology of stall cell (SC) was investigated using the experimental apparatus introduced in Section 3.1. The measurements were performed at a chord-based Reynolds number of 672,000, which corresponds to a freestream velocity of 10.5 m/s. The effect of varying α on the SC pattern was evaluated at the pre-stall regime, in a range of angle-of-attack (α) from 9° to 11°. Note that, the maximum lift coefficient of the NACA 4418 airfoil occurs at approximately 14° (Abbott & Von Doenhoff, 2012). The tested α was increased in increments of 0.5° with an uncertainty of ±0.1° following α = 9.0°, 9.5°, 10.0°, 10.5°, 11°. An extra measurement was carried out at α = 9.7°, where the SC forms. Tuft visualization was conducted to confirm that there was no large-scale separation close to the leading edge and that the flow separation only occurred close to the TE.

4.2.1 Planar particle image velocimetry

The effect of varying α on the pattern of the separated flow was investigated by performing full-span planar PIV measurements at the TE region of the wing. The experimental setup is illustrated in Figure 4.1. A CCD camera (Imager ProX, LaVision GmbH) with a sensor size of 2048 × 2048 pixels was used. Each pixel was 7.4 × 7.4 μm^2 and had a dynamic range of 14 bits. The camera was equipped with a Nikon lens with a focal length of F = 105 mm and an aperture of F/5.6. The camera imaged a field-of-view (FOV) of 268 × 268 mm at a digital resolution of 0.13 mm/pixel. The camera location and the FOV are illustrated in Figure 4.1. The whole span (1190 × 268 mm) was scanned by moving the camera in the z-direction as shown by multiple dashed line boxes in Figure 4.1. The combined FOV was stitched using vector mapping in DaVis 8.4 (LaVision GmbH). The stitched FOV was 268 mm × 1190 mm in the x-and z-directions, respectively. An Nd:YAG laser (Spectra-Physics, PIV 400) with a maximum power of 400 mJ per pulse at 532 nm wavelength was used to illuminate the measurement plane. The laser sheet was generated using a combination of spherical and cylindrical lenses and its thickness was kept below 2 mm across the entire FOV. The laser sheet was parallel to the wing surface and at a wall-normal distance of 4 mm. The 4 mm distance minimized the glares formed in the images due to the reflection of the laser sheet. The flow was seeded using ~1 μm fog particles.

Two independent sets of 500 double-frame images were collected for each measurement at a rate of 5 Hz with a laser-pulse separation of 200 μs. The SNR was improved by subtracting the ensemble minimum of the image intensity from each image, followed by normalization using the average image intensity. The double-frame images were cross-correlated in DaVis 8.4 (LaVision GmbH) using a multi-pass algorithm with a final interrogation window of 32 × 32 pixels (4.2 × 4.2 mm^2) at 75% overlap. Universal outlier detection was applied in the post-processing procedure to remove the spurious vectors (Westerweel & Scarano, 2005). The uncertainty of planar PIV measurements is estimated to be approximately 0.1 pixels (Raffel, et al., 2018). Therefore, using the digital resolution (0.13 mm/pix) and separation time between the two laser pulses (200 μs), the error in the velocity vector is 0.063 m/s ($6\times10^{-3}U_\infty$). In addition, evaluations of displacement histograms did not show any evidence of peak-locking. The statistical convergence of the planar PIV measurements was examined for both U and W components. The results showed that the arithmetic mean of both U and W converged to the expected mean after averaging about 500 vector fields. The maximum variation of the arithmetic mean was approximately 2% when the number of planar-PIV vectors increased from 900 to 1,000.

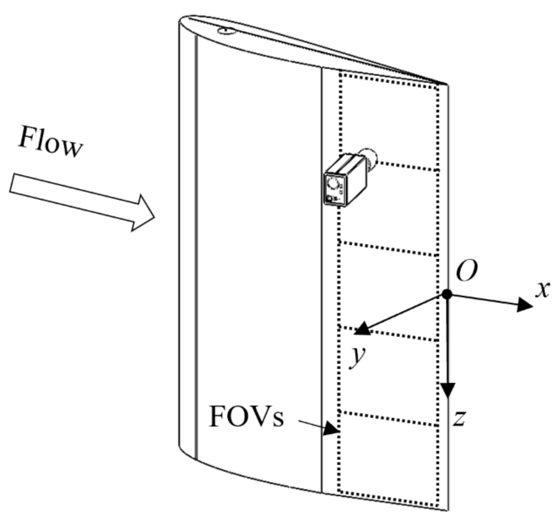

Figure 4.1. A schematic of the full-span planar PIV measurements. The stitched FOV is shown in dashed line boxes, and the origin of the coordinate is placed at the center of TE. The free stream flows from left to right.

An additional planar PIV measurement was carried out to characterize the mean velocity profile of the boundary layers (BLs) developed on the lower and upper walls of the empty test section, at the location of the airfoil. It was found that the BL thicknesses, δ_{99}, on the lower and upper walls were 70 mm and 146 mm, respectively. The thicker δ_{99} observed on the upper wall is potentially associated with the large gaps between the panels of the wind tunnel ceiling. The laminar-to-turbulent transition points may also be different on the upper and lower walls due to the closed-loop design of the wind tunnel and the asymmetry of the curved section upstream of the settling chamber.

4.2.2 Vortex generators

The current experiment also investigated the usage of vortex generators (VGs) to isolate the SC pattern from the separated flows on the spanwise ends of the airfoil. This approach aimed at enforcing an attached flow on the spanwise boundaries of the stall cell. Vane-type VGs were selected due to their simple geometry and effectiveness in controlling flow separation as shown by previous investigations (Lin, 2002; Velte & Hansen, 2013; Wang & Ghaemi, 2019). The rectangular shape was shown to maximize the wall-normal momentum transport relative to the delta and trapezoidal type VGs (Wang & Ghaemi, 2019). The VGs used here were 3D printed using polylactic acid (PLA) in a Dremel 3D45 printer with a nozzle size of 0.2 mm.

As shown in the inset of Figure 4.2a, the vanes of VG were arranged in pairs with an incidence angle, β, of 18° as suggested by Godard & Stanislas (2006). To produce large-scale streamwise vortices, also following Godard & Stanislas (2006), the height of the VGs, h, was scaled as $0.4\delta_{99}$. Here, δ_{99} is the BL thickness just upstream of the SC location which is approximately 26 mm based on measurements of Ma et al. (2020). Therefore, the height of VGs was 10 mm in the current experiment. The gap between the TEs of the vanes was fixed to $1h$ to minimize the decay of the vortex strength (Betterton, et al., 2000). In addition, to ensure the strong vortices, the chord of the VGs was set to $6h$ (Lin, 1999).

According to the parametric study on vane-type VGs by Ashill et al. (2002), the vortices produced by counter-rotating vanes evolve within a distance of $30h$ downstream of the VG, and then remain approximately constant between 30 to $50h$ downstream of the VG. Hence, the VGs were installed $40h$ (400 mm) upstream of the primary saddle point of the SC, which is around 25% of the chord. As will be discussed in Section 4.3, the asymmetry of the SC is associated with the secondary saddle and focus points that develop on the spanwise sides of the SC. Therefore, the spanwise VG locations were chosen according to the z locations of these secondary structures in an attempt to enforce a symmetric flow on the two spanwise sides of the SC. Three VG arrangements were selected as shown in Figure 4.2: (a) two pairs of VGs at z/c =

−0.5 and 0.32, (b) two additional VG pairs added at $z/c = -0.39$ and 0.51, (c) an additional VG pair was installed at $z/c = -0.2$. The VGs were investigated at an airfoil α of 9.7°, where the SC was first observed with increasing α.

(a) (b) (c)

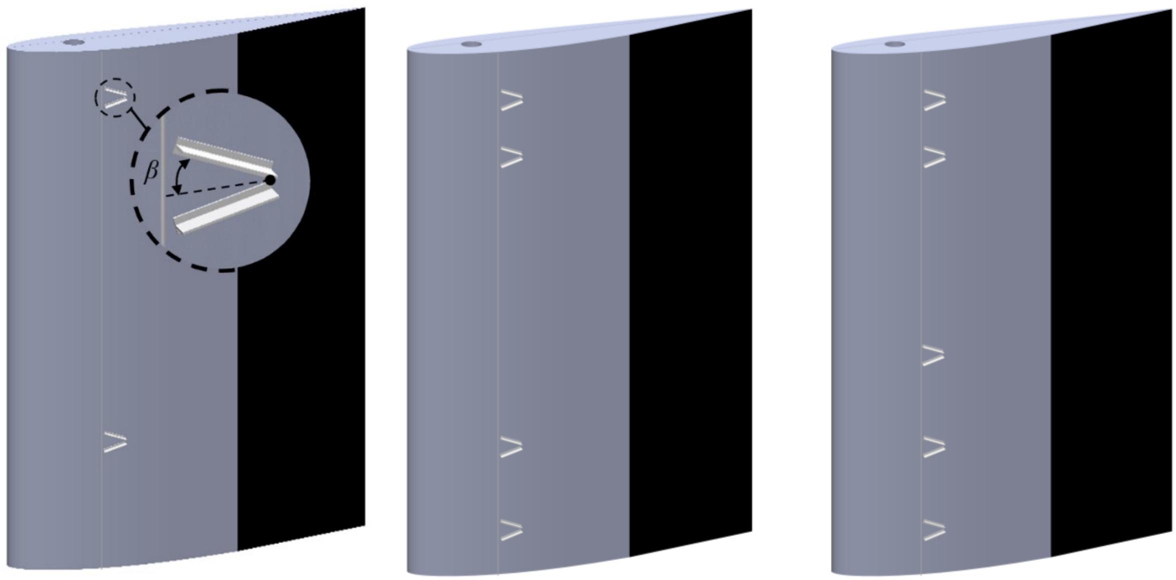

Figure 4.2. The three arrangements of VG pairs used to enforce a symmetric flow around the SC.

To investigate the 3D topology of SC, 3D PTV measurements were carried out using a novel helium-filled soap bubble (HFSB) system. The employment of the HFSB system resulted in a displacement of the SC toward the TE, which was compensated by increasing the freestream velocity to 11.5 m/s for the 3D PTV measurements that will be introduced in Section 4.2.3. The details regarding the HFSB system are provided in Section 3.4. In this measurement, a total of 10,800 images were recorded by each camera at an acquisition frequency of 4 kHz. Similar to the planar PIV, the ensemble minimum intensity was subtracted from each image and an image normalization using the ensemble average was conducted. An optical transfer function was calculated for the iterative particle reconstruction and particle shaking processes of the shake-the-box (STB) algorithm (Schanz et al., 2012; Schanz et al., 2016), conducted in DaVis 8.4 (LaVision GmbH). For the STB process, the maximum allowable particle shift was set to 15 pixels. On average, 3,500 particles were detected per image, which resulted in a particle image density of approximately 0.003 particle per pixel (ppp). The particle image density was limited by the number of bubbles generated by the HFSB system and their dispersion in the wind tunnel. The particle image density was well below the 0.075 ppp upper threshold of the STB algorithm (Schanz et al., 2016). The 3D PTV algorithm detected 2000 tracks per image. A second-order polynomial with a kernel of 2.8 ms (11 time steps) was applied to the particle tracks. The velocity measurements from all the images were binned into a grid with a final window of 48 × 48 × 48 voxels (15 × 15 × 15 mm^3) at 75% overlap. Approximately 8,000 particle tracks were found in each bin. The uncertainty of the 3D PTV measurement is estimated to be 0.1, 0.2, and 0.1 pixels in the *x*-, *y*-, and *z*-directions based on the analysis of Ebrahimian et al. (2019) and Rowin & Ghaemi (2019). Here, the largest uncertainty of 0.2 pixels corresponds to the out-of-plane direction of the 3D PTV system. Using the digital resolution of 0.32 mm/pixel and acquisition frequency of 4 kHz, the velocity uncertainties are 0.13 m/s ($0.011U_\infty$), 0.26 m/s ($0.023U_\infty$), and 0.13 m/s ($0.011U_\infty$) in the *x*-, *y*-, and *z*-directions, respectively. The statistical convergence of the mean of the velocity components obtained from 3D PTV was investigated by calculating the arithmetic mean values using different numbers of detected particles. The results showed that the arithmetic mean calculated based on 90% of the total number of particles was no more than 3% different with respect to the mean value calculated using the total number of particles.

4.2.3 Three-dimensional particle tracking velocimetry

To study the 3D topology of the SC, a large-scale 3D PTV measurement was conducted. Relative to the planar PIV, the 3D PTV measurement covered a smaller spanwise extent but provided a volumetric measurement. The 3D PTV experiment was conducted at α of 9.7° and covered the midspan of the airfoil as demonstrated in Figure 4.3. The imaging system consisted of four high-speed cameras (v611 phantom). Each camera had a sensor size of 1280 × 800 pixels, with a pixel dimension of 20 × 20 μm^2. Nikon lenses with a focal length of F =105 mm were set to an aperture size of F/11 to obtain a depth-of-focus of approximately 100 mm. An angle of approximately 40° was kept between the opposite cameras. Sheimpflug adapters were used to align the depth-of-focus of the cameras and the measurement volume. The latter was illuminated by a high-speed Nd:YLF laser (Photonics Industries, DM20-527DH) at 4 kHz. The laser beam was expanded by a combination of two cylindrical lenses. To obtain a top-hat laser intensity profile, the laser beam was cropped at four edges. The measurement volume was 260 × 100 × 380 mm^3 in the *x*-, *y*-, and *z*-directions, respectively, which is equivalent to 807 × 310 × 1180 pixels. The initial calibration of the cameras was obtained by fitting a third-order polynomial on an image recording of a 3D calibration plate (Type 22, LaVision GmbH). The self-calibration algorithm was then applied to reduce the root-mean-square of image distortion residual to 0.1 pixels (Wieneke, 2008).

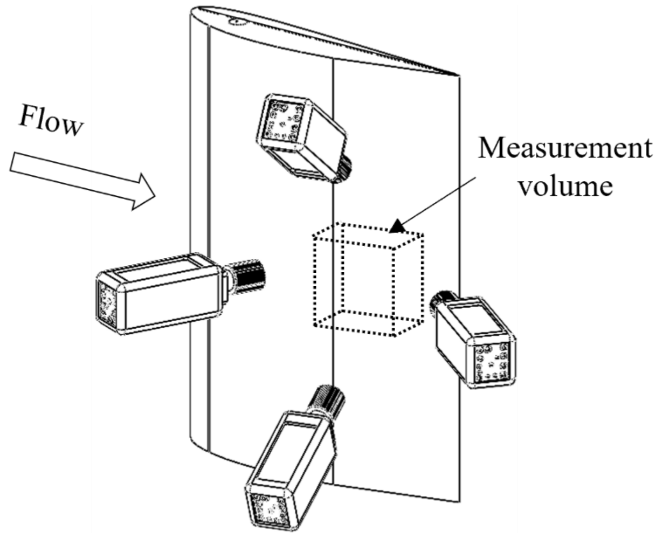

Figure 4.3. A schematic view of the 3D PTV measurements. The measurement volume at midspan is shown in the dashed line box.

4.3 Results and discussion

To investigate the effect of α on the SC pattern, the near-wall streamlines obtained from the planar PIV measurements are demonstrated in Section 4.3.1. The investigation of the 3D structure of SC using the large-scale 3D PTV is discussed in Section 4.3.2. Finally, the results of addressing spanwise asymmetry in the SC pattern with vortex generators are presented in Section 4.3.3.

4.3.1 The effect of angle-of-attack on stall cell

The flow streamlines over the full span of the wing for different α are plotted in Figure 4.4. The upper and lower wind tunnel walls are at $z/c = -0.61$ and 0.61, respectively. The measurement domain covers the area close to the TE, with the TE located at $x/c = 0$. The saddle points and foci are labeled with the cross sign (×), and plus sign (+), respectively. The separation lines are also highlighted with dashed lines. Note that the HFSB apparatus or VGs were not installed during the planar-PIV measurement reported in this section.

The streamline pattern at $\alpha = 9°$ in Figure 4.4a shows a large recirculating vortex (labeled as A) near the upper spanwise end ($z/c = -0.61$). The corresponding focus point of this vortex is at $(x/c, z/c) = (-0.09, -0.5)$. Near the midspan of the wing, a saddle point is observed at $(x/c, z/c) = (-0.09, -0.06)$, and a focus point is located close to the TE at $(x/c, z/c) = (-0.05, -0.13)$. A short separation line also occurs in the mid-span region, crossing through the saddle point. No large recirculating flow is visible near the bottom end of the span at $z/c = 0.61$. Therefore, the corner flows at the two spanwise ends of the wing are dissimilar although the wing and wind tunnel walls are symmetric (within the manufacturing tolerances). As noted in section 4.2. the turbulent BL thickness on the upper wind tunnel wall ($z/c = -0.61$) is approximately twice that on the lower wall ($z/c = 0.61$). The smaller flow momentum on the upper wall contributes to the formation of vortex A on the upper end of the airfoil. When α is increased to 9.5° in Figure 4.4b, the focus point A moves slightly to $(x/c, z/c) = (-0.1, -0.49)$, and the associated recirculating region is enlarged. At midspan, the separation line extends and covers a larger spanwise domain. The separation line undulates in the spanwise direction and crosses two saddle points at $(x/c, z/c) = (-0.11, -0.01)$ and $(-0.13, 0.11)$. There are also three foci at $(x/c, z/c) = (-0.06, -0.13)$, $(-0.12, 0.04)$, and $(-0.07, 0.38)$. However, no SC pattern is apparent at this α.

As α further increases to 9.7° in Figure 4.4c, the focus A moves farther upstream to (x/c, z/c) = (−0.12, -0.51). A SC is observed with a saddle point M at (−0.25, 0.061) and two counter-rotating foci indicated as B and C. The combination forms a mushroom-shape separation line. An adjacent secondary vortex D is also seen at (x/c, z/c) = (0.21, 0.27), and a secondary saddle point N forms at (x/c, z/s) = (0.20, 0.19). The lower spanwise section from z/s = 0.35 to 0.5 still shows no sign of flow separation or a recirculating region. The SC is formed here for a wing with a low AR of 1.2 relative to the previous investigations that observed SC over wings with higher ARs (Winkelmann, 1981; Yon & Katz, 1998).

For α of 10° in Figure 4.4d, the primary saddle point M and the focus point B remain at the same location while the focus C moves slightly upstream and down to (x/c, z/s) = (−0.09, 0.12). The secondary saddle point N also moves upstream and down to (x/c, z/c) = (−0.13, 0.23). The curvature of the separation line connecting B and M also increases, and the reversed flow area becomes larger. Foci A and D remain in their former locations. The distance between the two foci of the SC in the current investigation at α of 10° is 0.26c. This is close to the SC width of 0.32c observed in the numerical simulation of flow over a 2D wing with AR = 2 at α = 10° and Re_c of 8.7×10^5 (Manolesos & Voutsinas, 2014a). The SC observed by Dell'Orso and Amitay (2018) for a wing with AR = 4 at α = 16.5° and Re_c of 4.11×10^5 had a larger width of 0.52c. This larger spacing with respect to the current investigation is potentially due to the larger α and AR. A larger α can result in a larger separation zone while a larger AR also allows the SC to expand in the z-direction without being confined by the corner flows.

In Figure 4.4e, corresponding to α of 10.5°, the separation front moves farther upstream. As a result, the primary saddle point M and part of the separation line move out of the measurement field. The focus point C moves away from focus B, and the SC widens. A new saddle point also appears at (x/c, z/c) = (−0.04, -0.29). With a further increase of α to 11° in Figure 4.4f, the focus point A is pushed downstream to (x/c, z/c) = (−0.05, −0.50), and the SC has a larger recirculating region. The two foci B and C move to (x/c, z/c) = (−0.20, −0.16) and (−0.25, 0.23), resulting in a larger spanwise spacing of 0.39c. The adjacent focus point D and the secondary saddle point N no longer exist. It is conjectured that the expansion of SC accelerated the flow around the SC and removed the secondary focus and saddle points (N and D from Figure 4.4e). Note that the saddle point between foci A and B is no longer visible when α reaches 11°. The topology for α higher than 11° was not investigated since the main flow features shifted outside of the measurement domain that covered the flat TE section.

The investigation of the streamlines showed that the flow separation pattern is sensitive to the variation of α. At the early stages of the TE separation (α = 9°), the flow along the span of the airfoil consisted of small, isolated pockets of backflow. With a slight increase of α to 9.5°, the isolated pockets merged forming an undulated separation front with multiple foci and saddle points. When α increased further to 9.7°, an asymmetric SC pattern formed. A secondary saddle point and a secondary focus structure also appeared on one side of the SC, forming an asymmetric pattern with respect to the midspan. The flows at the two spanwise ends of the wing were not symmetric; a corner vortex with large backflow existed at one side while the flow was attached on the other spanwise end of the wing. This asymmetric flow pattern can be caused by imperfections in the experimental apparatus that are difficult to avoid. In particular, the difference in the BLs on the wind tunnel walls at the two spanwise ends of the wing produces the dissimilar corner flows observed in Figure 4.4. Similar asymmetric flow patterns were also observed in the tuft visualization by Broeren & Bragg (2001) and the oil-flow visualization by Dell'Orso & Amitay (2018): a corner vortex with a reverse flow region was present only at one of the spanwise ends and persisted with increasing α. In the current investigation, as a result of the blockage caused by the corner vortex of the upper spanwise end, the flow between the corner vortex and SC accelerates and remains attached at higher α. In contrast, between the other spanwise end of the wing and the SC, a short separation line with a focus point D and a saddle point N forms. The observation suggests the absence of a corner vortex at z/c = 0.61 may be responsible for the existence of the saddle point N and focus point D on the lower side of the SC. Further increase of α to 10.5° expands the SC in the spanwise direction. When the SC covers approximately 50% of the span (α = 11°), the secondary saddle point and focus point disappear. In addition, the reverse flow region observed at the upper spanwise corner of the wing appears to weaken: the saddle point observed in Figure 4.4e is not visible anymore in Figure 4.4f as the corner vortex A moves more downstream and the associated reverse flow area is smaller within the FOV. Based on these results, one can predict that the SC will continue to expand with the increasing α and will cover most of the wingspan. Note that it is also rare to observe a SC at a low AR of 1.2 since most of the studies of the SC were conducted on airfoils with larger AR (Moss & Murdin, 1971; Winkelman & Barlow, 1980; Weihs & Katz, 1983;

Boiko et al.,, 1996; Yon & Katz, 1998; Broeren & Bragg, 2001; Manolesos & Voutsinas, 2014a; Manolesos & Voutsinas, 2014b; DeMauro et al., 2015; Dell'Orso et al., 2016a; Dell'Orso et al., 2016b; Dell'Orso & Amitay, 2018; Esfahani et al., 2018; Sarlak et al., 2018)

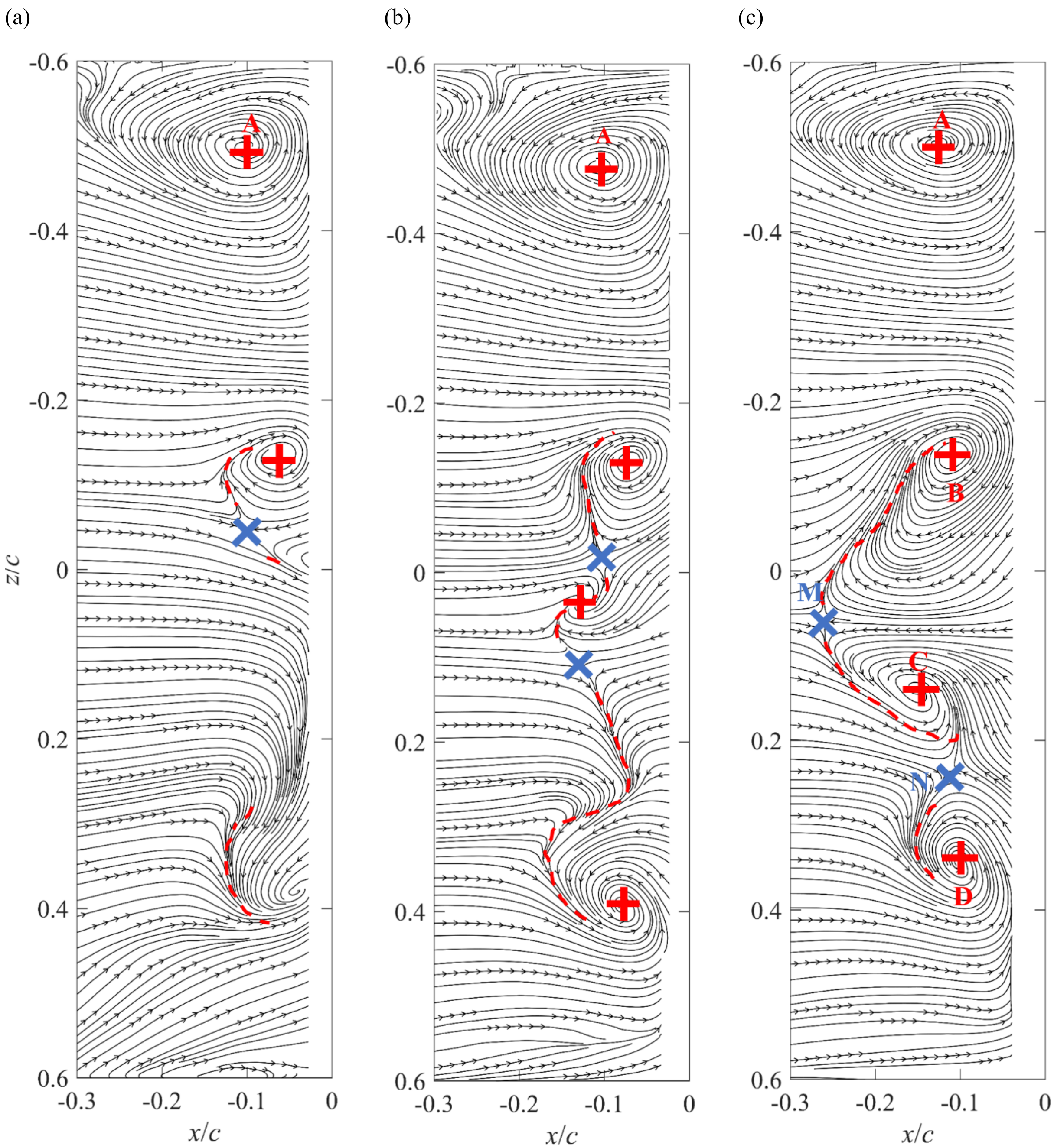

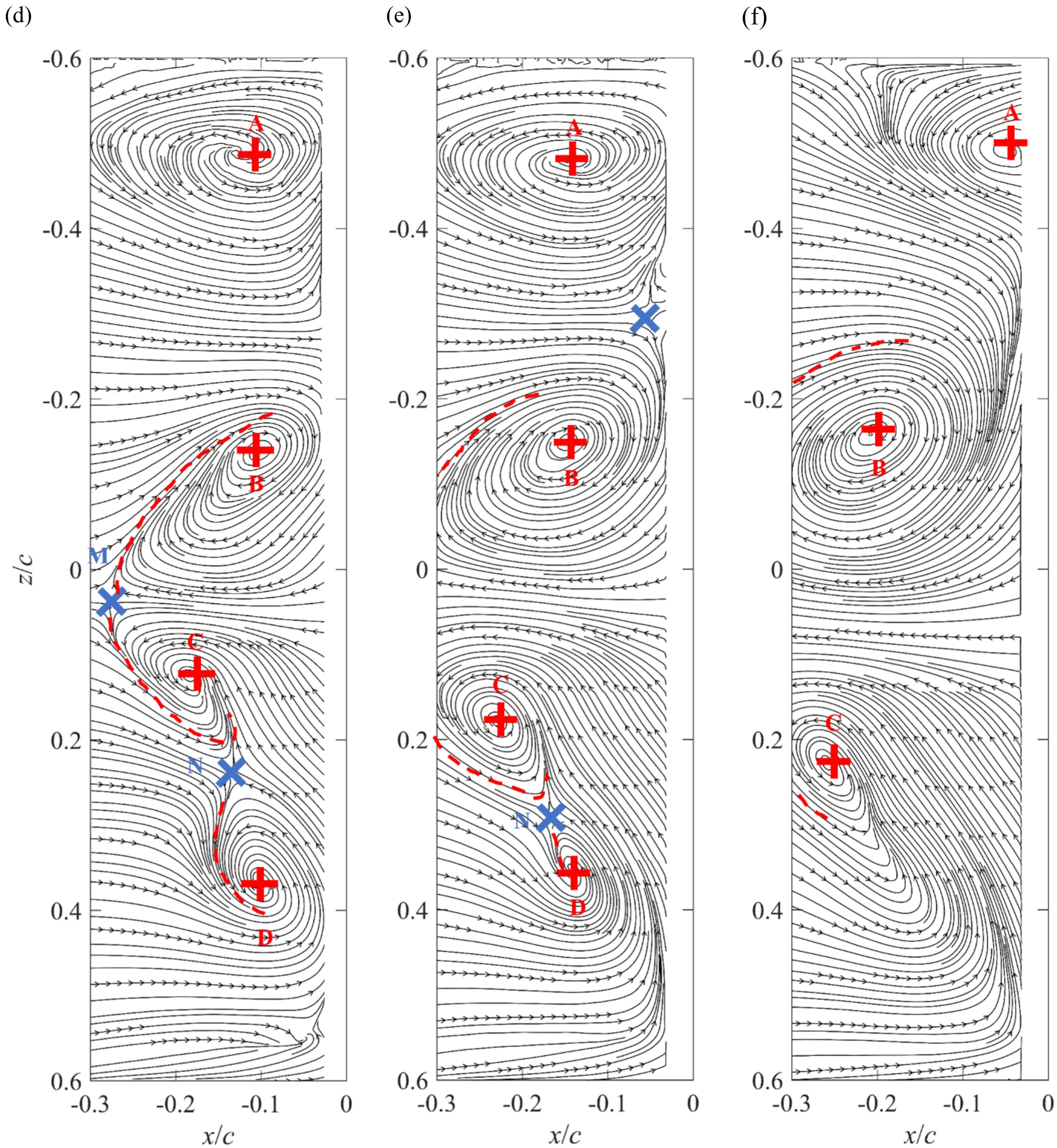

Figure 4.4. Streamline pattern over the airfoil at α of (a) 9°, (b) 9.5°, (c) 9.7°, (d) 10°, (e) 10.5° and (f) 11°.

4.3.2 Three-dimensional characterization of the separation bubble

The 3D PTV was performed to obtain the 3D topology of the SC. The mean velocity fields from the 3D PTV are presented in 3 planes in Figure 4.5: a near-wall *x*-*z* plane ($y/c = 4 \times 10^{-3}$), a *x*-*y* plane at $z/c = -0.02$, and a *y*-*z* plane at $x/c = -0.1$. The figure shows the 2D streamlines with contours of normalized streamwise velocity, $\langle U \rangle / U_\infty$, in the background. The streamlines of the

x-z view show the mushroom-shape separation front and two counter-rotating foci of the SC. The SC is relatively symmetric in the spanwise direction. The x-y plane shows that the maximum height of the separation bubble, characterized by $\langle U \rangle / U_\infty = 0$, is about 0.018$c$ at $x/c = -0.08c$. The short wall-normal height of the separation bubble leaves little space for the foci structures to develop in the wall-normal direction. This is confirmed in Figure 4.6, where x-z planes at higher wall-normal locations of $y/c = 9.2 \times 10^{-3}$, 0.012, and 0.018 are presented. As observed in Figure 4.5, the foci structure quickly disappears with increasing y/c when approaching the boundaries of the separation bubble. The counter-rotating vortices are not visible anymore at $y/c = 0.018$. This shallow separation bubble is consistent with the pre-stall condition of the airfoil. For example, Dell'Orso & Amitay (2018) observed a SC with a wall-normal height of 0.3c at 0.12c upstream of the TE at α of 16.5°. The thicker separation bubble in the investigation of Dell'Orso & Amitay (2018) is associated with the larger α and the corresponding post-stall regime. As is observed in the y-z plane of Figure 4.5, the height of the separation bubble increases with increasing x/c.

The streamlines in the y-z plane of Figure 4.5 do not show any streamwise vortex. To confirm the absence of streamwise vortices, additional y-z planes are shown at different streamwise locations in Figure 4.7. At $x/c = -0.15$, upstream to the two counter-rotating foci, a 3D node of detachment-type is observed. The streamlines show that the flow moves away radially from the node and departs from the wall. When viewing the y-z planes farther downstream at $x/c = -0.13$ and -0.12, where the two foci are present, the node is no longer visible. At these two planes, a large-scale wall-normal motion of the flow away from the surface is seen, while the streamlines are slightly skewed towards the positive z-direction. The most downstream y-z plane at $x/c = -0.11$ also shows no evidence of a streamwise vortex pair. In this y-z plane, an upward flow with a half-saddle structure is observed approximately at $z/c = 0$.

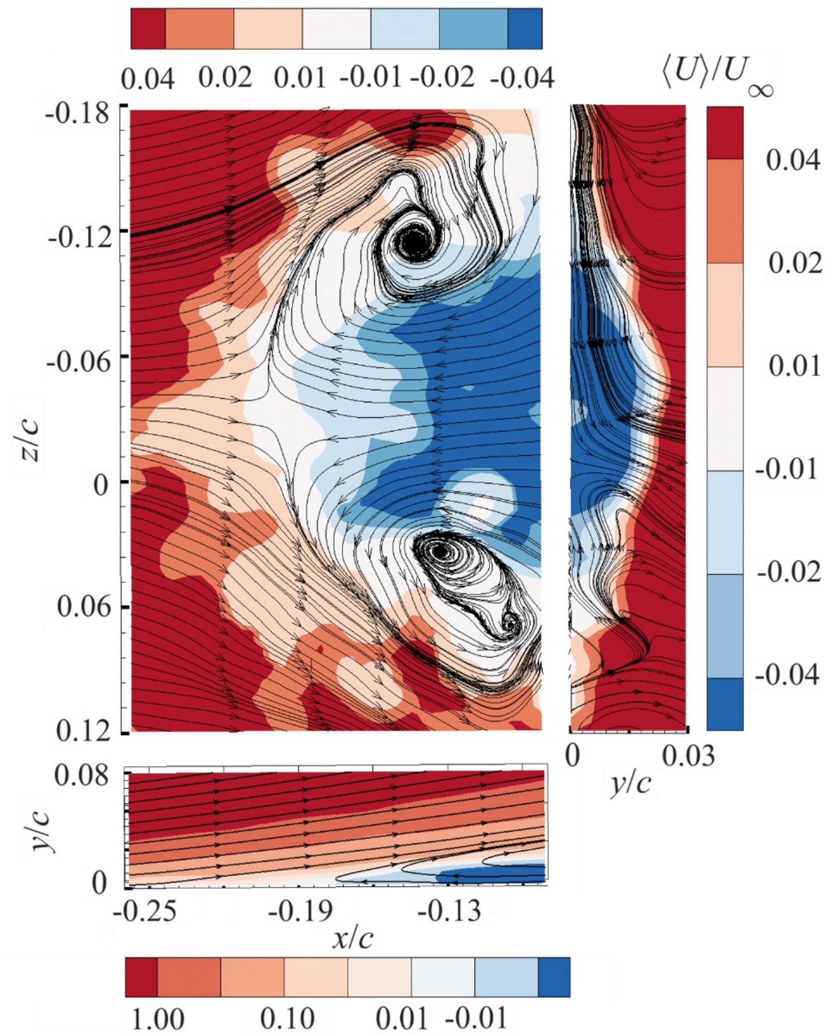

Figure 4.5. Visualization of the SC in a *x*-*z* plane at $y/s = 4 \times 10^{-3}$, a *x*-*y* plane at $z/s = 0.02$ and a *y*-*z* plane at x/c = 0.22.

The 3D visualization of the SC did not show any evidence of strong streamwise vortices at the pre-stall condition in the current experiment. The streamwise-spanwise planes showed that the wall-normal vortices weaken and disappear at the boundary of the separation bubble, before tilting in the freestream direction. This observation agrees with the results of Dell'Orso et al. (2016b) which was carried out for an airfoil at near stall condition.

The mean 3D flow field of the separated flow is demonstrated in Figure 4.8. The boundaries of the separation bubble are visualized using an iso-surface of $\langle U \rangle = 0$, colored by transparent green. The flow motion is represented using colored 3D streamlines. The streamline sections with forward-moving flow (positive *U*) are colored in red, while the backward-moving sections are shown in blue. Short segments of white streamlines are used to represent near-zero streamwise velocity, which coincides with the boundary of the separation bubble. The blue color of the streamlines with spiral motion shows that two large vortices are confined within the separation bubble, which agrees with the streamline pattern of *x*-*z* planes in Figure 4.5 and Figure 4.6. The streamlines illustrate that most of the flow within the separation bubble is brought into the bubble by the backflow induced between the two counter-rotating foci. The flow within the separation bubbles moves upstream against the freestream flow forming the front separation line.

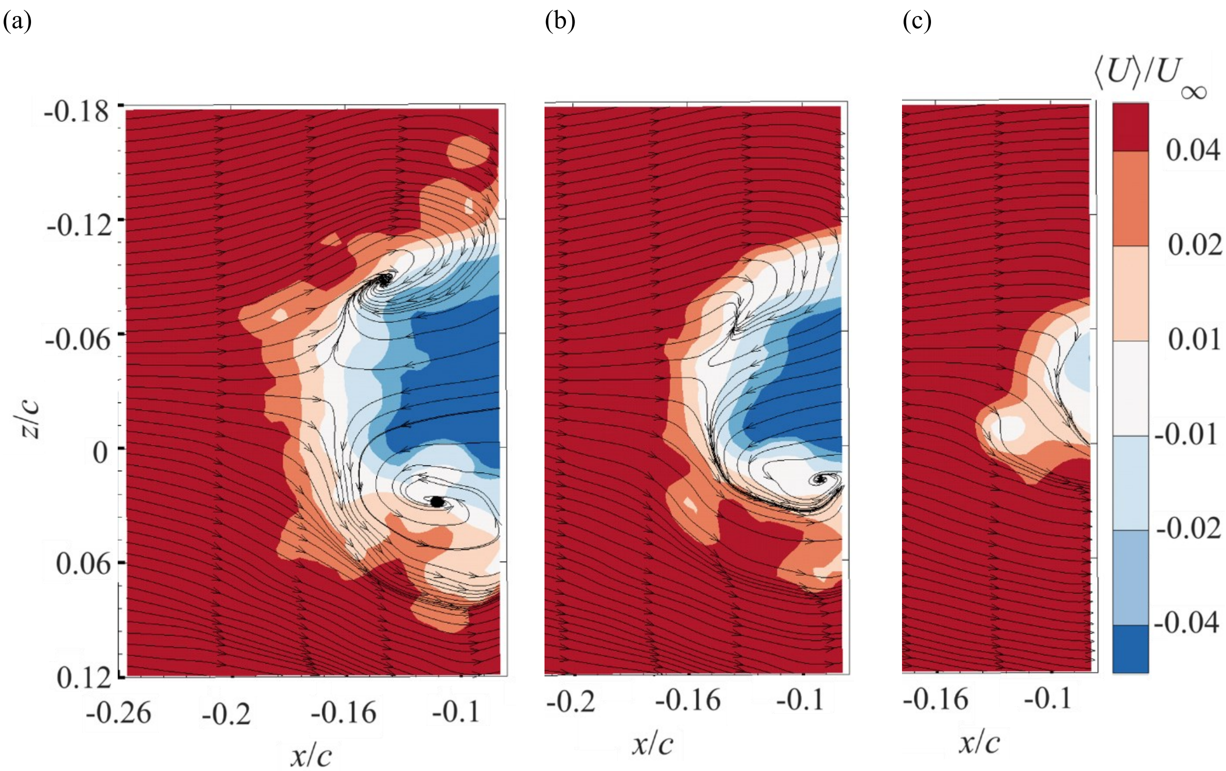

Figure 4.6. The velocity field in *x*-*z* planes at (a) y/c = 0.0092, (b) y/c = 0.012, and (c) y/c = 0.018.

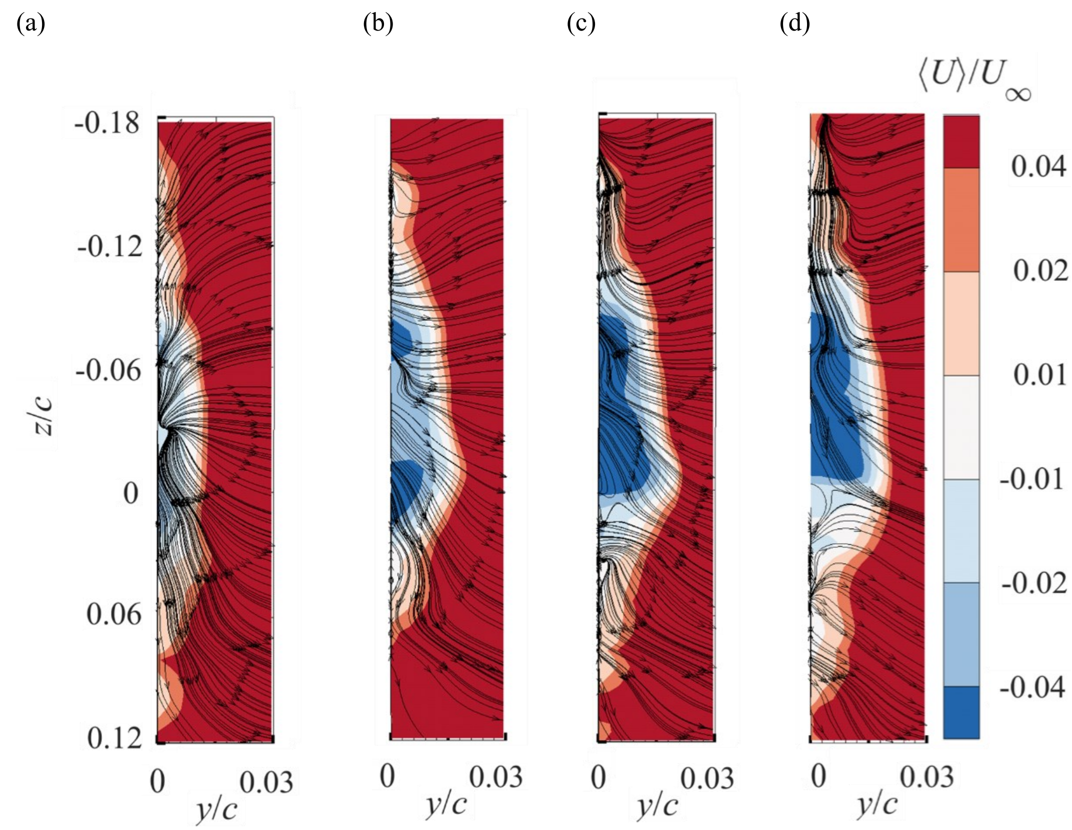

Figure 4.7. The velocity field in the *y*-*z* plane at (a) $x/c = -0.15$, (b) $x/c = -0.13$, (c) $x/c = -0.12$, and (d) $x/c = -0.11$.

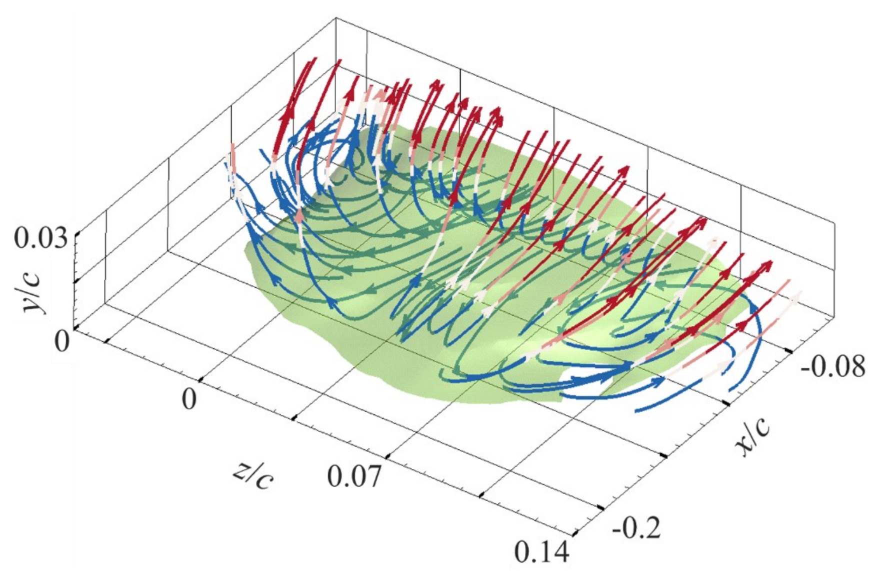

Figure 4.8. The 3D streamlines of the SC. The green iso-surface shows $\langle U \rangle / U_\infty = 0$. The blue, white, and red streamlines indicate negative, zero, and positive streamwise velocity (backward-to-forward flow).

4.3.3 Application of vortex generators

The streamline patterns of the SC after applying the VG combinations are presented in Figure 4.9. The green v-shape marks demonstrate the spanwise location of the VGs. Note that the streamwise location of the VGs is at 0.25c downstream of the leading edge, which is outside of the domain shown in Figure 4.9. To characterize the asymmetry of the SC, the parameter S is defined as the $|l_B - l_C| / |l_B + l_C|$. Here, l_B and l_C represent the distance between the saddle point M and foci B and C in the z-direction, respectively. For a symmetric SC, a S value of zero is expected.

The streamline pattern of Figure 4.4c showed that foci A and D contributed to the asymmetry of the SC. This is also observed by the large S value of 0.39 for this flow field. Therefore, as shown in Figure 4.9a, two pairs of VGs are installed at $z/c = -0.450$ and 0.32 to prevent the formation of foci A and D. The results in Figure 4.9a show a significant improvement in the spanwise symmetry of the SC by applying the VGs, which resulted in S value of 0.26. However, a slight spanwise asymmetry persists, such that, in the z-direction, the upper focus point B is farther from the primary saddle point M relative to the distance between the saddle point M and focus C. The additional momentum brought in by applying the VG at $z/c = -0.50$ slightly pushed the focus point A downstream. The VG installed at $z/c = 0.32$ removed the focus point D and saddle point N that were presented in Figure 4.9c. A recirculating region is created near $z/c = 0.61$ at the lower spanwise end of the wing.

To further improve the symmetry of the SC pattern, two additional pairs of VGs are added at $z/c = -0.39$ and $z/c = 0.51$ as seen in Figure 4.9b. The saddle point M makes a small downstream movement of 0.01c. The two foci barely move. Hence, the new VGs provide little improvement in terms of SC symmetry. In particular, the VG installed at $z/c = -0.39$ does not affect the high-speed flow formed between the recirculating flow at the upper corner of the wing and the SC. The VG at $z/c = 0.51$ removes a part of the backward flow near the lower wind tunnel wall and confines it to a small spanwise region. However, this has a negligible effect on the SC, the value of S changed from 0.26 to 0.28 with the addition of the VGs, which suggests that the small recirculating flow at the lower spanwise end did not affect the SC.

One more attempt is conducted to enhance the symmetry of the SC by adding a pair of VGs at $z/c = -0.20$, and the result is shown in Figure 4.9c. The added VG increases the streamwise momentum of the flow and shifts the focus point B in the positive z-direction. Note that the two foci B and C are drawn closer together, and are relocated to (x/c, z/c) = (0.12, −0.05) and (−0.11, 0.18). The corner vortex near the top end of the span at z/c = −0.61 still exists. The VGs induced a symmetric boundary on the two spanwise sides of the SC and formed a symmetric SC with a small S value of 0.05. The investigation shows that VGs can effectively reduce the interference of the corner flows with the flow at the mid-span of the wing and remove the undesired secondary flow structures. This technique can be used for generating SCs that are isolated from the corner flows at the spanwise ends of the airfoil, improving the repeatability of the experiments.

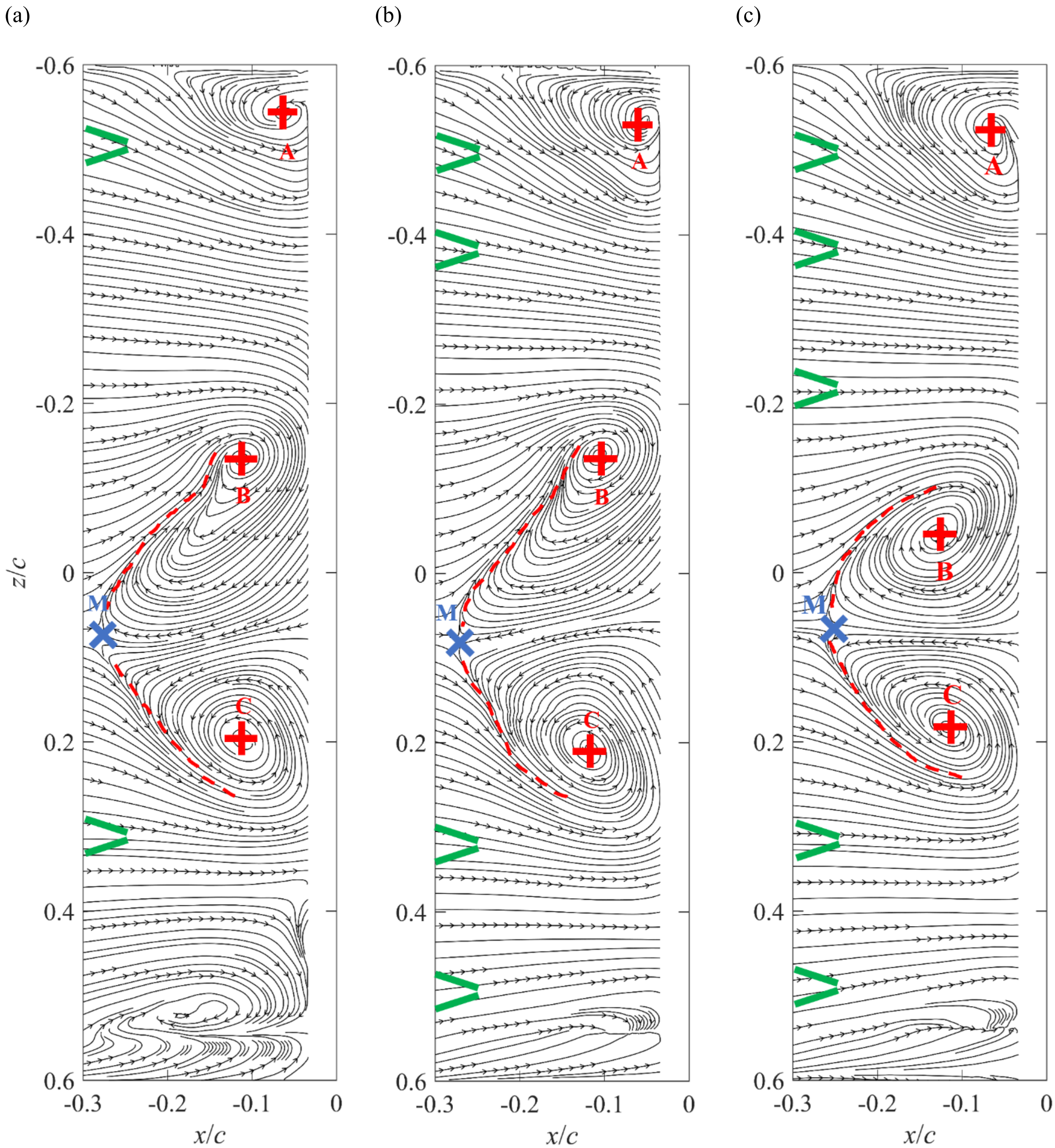

Figure 4.9. The effect of VG arrangements on the streamlines at α of 9.7°.

4.4 Conclusion

The current investigation characterized the stall cell (SC) pattern over a 2D wing with NACA 4418 airfoil at pre-stall conditions. The flow streamlines over the full span of the 2D wing at various α were measured using planar particle image velocimetry (PIV) measurements. The measurements showed a recirculating vortex near one of the spanwise ends of the wing and an attached forward flow near the other spanwise end of the wing. This asymmetry was likely due to the dissimilar boundary layers (BLs) developed along the upper and lower wind tunnel walls. With increasing α from 9° to 11°, the 2D topology of the separation zone evolved from isolated pockets of backflow to a spanwisely asymmetric SC that covered more than half of the span. The separation zone expanded with increasing α. The SC formed at $\alpha = 9.7°$ and secondary saddle and vortex structure were observed between the SC and spanwise end of the airfoil. In the present study, the SC formed at a low AR of 1.2, which was not commonly seen in the literatures. Previous studies were mostly conducted on airfoils with greater AR. In addition, only one SC was observed within the tested α, which is attributed to the pre-stall regime and the low AR of the wing.

The state-of-the-art 3D particle tracking velocimetry (PTV) measurements were performed over a volumetric domain that covered the entire separation bubble. The 3D PTV measurements showed that the SC formed a shallow separation bubble at α of 9.7°. The two counter-rotating vortices of the SC only extended a short distance in the wall-normal direction which was up to the boundary of the separation bubble. The 3D streamlines of the mean flow did not show any evidence of streamwise vortices. The 3D streamlines showed that the upstream flow enters the two foci structures from the outer bounds of the SC and is then transported away in the wall-normal direction.

Vane-type vortex generators (VGs) were deployed as a simple technique to enhance the symmetry of the SC pattern. It was shown that by installing the VGs in the outer bounds of the SC, the symmetry-breaking secondary structures can be removed. As a result, similar attached flows were introduced on the two spanwise sides of the SC, which formed a symmetric SC. The symmetric SC pattern can be used as a benchmark flow for fundamental investigation and control of separated flows.

Chapter 5. Unsteady motions in trailing-edge separation

Chapter 5 is derived from the published work of project 2. This chapter encompasses the investigation into the unsteady characteristics of trailing-edge separation, along with the characterization of the energetic flow motions. Towards the end of the chapter, the connection between the unsteadiness in trailing-edge separation and the breathing motion is also probed. This aims to improve the mechanism of the breathing motion and identify the unsteadiness that has more contribution to the breathing behavior.

5.1 Introduction

It is well known that turbulent separated flow is unsteady in nature and is commonly observed on various fluidic devices, e.g., blades of a wind turbine, compressor, and aerial vehicle wings (Simpson, 1981), which usually leads to a reduction in their performance. When a turbulent boundary layer (TBL) detaches from the wing surface near the trailing edge of an airfoil, unsteady force fluctuations are produced and undesired structural vibrations are introduced to the system. This type of unsteadiness is associated with an energetic flow motion that has been observed in numerous turbulent separation bubbles, a.k.a., the breathing motion, which usually occurs at frequencies much lower than the natural vortex shedding frequencies (Mohammed-Taifour & Weiss, 2016; Liu & Xiao, 2020).

A brief survey of investigations on turbulent separation bubbles (TSBs) shows that the breathing motion is not limited to pressure-induced TSBs, it was observed in early investigations on geometry-induced TSBs, where flow separation is produced by geometry singularities (Eaton, 1980; Eaton & Johnston, 1982). In these studies, TSBs downstream a backward-facing step were investigated. The breathing of TSB is observed as a large-scale oscillation of the reattachment point which is attributed to the flapping of the shear layer (Eaton & Johnston, 1982). Eaton & Johnston (1982) proposed that the flapping motion is due to the instantaneous imbalance of entrainment and reinjection of reversed fluid. Here, the flow separation is fixed at the edge of the step, and the unsteadiness that is responsible for the breathing motion is downstream of the separation.

In contrast to the hypothesis from Eaton & Johnston (1982), Pearson et al. (2013) suggested that the perturbation that led to the breathing motion originates from the incoming TBL. In their study, the TSB occurs upstream of a forward-facing step, and the spatial variation happens at both the streamwise (detachment point) and wall-normal directions (reattachment point) simultaneously. In a recent experimental investigation of pressure-induced TSB on a flat plate, Mohammed-Taifour & Weiss (2021) demonstrated that controlled perturbation upstream of the TSB can affect the detachment point, and then indirectly modify the oscillation of the reattachment point. Their investigation further supported that the breathing motion originates from the upstream perturbations. Note that, the flat-plate TSB also has its detachment and reattachment points free to oscillate.

An apparent discrepancy is seen between the hypotheses proposed by Eaton & Johnston (1982) and Pearson et al. (2013). It may be attributed to the differences in flow configuration, which indicates that the mechanism that drives the breathing behavior is configuration-dependent. For this reason, it is also speculated that the proposed hypotheses may not be applicable for a TE separated flow since none of the above-mentioned flows are a good representative of TE separation. For instance, it is shown in this study that TE separation has a TSB formed between two shear layers, while the TSBs discussed above are surrounded by only one. On top of that, the TSB in TE separation has an intermittent separation point and a relatively fixed reattachment point at the TE of a wing.

In this investigation, time-resolved planar PIV measurements were carried out in streamwise-wall-normal and streamwise-spanwise planes in the TE region of a rectangular wing with NACA 4418 profile. The objective of this investigation is to probe the mechanism of the breathing motion in TE separation. This is achieved by characterizing the unsteady energetic flow motions in TE separation, and investigating the relation between the breathing of TSB and unsteadiness upstream and downstream of the detachment point.

5.2 Experimental setup

In project 2, time-resolved planar PIV measurements were carried out to investigate the unsteady motions in a TSB. The experiments were conducted with the wing and wind tunnel introduced in Section 3.1. The wing was set to an angle-of-attack of 9.7° to have the mean detachment point at 0.13*c* upstream of the TE and ensure the measurements can capture a good amount of upstream boundary layer flow. All measurements were carried out with a freestream of U_∞ = 11.2 m/s, which corresponds to a chord-based Reynolds number of 720,000.

5.2.1 Planar particle image velocimetry

The unsteadiness and energetic flow motion in TE separation were investigated using time-resolved planar PIV measurements. For the measurement in the *x*-*y* plane of the midspan, multiple high-speed cameras (v611 Phantom) were employed (Figure 5.1a) to simultaneously capture a large FOV that covered the entire flat section of the airfoil and the wake region. The FOV is shown with dashed lines in Figure 5.1a. The combined FOVs were stitched together using vector mapping to produce combined dimensions of 660 × 145 mm^2 in the *x*- and *y*-directions. The camera sensor featured 1280 × 800 pixels with a pixel size of 20 × 20 μm^2. The cameras were equipped with macro lenses (Sigma) each with a focal length of *f* = 105 mm. The aperture size was maximized to a setting of *f*/2.8 to increase the light intensity within the images. Each camera imaged at a digital resolution of approximately 0.19 mm/pix, resulting in a FOV of 243 × 152 mm^2 in the *x*- and *y*-directions, respectively. The dimensions of the combined FOV for different measurements were specified in sections 5.2 and 6.2. The illumination was provided by a dual-cavity high-speed Nd:YLF laser (Photonics Industries, DM20-527DH) capable of producing 20 mJ beam pulses at 1 kHz. A combination of spherical and cylindrical lenses was used to produce a streamwise-wall-normal laser sheet with an average thickness of 1.5 mm across the entire FOV. To reduce the glaring line due to the reflection of the laser from the wing surface, the laser light was directed from the upstream side of the wing and the edge of the laser sheet was approximately parallel to the flat section. The airflow was seeded using water-based 1-μm droplets generated by a fog generator. In total, 15 sets of time-resolved data, each consisting of 5,464 single-frame images, were collected at 4.5 kHz. To improve the SNR, the minimum intensity of the ensemble was subtracted from each image, which was then normalized with the average intensity. The vector fields were obtained using a sliding-sum-of-correlation method which averaged the correlations from 3 successive image pairs (Ghaemi et al., 2012). The final interrogation window was 32 × 32 pixels (6 × 6 mm^2) with 75% overlap. The vector fields contained approximately 2-3% spurious vectors due to the strong three-dimensionality of the separated flow, mostly observed downstream of the TE. Universal outlier detection (Westerweel & Scarano, 2005) and bilinear interpolation were applied to remove and replace these spurious vectors. All image processing was carried out using DaVis 8.4 (LaVision GmbH). As suggested by Raffel et al. (2018), the uncertainty of planar PIV measurements is estimated to be approximately 0.1 pixels. The error in velocity vectors from the x-y plane is therefore estimated to be 0.086 m/s ($8\times10^{-3}U_\infty$), using the digital resolution (0.19 mm/pix) and time delay between the adjacent laser pulses (222 μs).

The spanwise dynamics of the TSB were investigated using time-resolved planar PIV in a wall-parallel streamwise-spanwise plane. This plane was located 4 mm away from the wing surface and was imaged using two cameras as shown in the schematic of Figure 5.1b. As explained before, the wall-normal distance was needed to reduce the scattered light from the surface in the PIV images and obtain a sufficient SNR. The same equipment from the previous PIV configuration was used. The two high-speed cameras were equipped with F = 105-mm macro lenses (Sigma) with aperture settings of F/4. Each camera imaged at a digital resolution of 0.28 mm/pixel to produce FOVs with dimensions of 226 × 360 mm^2 in the x- and z-directions, respectively. A combination of cylindrical and spherical lenses was used to generate a 1-mm thick laser sheet. The time-resolved data consisted of 10 sets of 5,395 single-frame images recorded at 4 kHz. The SNR of the images was enhanced using the same preprocessing steps discussed above. The images were sequentially cross correlated using a multi-pass algorithm with a final window size of 32 × 32 pixels (9 × 9 mm^2) with 75% overlap. The vector fields contained approximately 1% spurious vectors that were detected and replaced as before. Using a similar approach as introduced earlier, the error in the velocity vectors from the x-z plane is determined as 0.112 m/s ($10\times10^{-3}U_\infty$).

(a) 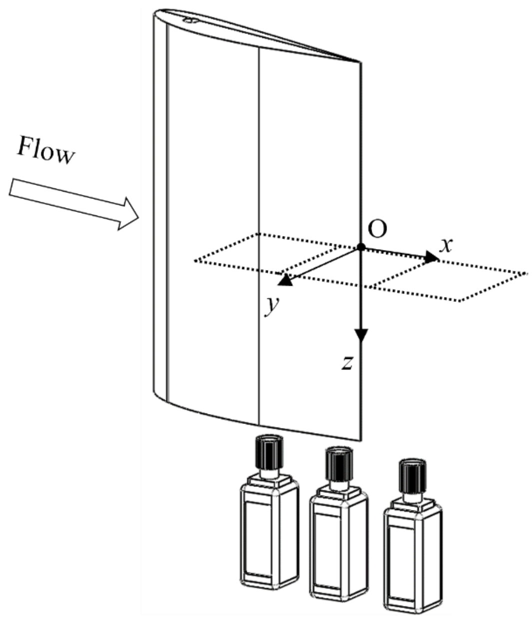

(b) 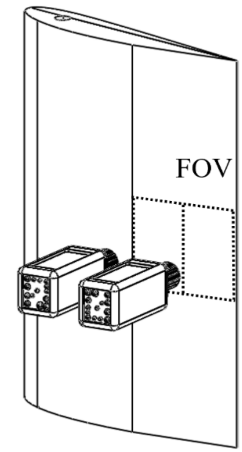

Figure 5.1. (a) Time-resolved planar PIV in a streamwise-wall-normal plane at the midspan of the wing using three high-speed cameras. The origin of the measurement system (point O) is at the TE of the midspan plane. (b) Time-resolved planar PIV in a wall-parallel plane using two high-speed cameras.

5.2.2 Wall-pressure measurement

Time-averaged pressure distribution along the midspan of wing near TE was characterized by performing differential pressure measurements along the midspan. For these measurements, the wing was set to $\alpha = 9.7°$, and free stream was 11.2 m/s, which corresponded to $Re_c = 720{,}000$. Twelve pinholes with diameters of 0.5 mm were evenly distributed between $x/c = -0.31$ and -0.08 along the midspan of the wing. The details regarding the wall-pressure setup can be found from Appendices C.2and C.3. Flexible tubes with 2.5-m length were used to connect the pinholes to the transducers (Ashcroft IXLdp), which could measure a maximum differential pressure of 62 Pa and featured ±0.25% accuracy. The output voltage was sampled at 100 Hz using a 16-bit National Instrument data acquisition device (USB-6218) over a duration of 120 s. The differential pressure of the pinholes, Δp, was measured with respect to the static pressure at the most upstream pinhole located at $x/c = -0.31$. These pressure differences were normalized as $2(\Delta p)/\rho U_\infty^2$ where ρ is air density at 23 °C.

5.3 Results and discussion

To investigate the unsteady motions in TE separation, the unsteadiness in the flow field of TSB is first explored and the results are presented in Section 5.3.1. Followings that, the flow motions that corresponding to different unsteadiness are discussed in Section 5.3.2. The temporal and spatial scales of these motions are evaluated in Section 5.3.3. In 5.3.4, spectral proper orthogonal decomposition analysis is performed to characterize the spatial pattern and the dominant frequency for the energetic flow motions. In the end, the coherence between the breathing motion and unsteadiness in the flow is discussed in Section 5.3.5 to probe the mechanism of the breathing motion.

5.3.1 Turbulent Separation Bubble

In this section, we first demonstrate the unsteadiness of the flow using instantaneous visualizations of streamwise velocity and contours of forward-flow probability. The mean velocity fields are then investigated to characterize the time-averaged TSB and to estimate the thickness and Reynolds number of the upstream TBL. Finally, we evaluate the contours of the Reynolds stresses to compare the shear layers with those from previous investigations of APG-induced and geometry-induced TSBs.

Figure 5.2a shows an instantaneous sample of the streamwise velocity field in the streamwise-wall-normal plane at the midspan of the wing. The TE is located at $x/c = 0$, and the measurement domain covers a large region of approximately 0.63 m from $x = -0.35c$ upstream of the TE to $x = 0.3c$ downstream of the TE. In Figure 5.2a, the black line indicates the contour of $U = 0$, which marks the instantaneous boundary of the TSB. The blue region inside the black contour represents the backflow region with negative U. The TBL separates from the wall at $x/c = -0.16$ as marked with the letter D′ (i.e., the detachment point). The TBL remains detached up to the TE while the backflow extends diagonally farther downstream of the TE into the wake region. The most downstream location of the TSB (i.e., the endpoint) is indicated with the letter E′ in Figure 5.2a. The extension of the backflow region is inclined with respect to the airfoil surface such that it aligns with the high-velocity flow entering the wake from the pressure side of the airfoil. As indicated by the overlaid velocity vectors shown at $x/c = 0.1$, the flow coming from the pressure side has a strong positive V component due to the angle-of-attack of the airfoil. The velocity field shows the presence of two shear layers on the upper and lower edges of the

TSB. The "upper" shear layer forms from the detachment of the TBL from the suction side of the airfoil, while the "lower" shear layer forms from the detachment of the pressure-side boundary layer from the airfoil TE. The latter forms an interface between the high-velocity flow of the pressure side and the extension of the TSB in the wake region. These two shear layers are labeled in Figure 5.2a and form a triangular-shaped TSB between D′, E′, and the TE. Downstream from the TE, the two shear layers evolve free from the wall and gradually merge into a double-sided shear layer.

The contours of the forward-flow probability, γ, in Figure 5.2b show the intermittency of the TSB boundaries. Starting from an upstream location, γ gradually reduces with increasing x/c approximately until the TE. Along a near-wall line of $y/c = 0.003$, γ reaches a minimum value of $\gamma = 0.06$ at $x/c = -0.02$, which is just upstream of the TE. Between $x/c = -0.02$ and the TE, γ rapidly increases to $\gamma = 1$ over a short distance. Scrutiny of the instantaneous visualizations shows occasional forward flows in the small region between $x/c = -0.02$ and the TE. However, since γ reaches a negligible value of 0.06 at a small distance of $0.02c$ upstream of the TE, the TE can be assumed as a fixed corner of the TSB. Downstream of the TE along $y/c = 0$, γ remains equal to 1 due to the high-velocity flow of the pressure side crossing the wake centerline. In contrast, along the diagonal path that is indicated with a dashed line in Figure 5.2b, γ gradually increases from 0.1 to 0.99 over a distance of approximately $0.1c$. The trailing region of the TSB is therefore highly intermittent as the backflow region moves back and forth along the dashed line. Overall, the results indicate that the TSB features an intermittent detachment on the airfoil surface, an intermittent backflow region that extends diagonally into the wake region, and a point just upstream of the TE that is approximately fixed. This triangular-shaped TSB is different from the dome-shaped TSBs of Mohammed-Taifour & Weiss (2016), Le Floc'h et al. (2020), and Wu et al. (2020) which consist of a single shear layer evolving near a wall. For this configuration, the breathing motion is defined as low-frequency variations of the TSB cross-sectional area in the streamwise-wall-normal plane.

An instantaneous streamwise velocity field from the streamwise-spanwise PIV plane is shown in Figure 5.2c. The TE is located at the most downstream location of this measurement plane at $x/c = 0$. The black line indicates the contour of $U = 0$ which separates the upstream forward flow from the downstream backflow region and therefore outlines the TSB. This separation line is oriented in the spanwise direction, but it undulates due to the intermittency of the separation location. The undulating pattern of the separation line is attributed to its interaction with the low- and high-speed structures of the incoming TBL (Eich & Kähler, 2020; Ma et al., 2020). The time instance shown in Figure 5.2c also contains a relatively rare event in which the flow stays attached till the TE at $z/c > 0.13$. There are also a few isolated backflow regions within the forward flow region and a few small pockets of forward flow within the separation bubble as indicated in the figure.

To statistically investigate the intermittency of the TSB in the streamwise-wall-normal plane, we have plotted the contours of forward-flow probability which are shown in Figure 5.2d. The iso-contours of γ are mainly oriented in the spanwise direction as the forward flow probability reduces with increasing x/c. A contour with a low γ of 0.1 is observed just upstream of the TE. It is also observed that the contours have a wavy pattern that undulates in the streamwise direction. The undulation is small relative to the chord length as the maximum oscillation of the $\gamma = 0.99$ contour is approximately $0.1c$. The wavy pattern is due to the presence of 3D flow structures that are known as stall cells. These structures commonly form during flow separation on 2D wings, and each stall cell consists of a saddle point and a pair of foci (Weihs & Katz, 1983). Multiple stall cells and asymmetric patterns can form along the wingspan depending on the angle-of-attack, Reynolds number, airfoil shape, and aspect ratio of the wing. In addition to the stall cells, Wang & Ghaemi (2021) observed that secondary structures are present at the two spanwise ends of the current wing configuration around $z/c = \pm 0.62$, which may contribute to the asymmetry of the wavy pattern of the separation line with respect to the centerline of the wing ($z/c = 0$). However, due to the large span of the wing, these structures are far from the measurement domain and are not expected to affect TSB dynamics.

Contours of normalized mean streamwise velocity, $\langle U \rangle / U_\infty$, in the streamwise-wall-normal plane are illustrated in Figure 5.3a. The solid line shows the contour of $\langle U \rangle = 0$, which represents the boundary of the mean TSB. The most upstream point of $\langle U \rangle = 0$ at $x/c = -0.13$ is the mean detachment point, as indicated by the letter D. The end of the mean TSB is specified by the letter E and is located at $(x_E/c, y_E/c) = (0.03, 0.02)$. The mean length of the separation bubble, l, is defined as the distance between D and E, which is $0.16c$. Similar to the instantaneous TSB, the mean TSB has a triangular shape with three vertices at D, E, and TE.

The TBL over the suction side of the airfoil detaches from the wall and forms the upper shear layer that extends along the DE line. The mean TSB is relatively shallow with an approximate height of $0.02c$, which is attributed to the pre-stall angle-of-attack of the wing (Wang & Ghaemi, 2021). As noted previously, the lower shear layer forms from the separation of the high-speed flow emerging from the pressure side of the airfoil. The upper and lower shear layers are labeled in Figure 5.3a.

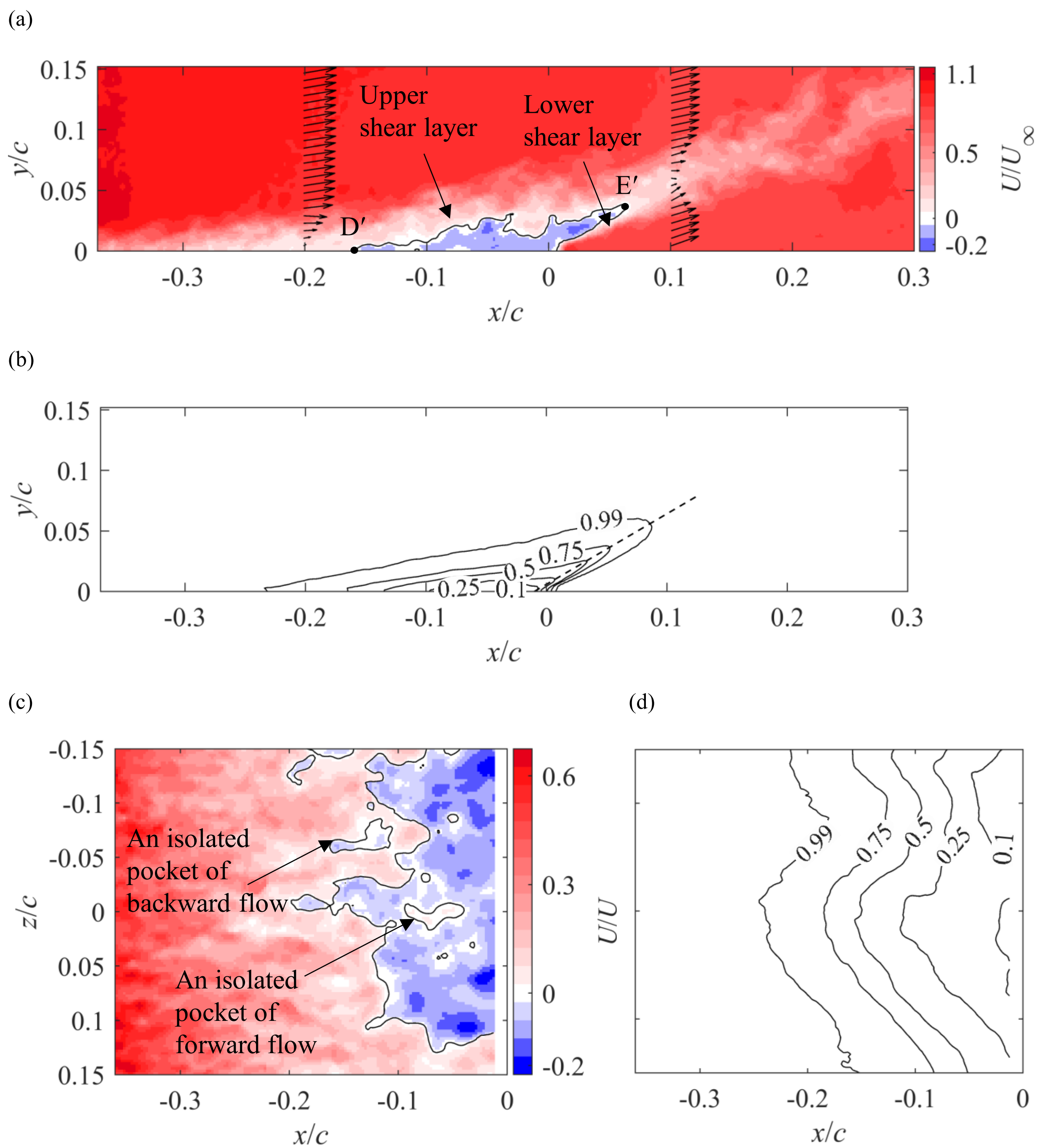

Figure 5.2. (a) Instantaneous contours of streamwise velocity and (b) contours of γ in the streamwise-wall-normal measurement plane. (c) Instantaneous contours of the streamwise velocity and (d) contours of γ in the streamwise-spanwise plane located at y/c = 0.004. The detachment and endpoints of the instantaneous TSB are labeled in (a) as points D′ and E′, respectively.

Figure 5.3b shows the contours of the normalized wall-normal velocity, $\langle V\rangle/U_\infty$, and the mean flow streamlines in the streamwise-wall-normal plane. The freestream flow upstream of the measurement domain has a small positive $\langle V\rangle/U_\infty$, mainly due to the downstream blockage caused by the TSB. The wall-normal component then increases with increasing x/c as the flow passes over the TSB. There is a small region of negative $\langle V \rangle / U_\infty$ within the TSB due to the downward motion of the recirculating vortex. A strong upward flow emerges from the pressure side of the airfoil into the wake region. This upward flow pushes the trailing section of the TSB in the positive y-direction.

The variation of the boundary layer thickness, δ_{95}, and momentum thickness, θ, of the incoming TBL with respect to x/c is demonstrated using the left-side axis of Figure 5.3c. The streamwise extent of the reported δ_{95} and θ in this figure is limited to the region where the TBL stays attached to the wall. Due to the wall-normal limit of the measurement domain, the boundary layer thickness has been obtained based on the y location where $\langle U \rangle = 0.95U_\infty$, and the integration of the velocity profiles for calculating θ is also carried out up to the same location where $\langle U \rangle = 0.95U_\infty$. Figure 5.3a shows that both δ_{95} and θ gradually increase with respect to x/c until $x/c = -0.22$ where the change in δ_{95} and θ suddenly increases. The sudden increase is attributed to the instantaneous presence of backflow (γ becoming smaller than 1) as can be seen in Figure 5.2b. The value of Re_θ, which is calculated based on U_∞ and θ at an upstream location of $x/c = -0.35$, is approximately 2,800. This Re_θ is larger than the Re_θ of 490 considered in the DNS of Wu et al. (2020) but smaller than the Re_θ of 5,000 considered by Weiss et al. (2015). The friction Reynolds number, Re_τ, defined using friction velocity and boundary layer thickness, is approximately equal to 900. This value is estimated here using the $Re_\tau = 1.13 \times Re_\theta^{0.843}$ equation proposed by Schlatter & Örlü (2010).

The right-side axis of Figure 5.3a also shows the variation of the static pressure coefficient, C_P, measured along the midspan of the wing from $x/c = -0.31$ to -0.08. The results reveal the presence of an APG with a larger increase in C_P upstream of the TSB from $x/c = -0.31$ to approximately $x/c = -0.2$. This is followed by a slower increase in C_P from $x/c = -0.2$ to -0.08, which overlaps with the mean TSB. The largest C_P observed here is approximately half of the maximum C_P reported in the experiments of Weiss et al. (2015) and Le Floc'h et al. (2020) and the simulations of Wu et al. (2020).

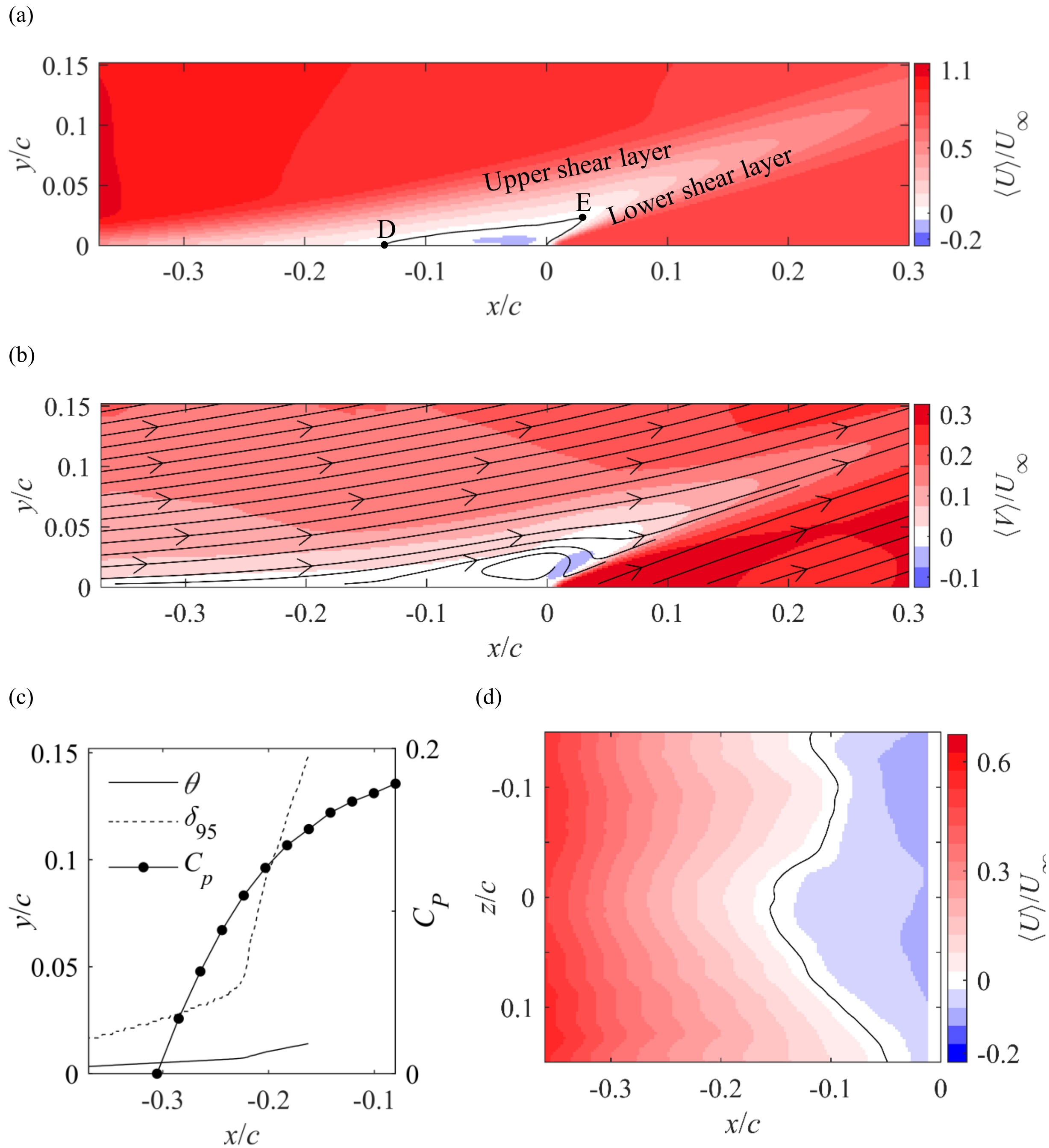

Figure 5.3. (a) Contours of $\langle U\rangle/U_\infty$ in the streamwise-wall-normal plane reveal the triangular-shaped TSB. (b) Contours of $\langle V\rangle/U_\infty$ in the streamwise-wall-normal plane with an overlay of mean flow streamlines. (c) The variation of boundary layer thickness, momentum thickness, and the pressure coefficient with streamwise distance. (d) Contours of $\langle U\rangle/U_\infty$ in the streamwise-spanwise plane. In (a) and (d), the black line shows the contour of $\langle U\rangle = 0$. The detachment and endpoints of the time-averaged TSB are labeled in (a) as points D and E, respectively.

The contours of $\langle U\rangle/U_\infty$ in the streamwise-spanwise plane are shown in Figure 5.3d. The separation point along the midspan ($z/c = 0$) is at $x/c = -0.15$, which is slightly downstream of point D detected in Figure 5.3a. This small shift is because the wall-parallel measurement plane is at approximately $y/c = 4 \times 10^{-3}$ while the first data point in the streamwise-wall-normal PIV plane is at $y/c = 3 \times 10^{-3}$. The contours of mean velocity exhibit a wavy separation line, which is similar to the pattern of the γ contours in Figure 5.3d. As was discussed previously, the wavy pattern and its asymmetry are associated with stall cells and secondary structures formed along the wingspan (Wang & Ghaemi, 2021).

The Reynolds stresses are calculated with respect to a curvilinear coordinate system with x_c and y_c axes based on a streamline that approximately follows the loci of maximum spanwise vorticity along the upper shear layer. The path of the curvilinear coordinate system is shown with a dashed line in Figure 5.4a. The x_c axis remains tangent to the line while its positive direction is in the flow direction. The y_c axis is perpendicular to x_c and is positive in the counterclockwise direction with respect to the positive x_c axis. The parameters calculated in this curvilinear coordinate system are shown with subscript c. The conversion of the Reynolds stresses from the fixed x-y coordinate system to this curvilinear coordinate system is performed following Wu & Piomelli (2018) and Fang & Tachie (2020). Inspection of the Reynolds stresses in the x-y and x_c-y_c coordinates shows that the magnitudes are different while the spatial pattern of the Reynolds stresses remains similar.

The normalized contours of streamwise Reynolds stress, $\langle u^2 \rangle_c$, in Figure 5.4a exhibit two high-intensity zones that correspond to the upper and lower shear layers. The upper shear layer is wider and has a slightly higher peak intensity. Along the upper shear layer, the magnitude of $\langle u^2 \rangle_c$ initially rises with increasing x/c and reaches its maximum downstream of the TE at approximately $x/c = 0.1$. Farther downstream, $\langle u^2 \rangle_c$ gradually decreases as the upper shear layer progresses into the wake region. This trend is similar to the distribution of streamwise Reynolds stress shown in the APG-induced TSBs of Mohammed-Taifour & Weiss (2016), Le Floc'h et al. (2020), and Mohammed-Taifour & Weiss (2021). In these investigations, the streamwise Reynolds stresses demonstrated a single peak within the shear layer, which was close to the detachment point. The DNS of Wu et al. (2020) also shows a single peak near the detachment location when they forced the shear layer to reattach by imposing an FPG. In contrast, when Wu et al. (2020) did not apply a FPG, a strong second peak appeared close to the reattachment region. The shear layer in the DNS of Na & Moin (1998) also shows two local peaks of streamwise Reynolds stress; the first one was close to the detachment point and the second one was in the downstream part of the TSB. In both Wu et al. (2020) and Na & Moin (1998), the second peak potentially forms due to stronger interactions between the shear layer vortices and the wall during the gradual reattachment process. Such an interaction is not present for the TE separation of the current investigation as the shear layer departs away from the airfoil surface and oscillates freely in the wake region. In addition, the current TSB has a strong lower shear layer with two peaks: a small intense region of $\langle u^2 \rangle_c$ near the TE and a second peak farther downstream at approximately $x/c = 0.05$.

Normalized contours of $\langle v^2 \rangle_c$ are shown in Figure 5.4b, where the upper shear layer has a significantly weaker magnitude relative to the lower shear layer. Our analysis indicates that the difference is not due to the alignment of the curvilinear coordinate system with the upper shear, as the magnitude of $\langle v^2 \rangle_c$ in the lower shear layer is greater than that of the upper shear layer even if the curvilinear coordinate system is aligned with the trajectory of the lower shear. The greater $\langle v^2 \rangle_c$ of the lower shear layer is associated with the greater velocity gradient across the lower shear layer as can be seen in Figure 5.3a. This results in the roll-up of stronger spanwise vortices. The intense wall-normal velocity fluctuations of the lower shear also result in stronger Reynolds shear stresses as shown in Figure 5.4c. The high $\langle uv \rangle_c$ region of the lower shear layer is narrower and more concentrated relative to the upper shear layer. The normalized $\langle uv \rangle_c$ in the lower shear layer reaches 0.012, while it only reaches -0.003 along the upper shear layer. As expected, both shear layers contribute to the production of turbulence; the opposite $\langle uv \rangle_c$ signs cancel with the opposite signs of mean velocity gradient, $d\langle U \rangle_c/dy_c$, for the two shear layers. The Reynolds stress distributions also show that the two shear layers do not fully merge within the measurement domain as they maintain separate regions of strong Reynolds stresses. However, the lower shear layer dominates the upper shear layer in terms of wall-normal and shear Reynolds stresses. This contrasts with the previous investigations of TSBs on flat plates in which the Reynolds stresses are concentrated in the single shear layer that forms above the TSB.

The normalized intensity of Reynolds stresses in the current TSB can be compared with those of turbulent plane mixing layers. The $\langle u^2 \rangle_c/U_\infty^2$ peaks of the upper and lower shear layers in Figure 5.4*a* reach 0.02, which is similar to the 0.03 peak observed in (Floriti et al., 2005) and (Loucks & Wallace, 2012) for plane shear layers. In contrast, only the $\langle v^2 \rangle_c/U_\infty^2$ peak of the lower shear layer is similar to the $\langle v^2 \rangle/U_\infty^2$ peak of 0.02 observed in Forliti, et al. (2005) and

Loucks & Wallace (2012). A similar observation is made for Reynolds shear stress. The $\langle uv \rangle_c/U_\infty^2$ peak of the lower shear layer in Figure 5.4c is similar to the 0.01 peak reported in Loucks & Wallace (2012), while the peak value of the upper shear layer is an order of magnitude smaller. Therefore, the intensity of Reynolds stresses in the lower shear layer of the TSB resembles those of plane shear layers, while the upper shear layer demonstrates smaller values of wall-normal and shear Reynolds stress.

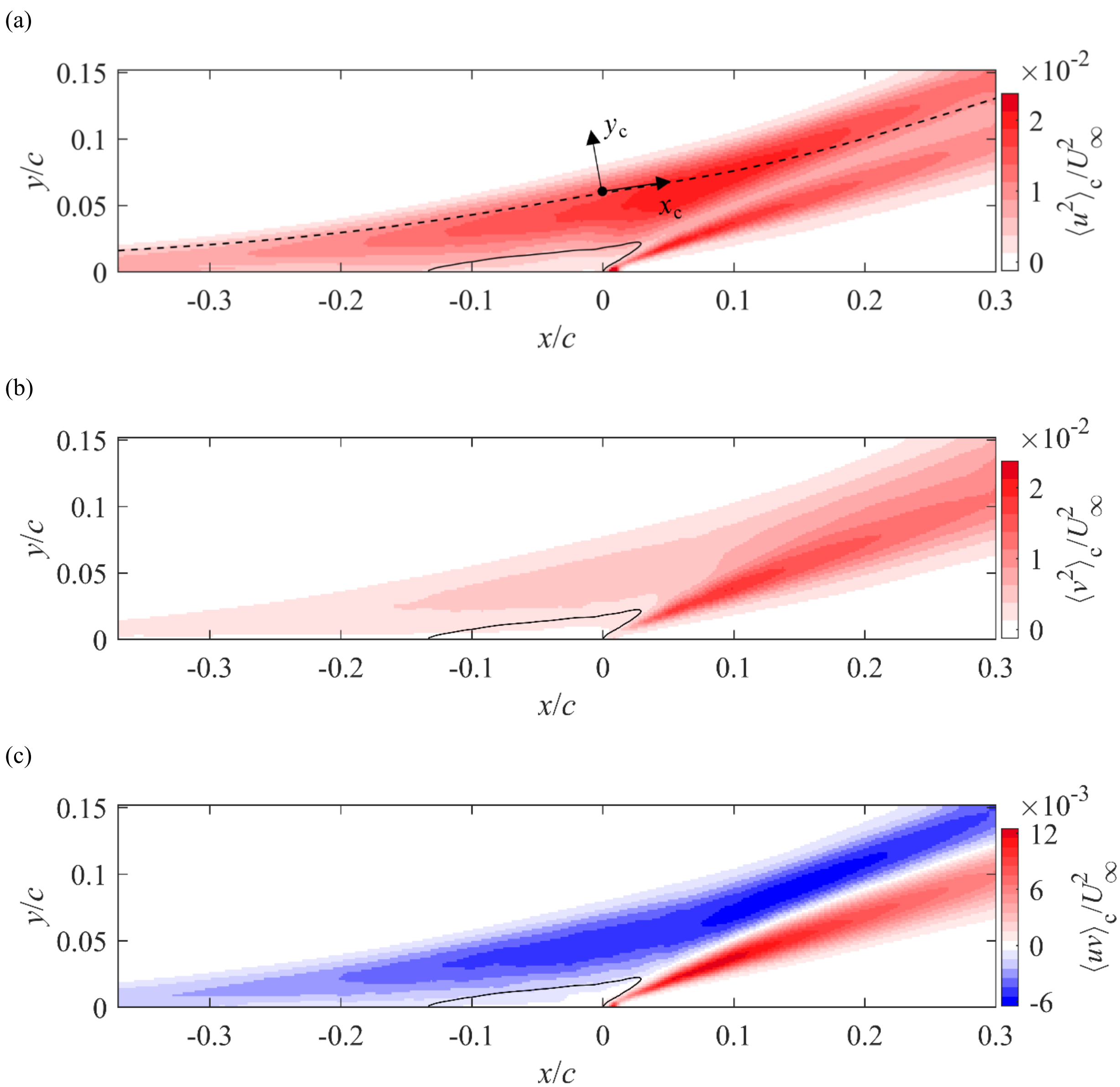

Figure 5.4. The contours of (a) $\langle u^2 \rangle_c$, (b) $\langle v^2 \rangle_c$, and (c) $\langle uv \rangle_c$, normalized by U_∞^2. The velocity components are computed in the curvilinear x_c-y_c coordinate system shown in (a). The contour line shows the boundary of the mean TSB based on $\langle U \rangle = 0$.

To characterize the thickness of the shear layers, the distribution of the normalized mean spanwise vorticity, $\langle\omega_z\rangle l/U_\infty$, is shown in Figure 5.5a. The trajectories of the maximum vorticity along each shear layer are also plotted as black dashed lines. The upper shear layer has a wide region of negative $\langle\omega_z\rangle$, while the lower shear layer has a thin zone of positive $\langle\omega_z\rangle$. For both shear layers, the $\langle\omega_z\rangle$ magnitude gradually reduces in the flow direction. The shear layer thickness δ is estimated as the wall-normal extent of the region where $|\langle\omega_z\rangle/\langle\omega_z\rangle_{\text{peak}}| > 1/\text{e}$. Here $\langle\omega_z\rangle_{\text{peak}}$ is the local maximum vorticity and e is the exponential constant. The estimated δ has been normalized using l and is shown in Figure 5.5b. The results show that the thickness of the upper shear layer initially increases with increasing x/c until the TE at which point the thickness of the layer reduces, potentially due to the appearance of the lower shear layer. Within $0.16 < x/c < 0.22$, the thickness of the upper shear stays relatively constant at $\delta/l \approx 0.24$, and then reduces again close to the end of the measurement domain. In contrast, the thickness of the lower shear layer continuously increases within the measurement domain, and even surpasses the thickness of the upper shear layer at $x/c = 0.24$.

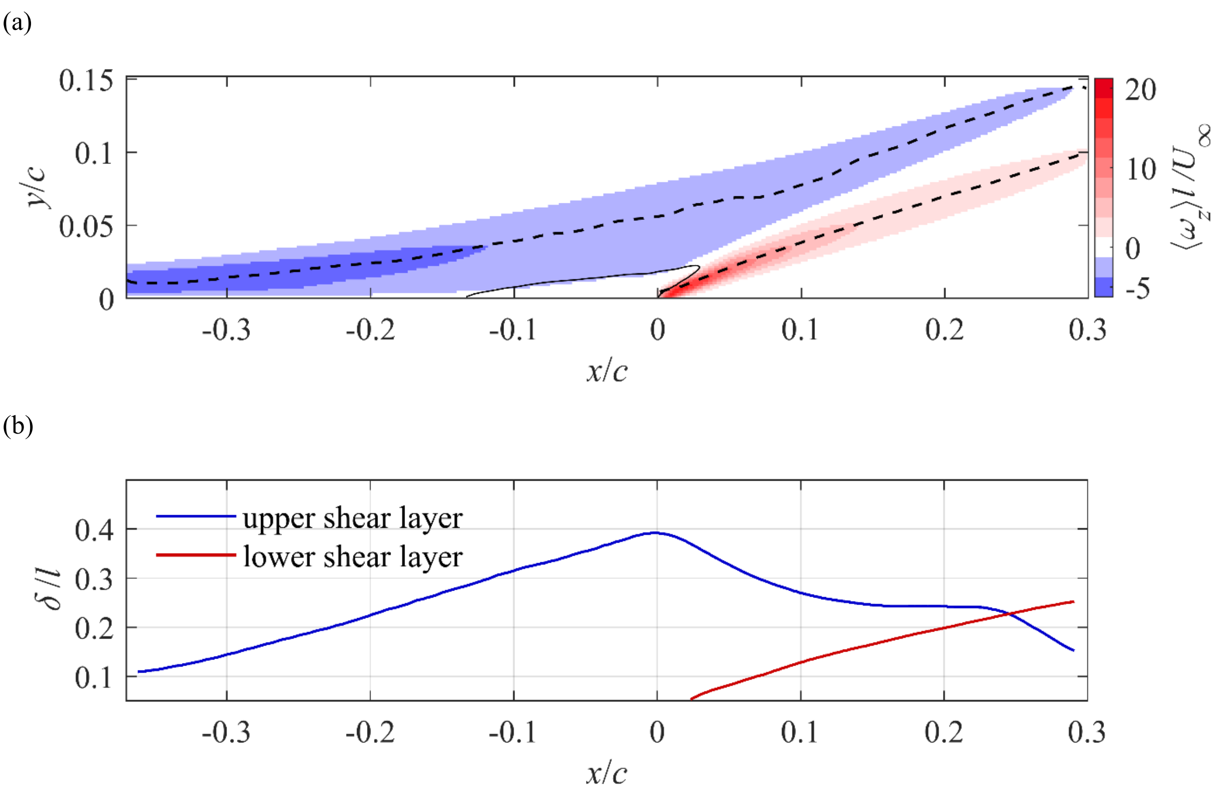

Figure 5.5. (a) The contour of $<\omega_z>$ normalized by U_∞/l. The black dashed lines follow the location of peak vorticity, $\langle\omega_z\rangle_{\text{peak}}$, along the upper and lower shear layers. (b) The variation of vorticity thickness, δ, for the upper and lower shear layers with respect to x/c.

5.3.2 Unsteady Motions

To characterize the frequency and energy of flow unsteadiness, the pre-multiplied power spectral density (PSD) of streamwise velocity fluctuations (u) along y/c = 0.02 is presented in Figure 5.6a. The PSD was calculated by dividing each of the 15 datasets into 3 segments with 50% overlap. This resulted in 45 periodograms, each $44l/U_\infty$ long, which were normalized using the square of the freestream velocity and then multiplied by f. Note again that St_l is defined as fl/U_∞ where the length scale, l, is equal to the length of the upper edge of the mean TSB (0.16c). The pre-multiplied PSD contours show strong unsteadiness in the upstream TBL, inside the TSB, and across the lower shear layer as labeled in Figure 5.6a. In the upstream TBL, the energetic flow motions have a high St_l of approximately 4, which gradually reduces to 0.1 with increasing x/c. The reduction in the St_l of the TBL fluctuations is attributed to the effect of the APG on the low- and high-speed structures (Skote & Henningson, 2002; Lee & Sung, 2009; Eich & Kähler, 2020).

A zone of energetic motions with small St_l is observed between $-0.15 < x/c < +0.02$, which overlaps with the streamwise location of the TSB where forward-flow probability is relatively small. According to Figure 5.2b, γ varies from 0.5 to 0.1 within this high-energy zone. The maximum energy of these motions is centered at St_l of 0.06 while some of the fluctuations occur at smaller St_l of 0.03. These frequencies are similar to the St_l = 0.03 reported for the breathing motion by Weiss et al. (2015). The current investigation indicates that energetic velocity fluctuations with small St_l = 0.03 are present in an APG-induced TSB. The observation of low St_l breathing motion by Weiss et al. (2015) was based on wall-pressure measurements, which can be the result of flow motions throughout the whole flow field. The PSD of streamwise velocity by Wu et al. (2020) also does not indicate the present of velocity fluctuations at such a low frequency, potentially because their spectra was limited to $St_l > 0.2$ and the streamwise velocity was averaged over the spanwise direction. We will further investigate these low St_l motions to characterize their spatial structure and indicate whether they are related to the breathing motion.

Figure 5.6a also reveals a zone of energetic flow motions with St_l varying from 0.1 to 10 at x/c = 0.04. This location is downstream of the TE and corresponds to the intersection of the lower shear layer with y/c = 0.02. The wide St_l range at this location is a result of the spatial displacement of the shear layer as seen by a fixed grid point of the PIV field-of-view. As the shear layer oscillates in space, the turbulent shear layer and the freestream flow intermittently occupy the PIV grid point, and therefore the pre-multiplied PSD spreads over a broad range of St_l from 0.1 to 10. To address this issue, the pre-multiplied PSD of u has been computed along the upper and lower shear layers and are presented in Figure 5.6b and Figure 5.6c, respectively. The trajectories along which the pre-multiplied PSDs were computed are the same as those shown with dashed lines in Figure 5.6a. Moreover, to allow for a comparison of the present results with previous characterizations of shear layers, the frequency was normalized as $St_\delta = f\delta/U_\infty$. Here, δ is the thickness of the upper shear layer at $x/c = 0.2$, which is equal to $0.24l$ based on Figure 5.5b. The contours of figure Figure 5.6b show that the energy of the fluctuations increases with increasing x/c along the upper shear layer. The strongest oscillations are observed close to the TE, at approximately $x/c = 0.1$, with a St_δ of 0.05 to 0.2 (equivalent to St_l of 0.2 to 0.8). With increasing x/c, the oscillations converge to St_δ of 0.15 (St_l of 0.4). The results for the lower shear layer in Figure 5.6c show energetic motions at St_δ of 0.1 to 0.2 (St_l of 0.4 to 0.8). The St_δ of the flow oscillations along both shear layers is similar to the Strouhal number of vortex shedding reported in previous experimental investigations (Sigurdson, 1995; Maull & Young, 1973)and the Strouhal number of the most amplified frequencies predicted by the linear stability theory for shear layers (Monkewitz & Huerre, 1982). Therefore, both shear layers are subject to Kelvin-Helmholtz instabilities, which result in the roll-up of the shear layer and vortex shedding.

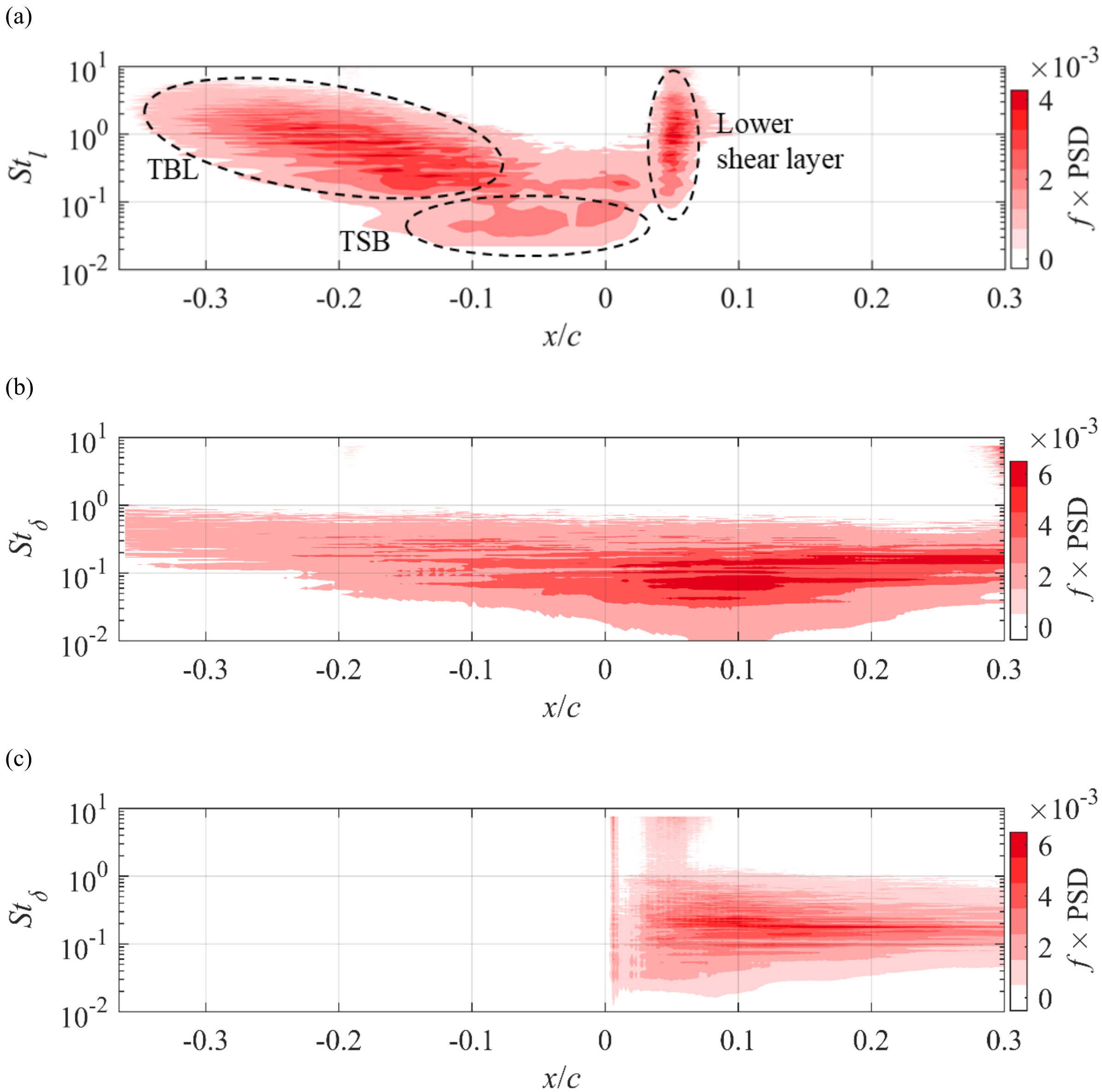

Figure 5.6. Contours of the pre-multiplied PSD of u along (a) y/c = 0.02, (b) the upper shear layer, and (c) the lower shear layer. Note that $St_l = 4.2 \times St_\delta$.

5.3.3 Temporal and Spatial Scales

The temporal evolution of spanwise profiles of u/U_∞ is shown in Figure 5.7 for three x/c locations of –0.25 (within the upstream TBL), -0.15 (close to the mean separation point), and –0.05 (within the TSB). The vertical axis of the figure is the spanwise axis of the flow, z/c, while the horizontal axis is the normalized time, t/T. Here, T is a timescale defined as l/U_∞. All the data correspond to $y/c = 4 \times 10^{-3}$, which is the wall-normal location of the streamwise-spanwise PIV plane. The flow pattern at x/c = –0.25 includes streamwise regions of low- and high-speed flows. The structures meander in the spanwise direction and they have a spanwise spacing of approximately 0.04c, which is equal to 1.1δ_{95} (based on the local thickness of the TBL at x/c = –0.25). This spanwise spacing is similar to the spanwise spacing of ~1δ_{95} reported by Ganapathisubramani et al. (2005) for large-scale motions at y/δ_{95} = 0.5 in a TBL with Re_τ = 1100. Therefore, the wall-normal location of the measurement plane ($y/c = 4 \times 10^{-3}$) and the spanwise spacing of the structures seen at x/c = –0.25 suggest that the pattern corresponds to the large-scale motions (LSM) and the very-large-scale motions (VLSM) of the outer layer (Balkakumar & Adrian, 2007; Hutchins & Marusic, 2007).

At x/c = –0.15 and –0.05 in Figure 5.7, which corresponds upstream of the mean TSB and within the TSB, the flow pattern consists of large zones of positive and negative velocity fluctuations. These zones have a large spatio-temporal coherence; they are several times wider than those observed at x/c = –0.25 and they appear longer along the time axis. The latter suggests that they have a slower advection velocity or a longer streamwise length. The large zones at x/c = –0.15 and –0.05 resemble the highly elongated streamwise structures that Wu et al. (2020) observed in the low-frequency modes of their DMD analysis. They attributed the structures to Görtler vortices generated by the curvature of the streamlines as the flow passes over the separated region. The zones also resemble the large Görtler structures shown by You, et al. (2021) in the DNS of a TBL over a concave wall.

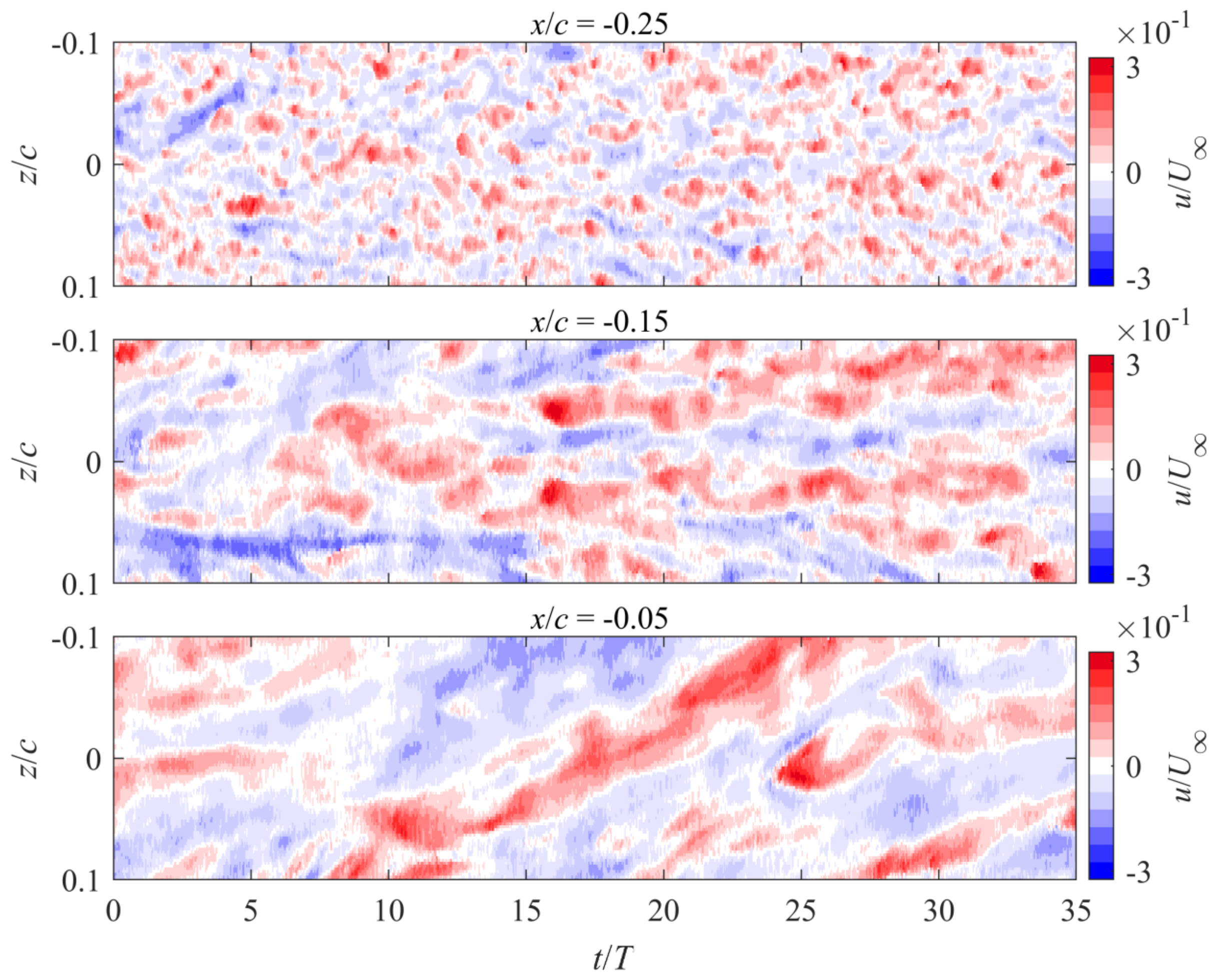

Figure 5.7. Instantaneous visualization of spanwise profiles of u/U_∞ as they evolve in time at three streamwise locations of x/c = –0.25, –0.15, and –0.05.

To further investigate the spatial and temporal scales of the structures, the fluctuating streamwise velocity along the x-axis is plotted versus time in Figure 5.8. The data correspond to a streamwise profile of u/U_∞ at the midspan of the wing (z/c = 0) and is extracted from the streamwise-spanwise PIV plane. To illustrate structures with both short and long temporal scales, Figure 5.8a shows a shorter duration of 20T while Figure 5.8b shows a longer duration of 98T. The instantaneous separation line, which is the location of U = 0, is also shown with a solid black line. A pattern of inclined low- and high-speed structures is seen upstream of the separation region at approximately x/c < –0.2 within Figure 5.8a. Each stripe shows the advection of a low- or high-velocity structure in the x-t domain. Since the large-scale structures of TBLs meander in the z-direction, the length of the stripes visible in Figure 5.8 does not reveal their full streamwise extent or lifetime. However, the inclination/slope of each stripe, i.e. dx/dt of the lines tangent to the stripes, indicates their advection speed. For example, the slope of the dashed line seen at $t/T \approx 2$ in Figure 5.8a indicates that the high-speed structure tangent to this line moves downstream at a speed of $0.4U_\infty$. As the structures approach the separation line, they become wider and their slopes reduce, thus indicating a slower advection speed. The widening is pronounced for the high-speed structures in the region immediately upstream of the instantaneous separation line. The slower advection speed is seen by the gradual departure of the high-speed structure at $t/T \approx 2$ from its corresponding dashed line. In addition, the horizontal spacing between the adjacent structures along the t/T axis represents their frequency. The closely-packed structures at $x/c < -0.2$ appear to alternate in periods as short as $0.5T$, which is equivalent to $St_l = 2$. Therefore, the high-frequency oscillations that were observed within the upstream TBL of Figure 5.6a are indeed associated with the TBL structures.

Once the flow reaches the separation region at approximately $x/c = -0.2$ of Figure 5.8a, the large zones of positive and negative velocity fluctuation emerge. These large zones correspond to the motions within the TSB (under the separated shear layer) along the $y/c = 4 \times 10^{-3}$ plane. They extend along the time axis and occasionally appear to linger at a fixed location due to their lower advection speeds. As seen from the negative slope of the dashed line drawn at $t/T \approx 7$ in Figure 5.8a, some of the zones with negative u appear to slowly advect in the upstream direction, i.e., a backflow motion within the TSB. The positive and negative zones of the TSB alternate slowly over long periods reaching up to $50T$ as seen in the longer sequence of Figure 5.8b. This duration is equivalent to $St_l = 0.02$, which is similar to the low St_l motions observed within the TSB in Figure 5.6a. It is also observed that the separation line in Figure 5.8b closely follows the pattern of these large zones. At $t/T \approx 50$ a negative zone results in the separation front moving in the upstream direction, while at $t/T \approx 90$ a positive zone results in the separation front moving downstream.

The present results indicate that the TSB is formed from large zones featuring positive and negative streamwise velocity fluctuations. When compared to the low- and high-speed structures of the upstream TBL, these TSB structures are several times wider, and their timescale is approximately two orders of magnitude greater. These low- and high-speed zones result in the energetic, low-frequency region labeled as TSB in the pre-multiplied PSD of Figure 5.6a.

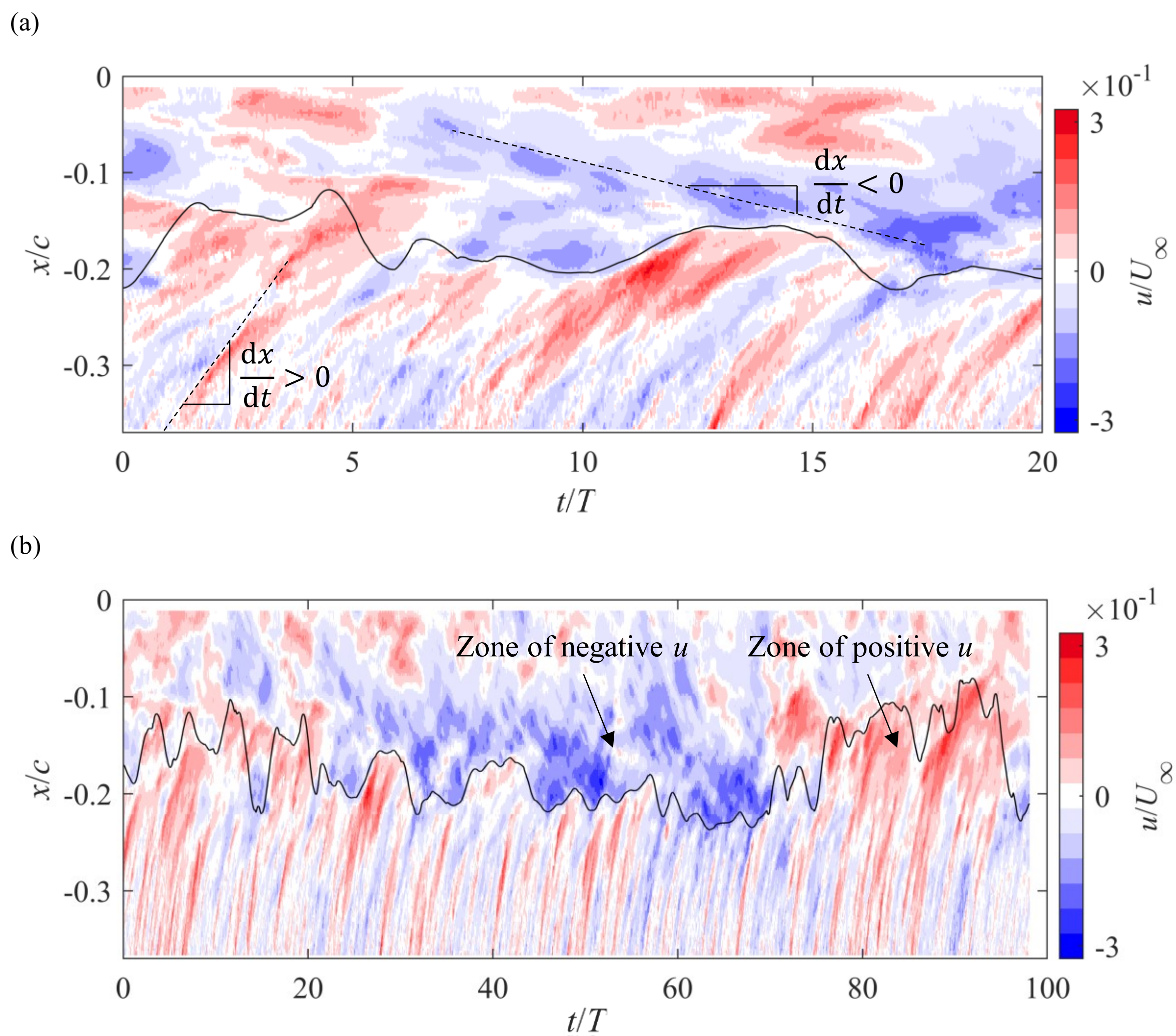

Figure 5.8. The temporal evolution of streamwise profiles of u/U_∞ over (a) a short duration of $20T$ and (b) a longer duration of $98T$. The data corresponds to the midspan of the wing (z/c = 0) from the streamwise-spanwise PIV plane at $y/c = 4 \times 10^{-3}$.

In Figure 5.9, the spatial and temporal scales of the turbulent structures are quantified using results extracted from two-point correlations of the streamwise velocity fluctuations. The reference point for these correlations was placed at a spatial location of (x_0, y_0, z_0) and at an arbitrary reference time, t_0. The correlation coefficient, R_{uu}, was calculated according to

$$R_{uu}(\Delta x, \Delta y, \Delta z, \Delta t) = \frac{\langle u_{(x_0, y_0, z_0, t_0)} u_{(x_0+\Delta x, y_0+\Delta y_0, z_0+\Delta z, t_0+\Delta t)} \rangle}{\sqrt{\langle u^2_{(x_0, y_0, z_0, t_0)} \rangle} \sqrt{\langle u^2_{(x_0+\Delta x, y_0+\Delta y_0, z_0+\Delta z, t_0+\Delta t)} \rangle}}. \tag{5.1}$$

In equation 5.1, Δx, Δy, Δz, and Δt indicate the spatial and temporal offsets of the traversed data point with respect to the reference point. Each offset was applied separately, e.g., when Δx was varied, Δy, Δz, and Δt were kept constant at zero. The streamwise location of the reference point was varied within $-0.35 < x_0/c < 0$ when Δy, Δz, and Δt were applied. A smaller streamwise extent of $-0.28 < x_0/c < -0.11$ was used while varying Δx to ensure that $x_0 \pm \Delta x$ remains within the measurement domain. To improve the statistical convergence, the correlation functions were averaged along the spanwise direction of the measurement domain where possible. Once the correlation functions were obtained, the length and time scales of the structures were determined as the point at which $R_{uu} = e^{-1}$. The estimated streamwise, wall-normal, and spanwise length scales are denoted by l_x, l_y, and l_z, and the temporal scale is denoted by l_t. The wall-normal scale, l_y, was obtained from the streamwise-wall-normal PIV plane, while l_x, l_z, and l_t were obtained from the streamwise-spanwise PIV plane. For consistency, the wall-normal location of the reference points in the streamwise-wall-normal PIV plane was selected as $y_0 = 4 \times 10^{-3}c$, which is the same location as the streamwise-spanwise plane.

In Figure 5.9a, all length scales can be seen to increase with increasing x_0/c. The largest rate of increase in l_x is seen at approximately $x_0/c = -0.24$, which overlaps with the start of the intermittency boundary of the TSB (the $\gamma = 0.99$ contour line, Figure 5.2b). Farther downstream at $x_0/c = -0.1$, the rate of increase in l_x is small as its curve appears to approach an asymptotic value. This asymptotic value is approximately twice the value of l_x at $x_0/c = -0.28$, which suggests that the structures become longer by a factor of 2. However, it is important to note that the estimated length scale does not consider the spanwise meandering of the associated structures and therefore l_x does not represent their true length. A similar trend is also observed for l_z, which indicates that the length-scale increases by a factor of three with increasing x_0/c. For l_y, we observe a sharp reduction just upstream of the TE at $x_0/\mathrm{c} = -0.02$. Inspection of the instantaneous velocity fields shows that this reduction is due to the frequent presence of forward flow in this region, which is indicated by the rapid increase in γ just upstream of the TE shown in Figure 5.2b. Overall, the larger length scales of the structures within the TSB are consistent with the visualizations of Figure 5.7 and Figure 5.8. The estimated timescale, l_t, in Figure 5.9b also increases with increasing x_0/c until approximately $x_0/c = -0.15$, where l_t can be seen to reach a maximum value. The large timescale at this location agrees with the low St_l motions observed within the TSB in Figure 5.6a. Farther downstream, l_t decreases and reaches a smaller value of approximately 2.7. This analysis using two-point correlations statistically confirms the TSB zones have a greater spatial and temporal scale with respect to the largest structures of the upstream TBL.

To identify the source of the large low- and high-speed zones of the TSB, we evaluate the formation of Görtler vortices (Görtler, 1954) following the procedure applied by Wu et al. (2020). The Görtler number, G_T, is calculated using the local radius of curvature of several streamlines that closely pass over the mean TSB. However, it is worth noting that G_T is originally employed for laminar flow. To enable the utilization of G_T for a turbulent flow, an effective eddy viscosity is calculated using the streamwise-wall-normal component of Reynolds shear stress, following Spalart & Strelets (2000) and Wu et al. (2020). The results show that G_T value reaches the 0.3 criteria that is required for the formation of Görtler vortices at approximately x/c = –0.22 and then rapidly increases beyond this limit until the mean separation point is reached. In addition, δ_{95}/R also serves as a criterion for predicting the presence of Görtler vortices (Floryan, 1991). The δ_{95}/R value reaches the proposed limit of 0.01 at approximately x/c = –0.25 and then rapidly increases beyond this limit to values in the order of 0.1 at x/c = –0.1. Therefore, both G_T and δ_{95}/R suggest that Görtler vortices can form upstream of the current TSB. We conjecture that the large low and high-speed zones that are observed at x/c = –0.15 and –0.05 of Figure 5.7 and the downstream region of Figure 5.8 correspond to the footprint of the Görtler vortices.

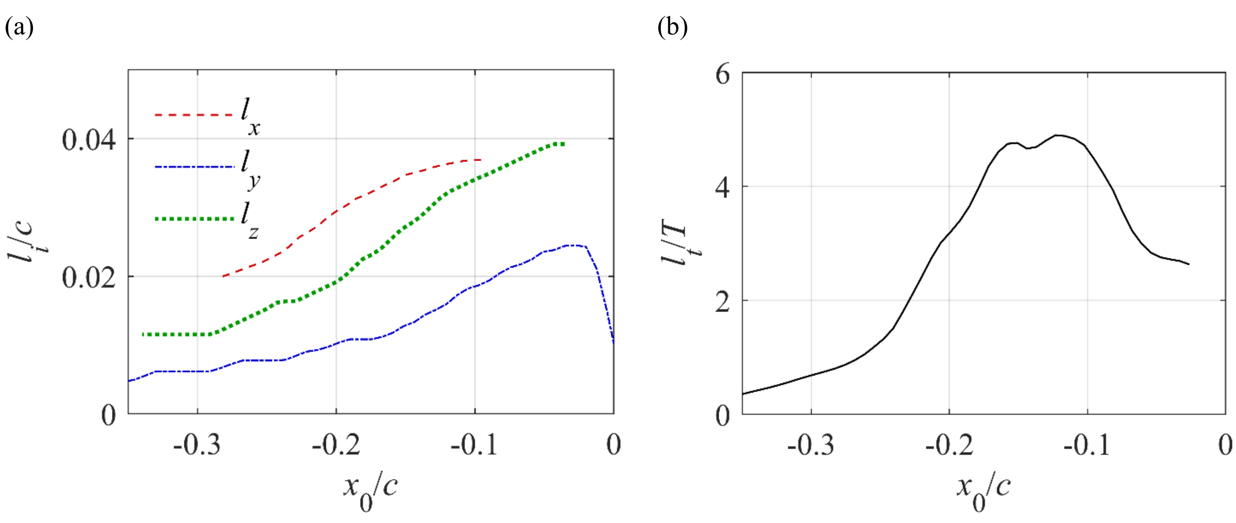

Figure 5.9. The (a) spatial and (b) temporal scales of the motions estimated based on two-point correlations of the streamwise velocity fluctuations. The spatial scales, l_i, are normalized using c, and the temporal scale is normalized using T, defined as l/U_∞.

The R_{uu} contours for simultaneous streamwise and wall-normal shifts (Δx and Δy) are shown in Figure 5.10. Five reference locations at $y_0/c = 4 \times 10^{-3}$ and x_0/c = –0.3, –0.25, –0.2, –0.15, and –0.05 were selected from the streamwise-wall-normal PIV plane. The centerlines of the upper and lower shear layers (from Figure 5.5a) are also shown in Figure 5.10 using dashed lines. As expected from Figure 5.9, the correlation function becomes larger in the streamwise and wall-normal directions with increasing x_0/c. The correlation patterns are also slightly inclined in the position x-direction. Interestingly, the last correlation function, which features a reference at $(x_0, y_0) = (-0.05c, 4 \times 10^{-3}c)$, shows a double peak pattern with the second peak located between the upper and lower shear layer at $(x/c, y/c) = (0.02, 0.04)$. This correlation pattern indicates that the large positive and negative zones of the TSB correlate with the velocity fluctuations generated between the two shear layers by the vortex shedding process.

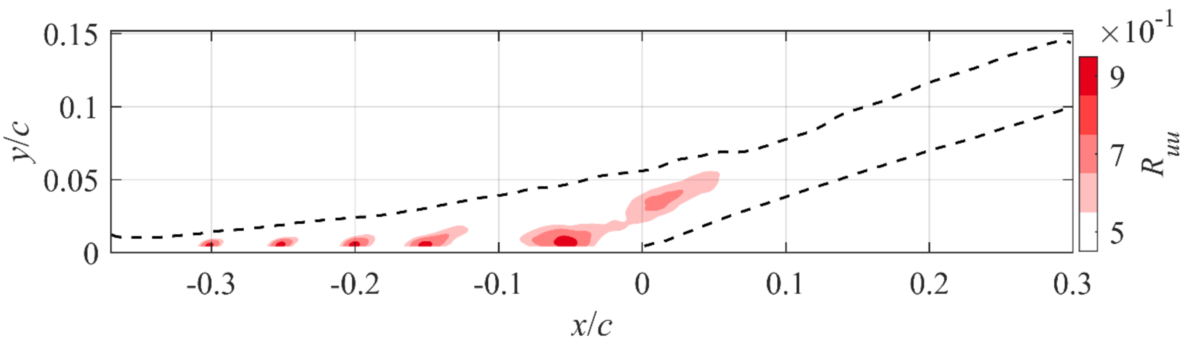

Figure 5.10. The correlation functions for five reference points located at $y_0/c = 4 \times 10^{-3}$ and $x_0/c = -0.3, -0.25, -0.2, -0.15$, and -0.05. The most downstream correlation function shows a double-peak pattern.

5.3.4 Energetic Motions

In this section, spectral proper orthogonal decomposition (SPOD) of the velocity fields, based on the algorithm described by Towne et al. (2018), is used to identify the frequency and spatial pattern of the energetic motions. This algorithm decomposes the Fourier transform of the velocity fields into spatial modes, $\Phi_i\,(x, f)$, and expansion coefficients, $a_i(f)$. Here, the index i denotes the mode number, and x is a vector indicating the spatial location. The details regarding the computation of SPOD is presented in Section 3.5.

Figure 5.11 shows the energy associated with the first 3 SPOD modes. These SPOD modes have been obtained from both components of the streamwise-wall-normal velocity fields using 15 planar PIV datasets. Each dataset is approximately 1.21 s long and is divided into 3 blocks with 50% overlap for SPOD calculations. As expected, the first mode captures the highest percentage of the energy, while the second and third modes have negligible energy across the frequency spectrum. The separation in the energy of the first and second modes is relatively large at $St_l < 0.1$, which indicates a low-rank behavior (Schmidt, et al., 2018). The first mode shows the highest energy at the lowest resolved St_l of 0.02, which is similar to the St_l of breathing motion reported by Weiss et al. (2015) and Mohammed-Taifour & Weiss (2016). The first mode also exhibits smaller local peaks at approximately St_l = 0.16 and 0.72. The St_l of these peaks is close to the vortex shedding frequency, which is approximately at St_l = 0.2 to 0.8 according to Figure 5.6.

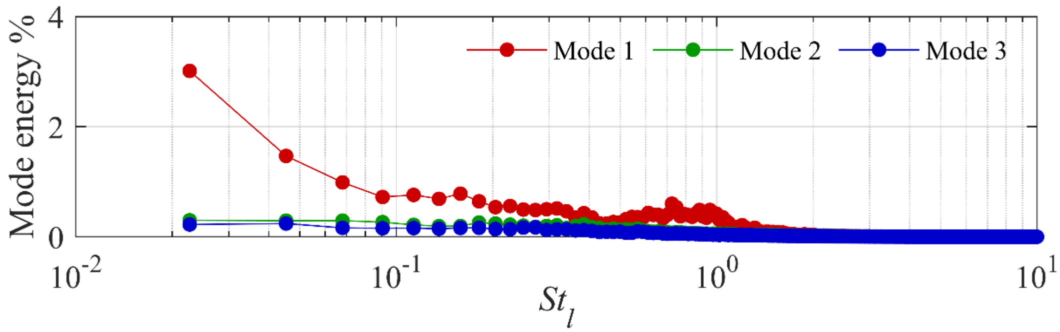

Figure 5.11. The energy spectra of the first 3 SPOD modes are calculated from the streamwise-wall-normal velocity fields.

The spatial patterns of the first SPOD mode at St_l = 0.02, 0.16, and 0.72 from the streamwise-wall-normal plane are shown in Figure 5.12. In addition, a reduced-order model (ROM) of the flow field, U_{ROM}, has been constructed using the mean velocity field and the selected mode following

$$U_{ROM,i} = \langle U \rangle + \Phi_{i(x,f_0)} e^{2\pi i f_0 t} \quad . \tag{5.2}$$

Here, t is time and f_0 is the frequency of the selected SPOD mode used for reconstructing the ROM. The forward-flow probability, γ, for the ROMs constructed from each spatial mode at the selected f_0 was then computed and is shown using the contour lines in Figure 5.12. The spatial pattern of the first mode at St_l of 0.02 consists of a large, inclined structure that is approximately aligned with the upper shear layer. The γ contours of this first mode show that it is associated with the large-scale expansion and contraction of the TSB. These contours are also similar to those of the forward-flow probability previously observed in Figure 5.2b, which shows that this spatial pattern captures the dominant large-scale unsteadiness within the streamwise-wall-normal plane. The small St_l of this SPOD mode and the fact that this mode is the main contributor to the intermittency of the TSB suggest that it is associated with the breathing motion of the TSB. As noted previously, in the context of TE separation, the breathing motion is defined as low-frequency variations of the TSB cross-section. This SPOD mode is consistent with the proper orthogonal decomposition (POD) analysis of Mohammed-Taifour & Weiss (2016), which showed that the first POD mode in the streamwise-wall-normal plane is associated with the breathing motion. The second and third spatial patterns at $St_l = 0.16$ and 0.72 in Figure 5.12 feature smaller structures that develop along the shear layers. The alternating spatial patterns and their large St_l suggest that they capture the vortex shedding process of the shear layers. The intermittency contours in Figure 5.12 indicate that the spatial pattern at St_l of 0.16 produce a considerable expansion/contraction of the TSB near the TE, while the spatial pattern at St_l of 0.72 does not result in a significant expansion or contraction of the TSB.

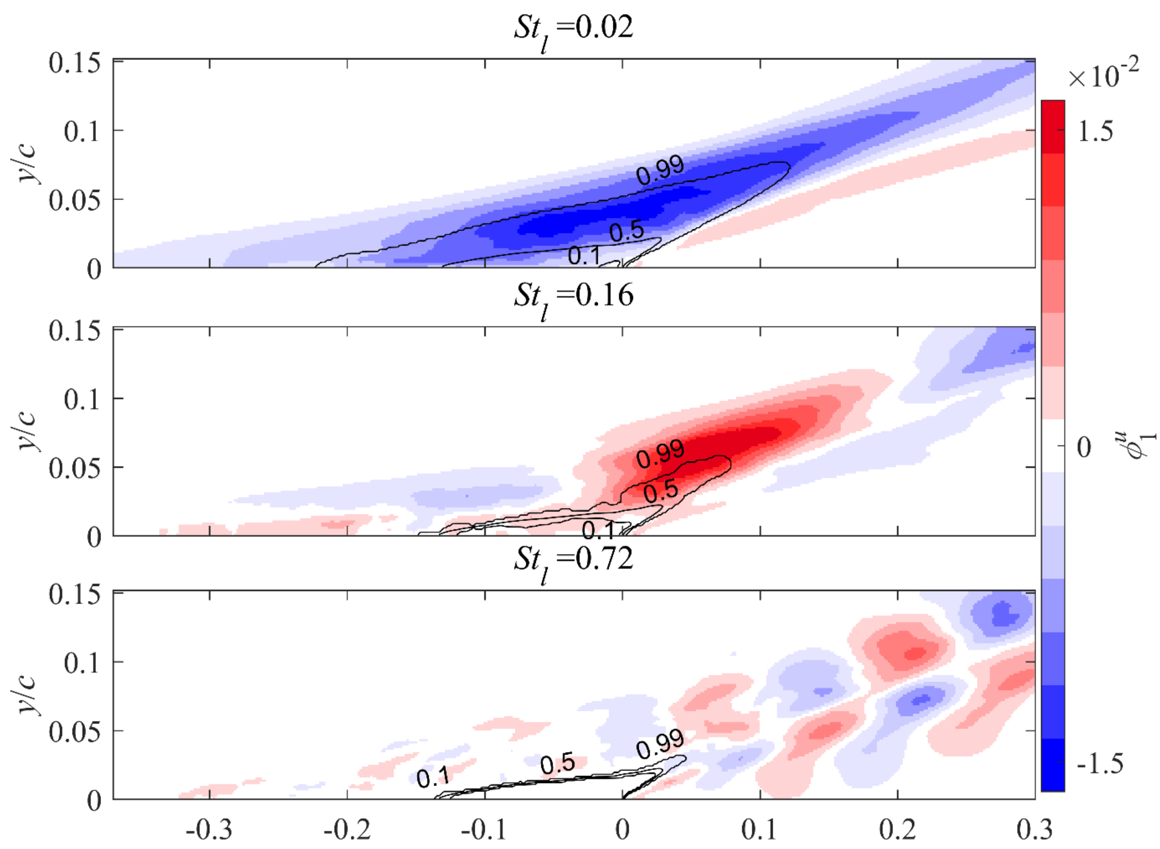

Figure 5.12. The spatial structures of the first SPOD mode from the streamwise-wall-normal plane at $St_l = 0.02$, 0.16, and 0.72. The contour lines represent the forward-flow probability obtained from the ROM following equation 5.2.

The three most energetic SPOD modes obtained using u and w from 10 datasets of the streamwise-spanwise PIV are shown in Figure 5.13. Each data set is approximately 1.35 seconds and is divided into 3 blocks with 50% overlap (30 blocks in total). For all 3 modes, the low-frequency oscillations have higher energy, with the maximum energy seen at the smallest St_l of 0.02. The energy of the modes quickly reduces with increasing St_l as most of the energy is at $0.02 < St_l < 0.1$. In contrast to the SPOD modes of the streamwise-wall-normal velocity fields, there is no secondary peak at higher St_l. The small St_l of the energetic range frequency band suggests that the spatial modes do not attribute to large-scale motions of the incoming TBL with $0.1 < St_l < 5$, or the vortex shedding process with $St_l = 0.4$.

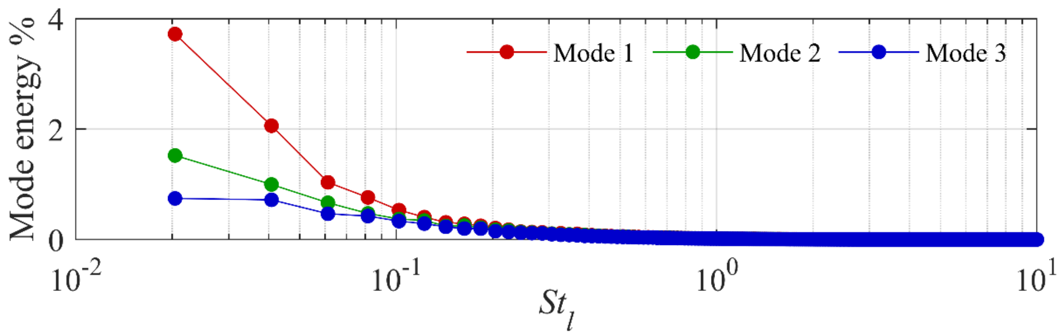

Figure 5.13. The energy spectra of the first 3 SPOD modes obtained from the streamwise-spanwise velocity fields.

The spatial patterns of the first SPOD mode at four St_l values of 0.02, 0.04, 0.06, and 0.08 are shown in Figure 5.14. The forward-flow probabilities from the associated ROMs are also shown using contour lines. At $St_l = 0.02$ and 0.04, a single large-scale structure results in large expansion/contraction of the separation front. The forward-flow probability contours at these St_l values show large advancement/recession of the backflow region. The spatial patterns at higher St_l of 0.04 and 0.06 consist of smaller alternating structures. However, their forward-flow probability contours still show considerable advancing and receding motions of the backflow region. Therefore, the lead SPOD mode at the energetic frequencies with $St_l < 0.1$ captures large-scale back-and-forth motions of the separation front.

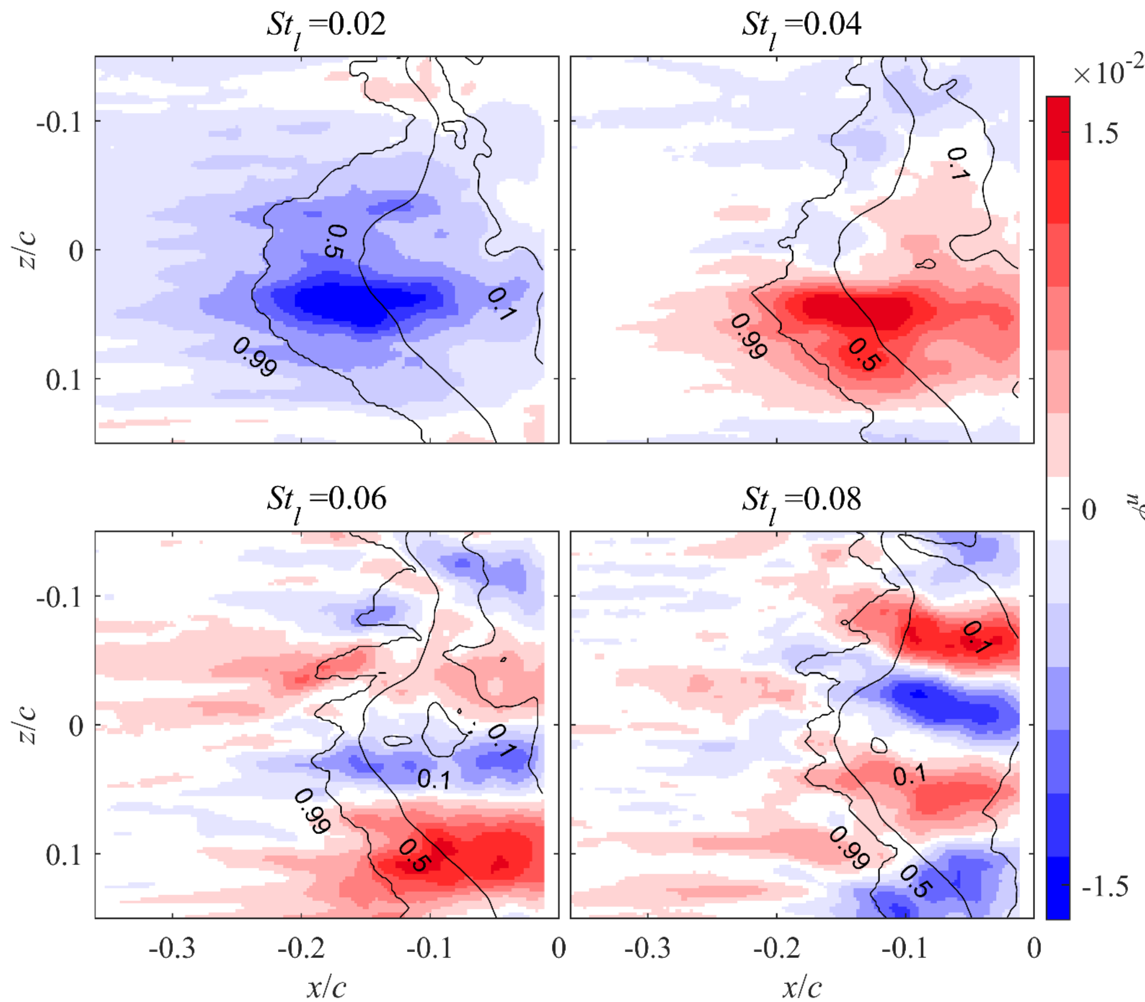

Figure 5.14. The spatial structures of the first SPOD mode of the streamwise-spanwise PIV plane at St_l = 0.02, 0.04, 0.06, and 0.08. The contour lines represent the forward-flow probability obtained from the ROM following equation 5.2.

5.3.5 The Breathing Motion

The breathing motion of the TSB is investigated in Figure 5.15a using the pre-multiplied PSD of the instantaneous backflow area, A, computed using the streamwise-wall-normal cross-section of the TSB. The figure also shows the pre-multiplied PSD of the streamwise location of the detachment point ($x_{D'}$), the streamwise location of the endpoint ($x_{E'}$), and the wall-normal location of the midpoint ($y_{M'}$). The coordinates of points D′, E′, and M′ are also obtained from the instantaneous streamwise-wall-normal PIV plane. The streamwise location of M′ is fixed at $x_{M'} = ½\times(x_D+x_E)$, which is the midpoint between the detachment and end points of the mean TSB, while its wall-normal location ($y_{M'}$) is detected from the instantaneous boundary of the

TSB. Here, M′ is investigated to characterize the flapping motion, i.e. the wall-normal motion of the shear layer. Before calculating the PSDs, the mean value of each variable was subtracted and then it was normalized using its standard deviation, σ. As a result, the area under each curve in Figure 5.15 is equal to one. Similar to the procedure applied for obtaining Figure 5.6, the PSDs were calculated using 45 periodograms (each of the 15 datasets were divided into 3 segments with 50% overlap). The pre-multiplied PSD of A shows a large peak at approximately $St_l = 0.05$. The peak indicates expansions and contractions of the TSB area at low St_l, which is attributed to the breathing motion. The pre-multiplied PSD of A rapidly decreases at higher St_l and therefore the energetic expansions and contractions of the TSB area are limited to $St_l < 0.1$. The pre-multiplied PSD of $x_{D'}$ shows a broader range of energetic fluctuations with a peak approximately at $St_l = 0.1$. The broader energy distribution in the pre-multiplied PSD of $x_{D'}$ is attributed to the superposition of the small- and large-scale motion of the separation front seen in the spatial pattern of the SPOD modes of Figure 5.14. The pre-multiplied PSD of $x_{E'}$ also has a broad energy distribution while it exhibits higher energy at frequencies within the $St_l = 0.1$ to 0.3 range. The latter is slightly smaller than the vortex shedding St_l (from 0.2 to 0.8 based on Figure 5.6). The discrepancy is associated with the interaction of the two shear layers, making the larger displacements of the endpoint occur at the lower frequencies. The pre-multiplied PSD of $y_{M'}$ is similar to that of A with most of the energy at lower frequencies. The peak value is also at approximately $St_l = 0.05$ which is similar to the St_l of the breathing motion. This observation suggests that the expansions and contractions of the TSB at $St_l = 0.05$ should correlate with the flapping motion of the shear layer.

To further substantiate the above observations, the correlation between A and $x_{D'}$, $x_{E'}$, and $y_{M'}$ is quantified using the coherence functions shown in Figure 5.15b. The results show that the coherence function of A and $x_{D'}$ is relatively small across the investigated spectrum. This shows that the breathing motion does not strongly correlate with the motions of the detachment point. In contrast, the coherence of A and $y_{M'}$, and the coherence of A and $x_{E'}$, are large at the low-frequency range of $St_l < 0.1$. Therefore, the breathing motion correlates with both the flapping motion of the shear layer and the streamwise displacements of the TSB endpoint. The correlation between A and $y_{M'}$ was suggested based on Figure 5.15a as both signals had high energy and similar pre-multiplied PSD shapes at $St_l < 0.1$. However, the correlation of A and $x_{E'}$ was not expected from Figure 5.15a since the pre-multiplied PSD of $x_{E'}$ did not exhibit large energy at $St_l < 0.1$. Figure 5.15b also shows that coherence between A and y_{M} rapidly declines with increasing St_l, while A and $x_{\mathrm{E}'}$ remain relatively correlated at higher frequencies. The coherence function of A and $x_{\mathrm{E}'}$ has a local peak at St_l of approximately 0.2, which overlaps with the peak energy observed in the pre-multiplied PSD of $x_{\mathrm{E}'}$ of Figure 5.15a. In summary, the results show that the breathing motion (low-frequency expansion and contraction of the TSB cross-section in the streamwise-wall-normal plane) correlates with the shear layer flapping and the displacements of the TSB endpoint.

The coherence functions between $x_{\mathrm{D}'}$, $y_{\mathrm{M}'}$, and $x_{\mathrm{E}'}$ displacements are also investigated in Figure 5.15c. The results show that the detachment point, $x_{\mathrm{D}'}$, does not correlate with the shear layer flapping, $y_{\mathrm{M}'}$, and the TSB endpoint, $x_{\mathrm{E}'}$. This agrees with the previous observations that indicated the displacement of the detachment point is derived from the fluctuations of the upcoming TBL (Eich & Kähler, 2020; Ma et al., 2020). Figure 5.15c also indicates that the flapping motion of the shear layer correlates with the streamwise displacements of the endpoint at the low frequency range of the spectrum.

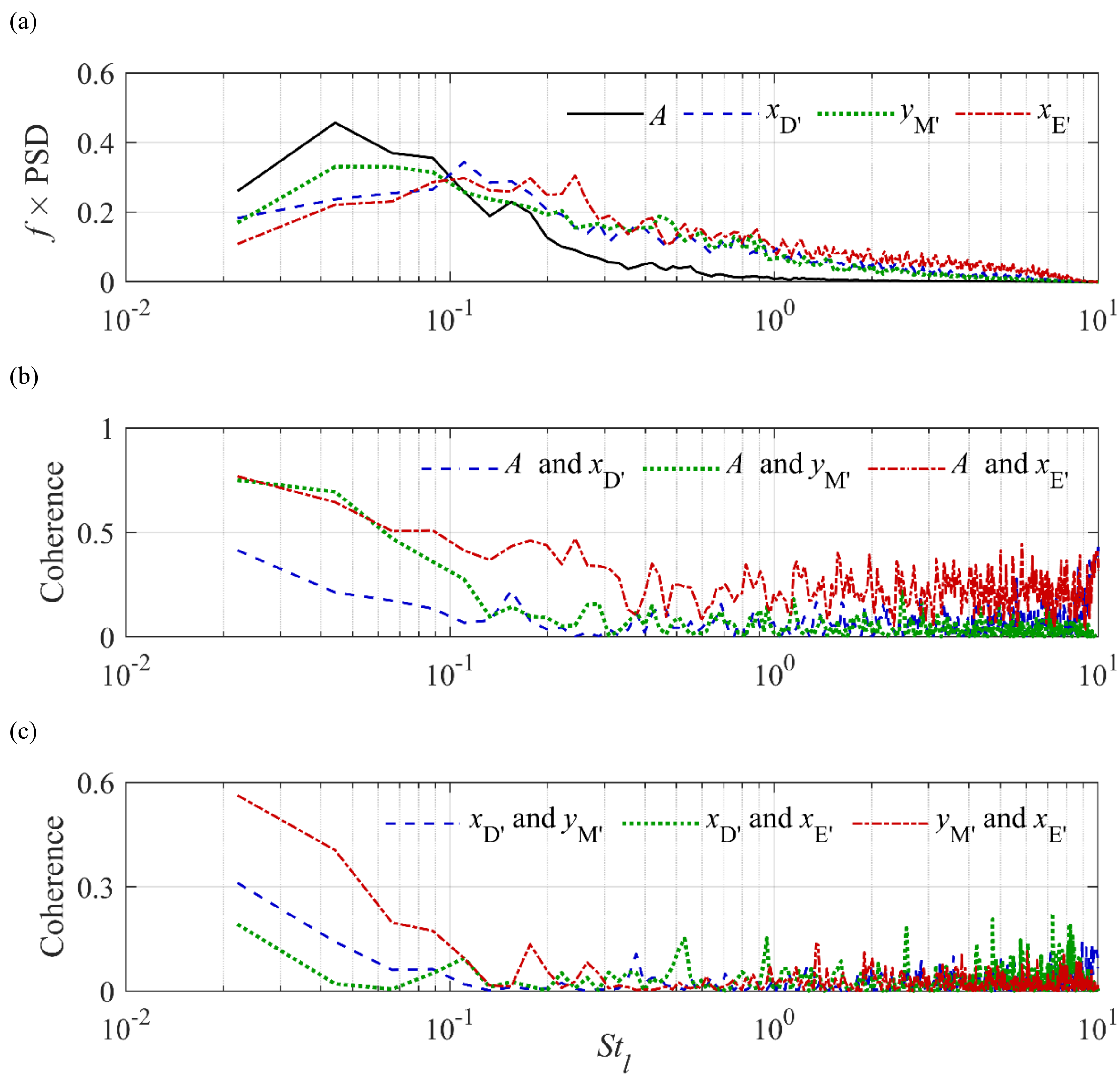

Figure 5.15. (a) Pre-multiplied PSD of the fluctuations in A, $x_{D'}$, $x_{E'}$, and $y_{M'}$. (b) The coherence functions between A and the three TSB coordinates $x_{D'}$, $x_{E'}$, and $y_{M'}$, and (c) the coherence between $x_{D'}$, $x_{E'}$, and $y_{M'}$.

The results showed that the large-scale expansion and contraction of the TSB area in the streamwise-wall-normal plane are mainly due to the oscillation of the endpoint and the wall-normal flapping of the TSB midpoint. In contrast, the motion of the detachment point has a smaller effect. However, the expansion and contraction of the TSB mainly occur at $St_l = 0.05$, which is smaller than the frequency of energetic motions of the detachment point at $St_l = 0.1$ to 0.3 (Figure 5.15) or the vortex shedding frequency at $St_l = 0.2$ to 0.8 (Figure 5.6). This discrepancy is associated with the spatial-averaging effect of the TSB. The mechanism is shown in Figure 5.16 by plotting the pre-multiplied PSD of pointwise and spatially averaged streamwise velocity fluctuations along the shear layers. The pre-multiplied PSD of u at (x, y) =

(0, 0.06c) corresponds to a single point in the upper shear layer, above the TE. As it is observed, the energetic flow motions are at $0.2 < St_l < 1$, which is consistent with the energetic motions seen in Figure 5.6b. The lines labeled as k = 0.5, 1, and 1.5 show the pre-multiplied PSD of streamwise velocity that is spatially average along the upper shear layer over a curvilinear trajectory that is centered at $(x, y) = (0, 0.06c)$ and extends in the upstream and downstream directions by $0.5l$, $1l$, and $1.5l$, respectively. Therefore, a spatially averaged velocity is first calculated as

$$u_{avg} = \int_{-kl}^{+kl} u \, dx_c, \tag{5.3}$$

and then its pre-multiplied PSD is calculated. In this equation, x_c is the curvilinear coordinate system defined in Figure 5.4a, and k is the kernel of the averaging line (k = 0.5, 1, and 1.5 in Figure 5.16). The results show that by spatially averaging the velocity fluctuation the St_l of the energetic motions reduces to $St_l = 0.2$ for $k = 0.5$, and finally to a small St_l of 0.07 for $k = 1.5$. Therefore, Figure 5.16 demonstrates that although the vortex shedding process is at a higher St_l of 0.2 to 0.8, the ensemble effect of the velocity fluctuations along the shear layer is at a smaller St_l. This observation also suggests that the St_l of the breathing motion inversely scales with the TSB size; the larger the TSB, the greater the effect of spatial averaging. This is consistent with the investigation of Le Floc'h et al. (2020) where three TSBs with small, medium, and large sizes were investigated. Their measurements show that the larger TSB has the smallest breathing frequency, which is potentially due to spatial averaging of the velocity fluctuations over a longer shear layer.

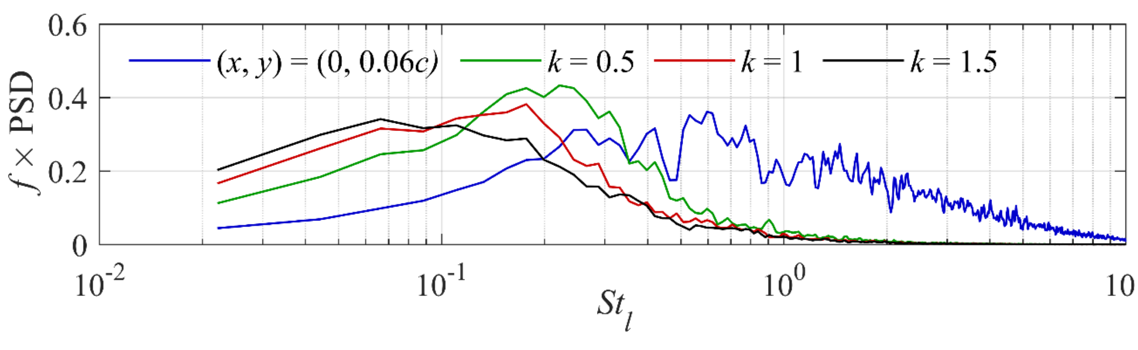

Figure 5.16. Pre-multiplied PSD of streamwise velocity fluctuations at $(x, y) = (0, 3.3c)$ and pre-multiplied PSD of spatially averaged velocity according to equation 5.3.

5.4 Conclusion

The turbulent separation bubble formed upstream of the trailing edge (TE) of a 2D wing was experimentally investigated. The wing was made from a NACA 4418 airfoil profile with a chord length, *c*, of 0.975 m and was set to an angle-of-attack of 9.7°. The Reynolds number based on *c* and the freestream velocity was 720,000. The transition of the boundary layer to turbulence was forced using a trip wire placed 0.2*c* downstream of the wing leading edge. Measurements using time-resolved planar particle image velocimetry (PIV) were conducted in a large streamwise-wall-normal plane at the midspan of the wing using three synchronized high-speed cameras. PIV measurements in a streamwise-spanwise plane that was parallel to and near the wing surface were also carried out using two synchronized high-speed cameras.

The PIV measurements showed that a turbulent boundary layer (TBL) formed on the suction side of the wing. At 0.35*c* upstream of the TE, the Reynolds number of the TBL based on the freestream velocity and the local momentum thickness was 2,800, and the estimated friction Reynolds number, Re_τ, was 900. Farther downstream, the TBL detached due to an adverse pressure gradient. The mean detachment point of the TSB was 0.13*c* upstream of the TE. The TSB had a triangular shape skewed in the downstream direction. The size of the TSB was characterized using the length of its upper edge, *l*, which was equal to 0.16*c*. The three vertices of the triangular-shaped TSB consisted of (a) an intermittent detachment point, (b) an approximately fixed corner near the airfoil TE, and (c) an intermittent endpoint in the wake region of the airfoil. The TSB featured two strong shear layers: an upper shear layer formed by the intermittent detachment of the suction-side TBL and a lower shear layer formed by the fixed detachment of the pressure-side boundary layer at the airfoil TE. The two shear layers generated zones of high Reynolds stress with peak intensities located downstream of the TE. The shear layers evolved in the wake region (free from the wall) and tended to gradually merge. The triangular shape of the TSB and the presence of the two shear layers differentiates this TSB from the dome-shaped TSB of previous investigations where a single TBL separates and reattaches over a flat plate. In the streamwise-spanwise plane, the TSB featured an undulating separation front.

Spectral analysis of the streamwise velocity fluctuations showed three energetic regions with different Strouhal numbers, St_l, defined as fl/U_∞. The first region consisted of the energetic motions of the upstream TBL. The TBL fluctuations started with a large $St_l = 4$ which gradually reduced to $St_l = 0.1$ as the TBL approached the detachment point. These fluctuations were attributed to the large-scale motions of the TBL, whose time scale gradually increased under the effect of an adverse pressure gradient. The second energetic region was at the TSB location and featured motions at smaller St_l ranging from 0.03 to 0.08. The peak of these energetic motions was at $St_l = 0.06$. The third region included the energetic motions of the two shear layers at St_l = 0.2 to 0.8, which is equivalent to St_δ = 0.05 to 0.2. Here, St_δ is defined as $f\delta/U_\infty$ where δ is the thickness of the shear layer at $x/c = 0.2$ in the wake. The St_δ of the fluctuations is consistent with the vortex shedding frequency of Kelvin-Helmholtz instabilities.

The spatial and temporal scales of the low-frequency energetic motions within the TSB were investigated using instantaneous visualizations and two-point correlations. The results show that the TSB consisted of large zones of positive and negative streamwise velocity fluctuation. The zones were several times wider than the large-scale motions within the upstream TBL. The timescale of these zones was also two orders of magnitude greater than the large-scale motions within the upstream TBL. This observation agrees with the smaller St_l = 0.03 to 0.08 observed within the TSB relative to the higher St_l = 0.1 to 4.0 within the TBL. The positive and negative zones modulated the location of the separation front. Zones with positive fluctuating velocity appeared when the detachment point shifted in the downstream direction, while zones with negative fluctuating velocity were present when the detachment point shifted in the upstream direction. Analysis of the mean flow field suggested that these large zones are formed by the Görtler structures as the flow follows the curved streamlines above the TSB. The two-point correlation functions showed that the zones strongly correlate with the velocity fluctuations between the two shear layers in the wake region.

Spectral proper orthogonal decomposition (SPOD) was performed to identify the energetic motions of the TSB. In the streamwise-wall-normal plane, the dominant SPOD mode captured a large-scale breathing motion at $St_l = 0.02$. The first mode also showed the vortex shedding processes at St_l =0.16 and 0.72. The vortex shedding process at $St_l = 0.16$ contributed to the intermittency of the TSB aft section, while no considerable intermittency was observed at St_l = 0.72. In the streamwise-spanwise plane, the SPOD modes had higher energy at the lower frequencies. The dominant SPOD mode demonstrates large-scale advancement/recessions of the TSB region at $St_l < 0.1$.

Spectral analysis of the TSB cross-section in the streamwise-wall-normal plane showed that the TSB expands and contracts (breathes) at a frequency of $St_l = 0.05$. Analysis using the coherence function confirmed that the TSB breathing correlates with the motion of the TSB endpoint and the wall-normal motion (flapping) of the upper shear layer. As a result, the breathing of the TSB was mainly attributed to the shear layer motion and the vortex shedding fluctuation. The lower frequency of the breathing motion with respect to the fervency of the vortex shedding process was attributed to the spatial-averaging effect of the TSB. The intermittency of the detachment point showed broad fluctuations within $0.01 < St_l < 0.2$ with no strong correlation with the cross-sectional area of the TSB.

Chapter 6. The breathing motion in wall pressure

In Chapter 6, the results of project 3 are presented. This chapter is an extension of the previous one, which focuses on determining the interaction between wall pressure and breathing motion. In this chapter, the relation between the two is evaluated through both pressure-velocity correlation and spectral proper orthogonal decomposition analysis. The results can help determine the optimal location to detect the breathing motion using wall-pressure sensor. The derived phase relation between the breathing motion and its signature in wall pressure can be used to predict the breathing behavior and is beneficial in developing a detection strategy for real-time identification of the breathing motion.

6.1 Introduction

The unsteady effects of turbulent separated flows refer to repeatable organized time dependent events (Simpson, 1981). In practical applications, the unsteadiness always leads to some adverse effects that may reduce the performance of fluidic devices, e.g., high-lift wings. When turbulent flow separation occurs near the trailing edge (TE) of an airfoil, i.e., TE separation, force fluctuations that will induce structural vibrations are produced. In the studies of unsteadiness in TE separation, some early investigations found that a significant amount of energy of the fluctuations resides in a frequency range that is much smaller than the natural vortex shedding process (Zaman et al., 1989; Broeren & Bragg, 2001). The corresponding force fluctuations also have an amplitude that is comparable with those produced by leading-edge separation (Broeren & Bragg, 1998).

Recent investigations of the unsteadiness in pressure-induced turbulent separated flow showed that the separation bubble features a low-frequency quasi-periodic breathing behavior. It has a St_l on the order of 0.01, when scaled by the characteristic length l of the separation bubble (Weiss et al., 2015; Mohammed-Taifour & Weiss, 2016; Mohammed-Taifour & Weiss, 2021). This Strouhal number is strikingly similar to the low-frequency force fluctuations (St_l = 0.02) observed on rectangular wings (Zaman et al., 1989). A more recent numerical simulation also demonstrated that the breathing of separation bubble is well correlated with the low-frequency lift fluctuations experienced by a 2D wing (Liu & Xiao, 2020). A clear connection was established between the breathing motion and the low-frequency force fluctuation.

Suppressing the breathing motion could significantly reduce the low-frequency force fluctuations on wings.

Due to the periodicity of the breathing motion, active flow control (AFC) is considered as a more effective control method than the passive ones. AFC has the advantages of broad adaptability, which is essential in tackling the breathing motion. For instance, AFC can be designed into a feedback or feedforward loop that can adapt the control model to the varying flow conditions in real time (Collis et al., 2004; Widerhold et al., 2010). An optimal AFC requires an adequate sensor to measure the flow status first and actuate the flow accordingly. An ideal sensor is wall-pressure measurement device (Cattafesta III & Sheplak, 2011; Greenblatt & Wygnanski, 2019), which is non-intrusive and can detect flow motion associated wall-pressure variation. To effectively carry out AFC, it is crucial to have sufficient understanding of the relation between the breathing motion and wall-pressure fluctuations, i.e., pressure-velocity relation. For example, the optimum location to install sensor can be determined by investigating the impact of breathing TSB on wall pressure at different locations; the phase relation between the breathing motion and wall pressure can help to find the optimal timing of actuating the flow.

In this work, investigation regarding the relation between the breathing motion and wall pressure was carried out by performing simultaneous planar PIV and wall-pressure measurements along the midspan of the wing. Spectral analysis is performed on measured wall-pressure fluctuations. To probe whether wall pressure fluctuations can sense the breathing motion and the ideal detection location, spatio-temporal cross-correlations between velocity fields and low-pass filtered wall-pressure are carried out. Spectral proper orthogonal decomposition (SPOD) analysis is also performed to investigate the interaction and phase difference between the breathing of turbulent separation bubble (TSB) and the wall pressure at $0.4l$ upstream and downstream of the mean detachment point.

6.2 Experimental setup

In project 3, time-resolved planar PIV measurements and wall-pressure fluctuation measurements were carried out to investigate the relation between wall-pressure fluctuation and breathing motion. The experiments employed the wing and wind tunnel introduced in Section 3.1. The wing was set to an angle-of-attack of 9.7° and the freestream speed was carefully adjusted to 10.2 m/s to have the mean detachment point at 0.19*c* upstream of the TE. All measurements were performed with a chord-based Reynolds number of 620,000.

6.2.1 Time-resolved planar PIV

Time-resolved planar PIV measurements were performed near the TE, in the *x*-*y* plane at midspan. The flow field was recorded by two high-speed cameras (Phantom v611). The acquisition rate was 2 kHz. Each camera has a sensor size of 1280 × 800 pixels with a pixel size of 20 × 20 μm^2. Two macro lenses (Sigma) with a focal length *F* of 105 mm were employed to image the combined field-of-view (FOV) at a digital resolution of 0.20 mm/pixel as shown in Figure 6.1a. The aperture setting was set to *F*/2.8 to increase the light intensity of the image plane. The combined FOV has a dimension of 500 × 125 mm^2 ($x \times y$), which approximately covered a streamwise range from $x/c = -0.35$ to 0.12, and a wall-normal distance up to 0.12*c* away from the wing surface ($y/c = 0$). The light source was a dual-cavity high-speed Nd:YLF laser (Photonics Industries, DM20-527DH). The light sheet was formed through a combination of spherical and cylindrical lenses and had an average thickness of 1.5 mm for the entire FOV. The light sheet was directed from an upstream direction at a shallow incidence angle with respect to the wing surface to minimize wall reflections. The flow was seeded by 1-μm fog droplets generated by a fog machine (ADJ, Fog Fury 3000) placed at the upper section of the wind tunnel. Each PIV dataset consisted of 6,903 single-frame images and has a time duration of 3.45 s. Note that the PIV measurements were conducted simultaneous to wall-pressure measurements. Further details regarding the number of datasets will be introduced in the next section, along with the details of wall-pressure measurements.

To obtain the velocity fields, the following processes were performed in DaVis 8.4 (LaVision GmbH). First, the signal-to-noise ratio of the images was improved by subtracting the ensemble minimum intensity from each image and then by normalizing the images using the ensemble average intensity. The velocity vectors were calculated based on a sliding-sum-of-correlation algorithm with 3 successive pairs of images (Ghaemi et al., 2012) using a final interrogation window of 32 × 32 pixels (6.4 × 6.4 mm^2) at 75% overlap. The first valid vector close to the wall is at approximately $y/c = 1 \times 10^{-3}$. The vector fields included approximately 2% spurious vectors. They are observed mostly at the immediate downstream of TE, and in the shear layer due to the three-dimensionality of the flow. Universal outlier detection (Westerweel & Scarano, 2005) and bilinear interpolation were employed to remove and replace the spurious vectors. As suggested by Raffel et al., (2018), the error of planar PIV measurements is approximately 0.1 pixels. The error in the velocity vectors is then determined to be 0.04 m/s ($4\times10^{-3}U_\infty$), estimated using the digital resolution (0.20 mm/pix) and time delay between the adjacent laser pulses (500 μs).

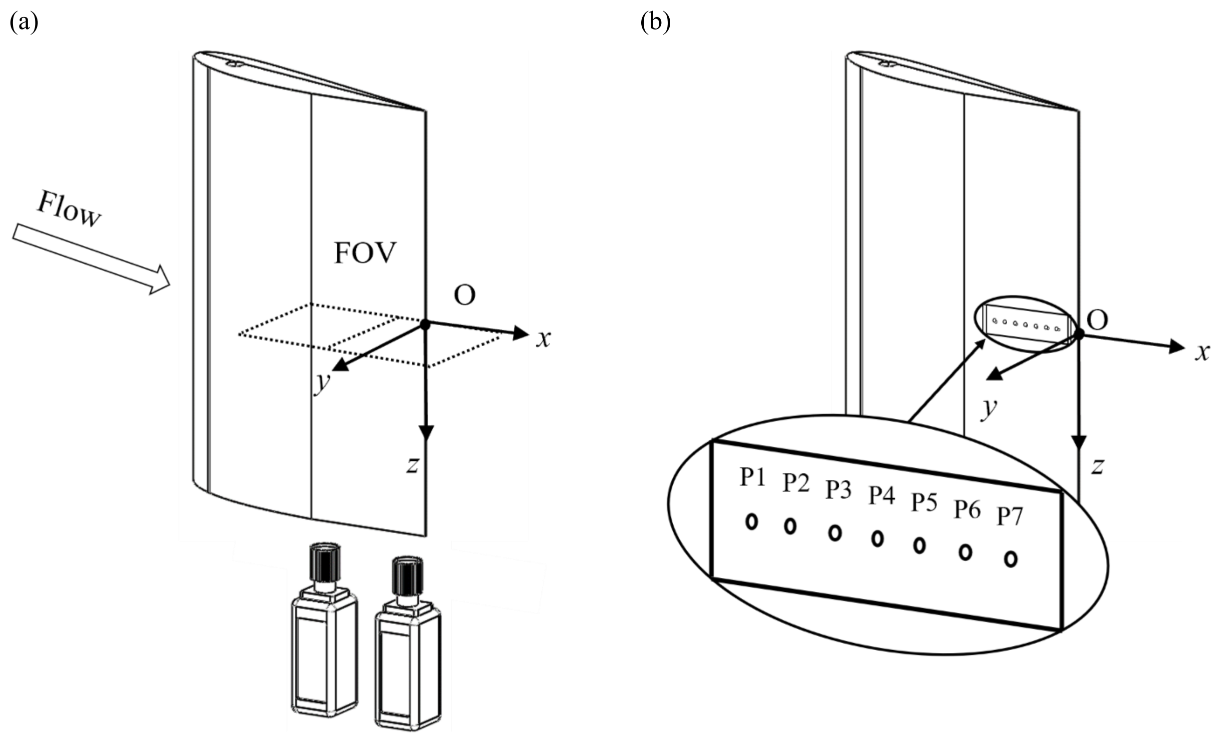

Figure 6.1. (a) A schematic of the experimental setup: a 2D wing is vertically installed in the test section at α = 9.7°. The two FOVs in the x-y plane are illustrated by dashed lines and are imaged by two high-speed cameras. The origin of the coordinate O is placed at the spanwise center of TE. (b) The 7 pinholes for wall-pressure measurements are labelled in the enlarged view, with P1 being the most upstream pinhole and P7 being the most downstream one. The pinholes are aligned along the midspan of the wing, evenly spaced between x/c = −0.300 to −0.084.

6.2.2 Wall-pressure measurement

Wall-pressure measurements were conducted near the TE along the midspan of the wing. The measurements took place at 7 streamwise locations, evenly spaced along the midspan (z/c = 0) as seen in Figure 6.1b. In the enlarged view, the pinholes are labeled as P1 to P7, with P1 being the farthest upstream position and P7 being the most downstream position. The corresponding streamwise coordinates for the pinholes are $x/c = -0.300$, -0.264, -0.228, -0.192, -0.156, -0.120, and -0.084. The MD coincided with the pinhole P4 at $x/c = -0.192$ through a careful adjustment of the freestream velocity.

Wall-pressure fluctuations were measured using infrasound microphones (1/2-inch Brüel & Kjær, 4964) paired with pre-amplifiers (Brüel & Kjær, 2669). The microphone-amplifier combination was capable of measuring frequency as low as 0.7 Hz, which is lower than the breathing frequency (~3 Hz) measured for a similar flow configuration (Wang & Ghaemi, 2022). The microphones were calibrated using a constant-frequency calibrator (Brüel & Kjær, 4231), which produced 1 Pa acoustic waves at 1 kHz. As suggested by the manufacturer, the calibrator has an uncertainty of ±0.2 dB for a nominal pressure of 94 dB. Therefore, the calibration uncertainty in instantaneous pressure measurement is approximately 2.1%. The pressure signals were sampled at 20 kHz and recorded by Simulink Real-Time (Mathworks) using a real-time target machine (Speedgoat, Mathworks) with a 16-bit input/output module (IO135). The microphones were installed behind pinholes to obtain accurate point measurements. The cross-section views of the pinhole in the *x*-*y* and *y*-*z* planes are illustrated in Figure 6.2a and b, respectively. From the *x*-*y* cross-section view (Figure 6.2a), it is seen that a pinhole with a 0.5-mm diameter and 3.5-mm length connects a cylindrical cavity (white) to the wing surface. The small diameter of the pinhole minimized the spatial-averaging effect in the measurement. The cavity has a diameter of 10.05 mm in the *y*-direction (as seen in Figure 6.2a) and a depth of 3 mm in the *z*-direction (as seen in Figure 6.2b). The microphone (light grey) was threaded into the cavity and closed it by its diaphragm (blue line). More details regarding the installation of microphone are provided in Appendices C.2 and C.4.

It is important to note that the cavity acts as a Helmholtz resonator, which distorts the amplitude and phase of the pressure signals (Tsuji et al., 2012). To correct the distortions, a transfer function was determined by performing dynamic calibration against a second identical microphone not attached to a pinhole. Both microphones were positioned in a quasi-anechoic chamber (Gibeau & Ghaemi 2021) and simultaneously recorded sound waves generated by a speaker from 1 to 2 kHz. The microphone without a pinhole attachment has a flat response across the frequency range. The comparison between the two recorded signals allows to find the transfer function of the resonator, which is modelled as a second-order linear, time-invariant system (Tsuji et al., 2012). The transfer function is then used to correct the distorted pressure signals, which provides a reliable frequency response that can reach up to approximately 460 Hz. The MATLAB (MathWorks) code used to correct Helmholtz resonance is provided in Appendix B.1. Apart from the distortion caused by the installation of pinhole, the wall-pressure measurements were also polluted by wind tunnel background noise. To address the issue, a Wiener noise canceling filter (Hayes, 1996) was employed. The filter estimated the noise component of a wall-pressure signal from a simultaneously acquired background noise signal. The noise signal was measured using a third infrasound microphone (1/2-inch Brüel & Kjær, 4964) placed in the freestream, away from the wing with a nose cone attached (for details see Gibeau & Ghaemi, 2021). The estimated noise component was subtracted from the wall-pressure signal to retain only the hydrodynamic component. The noise component is estimated using the MATLAB (MathWorks) code attached in Appendix B.2.

Since only two microphones were available for surface pressure measurements, for each data acquisition, the wall-pressure fluctuations were recorded at P4 and another pinhole position. This resulted in 6 pinhole pairs: (P4, P1), (P4, P2), (P4, P3), (P4, P5), (P4, P6), and (P4, P7). An additional measurement was performed to record wall-pressure fluctuations at P1 and P7 together, (P1, P7). For each wall-pressure measurement pair, 10 simultaneous time-resolved PIV datasets were recorded at 2 kHz, each 3.45 s. Therefore, a total number of 70 time-resolved PIV datasets were collected for the 7 pressure measurement combinations. The laser trigger signals sent to the PIV measurements were recorded for the purpose of data synchronization in post-processing. The vector fields were synchronized with the wall-pressure signal by aligning the signals of the laser trigger and wall-pressure acquisition. To obtain converged statistics of the pressure field, two additional long-duration sets of wall-pressure measurements were conducted for each pinhole pair without PIV recordings. Each of these sets spanned a time duration of 60 s.

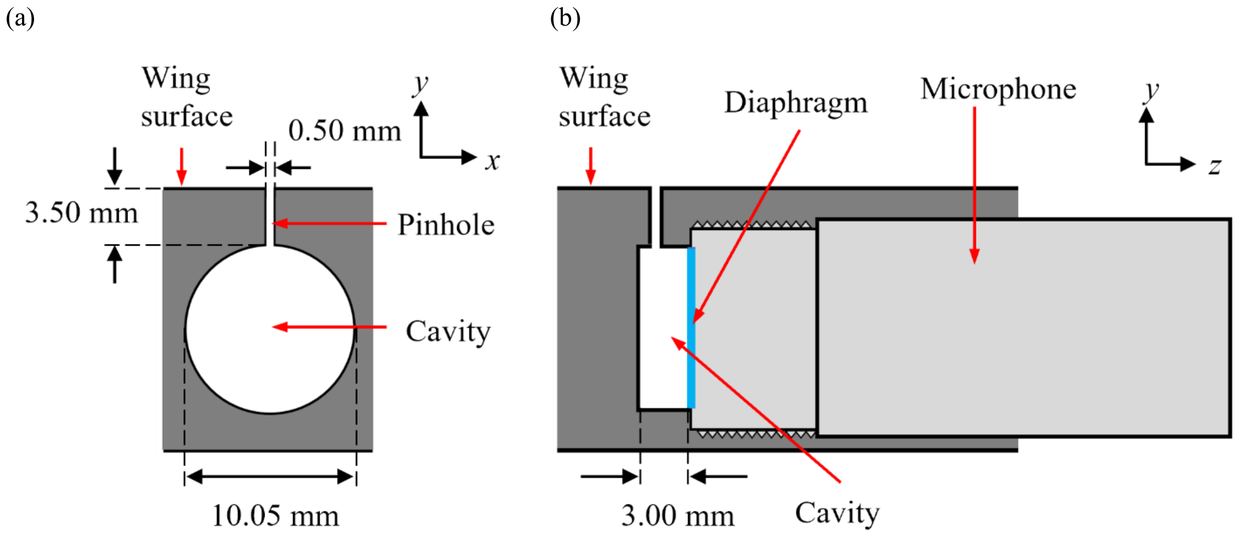

Figure 6.2. The cross-section view of the pinhole attachment in the (a) *x*-*y* and (b) *y*-*z* planes. The pinhole connects the wing surface to a cavity, sealed by the microphone diaphragm. The small diameter of pinhole reduces the spatial-averaging effect in wall-pressure measurements.

6.3 Results and discussion

The mean velocity and pressure fields and their unsteadiness are first independently characterized based on PIV and wall-pressure measurements. Next, the relation between the breathing of TSB and wall pressure is investigated using the synchronized measurements of velocity fields and wall pressure fluctuations. Specifically, the pressure-velocity correlations are obtained to identify the relation between breathing motion and wall-pressure fluctuations. The dynamics of the velocity and pressure fields, and their phase relation are also investigated by employing spectral proper orthogonal decomposition (SPOD).

6.3.1 Velocity field

The mean flow is characterized here using contours of $\langle U\rangle/U_\infty$ as seen in Figure 6.3a. The contour plot covers a streamwise distance from $x/c = -0.35$ to 0.12, while the TE is at $x/c = 0$. A black contour line that indicates $\langle U\rangle = 0$ is overlaid on the contours to show the boundary of the mean TSB. For reference, the pinhole locations are marked using blue dots along the wall, which represent P1 to P7 from left to right. The MD is located at $x/c = -0.192$, overlapping with P4, where upstream of this point $\langle U\rangle$ is positive and downstream of it $\langle U\rangle$ is negative. The endpoint of the mean TSB is defined as the most downstream point and is located at $x/c = 0.047$ and $y/c = 0.030$. The diagonal distance between these upstream and downstream points defines the characteristic length, l, of the TSB, which is approximately $0.25c$. The mean TSB has a unique triangular shape due to the two shear layers emerging from the two sides of the wing (Wang & Ghaemi, 2022). The shear layer on the suction side is labeled as the "upper shear layer" as seen in Figure 6.3a. It detaches from the wing surface due to an APG and advects diagonally into the wake. The other shear layer that emerges from the pressure side of the wing is labelled as the "lower shear layer". These two shear layers and the wing surface confine the triangular-shaped mean separation bubble.

Next, the contour of forward-flow probability γ is illustrated in Figure 6.3b to show the intermittency of the flow field. Here, the mean TSB edge approximately overlaps with the contour of $\gamma = 0.5$. Moving along a wall-parallel line at $y/c = 0.002$ and in the flow direction, γ gradually reduces from 0.99 to 0.10 over a relatively long streamwise distance of $0.23c$, which indicates strong intermittency of the detachment point. Additionally, the intermittency of end point leads to the recovery of γ from 0.10 to 0.99 over approximately $0.14c$ along the red dashed line shown in Figure 6.3b. These observations demonstrate that the expansion and contraction of the TSB occur primarily by the motions of the detachment and the end point of the TSB.

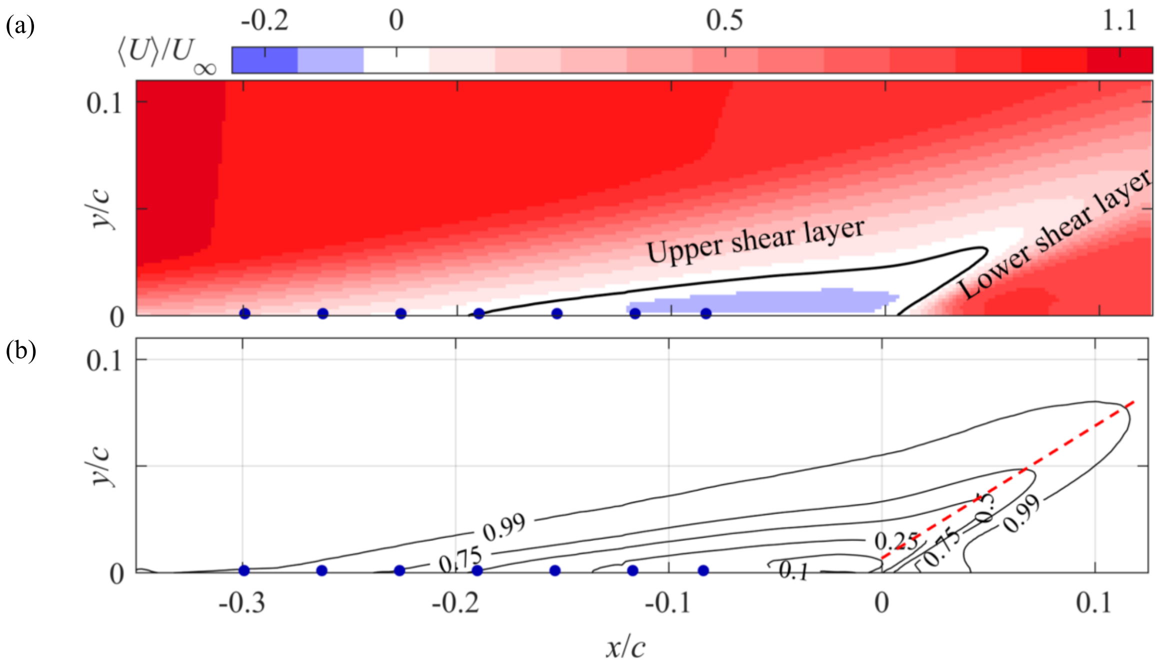

Figure 6.3. The contours of (a) $\langle U \rangle / U_\infty$ and (b) forward-flow probability (γ). The upper and lower shear layers are annotated and the black line shows $\langle U \rangle = 0$ contour. Blue dots represent the pinhole locations in both (a) and (b), indicating P1 to P7 pinholes from left to right.

To further investigate the unsteadiness of the velocity field, a spectral analysis of u/U_∞ is performed for all the PIV grid points that are along $y/c = 0.011$ line. The selected wall-normal distance is chosen close to the wall to capture the unsteadiness of the incoming turbulent boundary layer (TBL), TSB, and lower shear layer. The time-series signals of u are extracted from 70 time-resolved PIV datasets. To improve the statistical convergence, each dataset is divided into 3 segments with 50% overlap, which results in a total number of 210 periodograms. Each periodogram is approximately $74T$ long, where T is defined as l/U_∞. The Strouhal number St_l is also formulated as $St_l = f \times T$. The power spectral density (PSD) is calculated with a resolution of $St_l = 0.014$ (0.6 Hz), which represents the smallest resolvable frequency in each periodogram. The resulting PSDs are presented in Figure 6.4 as contours for various x/c locations along the $y/c = 0.011$ line.

As seen in Figure 6.4, the PSD peak is observed at $x/c = -0.11$, which is downstream of MD located at $x/c = -0.192$. The offset between the peak and MD locations is because the $y/c = 0.011$ line intersects the mean TSB downstream of the MD at approximately $x/c = -0.12$.

Therefore, the PSD peak at $x/c = -0.11$ overlaps with the boundary of the mean TSB along the $y/c = 0.011$ line. This PSD peak is also attributed to the breathing motion since it occurs at a low St_l of 0.03, which is comparable to the St_l values reported previously for the breathing motion (Weiss, et al., 2015; Wang & Ghaemi, 2022). Downstream of the TE, an isolated low-energy region is observed at x/c = 0.04 with a wide range of fluctuations spanning up to $St_l \approx 0.4$. At this location, the reference line y/c=0.011 crosses the lower shear layer. As discussed by Wang & Ghaemi (2022), the wide St_l range of fluctuations is attributed to intermittent switching between the lower shear layer and freestream at this location. Therefore, the results reveal that the unsteadiness attributed to the breathing motion is present in the near-wall region of the TSB, and it can be potentially detected by wall-pressure measurements.

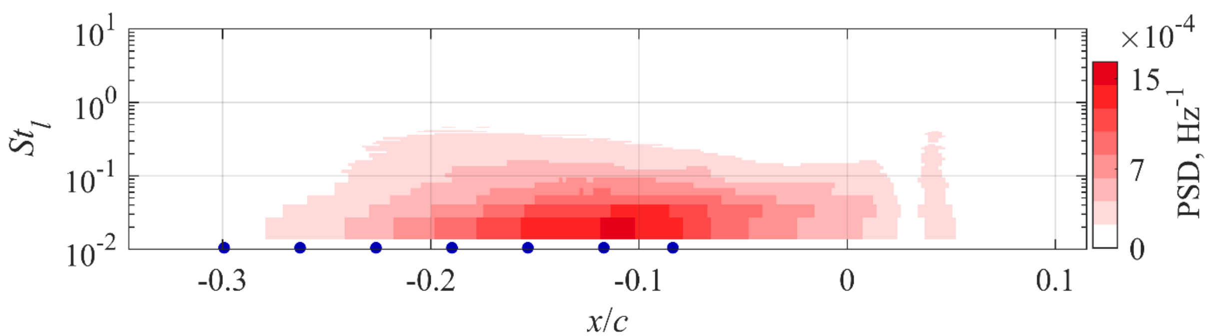

Figure 6.4. The PSD of u/U_∞ along $y/c = 0.011$ line. Blue dots indicate the pinhole locations, representing P1 to P7 from left to right. The largest unsteadiness is associated with the breathing motion with a peak at $St_l = 0.03$ and $x/c = -0.11$, overlapping with the front edge of the TSB.

6.3.2 Wall pressure

As previously determined, the velocity unsteadiness attributed to the breathing motion is most pronounced at the front edge of the TSB and has a St_l of approximately 0.03. To investigate its trace in wall-pressure fluctuations, p, spectral analyses of p measured at various x/c are carried out. Here, p is first normalized by q_∞, where q_∞ is calculated from $0.5\rho U_\infty^2$ with ρ being the air density. The PSD at each pinhole is computed based on two 60-s time-series data. To enhance the statistical convergence of the PSD, each of these datasets is divided into smaller 1-second segments with 50% overlap (Welch, 1967). Therefore, the smallest resolvable frequency from each segment is 1 Hz, which corresponds to a St_l of 0.024. The segmentation produces a total number of 238 periodograms. The resulting PSDs are presented in Figure 6.5, where warm and cold colors are utilized to distinguish PSDs upstream and downstream of P4, respectively. The PSD at P4, which overlaps with MD, is presented with a black line. Note that the horizontal axis is shown in a logarithmic format to make low St_l range visible. Therefore, the area under the PSDs in Figure 6.5 is not a representative of the fluctuations' energy.

Inspecting the PSDs of P1 to P3, a relatively flat distribution is observed for $St_l < 1$. In addition, the PSDs at P1 and P2 overlap, which can be attributed to the small variations in TBL at these two locations. Note that γ at these locations is above 0.75 as seen in Figure 6.3b. Moving to P3, where γ drops to approximately 0.7, a slight increase in PSD is noticed over a broad range of $0.04 < St_l < 1.6$ with two stronger peaks at $St_l = 0.07$ and 0.5. The relative flat PSD distribution suggests that wall pressure is mainly influenced by the broad flow motions of the incoming TBL. At P4 location, there is a more pronounced peak at approximately $St_l = 0.07$. This is close to the reported breathing Stl of 0.05 by Wang & Ghaemi (2022) in a similar flow configuration. The investigation of Weiss et al. (2015) also reported that the St_l of the breathing motion is on the order of 0.01 for a TSB formed on a flat plate. For P4, the PSD at $St_l > 1$ exhibits a noticeable reduction relative to P3, P2, and P1. This can be attributed to the higher probability of detached flow at P4. When the TBL is detached from the wall, the influence of small-scale turbulent structures with high St_l on wall pressure is expected to weaken (Weiss et al., 2015).

At P5 location, which is downstream of MD, the PSD energy significantly increases. The local flow is also intermittent at P5 with a small γ value of approximately 0.35 as seen in Figure 6.3b. A strong low-frequency peak is seen at approximately $St_l = 0.05$, which is close to the St_l of the breathing motion observed in the PSD of velocity from Figure 6.4. In addition to this low-frequency peak, another peak is seen near $St_l = 0.3$. The value of St_l for the latter peak is close to the vortex shedding oscillations observed at $St_l \approx 0.2$ to 0.4 (Weiss et al., 2015; Mohammed-Taifour & Weiss, 2016; Wang & Ghaemi, 2022). The results suggest that both the breathing and vortex shedding motions strongly impact wall pressure immediately downstream of MD.

The PSDs at P6 and P7 have similar shapes. The flow above these two pinholes is predominantly backflow with the γ values varying from 0.1 to 0.25. The PSD in the range of $St_l < 0.25$ at P6 and P7 is smaller than the PSD at P5 and they do not exhibit a distinct peak in the range. This suggests that the influence of the breathing motion on wall pressure has reduced in this region. Nevertheless, the PSDs remain higher than those upstream of MD, indicating that the p measured at P6 and P7 is still stronly impacted by the breathing motion. A peak still seen at $St_l = 0.35$ in the PSD of P6 and P7 with a similar magnitude as the vortex-shedding peak seen at P5. Therefore, the impact of vortex shedding on wall pressure does not change significantly downstream of the MD, suggesting that the vortex shedding is well sensed by wall-pressure fluctuations inside the mean TSB. The above observation is also consistent with the pre-multiplied PSDs reported by Weiss et al. (2015), which showed the fluctuations of p at St_l = 0.35 are more pronounced inside the TSB compared to the upstream region. The additional attenuation of PSD at $St_l > 0.70$ indicates that the small-scale turbulent fluctuations are farther away from the wall.

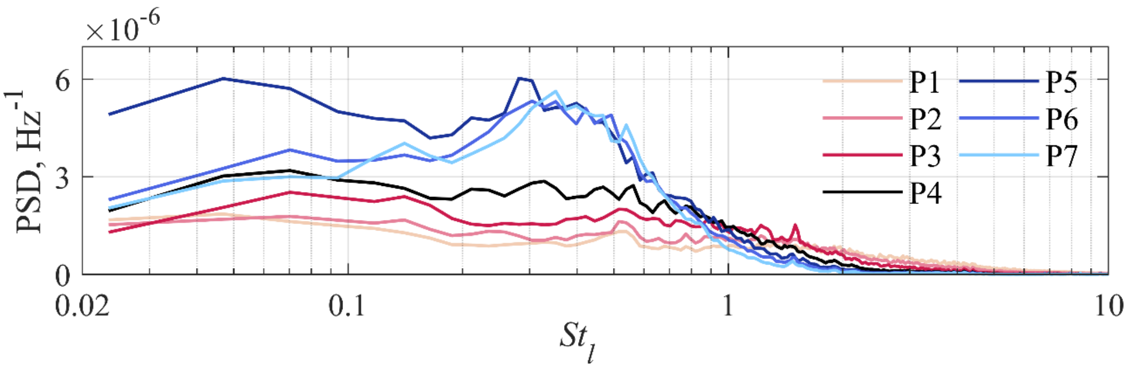

Figure 6.5. The PSD of p/q_∞ is shown for various streamwise locations along the mid-span. The PSD at P5 shows strong evidence of the breathing motion with a peak at $St_l = 0.05$. The effect of vortex shedding is pronounced downstream of MD with a peak at $St_l = 0.35$.

Based on the shape of PSDs from Figure 6.5, it is evident that there are two ranges of St_l that correspond to different energetic flow motions. The lower range of St_l corresponds to the crest that notably stands out in the PSD at P5 in the range of $St_l < 0.16$ with its peak at $St_l = 0.05$. Here, the cut-off St_l is the local minimum of PSD at $St_l = 0.16$. This region is attributed to the breathing motion. The second range of energetic motions corresponds to the vortex shedding motion and spans over $0.16 < St_l < 0.7$, with the local maximum observed near $St_l = 0.35$. The upper threshold of $St_l = 0.7$ is defined as the St_l at which the PSD at P5 is 36.8% (e^{-1}) of its local peak.

To understand how different flow motions affect wall-pressure fluctuation, the coefficients of wall-pressure fluctuations cp for each St_l range are computed. To calculate c_p, the root-mean-square (rms) of wall-pressure fluctuation (p_{rms}) is normalized by q_∞. The same computation is also carried out using the rms values of p' and p'' Here, p' corresponds to the wall-pressure fluctuation due to the breathing motion and is obtained by employing a low-pass filter on p with a cut-off St_l of 0.16. Correspondingly, p'' represents the band-pass filtered p within the range of $0.16 < St_l < 0.70$ and is attributed to the vortex shedding motion.

The c_p based on rms of p against x/c is presented in Figure 6.6 using a solid line with circles. Inspecting result of c_p, the values appear to vary between 0.016 and 0.018 across a streamwise distance from $x/c = -0.300$ to -0.084 ($\pm$ 0.44l with respect to MD). A small local peak of c_p = 0.018 is detected at $x/c = -0.156$, which is 0.15l downstream of MD. The range of variation is similar to the one observed by Weiss et al. (2015), where c_p varies between 0.013 and 0.015 in a region from $-0.4l$ to $0.5l$ with respect to MD. However, Weiss et al. (2015) found that the local peak in this region was at 0.4l upstream of MD, close to ID. The discrepancy in the distribution of c_p might be attributed to the differences in TSB configuration. In this investigation, the TSB was enclosed by the wing surface and two shear layers, which differs from the previous work of Weiss et al. (2015), where the TSB was confined by a flat plate and only one shear layer. In addition, the experimental investigation conducted by Le Floc'h et al. (2020) revealed that the c_p near ID is proportional to the size of TSB. The TSB in this investigation might not be sufficiently large to produce a prominent peak near ID.

The c_p based on rms of p' is also depicted in Figure 6.6 using a dashed line with diamond symbols. A steady increase in c_p is observed from P1 to P5 with increasing x/c. The maximum c_p is found to be 0.007 at $x/c = -0.156$. This observation aligns with the findings from Figure 6.5, where the impact of breathing motion on wall-pressure fluctuation is most pronounced at P5 in comparison to the other pinholes. Continuing along the TSB, the c_p value undergoes a minor reduction at P6 and P7, while still maintaining a higher level than those observed upstream of P5.

Furthermore, the spatial variation of c_p based on rms of p'' is illustrated in Figure 6.6 using a dashed line with squares. The level of c_p is seen to increase as x/c rises from P1 to P5 and stays at $c_p \approx 0.012$ from P5 to P7. The finding matches well with the observed PSD patterns in Figure 6.5, in which the impact of vortex shedding motions on the wall-pressure fluctuations is more significant in the TSB compared to upstream of the TSB. In addition, it is evident from Figure 6.5 that the vortex shedding process has a more substantial influence on wall-pressure fluctuation compared to the breathing motion over the entire measurement domain. The relatively small contribution of the breathing motion to c_p is attributed to the shallow TSB, as the corresponding wall-pressure fluctuation is known to be proportional to the TSB size (Mabey, 1992; Le Floc'h et al., 2020).

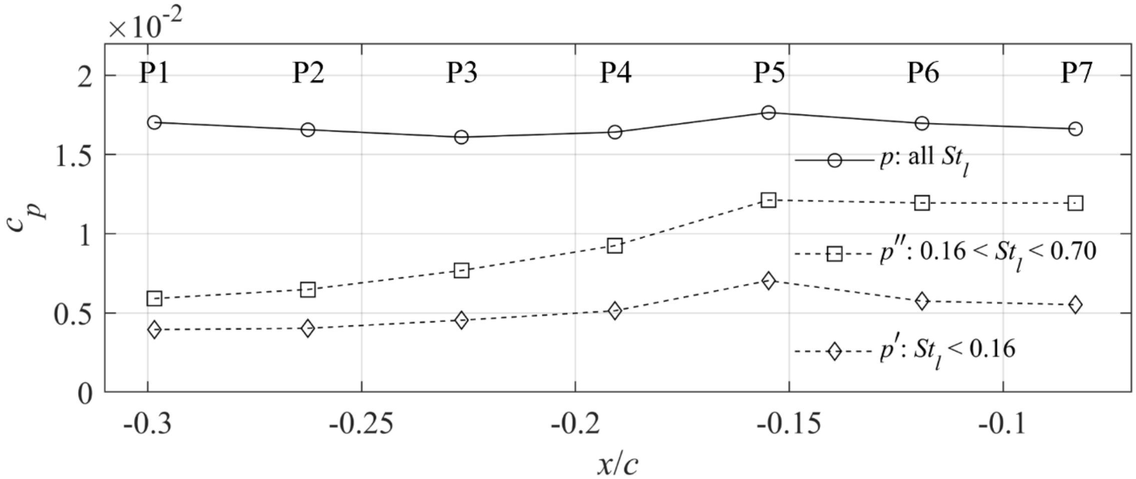

Figure 6.6. The coefficient of wall-pressure fluctuation c_p is plotted against x/c. The solid line corresponds to c_p calculated using p. The dashed lines with diamonds and squares represent c_p calculated using p' and p'', respectively. The former one is low-pass filtered p at $St_l < 0.16$, and is associated with the breathing motion. The latter one is the rms of band-pass filtered p within $0.16 < St_l < 0.7$ and is due to the vortex shedding motions.

The relation between the wall pressures measured at various pinhole locations is investigated here using spatio-temporal cross-correlation with respect to pressure fluctuations at P4. The normalized correlation coefficient $R^i_{pp}(\Delta t)$ is defined by the following equation,

$$R^i_{pp}(\Delta t) = \frac{\langle p^i(\Delta t) p^{\mathrm{P4}}(0) \rangle}{\sqrt{R^i_p R^{\mathrm{P4}}_p}}, \tag{6.1}$$

where the superscript 'i' indicates the pinhole number, ranging from P1 to P7. The autocorrelation of p^i at zero lag is represented by R^i_p and is used to normalize the cross-correlation. Note that the correlations are performed using filtered pressure fluctuations, p' and p'' and the results are shown in Figure 6.7a and b, respectively. The same color code as Figure 6.5 is employed to represent the pinholes upstream and downstream of the MD overlapping with P4. Note that the distance between neighboring pinholes is $0.15l$.

The analysis begins with investigating R^i_{pp} of the breathing motion calculated using p'. As seen in Figure 6.7a, the peaks in R_{pp} for the pinholes that are far away from P4 are small, and the cross-correlation strength increases as the distance between the pinhole pairs decreases. The maximum correlation values for R^{P3}_{pp} and R^{P5}_{pp} of the neighboring pinholes are larger and equal to 0.57 and 0.51, respectively. The maxima are observed at $\Delta t \approx 0$, indicating that the p' detected at P3 and P5 varies almost simultaneously with respect to the p' from P4. This is possibly due to the distance between P4 and the adjacent pinholes (P3 and P5) being smaller than the length scale of the pressure fluctuation in the x-direction, thus p' at these pinholes were in phase. The same small Δt is observed for the maxima in $R^{\mathrm{P1}}{}_{pp}$ and $R^{\mathrm{P2}}{}_{pp}$. In contrast, the peaks of $R^{\mathrm{P6}}{}_{pp}$ and $R^{\mathrm{P7}}{}_{pp}$ are detected at $\Delta t = -0.34T$ and $-0.64T$, respectively, and the magnitude of Δt for these pinholes is much larger than for their counterparts. An advection speed can be derived using $\Delta x/\Delta t$ to represent how fast the pressure fluctuations propagate. For $R^{\mathrm{P6}}{}_{pp}$ and $R^{\mathrm{P7}}{}_{pp}$, the advection speeds are computed as $0.86U_\infty$ and $0.69U_\infty$, respectively. The reduction in the advection speeds from P6 to P7 can be attributed to the slow down of flow due to the APG. Therefore, the breathing motion is estimated to advect at an averaged speed of $0.78U_\infty$ downstream of MD.

In addition, the dominant time scale of wall-pressure fluctuation in p' can be estimated from the time difference between the positive and negative peaks of $R^{\mathrm{P4}}{}_{pp}$. This time difference is found to be $3.76T$, representing half of the signal period. The corresponding periodicity is determined to have a St_l of 0.13. This value is higher than the spectral peak ($St_l = 0.05$) of the breathing motion observed in Figure 6.5 but is slightly smaller than the filter cut-off St_l of 0.16 used for extracting p'.

As the vortex shedding process was shown to have a significant contribution on wall-pressure fluctuations, the associated pressure correlations are also discussed here. The results of R_{pp} in Figure 6.7b exhibits patterns that are similar to Figure 6.7a. First, the correlation strength increases with reduction in the pinholes' distance. P3 and P5 exhibit correlation peaks with $R_{pp} \geq 0.5$. The peak of $R^{\mathrm{P3}}{}_{pp}$ is observed at $\Delta t = 0.28$ with a value of 0.55, and the peak of $R^{\mathrm{P5}}{}_{pp}$ is seen at $\Delta t = -0.36T$ with a value of 0.53. The derived advection speeds are $0.52U_\infty$ and $0.40U_\infty$, respectively. The average speed is $0.46U_\infty$, indicating the vortex shedding structures are advected slower than the breathing motion. Comparing figure Figure 6.7a and b also shows that correlation peaks of the breathing motion is wider than those of the vortex shedding. This is expected due to the lower frequency content of p'.

(a)

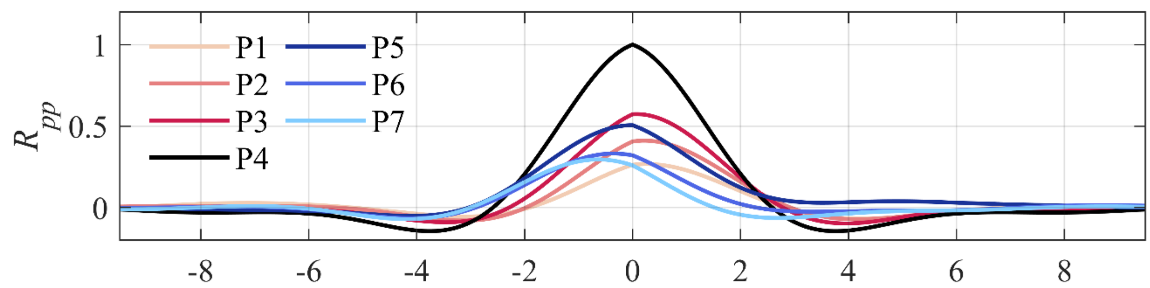

(b)

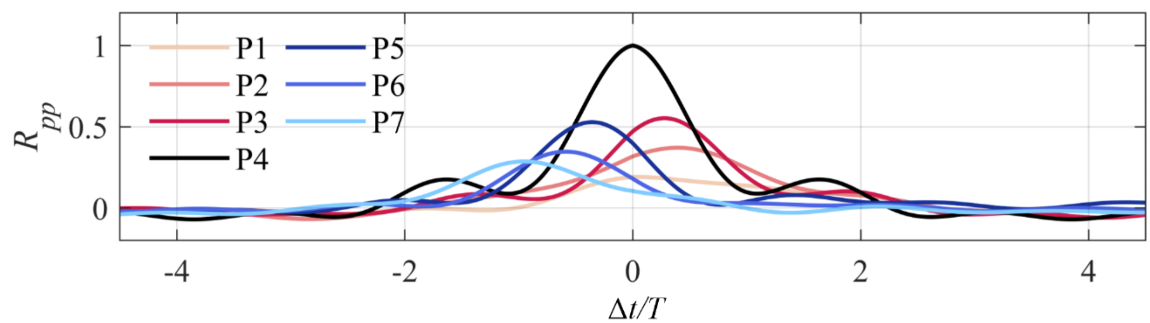

Figure 6.7 Spatio-temporal cross-correlation between (a) p' (with $St_l < 0.16$), and (b) p'' (with $0.16 < St_l < 0.70$) measured at various pinholes with the measurement at P4.

In summary, the results demonstrate that the influence of various flow motions on wall-pressure fluctuations varies with the streamwise locations. Upstream of the mean TSB and extending up to the MD point (P1 to P4), wall-pressure fluctuations exhibit weak indications of breathing motion and vortex shedding processes/ However, these indications become more pronounced as approaching MD and entering the mean TSB. Inside the mean TSB (P5 to P7), the vortex shedding process exerts a more significant influence on wall-pressure fluctuations compared to the breathing motion. At P5, which is situated $0.15l$ downstream of MD, the energy associated with the breathing motion reaches its peak. Furthermore, the advection speed of the breathing motion becomes discernible only downstream of MD, measuring approximately $0.78U_\infty$. This advection speed is approximately double the measured advection speed of the vortex shedding structures.

6.3.3 Relation between wall pressure and breathing motion

In this section, the correlation between the velocity field and wall-pressure fluctuations that are attributed to the breathing motion are investigated. Note that only the low-pass filtered pressure (i.e., p') is considered here, as the primary interest of this investigation is relation between the velocity field and the footprint of the breathing motion. The relations are evaluated through cross-correlation between p' and simultaneously measured u and v from the time-resolved PIV measurements. Before computing the cross-correlations, p' is divided into positive and negative sections to investigate motions associated with positive and negative wall pressure fluctuations, separately. The correlations coefficients for positive and negative p' are indicated with superscripts '+' and '–', respectively and calculated according to

$$R^{+}_{pu}(x, y, \Delta t) = \left.\frac{\langle p'(t+\Delta t)u(x,y,t)\rangle}{p'_{\mathrm{rms}} u_{\mathrm{rms}}}\right|_{p'>0}, \text{ and} \tag{6.2}$$

$$R^{-}_{pu}(x, y, \Delta t) = \left.\frac{\langle p'(t+\Delta t)u(x,y,t)\rangle}{p'_{\mathrm{rms}} u_{\mathrm{rms}}}\right|_{p'<0}. \tag{6.3}$$

The correlation is normalized by the rms values of p' and u. Specifically, urms is acquired from a near-wall position of y/c = 0.001 directly above the corresponding pinhole. The subscript u indicates that correlation coefficient is computed using the streamwise velocity component. A similar correlation coefficient is also calculated using the wall-normal velocity component and are denoted with $R^{+}{}_{pv}$ and $R^{-}{}_{pv}$. The correlations are computed using 20 sets of wall-pressure and PIV velocity data (~2960T in total). To obtain an indicator of the net correlation over the entire PIV measurement domain, $R^{+}{}_{\mathrm{sum}}$ and $R^{-}{}_{\mathrm{sum}}$ are calculated based on

$$R^{+}_{\mathrm{sum}}(\Delta t) = \sum_x \sum_y R^{+}_{pu}(x, y, \Delta t), \text{ and} \tag{6.4}$$

$$R^{-}_{\mathrm{sum}}(\Delta t) = \sum_x \sum_y R^{-}_{pu}(x, y, \Delta t). \tag{6.5}$$

Here, the summation is carried out over the full PIV measurement domain (x/c = −0.35 to 0.12, and y/c = 0.001 to 0.12c). As it will be discussed, this indicator can show the presence of large-scale streamwise motions that correlate with wall-pressure.

The variation of $R^{+}{}_{\mathrm{sum}}$ and $R^{-}{}_{\mathrm{sum}}$ with Δt for the correlation results associated with wall-pressure measurements at P1 are shown in Figure 6.8a. The positive peaks for $R^{+}{}_{\mathrm{sum}}$ and $R^{-}{}_{\mathrm{sum}}$ are observed in a band of Δt that is centered at –4.82T. As illustrated in Figure 6.8a, the band is labelled as T1 and is marked by a green bar with its center highlighted by a green line. Here, the center of T1 is determined from the average Δt of the local peaks of $R^{+}{}_{\mathrm{sum}}$ and $R^{-}{}_{\mathrm{sum}}$ in the band. The correlation fields that correspond to the peaks of $R^{+}{}_{\mathrm{sum}}$ and $R^{-}{}_{\mathrm{sum}}$ within T1 are depicted in Figure 6.8b and c, respectively. The visualizations show contours of R_{pu}, with vector fields of (R_{pu}, R_{pv}) overlayed on the contours. The correlations for $p' < 0$ are multiplied by –1 to retain the true flow direction in the visualizations of Figure 6.8c. For ease of access, the position of the mean TSB is illustrated using a green-line contour, and the location of P1 is indicated by a dark blue dot. The results reveal that positive p' correlates with a large-scale forward motion in Figure 6.8b and negative p' correlates with a large-scale backward motion in Figure 6.8c. These forward and backward flow motions are indicative of contraction and expansion of the TSB, respectively. The negative sign of Δt for the peaks detected in Figure 6.8a indicates that the corresponding wall-pressure fluctuation at P1 occurs after the expansion and contraction motions (wall-pressure P1 lag these motions). Therefore, both flow motions initiate from the region downstream of the P1 and within the TSB.

For both R^{+}_{pu} and R^{-}_{pu}, the region exhibiting the highest correlation is observed above the mean TSB along the upper shear layer in Figure 6.8b and c. This observation suggests that the variation of low-frequency wall pressure is primarily associated with low- and high-speed motions occurring along the upper shear layer. This is supported by the results of Wang & Ghaemi (2022) that demonstrated a strong correlation between the contraction and expansion of the TSB and the unsteadiness in the upper shear layer.

Figure 6.8a also shows a subsequent anti-correlation between p' and the velocity field where Δt is positive. The peaks for R^{-}_{sum} and R^{+}_{sum} are observed in a band that is denoted by T2, illustrated by a green bar. As depicted in Figure 6.8a, the center of T2 is indicated by a green line at $\Delta t = 3.43T$, determined by averaging the Δt of the local minima in R^{-}_{sum} and R^{+}_{sum}. The correlation contours corresponding to the anti-correlation peaks of R^{+}_{pu} and R^{-}_{pu} are shown in Figure 6.8d and e, respectively. In Figure 6.8d, positive p' is observed to correlate with a large low-speed region, indicating expansion of the TSB. While Figure 6.8e reveals the negative p' correlates with a large high-speed region showing the TSB contraction. The positive Δt sign indicates that positive and negative p' at P1 occur before the correspond motions of Figure 6.8d and e.

The presence of the positive and negative correlations in Figure 6.8a indicates periodic behaviour of low-frequency wall pressure and the correlated velocity field. This is also supported by the fact that the contours from T2 are opposite to those from T1. For instance, the contour and vector field that correspond to $+p'$ from T2 show expansion of the TSB, while the contour and vector field that correspond to $+p'$ at T1 corresponds to contraction of the TSB. Considering a full breathing cycle involves both expansion and contraction of the TSB, the time interval from the positive to negative peaks in Figure 6.8a corresponds to half of a breathing cycle. Using the Δt between the center of T1 and T2, the St_l is calculated to be 0.06. The derived St_l agrees well with the breathing St_l obtained from Figure 6.5, in which the spectral peak is observed near $St_l = 0.05$.

The same analysis is also performed with p' measurement at P7, which is located close to the middle of the mean TSB. The time trace of R_{sum} presented in Figure 6.9a is relatively noisy. However, an opposite pattern compared to Figure 6.8a is observed. In Figure 6.9a, anti-correlation peaks in R^{+}_{sum} and R^{-}_{sum} are seen in the band of T1 that is centered at $\Delta t = -10.40T$. The inverted correlation pattern with respect to Figure 6.8a is attributed to the change of pinhole location. The correlation contours presented in Figure 6.9b show that the positive p' correlates with a backward flow motion in T1, and therefore an expansion of the TSB. In contrast, Figure 6.9c shows that negative p' correlates with a forward flow motion in T1, which indicates TSB contraction.

Returning to Figure 6.9a, positive correlations are observed for R^{+}_{sum} and R^{-}_{sum} in the range of $0 < \Delta t < 20T$. The maxima of R^{+}_{sum} and R^{-}_{sum} are seen in the band T2, which is centered at $8.06T$. As previously explained, the presence of both positive and negative correlation pattern is due to the periodic nature of the breathing motion. The correlation contours corresponding to T2 in Figure 6.9d and e show that positive and negative p' correlate with subsequent contraction and expansion of TSB that occur later in time relative to the wall pressure fluctuations at P1, respectively.

An analysis to verify the frequency of the breathing motion is carried out using the center-to-center Δt between T1 and T2 from Figure 6.9a. The corresponding St_l is determined as 0.03. The values are slightly smaller than the one obtained from Figure 6.8a and can be attributed to the uncertainties in the peak locations. Numerous local peaks are observed at $-20 < \Delta t < 20$, which brings challenges in determining the true range of frequencies for the breathing motion.

The correlations between the velocity field and p' measured at the remaining were also evaluated. However, the results do not appear converged as the patterns of R_{sum} are noisy and harder to interpret relative to those shown in Figure 6.8 and Figure 6.9. A possible cause is local flow frequently switches between forward and backward flow states, which suggests a larger size of data should be considered to obtain a reasonable correlation pattern. In general, the correlation pattern appears to be clearer as pinhole moves away from P4. For the sake of brevity, the results related to the other pinholes are not presented here.

Overall, the correlation results for P1 and P7 suggest that the breathing motion can be detected by wall-pressure fluctuations measured at $\pm$ 0.44l with respect to MD, despite the energy of p' is relatively weak as shown in Figure 6.5 and Figure 6.6. When the TSB contracts (u > 0), the detachment point will move away from P1 and approach P7. The contraction is followed by an increase in p' at P1 and a decrease in p' at P7, leading to two opposite correlation patterns as shown in Figure 6.8a and Figure 6.9a. When comparing the time trace of R_{sum} for P1 and P7, the correlation peak was stronger in case of P1 compared to P7. The results suggest that an adequate sensor for detecting the breathing motion should be placed upstream of the TSB at a suitable distance. The phase relation between the breathing motion and p', may also vary based on the location of pinhole. However, the relations cannot be determined due to the noisy correlation patterns of the remaining pinholes.

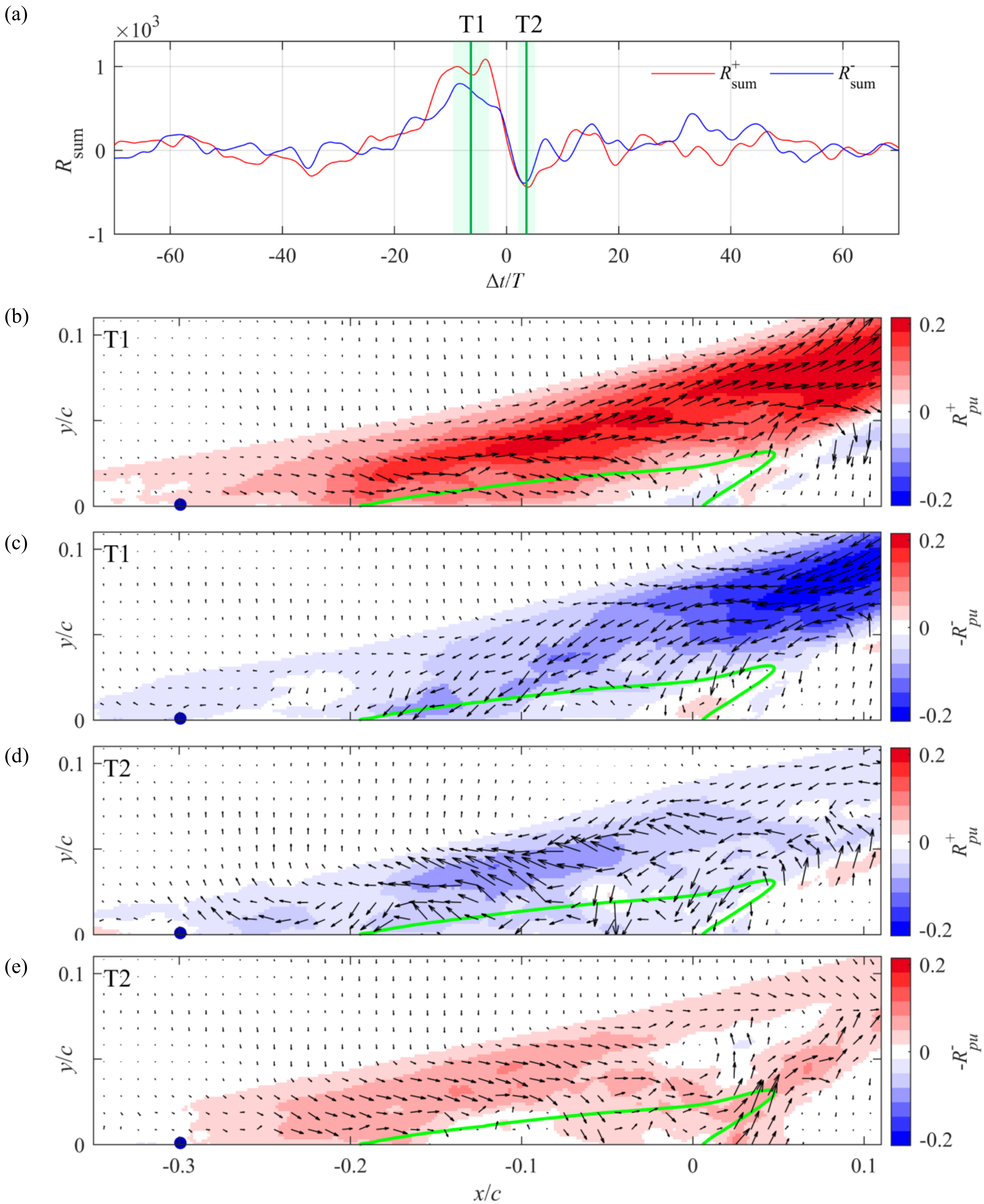

Figure 6.8 The cross-correlation between (u, v) and p' measured at x/c = −0.300 (P1). The time trace of R_{sum} is displayed in (a), with the bands of Δt that include the local peaks marked as T1 and T2. The correlation contours corresponding to the maxima of R^{+}_{sum} in T1 and T2 are depicted in (b) and (d), respectively. The correlations contours corresponding to the minima of R^{-}_{sum} in T1 and T2 are presented in (c) and (e), respectively.

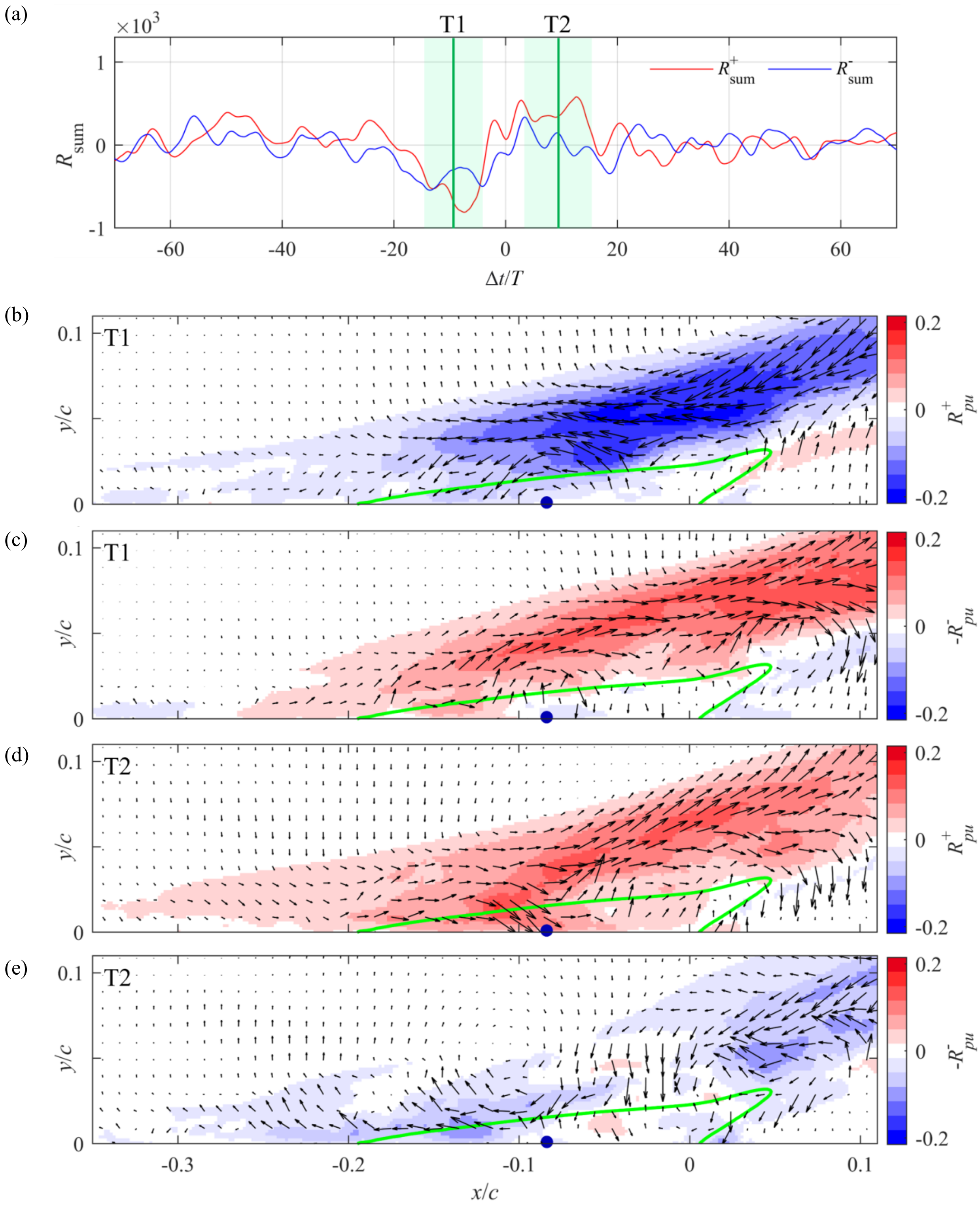

Figure 6.9 The cross-correlation between (u, v) and p' at $x/c = -0.084$ (P7). The time trace of R_{sum} is displayed in (a), with the bands of Δt that include the local peaks marked as T1 and T2. The correlation contours corresponding to the minima of R^+_{sum} in T1 and T2 are depicted in (b) and (d), respectively. The correlations contours corresponding to the maxima of R^-_{sum} in T1 and T2 are presented in (c) and (e), respectively.

To characterize the phase relation between wall-pressure fluctuation and the breathing motion, spectral proper orthogonal decomposition (SPOD) analyses are performed (Towne et al., 2018; Schmidt et al., 2018; Schmidt & Colonius, 2020; Nekkanti & Schmidt, 2021). The SPOD computations use synchronized velocity and wall-pressure data collected at P1 and P7 together. In total, 10 time-resolved datasets were employed. To improve the statistical convergence in spectral analysis, each dataset is segmented into 5 blocks with 50% overlap (Welch, 1967). This results in an ensemble of 50 blocks and a lowest resolvable frequency of 1 Hz (St_l = 0.024). Following the procedures detailed by Towne et al. (2018) and Fiore et al. (2022), the normalized fluctuating velocities and wall pressures segments (u/U_∞, v/U_∞, and p/q_∞) are stacked into a column vector $q_s \in R^N$ with s being the index of snapshot and N represents the total number of grid points of all input signals. The vectors q_s are then assembled into a 2D matrix Q with a size of (N, M), in which M represents the total number of snapshots. The SPOD algorithm decomposes Q into SPOD modes Φ_j, with their temporal behavior expressed as exp(iθ), where θ represents the phase and is defined as $2\pi ft$ (Nekkanti & Schmidt 2021). Here, the rank of mode is denoted by j and Φ_j contain the jth SPOD mode at all frequencies along with their associated energies. For the details on the decomposition process, please refer to Section 3.5. The SPOD analysis was performed using the SPOD code developed by Towne et al. (2018) in MATLAB (MathWorks).

The energy spectra of the first 3 SPOD modes are plotted in Figure 6.10. These spectra are similar to the ones observed by Wang & Ghaemi (2022), where the leading SPOD mode exhibits the highest level of energy at the lowest resolved St_l of 0.024. A significant decrease in energy is observed with increasing St_l. At St_l > 0.07, the energy of the first SPOD mode drops below 1%. It is also seen that the energy of higher-order modes is near negligible compared to the first mode for St_l smaller than 0.1.

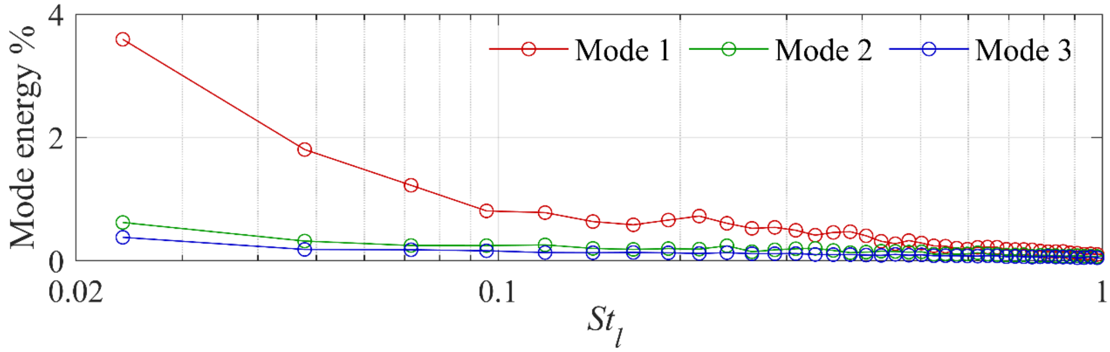

Figure 6.10 The energy spectra of the dominant SPOD modes. The leading SPOD mode at St_l = 0.024 has the highest energy and represents the breathing motion..

A reduced-order model (ROM) of the velocity and pressure field is obtained by expanding the leading SPOD mode Φ_1 at the selected f_0 = 1 Hz (St_l = 0.024) over θ, following

$$u_{\mathrm{ROM}} = \Phi_1^u e^{\mathrm{i}\theta}\text{, and} \tag{6.6}$$

$$p_{\mathrm{ROM}} = \Phi_1^p e^{\mathrm{i}\theta}\,. \tag{6.7}$$

Here, the superscript u and p of Φ_1 corresponds to the fluctuating streamwise velocity and wall-pressure component of the leading mode. According to Wang & Ghaemi (2022), $\Phi_1{}^u$ at St_l = 0.024 represents the breathing motion since it is the dominant contributor to the intermittency of the TSB. The obtained ROM of wall-pressure fluctuation at P1 and P7 are denoted by $p^{\mathrm{P1}}{}_{\mathrm{ROM}}$ and $p^{\mathrm{P7}}{}_{\mathrm{ROM}}$, respectively.

The spatial organization of $\Phi^u{}_1$ at St_l = 0.024 is presented in Figure 6.11a. The mean TSB is represented by a black-line contour, and the locations of P1 and P7 are indicated by blue and green dots, respectively. The pattern in Figure 6.11a features a large-scale energetic zone, primarily extending diagonally from the surface into the wake region. The core of this pattern is seen above the mean TSB, and along the upper shear layer. The extension of this core intercepts the wall near the MD.

Further investigation into the breathing motion is performed through analyzing the time trace of u_{ROM} over the entire measurement domain and the fluctuations of the backflow area, both computed from the ROM of the velocity field. The large-scale flow motion associated with the breathing of TSB is identified using the spatial summation of u_{ROM} over the entire measurement domain and is denoted by u_{sum}. The time trace of u_{sum} can provide information on the evolution of large-scale streamwise flow motion. For calculating the backflow area, U_{ROM} is reconstructed by adding $\langle U\rangle/U_\infty$ to u_{ROM}. The backflow area is then calculated as the area of the region where $U_{\mathrm{ROM}} < 0$, and its fluctuations are denoted by A (i.e., the mean backflow is subtracted). The rise and fall of A indicate whether the TSB is expanding or contracting; an increase in A corresponds to an expansion motion and vice versa.

To investigate the relation between A and u_{sum}, their variation with respect to phase, θ, is plotted in Figure 6.11b. To visualize the signals of A and u_{sum} on the same scale, each signal is normalized by its own rms value. Upon examining Figure 6.11b, it is observed that u_{sum} takes on the form of a sine while the time trace of A does not have a perfect sine-wave shape. The result of Figure 6.11b reveals that A and u_{sum} have a near perfect anti-correlation relation with a phase difference of 1.05π. This is consistent with the previous argument that expansion and contraction of TSB are associated with large-scale backward and forward flow motions, respectively.

To examine the phase relation between the breathing of TSB and wall pressure, the evolution of A and $p^{\mathrm{P1}}{}_{\mathrm{ROM}}$ with phase are plotted in Figure 6.11c after being normalized using their rms values. The plot suggests that the expansion and contraction of TSB are followed by a fall and rise in $p^{\mathrm{P1}}{}_{\mathrm{ROM}}$, respectively. The minima and maxima of A precede the maxima and minima of $p^{\mathrm{P1}}{}_{\mathrm{ROM}}$ by a phase difference of $\Delta\theta = 0.37\pi$. By the definition of θ, the phase difference can be converted back in time delay using $\Delta t = \Delta\theta/(2\pi f_0)$. When expressed in time delay, it corresponds to a normalized Δt of $7.94T$. The result is in reasonable agreement with the findings of Figure 6.8a, where a large-scale streamwise flow motion appears to lead p' by a Δt approximately $4.82T$. The difference arises because SPOD analysis corresponds to St_l=0.024, whereas the correlation results in Fig 8a encompass all motions with $St_l < 0.16$.

The same analysis is performed between A and $p^{\mathrm{P7}}{}_{\mathrm{ROM}}$. The resulting comparison is presented in Figure 6.11d. It is observed that the relation between A and $p^{\mathrm{P7}}{}_{\mathrm{ROM}}$ exhibits a pattern opposite to the one seen in Figure 6.11c. Specifically, the expansion and contraction of TSB are followed by rise and fall in $p^{\mathrm{P7}}{}_{\mathrm{ROM}}$, respectively. As seen in Figure 6.11d, the maxima of A lead the maxima of $p^{\mathrm{P7}}{}_{\mathrm{ROM}}$ by a phase difference of $\Delta\theta = 0.34\pi$, which is equivalent to a time delay of $7.30T$. This observation is consistent with the presence of negative correlation peaks seen on the side of $\Delta t < 0$ in Figure 6.9a. The value is similar to the time shift of T1 ($10.40T$) observed in Figure 6.9a.

Upon inspecting the temporal evolution of A, $p^{P1}{}_{ROM}$, and $p^{P7}{}_{ROM}$, it is evident that the wall pressure at P1 and P7 exhibit opposite behavior as the TSB breathes. This relation explains the opposite correlation pattern observed in Figure 6.8a and Figure 6.9a and is likely associated with the position of the pinhole with respect to the detachment point. The same relation between wall-pressure fluctuations upstream and downstream of MD was also seen by Mohammed-Taifour & Weiss (2021). When they performed cross-correlation analysis between the low-pass filtered p measured in and out of a TSB, they noticed an anti-correlation relation. Moreover, the SPOD results further reveal that the phase lags between the breathing motion and the variation in wall pressure at P1 and P7 are 0.37π and 0.34π, respectively. The phase relation can be utilized for timing the actuators when utilizing an active control system.

(a)

(b)

(c)

(d)

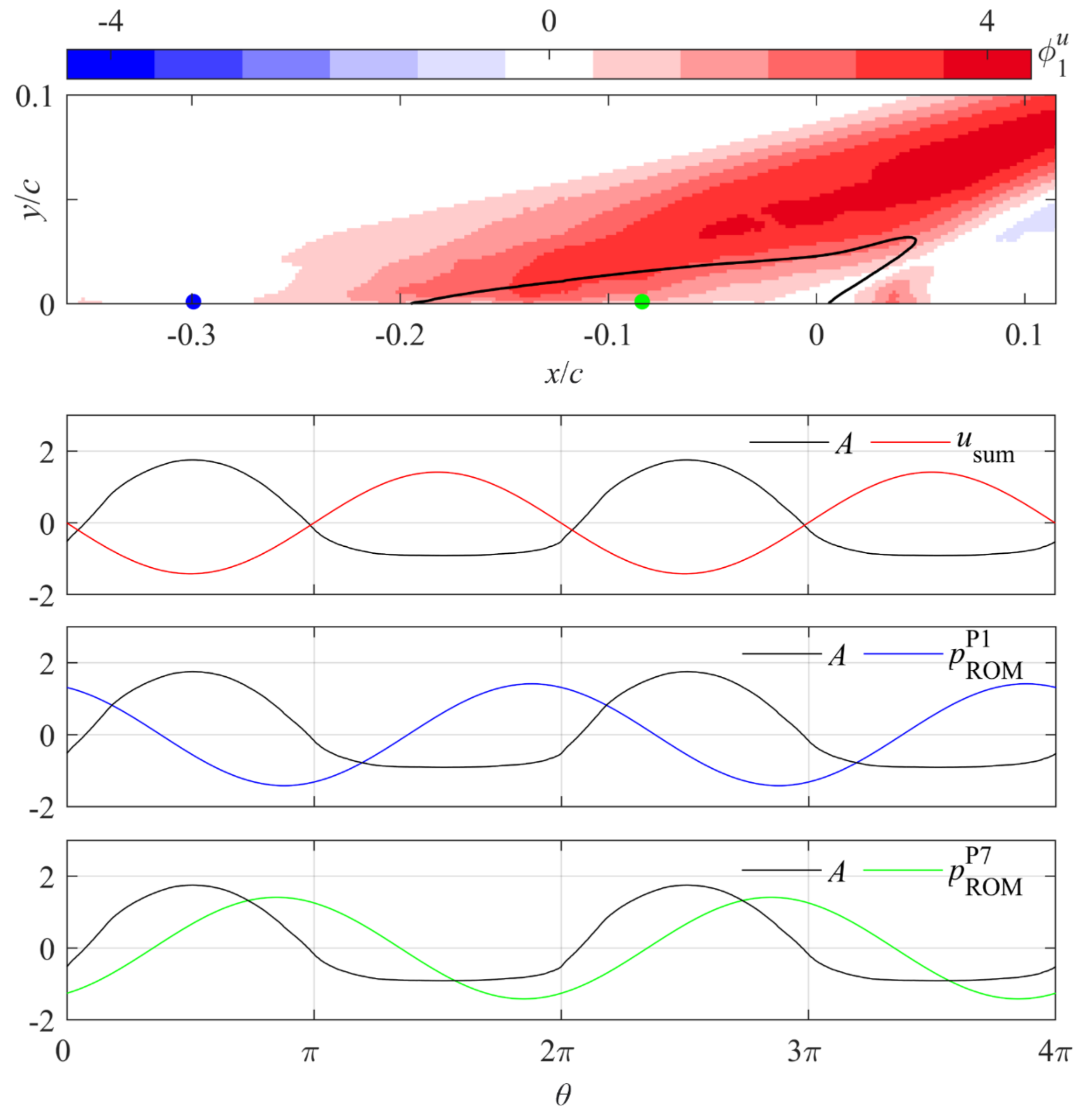

Figure 6.11 (a) The spatial organization of the first SPOD mode at Stl = 0.024. The locations of P1 and P7 are labeled with blue and green dots, respectively. (b) The temporal evolution of A and usum are plotted with respect to θ. The evolutions of (c) pP1ROM and (d) pP7ROM in θ are plotted along with A.

6.3.4 A conceptual model

Based on the previously presented results, a conceptual model is developed to show the relation between the breathing motion and wall pressure field, as depicted in Figure 6.12. In this figure, the TE section of the wing is shaded in grey, and the mean TSB is indicated by a green contour. As expected for thick airfoils prior to stall, the TBL separates from the airfoil surface upstream of the TE region due to APG. The APG field is represented in Figure 6.12 by a combination of negative relative pressure in the upstream region of MD (indicated by blue) and positive relative pressure near the TE (indicated in red).

Figure 6.12a shows a strong APG, characterized by a more pronounced negative pressure upstream of MD and a stronger positive pressure downstream of MD. This decrease in upstream pressure and increase in downstream pressure leads to a greater APG, corresponding to an expansion of the TSB. Conversely, Figure 6.12b displays a contracting TSB. In this case, the negative and positive pressure magnitudes both diminish in the regions upstream and downstream of the MD, representing a reduction in the APG and a smaller TSB.

The proposed model is corroborated by the results from both the pressure-velocity correlation and SPOD analyses. These analyses showed that TSB expansion corresponds to a decrease in negative pressure fluctuation (p) at P1 but an increase in positive pressure fluctuation at P7, enhancing the APG between P1 and P7. The analyses also demonstrate that TSB contraction leads to an increase in negative pressure fluctuation at P1 and a decrease in positive pressure fluctuation at P7. This change in wall pressure fluctuations consequently decreases the APG between P1 and P7.

(a)

(b)

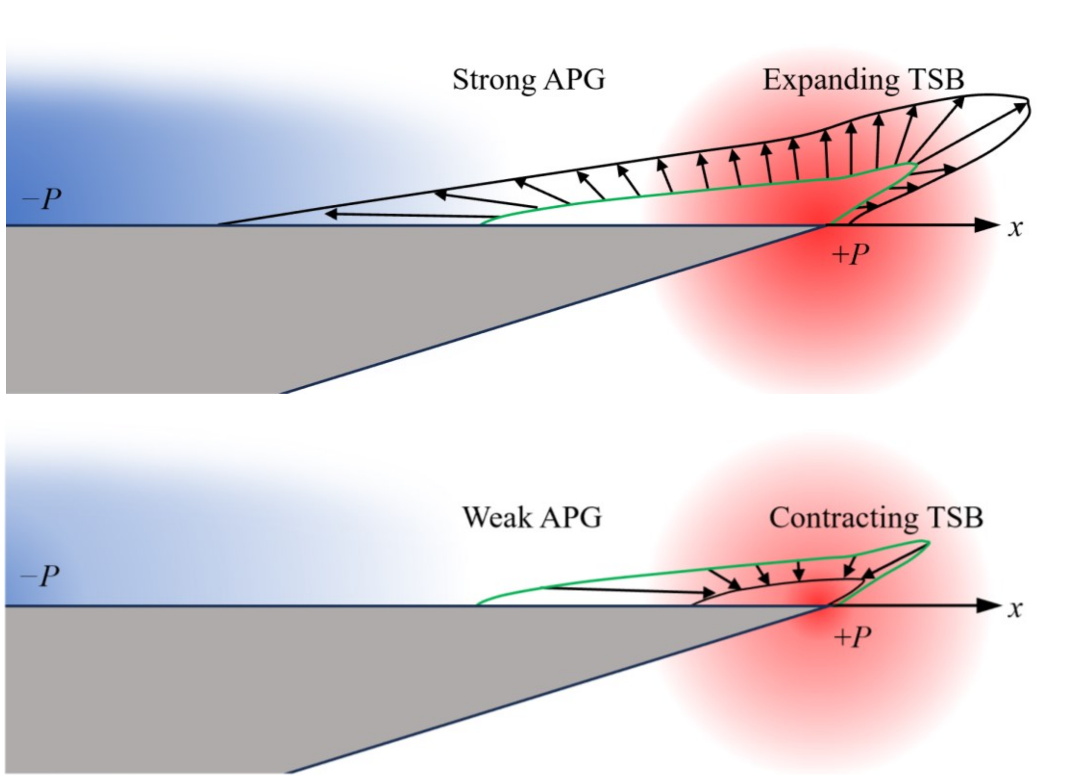

Figure 6.12 A conceptual model of the relation between pressure and breathing motion. The green contour shows the mean TSB, and the arrows shows expansion/contraction of the TSB. (a) The TSB expansion corresponds to an increase in APG, while (b) the TSB contraction is associated with a reduction in APG

6.4 Conclusion

The current study experimentally investigated the relation between the breathing of turbulent separation bubble (TSB) and wall-pressure fluctuation in the trailing-edge (TE) region of a two-dimensional wing. The wing featured a NACA 4418 profile and had a chord length c = 975 mm. A full-span trip wire was installed at $0.2c$ downstream of the leading edge to trigger the turbulent boundary layer (TBL). The TE separation was produced by setting the wing to an angle-of-attack of 9.7°. The experiments were performed at a chord-based Reynolds number of 620,000. The measurements included simultaneously performed time-resolved planar particle image velocimetry (PIV) and wall-pressure fluctuation measurements along the midspan of the wing. The wall-pressure fluctuations were acquired from 7 pinholes, evenly spaced over a streamwise distance. This distance covered a range of approximately equal to the mean characteristic length l of the separation bubble, spanning over $\pm\ 0.44l$ with respect to the mean detachment (MD) point.

Spectral analysis of velocity fluctuations revealed the presence of energetic flow motions caused by the breathing motion, particularly near the wall. The highest energy levels were observed near the front edge of the mean TSB, occurring at a Strouhal number of $St_l = 0.03$. Additionally, the influence of the breathing motion was evident in the spectra of wall-pressure fluctuations, with a predominant frequency centered at $St_l = 0.05$. These pressure fluctuations were relatively weak upstream of MD but reached their maximum intensity $0.15l$ downstream of the MD point. However, the most significant source of unsteadiness in wall-pressure fluctuations was attributed to the vortex shedding process centered at $St_l \approx 0.35$. The energy of wall-pressure fluctuations due to vortex shedding increased for locations closer to the MD and remained strong within the TSB. Furthermore, the spatio-temporal cross-correlation of wall-pressure fluctuations revealed that the motions associated with breathing and vortex shedding propagated at speeds of $0.78U_\infty$ and $0.46U_\infty$ in the streamwise direction, respectively.

The correlation between low-pass filtered wall pressure and velocity fields was investigated to identify the spatial structures of the flow motions. The cut-off frequency for the low-pass filter applied to the wall pressure was set at $St_l = 0.16$, based on the endpoint of the energetic peak associated with the breathing motion observed in the wall pressure spectra. Statically converged correlation patterns were obtained for only two pressure measurements located farthest from MD (0.44l upstream and 0.44l downstream of MD). Obtaining statically converged correlation patterns for wall-pressure locations closer to the MD proved challenging due to the higher intermittency of the flow field. The spatial pattern of the correlations showed that large-scale forward motions were associated with positive pressure fluctuations upstream of the MD and negative pressure fluctuations downstream of the MD. Similarly, large-scale backward motions correlated with negative pressure fluctuations upstream of the MD and positive pressure fluctuations downstream of the MD. These forward and backward flow motions indicated contraction and expansion of the TSB, respectively.

To characterize the phase relationship between the breathing motion and wall-pressure fluctuations, spectral proper orthogonal decomposition (SPOD) was applied to synchronized wall-pressure and velocity data. A reduced-order model was reconstructed to simulate the flow field and wall-pressure fluctuations using the leading SPOD mode at St_l = 0.024. The results demonstrated that the expansion (contraction) of the TSB preceded a decrease (increase) in wall-pressure fluctuation at 0.44l upstream of the MD by a phase lead of 0.37π and an increase (decrease) in wall-pressure fluctuation at 0.44l downstream of the MD by a phase lead of 0.34π. These findings are consistent with the notion that the expansion and contraction of TSBs correspond to an increase and decrease in the magnitude of the adverse pressure gradient (APG), respectively.

.

Chapter 7. Conclusion

This thesis experimentally investigated the trailing-edge (TE) separated flow on a NACA 4418 airfoil at pre-stall regimes. The primary aim of the study was to investigate and predict the characteristics of TE separation. Specifically, an extensive exploration into the low-frequency breathing motion and its impact on wall pressure was carried out to ascertain crucial information for devising a real-time detection strategy targeting the breathing motion. The investigation was divided into three projects to progressively uncover the flow topology, energetic unsteady motions, and its corresponding relation with wall pressure during TE separation. Accordingly, the main conclusions of each project are presented in the following sections. Recommendations on future research opportunities are provided at the end.

7.1 Topology of trailing-edge separation

The first project (project 1) focused on characterizing the effect of varying angle-of-attack (α) on the skin friction pattern of separated flow through full-span planar particle image velocimetry (PIV). At shallow angles of attack ($9° < \alpha < 9.7°$), isolated pockets of back flows were observed near the TE. These back flow regions expanded with increasing α and merged into a cellular structure, the stall cell (SC) at $\alpha = 9.7°$. The SC continued to expand with further increase in ($9.7° < \alpha < 11°$). The observed SC had a mushroom-shape separation front, which spiraled into two foci that corresponded to wall-normal vortices. Note that, the SC produced in this experiment was asymmetric in the spanwise direction and was attributed to the dissimilar corner flows developed at the spanwise ends of the wing. To address the asymmetry, vane-type vortex generators (VGs) were installed at 20% chord to accelerate the attached flow between the SC and wing tip, minimizing the effect of dissimilar corner flows. A significant improvement in symmetry was observed after the deployment of VG. Three-dimensional (3D) topology of the SC was also investigated using large-scale 3D particle tracking velocimetry. The results revealed that the SC at $\alpha = 9.7°$ did not exhibit any streamwise vortices as some other literatures suggested. This was likely attributed to the small α, which produced a shallow SC with a wall-normal height less than 10% of its spanwise width. The results of 3D streamlines suggested that the back flow in the separation bubble was pushed away from the wall through a rotational motion induced by the two wall-normal counter-rotating vortices.

7.2 Unsteady motions in trailing-edge separation

Continuing from project 1, the investigation proceeded at $\alpha = 9.7°$. The energetic unsteady motions in trailing-edge separation were investigated in project 2 through time-resolved planar PIV measurements. The results from the streamwise-wall-normal measurement plane showed that the flow consisted of a triangular shape turbulent separation bubble (TSB), formed between two shear layers emerged from the suction and pressure side of the wing. The TSB had three vertices, which includes an intermittent detachment point, and relatively fixed reattachment point at the TE, and an intermittent end point in the wake. The detachment point was free to oscillate in the streamwise direction along the wing surface, while the end point oscillated in both the streamwise and wall-normal directions. Spectral analysis of the fluctuating streamwise velocity showed that the TSB featured energetic unsteadiness ranged from $St_l = 0.03$ to 0.08, with its peak at $St_l = 0.06$. This was close to the dominant peak in the spectral of TSB size, which had a St_l of 0.05. Spectral proper orthogonal decomposition (SPOD) was carried out to characterize the breathing motion. The results revealed that a reduced-order model reconstructed from the lead mode at $St_l = 0.02$ had the most contribution to the breathing motion. The corresponding spatial pattern was a large-scale, inclined structure that generally overlapped with the shear layer developed above the wing. The energetic leading modes at higher St_l (0.16 and 0.72) were proven to associate with the vortex shedding process in shear layer. The mechanism responsible for the breathing motion was probed through a conference analysis between the size of TSB and unsteadiness in the flow. It was determined that the breathing of TSB was highly correlated with the flapping of top shear layer and the oscillation of the end point. It is obvious that both of them were affected by the natural vortex shedding process of shear layer that happened at a St_l much higher than the breathing motion. The findings suggest that the TSB plays a role of low-pass filter on the entrainment process associated with vortex shedding process, as spatial averaging the unsteadiness along the upper shear layer converts the unsteadiness with St_l on the order of 0.1 to 0.01.

7.3 The breathing motion in wall pressure

In the end, the relation between the breathing motion and wall pressure was explored in project 3 through simultaneously performed time-resolved planar PIV and wall-pressure fluctuation measurements. The investigation discovered that the signature of breathing motion in wall pressure only exhibited significant energy at the position slightly downstream of the mean detachment point. Its energy was mainly observed at $St_l < 0.16$ and the spectral peak occurred at $St_l = 0.05$. Farther downstream from there, the vortex shedding process had a more prominent influence on wall pressure than the breathing motion, and a significant amount of energy is detected in a range of St_l from 0.16 to 0.7 with a spectral peak at approximately St_l of 0.3. Analysis of pressure-velocity correlation found that the optimal location to detect the breathing motion was in the region where local flow is less intermittent. For this study, the ideal sensor installation was determined at $\pm$ 0.44l with respect to the mean detachment point. The correlation results also uncovered that a phase difference existed between the breathing motion and low-frequency wall pressure. SPOD analysis was thereby performed to characterize the phase relation between the two. The results showed that the contraction of TSB preceded an increase in wall-pressure fluctuation at $x/c = -0.300$ by a phase of 0.37π and a reduction in wall-pressure fluctuation at $x/c = -0.084$ by a phase of 0.34π. The results indicated that the contraction of TSB reduced the local adverse pressure gradient, while the expansion increased it. The evolution of local wall-pressure gradient in time can therefore be predicted with the established phase relation. Ultimately, the reported ideal sensor installation location and phase relation can be utilized to develop a detection strategy for the breathing motion and contributing to future advancement in active flow control.

7.4 Recommendation for future work

Based on the presented results of this thesis, several research opportunities are raised. The suggestions are suggested below.

Characterization of the instantaneous three-dimensional topology of a stall cell

The results of this thesis are associated with the 2D and 3D time-averaged topology of SC. However, the investigation from Ma et al. (2020) has shown that the instantaneous near-wall flow field appears to be very different from the time-averaged flow field shown in this study. Instead of having two dominant counter-rotating wall-normal vortices, the instantaneous flow field consists of numerous SCs that are an order of magnitude smaller than the mean SC pattern (Ma et al. 2020). Based on their observation, these small SC resembles some features of the time-averaged SC and it will be interesting to investigate how these small SCs contributes to the formation of the time-averaged SC pattern. The relation between the two can only be fully understood through time-resolved 3D velocimetry, as both are highly three-dimensional structures.

Investigating the three-dimensional breathing motion

The primary emphasis of this study was directed towards the investigation of the streamwise-wall-normal velocity fields at the midspan, where the time-averaged flow field lacked a pronounced spanwise velocity component. However, as previously mentioned, the three-dimensionality of the flow in TSB is notably strong in regions away from the midspan, which is different from the flat-plate flow. In those regions, the shear layer potentially induces wall-normal vortices, leading to an entrainment process facilitates the exchange of flow between the separation zone and the relatively low-speed flow near the wing, as opposed to the high-speed freestream observed in this investigation. It will be of interest to ascertain how the low-frequency expansion/contraction of TSB manifest in both the streamwise, wall-normal, and spanwise directions. For instance, a streamwise expansion may occur simultaneously with a spanwise contraction instead of an expansion. The former scenario is associated with the local lift fluctuation on a wing but may have limited impact on the overall lift fluctuations. The latter scenario, however, is directly related to the overall lift fluctuations. Therefore, it will be beneficial to investigate the three-dimensional breathing of TSB in the future. This future investigation can also offer more insights into the mechanism by which the TSB functions as a low-pass filter, converting higher-frequency unsteadiness to low-frequency fluctuations.

Designing an active flow control strategy to suppress breathing motion

With the results of this study, it will be intriguing to explore their application in suppressing breathing motion in real-time. The first step of this future research will be designing a real-time digital filter to low-pass the measured wall-pressure signal at a certain distance upstream from the mean TSB. Subsequently, the breathing event can be detected, and the phases of expansion and contraction can be identified. The latter information will be useful in controlling the actuator, e.g., turning on the actuation when an expansion is detected. It is important to note that the actuation timing cannot be conclusively determined with the results of this thesis, as the current study only reported the phase relation between the occurrence of event and its subsequent detection. To determine an effective actuation timing, it is essential to consider the response time between the actuation event and resulting change in separation zone. In a recent investigation by Mohammed-Taifour & Weiss (2021), an examination of the TSB reacting to upstream perturbation induced by pulsed jet was carried out, and they found that the response time was similar to the characteristic time scale of the breathing motion. Considering all these factors, an effective actuation timing can be determined. To assess the effectiveness of the control strategy, the state of the TSB should be monitored in real-time through time-resolved PIV measurements, which will be conducted simultaneously with the wall-pressure measurements. Further investigations can be performed with various actuators to assess their effectiveness using this strategy.

Bibliography

Abbott, I. H., & Von Doenhoff, A. E. (2012). *Theory of wing sections: including a summary of airfoil data.* Courier Corporation.

Adrian, R. J., & Westerweel, J. (2011). *Particle Image Velocimetry.* Cambridge: Cambridge University Press.

Adrian, R. J., Meinhart, C. D., & Tomkins, C. D. (2000). Vortex organization in the outer region of the turbulent boundary layer. *Journal of Fluid Mechanics*, 665-681.

Ashill, P., Fulker, J., & Hackett, K. (2002). Studies of flows induced by sub boundary layer vortex generators (SBVGs). *40th AIAA Aerospace Sciences Meeting & Exhibit*, (p. 968).

Aubry, N., Holmes, P., Lumley, J. L., & Stone, E. (1988). The dynamics of coherent structures in the wall region of a turbulent boundary layer. *Journal of Fluid Mechanics*, 115-173.

Bak, C., Madsen, H. A., Fuglsang, P., & Rasmussen, F. (1999). Observations and hypothesis of double stall. *Wind Enegry*, 195-210.

Balkakumar, B. J., & Adrian, R. J. (2007). Large-and very-large-scale motions in channel and boundary-layer flows. *Phil. Trans. R. Soc. A: Math. Phys. Engng Sci.*, 665-681.

Betterton, J. G., Hackett, K. C., Ashill, P. R., Wilson, M. J., Tilman, C. P., & Langan, K. J. (2000). Laser doppler anemometry investigation on sub boundary layer vortex generators for flow control. *10th Symposium on Application of Laser Techniques to Fluid Mechanics*, (pp. 10-12). Lisbon.

Boiko, A. V., Dovgal, A. V., Zanin, B. Y., & Kozlov, V. V. (1996). Three-dimensional structure of separated flows on wings. *Thermophysics and Aeromechanics*, 1-13.

Broeren, A. P., & Bragg, M. B. (1998). Low-frequency flowfield unsteadiness during airfoil stall and the influence of stall type. *AIAA Journal*.

Broeren, A. P., & Bragg, M. B. (2001). Spanwise variation in the unsteady stalling flowfields of two-dimensional airfoil models. *AIAA*, 1641-1651.

Camussi, R., Felli, M., Pereira, F., Alosio, G., & Di Marco, A. (2008). Statistical properties of wall pressure fluctuations over a forward-facing step. *Physics of Fluids*, 253-272.

Carmichael, B. H. (1981). *Low Reynolds number airfoil survey.* NASA Contractor Rep. .

Castro, I. P. (1981). Measurements in shear layers separating from surface-mounted bluff bodies. *Journal of Wind Engineering and Industrial Aerodynamics*, 253-272.

Castro, I. P., & Haque, A. (1987). The structure of a turbulent shear layer bounding a separation region. *Journal of Fluid Mechanics*, 439-468.

Cattafesta III, L. N., & Sheplak, M. (2011). Actuators for active flow control. *Annual Review of Fluid Mechanics*, 247-272.

Cherry, N. J., Hilier, R., & Latour, M. E. (1984). Unsteady measurements in a separated and reattaching flow. *Journal of Fluid Mechanics*, 13-46.

Cicatelli, G., & Sieverding, C. H. (1997). The effect of vortex shedding on the unsteady pressure distribution around the trailing edge of a turbine blade. *Journal of Turbomachinery*, 810-819.

Clemens, N. T., & Narayanaswamy, V. (2014). Low-frequency unsteadiness of shock wave/turbulent boundary layer interactions. *Annual Review of Fluid Mechanics*, 469-492.

Collis, S. S., Joslin, R. D., Seifert, A., & Theofilis, V. (2004). Issues in active flow control: theory, control, simulation, and experiment. *Progress in Aerospace Sciences*, 237-289.

Crow, S. C. (1970). Stability theory for a pair of trailing vortices. *AIAA Journal*, 2172-2179.

Délery, J. (2013). *Three-dimensional separated flow topology: Critical Points, Separation Lines and Vortical Structures.* John Wiley and Sons.

Dell'Orso, H., & Amitay, M. (2018). Parametric investigation of stall cell formation on a NACA0015 airfoil. *AIAA Journal*, 3216-3288.

Dell'Orso, H., Chan, W., & Amitay, M. (2016a). Induced stall cells on a NACA0015 airfoil using passive and active trips. *8th AIAA Flow Control Conference* (p. 3621). AIAA Paper.

Dell'Orso, H., Tuna, B. A., & Amitay, M. (2016b). Measurement of three-dimensional stall cells on a two-dimensional NACA0015 Airfoil. *AIAA Journal*, 3872-3883.

DeMauro, E. P., Dell'Orso, H., Sivaneri, V., Tuna, B. A., & Amitay, M. (2015). Measurement and formation of 3-D stall cells on 2-D airfoil. *45th AIAA Fluid Dynamics Conference*, (p. 2633).

Dianat, M., & Castro, I. P. (1991). Turbulence in a separated boundary layer. *Journal of Fluid Mechanics*, 91-123.

Driver, D. M., Seegmillrt, H. L., & Marvin, J. G. (1987). Time-dependent behavior of a reattaching shear layer. *AIAA Journal*, 914-919.

Eaton, J. K. (1980). *Turbulent flow reattachment: an experimental study of the flow and structure behind a backward-facing step.* Stanford University.

Eaton, J. K., & Johnston, J. P. (1982). Low-frequency unsteadiness of a reattaching turbulent shear layer. In L. J. Bradbury, F. Durst, B. E. Launder, F. W. Schmidt, & J. H. Whitelaw, *Turbulent Shear Flows* (pp. 162-170). Berlin, Heidelberg: Springer.

Ebrahimian, M., Sanders, R. S., & Ghaemi, S. (2019). Dynamics and wall collision of inertial particles in a solid-liquid turbulent channel flow. *Journal of Fluid Mechanics*, 872-905.

Eich, F., & Kähler, C. J. (2020). Large-scale coherent motions in turbulent boundary layers. *International Journal of Heat and Fluid Flow*, 108645.

Esfahani, A., Webb, N., & Samimy, M. (2018). Stall cell formation over a post-stall airfoil: effects of active perturbations using plasma actuators. *Experiments in Fluids*, 1-16.

Fang, X., & Tachie, M. F. (2020). Spatio-temporal dynamics of flow separation induced by a forward-facing step submerged in a thick turbulent boundary layer. *Journal of Fluid Mechanics*.

Fiore, M., Parisot-Dupuis, H., Etchebarne, B., & Gojon, R. (2022). Spectral proper orthogonal decomposition of coupled hydrodynamic and acoustic fields: Application to impinging jet configurations. *Computers & Fluids*, 105484.

Fischer, G. R., Kipouros, T., & Savill, A. M. (2014). Multi-objective optimisation of horizontal axis wind turbine structure and energy production using aerofoil and blade properties as design variables. *Renewable Energy*, 506-515.

Floriti, D. J., Tang, B. A., & Strykowski, P. J. (2005). An experimental investigation of planar countercurrent turbulent shear layers. *Journal of Fluid Mechanics*, 241-264.

Floryan, J. M. (1991). On the Görtler instability of boundary layers. *Prog. Aerosp. Sci.*, 235-271.

Gad-el-Hak, M., Pollard, A., & Bonnet, J. P. (2003). *Flow Control: Fundamentals and Practices.* Berlin: Springer.

Gad-el-Hak, M., Pollard, A., & Bonnet, J. P. (2003). *Flow control: fundamentals and practices* . Berlin: Springer.

Gao, L., Zhang, H., Liu, Y., & Han, S. (2015). ffects of vortex generators on a blunt trailing-edge airfoil for wind turbines. *Renewable Energy*, 303-311.

Garland, M. G., Santer, M. S., & Morrison, J. F. (2019). Control of celluar separation using adaptive surfaces. *Journal of Fluids and Structures*, 102609.

George, W. K. (2017). A 50-year retrospective and the future. In W. K. George, *Whither Turbulence and Big Data in the 21st Century?* (pp. 13-43). Springer.

Ghaemi, S., Ragni, D., & Scarano, F. (2012). PIV-based pressure fluctuations in the turbulent boundary layer. *Experiments in Fluids*, 1823-1840.

Gibeau, B., & Ghaemi, S. (2018). A modular, 3D-printed helium-filled soap bubble generator for large-scale volumtric flow measurements. *Experiments in Fluids*, 178.

Gibeau, B., & Ghaemi, S. (2021). Low- and mid-frequency wall-pressure fluctuations in the turbulent boundary layer. *Journal of Fluid Mechanics*.

Gibeau, B., Gingras, D., & Ghaemi, S. (2020). Evaluation of a full-scale helium-filled soap bubble generator. *Experiments in Fluids*, 1-18.

Godard, G., & Stanislas, M. (2006). Control of a decelerating boundary layer. part 1: optimization of passive vortex generators. *Aerospace Science and Technology*, 181-191.

Görtler, H. (1954). *On the three-dimensional instability of laminar boundary layers on concave walls.* National Advisory Commitee for Aeronautics.

Greenblatt, D. W., & Wygnanski, I. J. (2019). Introduction to the flow control virtual collection. *AIAA Journal*, 3111-3114.

Gregory, N., Quincey, V. G., O'Reilly, C. L., & Hall, D. J. (1971). *Progress report on observations of three-dimensional flow patterns obtained during stall development on aerofoils, and on the problem of measuring two-dimensional characteristics.* HM Stationery Office: Aeronautical Research Council.

Guala, M., Hommema, S. E., & Adrian, R. J. (2006). Large-scale and very-large-scale motions in turbulent pipe flow. *Journal of Fluid Mechanics*, 521-542.

Holmes, P. J., Lumley, J. L., Berkooz, H., Mattingly, J. C., & Wittenberg, R. W. (1997). Low-dimensional modes of coherent structures in turbulence. *Physics Reports*, 337-384.

Hutchins, N., & Marusic, I. (2007). Evidence of very long meandering features in the logarithmic region of turbulent boundary layers. *Journal of Fluid Mechanics*, 1-28.

Jones, B. M. (1933). *An experimental study of the stalling of wings.* Aeronautical Research Council Reports and Memoranda.

Jones, B. M. (1933). *An experimental study of the stalling of wings.* Cambridge: Aero. Res. Counc. R & M 1588.

Kiya, M., & Sasaki, K. (1983). Structure of a turbulent separation bubble. *Journal of Fluid Mechanics*, 83-113.

Lago, L. I., Ponta, F. L., & Otero, A. D. (2013). Analysis of alternative adaptive geometrical configurations for the NREL-5 MW wind turbine blade. *Renewable Energy*, 13-22.

Le Floc'h, A., Weiss, J., Mohammed-Taifour, A., & Dufresne, L. (2020). Measurements of pressure and velocity fluctuations in a family of turbulent separation bubbles. *Journal of Fluid Mechanics*.

Lee, J. H., & Sung, H. J. (2009). Structures in turbulent boundary layers subjected to adverse pressure gradients. *Journal of Fluid Mechanics*, 101-131.

Lin, J. C. (1999). Control of turbulent boundary-layer separation using micro-vortex generators. *30th Fluid Dynamics Conference*, (p. 3404).

Lin, J. C. (2002). Review of research on low-profile vortex generators to control boundary-layer separation. *Progress in Aerospace Sciences*, 289-420.

Liu, J., & Xiao, Z. (2020). Low-frequency oscillation over NACA0015 airfoil near stall at high Reynolds number . *AIAA Journal*, 53-60.

Loucks, R. B., & Wallace, J. M. (2012). Velocity and velocity gradient based properties of a turbulent plane mixing layer. *Journal of Fluid Mechanics*, 280-319.

Lumley, J. L. (1970). *Stochastic tools in turbulence.* New York: Academic Press.

Ma, A., Gibeau, B., & Ghaemi, S. (2020). Time-resolved topology of turbulent boundary layer separation over the trailing-edge of an airfoil. *Journal of Fluid Mechanics*.

Mabey, D. G. (1992). Review of the normal force fluctuations on aerofoils with separated flow. *Progress in Aerospace Sciences*, 43-80.

Manolesos, M., & Voutsinas, S. G. (2014a). Study of a stall cell using stereo particle image velocimetry. *Physics of Fluids*, 045101.

Manolesos, M., & Voutsinas, S. G. (2014b). Geometrical characterization of stall cells on rectangular wings. *Wind Energy*, 1301-1314.

Manwell, J. F., McGowan, J. G., & Rogers, A. L. (2010). *Wind energy explained: theory, design and application.* John Wiley & Sons.

Maull, D. J., & Young, R. A. (1973). Vortex shedding from bluff bodies in a shear flow. *Journal of Fluid Mechanics*, 401-409.

McCullough, G. B., & Gault, D. E. (1951). *Examples of three representative types of airfoil-section stall at low speed.* NACA TN 2502.

Mei, R. (1996). Velocity fidelity of flow tracer particles. *Experiments in Fluids*, 1-13.

Mohammed-Taifour, A., & Weiss, J. (2016). Unsteadiness in a large turbulent separation bubble. *Journal of Fluid Mechanics*, 383-412.

Mohammed-Taifour, A., & Weiss, J. (2021). Periodic forcing of a large turbulent separation bubble. *Journal of Fluid Mechanics*.

Monkewitz, P. A., & Huerre, P. (1982). Influence of the velocity ratio on the spatial instability of mixing layers. *Physics of Fluids*, 1137-1143.

Moss, G. F., & Murdin, P. P. (1971). *Two-dimensional low-speed tunnel tests on the NACA 0012 section including measurements made during pitching oscillation at the stall.* London: Her Majesty's Stationary Office, Aeronautical Research Council.

Mueller, T. J. (1985). *Low Reynolds number vehicles.* AGARD-AG-288.

Nekkanti, A., & Schmidt, O. T. (2021). Frequency-time analysis, low-rank reconstruction and denoising of turbulent flows using SPOD. *Journal of Fluid Mechanics*, A26.

Noack, B. R., Afanasiev, K., Morzyński, M., Tadmor, G., & Thiele, F. (2003). A hierarchy of low-dimensional models for the transient and post transient cylinder wake. *Journal of Fluid Mechanics*, 335-363.

Ozkan, G. M. (2021). Control of the flow in the near wake of an airfoil at full stall using fixed trailing-edge plates. *Experimental Thermal and Fluid Science*, 110296.

Pasqiariello, V., Hickel, S., & Adams, N. A. (2017). Unsteady effects of strong shock-wave/boundary-layer interaction at high Reynolds number. *Journal of Fluid Mechanics*, 617-657.

Pearson, D. S., Goulart, P. J., & Ganapathisubramani, B. (2013). Turbulent separation upstream of a forward-facing step. *Journal of Fluid Mechanics*, 284-304.

Priebe, S., Tu, J. H., Rowley, C. W., & Martin, M. P. (2016). Low-frequency dynamics in a shock-induced separated flow. *Journal of Fluid Mechanics*, 441-477.

Raffel, M., Willert, C. E., Scarano, F., Kähler, C. J., Wereley, S. T., & Kompenhans, J. (2018). *Particle image velocimetry; a practical guide.* Berlin: Springer.

Ragni, D., & Ferreira, C. (2016). Effect of 3D stall-cells on the pressure distribution of a laminar NACA64-418 wing. *Experiments in Fluids*, 127.

Rowin, W. A., & Ghaemi, S. (2019). Streamwise and spanwise slip over a superhydrophobic surface. *Journal of Fluid Mechanics*, 1127-1157.

Sarlak, H., Frèrre, A., Mikkelsen, R., & Sørensen, J. (2018). Experimental investigation of static stall hysteresis and 3-dimensional flow structures for an NRELS826 wing section of finite span. *Energies*, 1418.

Schanz, D., Gesemann, S., & Schröder, A. (2016). Shake-the-box: lagrangian particle tracking at high particle image densities. *Experiments in Fluids*, 70.

Schanz, D., Gesemann, S., & Schröder, A. (2016). Shake-the-box: Lagrangian particle tracking at high particle image densities. *Experiments in Fluids*, 70.

Schanz, D., Gesemann, S., Schröder, A., Wieneke, B., & Novara, M. (2012). Non-uniform optical transfer functions in particle imaging: calibration and application to tomographic reconstruction. *Measurement Science and Technology*.

Schewe, G. (2001). Reynolds-number effects in flow around more-or-less bluff bodies. *Journal of wing engineering and industrial aerodynamics*, 1267-1289.

Schlatter, P., & ÖrlÜ, R. (2010). Assessment of direct numerical simulation data of turbulent boundary layers. *Journal of Fluid Mechanics*, 116-126.

Schmidt, O. T., Towne, A., Rigas, G., Colonius, T., & Brès, G. (2018). Spectral analysis of jet turbulence. *Journal of Fluid Mechanics*, 953-982.

Schmidt, O., & Colonius, T. (2020). Guide to spectral proper orthogoal decomposition. *AIAA Journal*, 1023-1033.

Schmidt, O., & Towne, A. (2019). An efficient streaming algorithm for spectral proper orthogonal decomposition. *Computer Physics Communications* , 98-109.

Schröder, A., Geisler, R., Staak, K., Wieneke, B., Elsinga, G., & Scarano, F. (2011). Lagrangian and Eulerian views into a turbulent boundary layer flow using time-resolved tomographic PIV. *Experiments in Fluids*, 1071-1091.

Schubauer, G. B., & Spangenberg, W. G. (1960). Forced mixing in boundary layers. *Journal of Fluid Mechanics*, 10-32.

Sciacchitano, A. (2019). Uncertainty quantification in particle image velocimetry. *Measurement Science and Technology*, 092001.

Sciacchitano, A., & Wieneke, B. (2016). PIV uncertainty propagation. *Measurement Science and*, 084006.

Sigurdson, L. W. (1995). The structure and control of a turbulent reattaching flow. *Journal of Fluid Mechanics*, 139-165.

Simpson, R. L. (1981). Review - a review of some phenomena in turbulent flow separation. *ASME Journal of Fluids Engineeing*, 520-533.

Skote, M., & Henningson, D. S. (2002). Direct numerical simulation of a separated turbulent boundary layer. *Journal of Fluid Mechanics*, 107-136.

Spalart, P. R., & Strelets, M. K. (2000). Mechanisms of transition and heat transfer in a separation bubble. *Journal of Fluid Mechanics*, 329–349.

Taira, K., Brunton, S. L., Dawson, S. T., Rowley, C. W., Colonius, T., McKeon, B. J., . . . Ukeiley, L. S. (2017). Modal analysis of fluid flows: an overview. *AIAA Journal*, 4013-4041.

Taylor, H. D. (1947). *The elimination of diffuser separation by vortex generators.* East Hartford: Uniter Aircraft Corporation.

Tobak, M., & Peake, D. J. (1982). Topology of three-dimensional separated flow. *Annual review of fluid mechanics*, 61-85.

Towne, A., Schmidt, O. T., & Colonius, T. (2018). Spectral proper orthogonal decomposition and its relationship to dynamic mode decomposition and resolvent analysis. *Journal of Fluid Mechanics*, 821-867.

Trünkle, J., Mohammed-Taifour, A., & Weiss, J. (2016). Fluctuating pressure measurements in a turbulent separation bubble. *Comptes Rendus Mecanique*, 60-67.

Tsuji, Y., Imayama, S., Schlatter, P., Alfredsson, P. H., Johansson, A. V., Marusic, I., . . . Monty, J. (2012). Pressure fluctuation in high-Reynolds-number turbulent boundary layer: results from experiments and DNS. *Journal of turbulence*, N50.

Tuck, E. O. (1991). A criterion for leading-edge separation. *Journal of Fluid Mechanics*, 33-37.

Velte, C. M., & Hansen, M. O. (2013). Investigation of flow behind vortex generators by stereo particle image velocimetry on a thick airfoil near stall. *Wind Energy*, 775-785.

Wang, S., & Ghaemi, S. (2019). Effect of vane sweep angle on vortex generator wake. *Experiments in Fluids*, 24.

Wang, S., & Ghaemi, S. (2021). Full-span topology of trailing-edge separation at different angles of attack. *AIAA Journal*, 5186-5197.

Wang, S., & Ghaemi, S. (2022). Unsteady motions in the turbulent separation bubble of a two-dimensional wing. *Journal of Fluid Mechanics*, 948.

Ward, J. W. (1963). The behaviour and e}ects of laminar separation bubbles on aerofoils in incompressible ~ow. *Journal*, 783-790.

Weihs, D., & Katz, J. (1983). Cellular patterns in post stall flow over unswept wings. *AIAA Journal*, 1757-1759.

Weiss, J., Mohammed-Tairfour, A., & Schwaab, Q. (2015). Unsteady behavior of a pressure-induced turbulent separation bubble. *AIAA Journal*, 2634-2645.

Welch, P. (1967). The use of fast Fourier transform for the estimation of power spectra: a method based on time averaging over short, modified periodograms. *IEEE Trans. Audio Electroacoust*, 70-73.

Westerweel, J., & Scarano, F. (2005). Universal outlier detection for PIV data. *Experiments in Fluids*, 1096-1100.

Widerhold, O., King, R., & Noack, B. R. (2010). Robust control in turbomachinery configurations. In *Active Flow Control II* (pp. 187-201). Berlin, Heideberg: Springer.

Wieneke, B. (2008). Volume self-calibration for 3D particle image velocimetry. *Experiments in Fluids*, 549-556.

Wieneke, B. (2013). Iterative reconstruction of volumtric particle distribution. *Meas. Sci. Technol.*, 024008.

Wiener, N. (1949). *Extrapolation, interpolation, and smoothing of stationary time series.* Cambridge: MIT Press.

Winkelman, A. E., & Barlow, J. B. (1980). Flow field model for a rectangular planform wing beyond stall. *AIAA Journal*, 1006-1008.

Winkelmann, A. E. (1981). An experimental study of separated flow on a finite wing. *AIAA Journal*, 1882.

Wu, W., & Piomelli, U. (2018). Effects of surface roughness on a separating turbulent boundary layer. *Journal of Fluid Mechanics*, 552-580.

Wu, W., Meneveau, C., & Mittal, R. (2020). Spatio-temporal dynamics of turbulent separation bubbles. *Journal of Fluid Mechanics*.

Yon, J., Buchta, D. A., & Zaki, T. A. (2021). Concave-wall turbulent boundary layers without and with free-stream turbulence. *Journal of Fluid Mechanics*.

Yon, S., & Katz, J. (1998). Study of the unsteady flow features on a stalled wing. *AIAA Journal*, 305-312.

Zaccai, D., Bertels, F., & Vos, R. (2016). Design methodology for trailing-edge high-lift mechanisms. *CEAS Aeronautical Journal*, 521-534.

Zaman, K. B., Bar-Sever, A., & Mangalam, S. M. (1987). Effect of acoustic excitation on the flow over a low-Re airfoil. *Journal of Fluid Mechanics*, 127-148.

Zaman, K. B., McKinzie, K. J., & Rumsey, C. L. (1989). A natural low-frequency oscillation of the flow over an airfoil near stalling conditions. *Journal of Fluid Mechanics*, 403-442.

Appendices

A. Uncertainty analysis

The analysis of uncertainty for the measured quantities in the thesis are presented in this section. The analyses are conducted for instantaneous measurement and statistical quantities of interest. Note that the analyses for more complicated quantities, e.g., spectra and those associated with tunable algorithm are not performed for this study. These estimations involve numerous ambiguous assumptions that are challenging to characterize. The following sections will introduce the sources of error and provide sample uncertainty analyses for Chapter 4, 5, and 6.

A.1. Sources of uncertainty

In this study, velocity measurements were conducted through two- and three-component PIV measurements. The errors in PIV measurement can be broadly categorized into three categories: the ones related to the system components, caused by flow itself, and introduced by evaluation technique (Raffel et al., 2018). In a measurement chain, they are introduced at different phases, e.g., experimental setup installation, image recording process, and image evaluation process (Sciacchitano, 2019).

The errors associated with the system components and flow are unavoidable in a PIV experiment. For instance, the calibration error can be affected by the manufacturing error of a reference plate. The illumination and recording systems contain errors raised from lens aberration, sensor distortion, and misalignment in viewing angle. The hardware timing and synchronization of the recording process also contributes error to the measurement and will impact the image evaluation process.

The tracing capability of the seeding particles is another source of error. The particle motion is assumed to be governed by Stoke's drag law, in which the slip velocity depends on the acceleration of surrounding fluid and the response time of particle. The response time is a function of the difference in densities between seeding particles and fluid and is proportional to the square of particle diameter (Mei, 1996; Raffel et al., 2018). Some of these errors can be minimized through carefully designing the experiment and make minimal impact to the system, while some are also challenging to quantitively characterize.

The uncertainty in the displacement of particles in image is introduced from the processes of particle detection and evaluation, and directly affects the vector results obtained from PIV measurements. A typical value of 0.1 pixels is estimated for the errors in the subpixel interpolation of the correlation function (Adrian & Westerweel, 2011). The uncertainty in the measured velocity components is thereby quantified using this value.

For the wall-pressure measurements, the quantifiable error mainly comes from the measurement devices themselves, e.g., transducer and microphone. Therefore, the manufacturer specified uncertainties are used in estimating the error in wall-pressure measurements.

A.2. Uncertainty analysis for Chapter 4

As suggested by Adrian & Westerweel (2011), the uncertainty in particle displacement is 0.1 pixels for the planar PIV measurements. For the full-span planar PIV measurements, the uncertainty in the measured velocity vectors is computed using the digital resolution (0.13 mm/pix) and separation time between the two laser pulses (200 μs). and is determined to be 0.063 m/s ($6\times10^{-3}U_\infty$). The statistical convergence of the planar PIV measurements is also examined for both U and W components. Sample convergence plots for the condition α = 11°are illustrated in Figure 6.4a and b for U and W, respectively. The velocity components are extracted from the center of FOV, at approximately $x/c = -0.16$ and $z/c = 0$. In Figure 6.4, the horizontal axis represents the number of images n, which is normalized by the total number of images N. The mean velocity components $\langle U\rangle_n$ and $\langle W\rangle_n$ based on n images are normalized with $\langle U\rangle_N$ and $\langle U\rangle_N$, respectively. Both U and V components appear to converge within $n/N < 0.4$. The results indicate that the last 20% of reliazations (from n/N = 0.8 to 1) have std of 0.5% and 0.4% for $\langle U\rangle_n$ and $\langle W\rangle_n$, respectively.

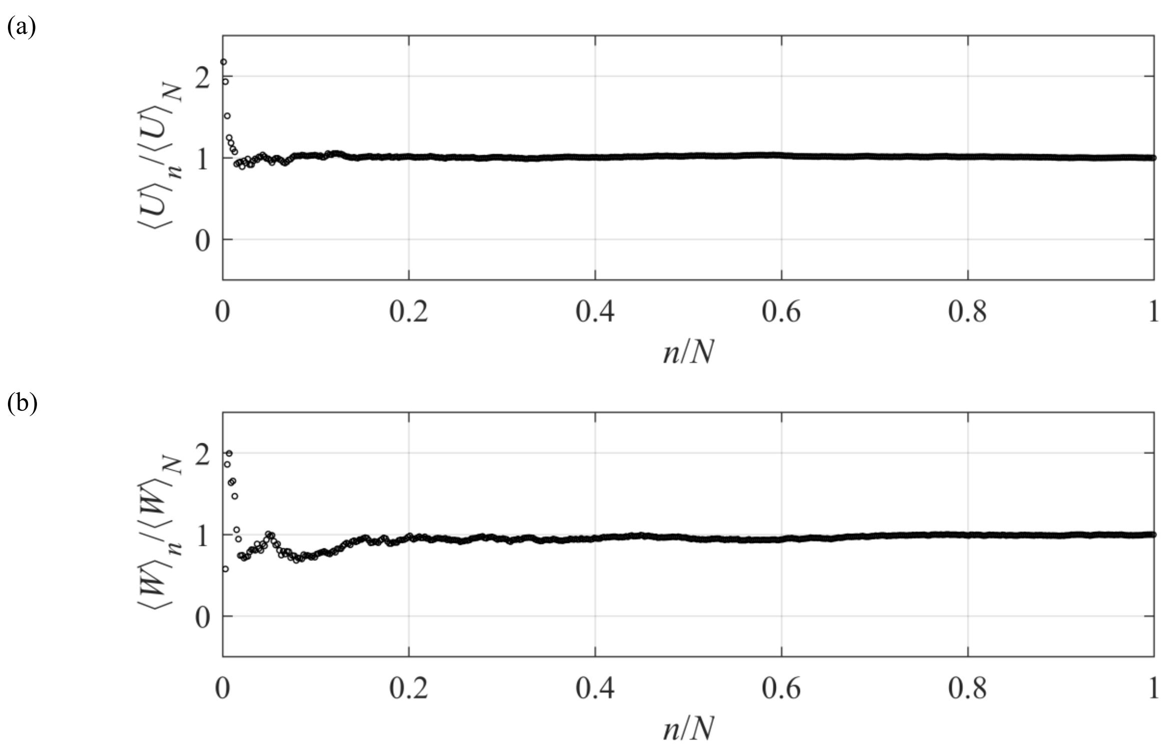

Figure A.1. Statistical convergence plots for (a) U and (b) W at α = 11°, near $x/c = -0.16$ and $z/c = 0$.

The 3D PTV measurements had estimated uncertainty in particle position of 0.1, 0.2, and 0.1 pixel in the x, y, and z directions (Ebrahimian et al. 2019; Rowin & Ghaemi 2019). The digital resolution in the 3D PTV measurements is around 0.32 mm/pixel. Hence the uncertainty in particle position was 3.1, 6.2, and 3.1 × 10^{-4} m in the *x*, *y*, and *z* directions, respectively. Using the digital resolution of 0.32 mm/pixel and acquisition frequency of 4 kHz, the velocity uncertainties are 0.13 m/s ($0.011U_\infty$), 0.26 m/s ($0.023U_\infty$), and 0.13 m/s ($0.011U_\infty$) in the *x*-, *y*-, and *z*-directions, respectively. The statistical convergence plots for the velocity components obtained in 3D PTV measurements are demonstrated in Figure A.2. The plots show that all three velocity vectors converge at $n/N > 0.8$. For the last 20% of realizations, the std of $\langle U\rangle_n$, $\langle V\rangle_n$, and $\langle W\rangle_n$ are 1.6%, 1.8%, and 0.9%, respectively.

(a)
(b)
(c)

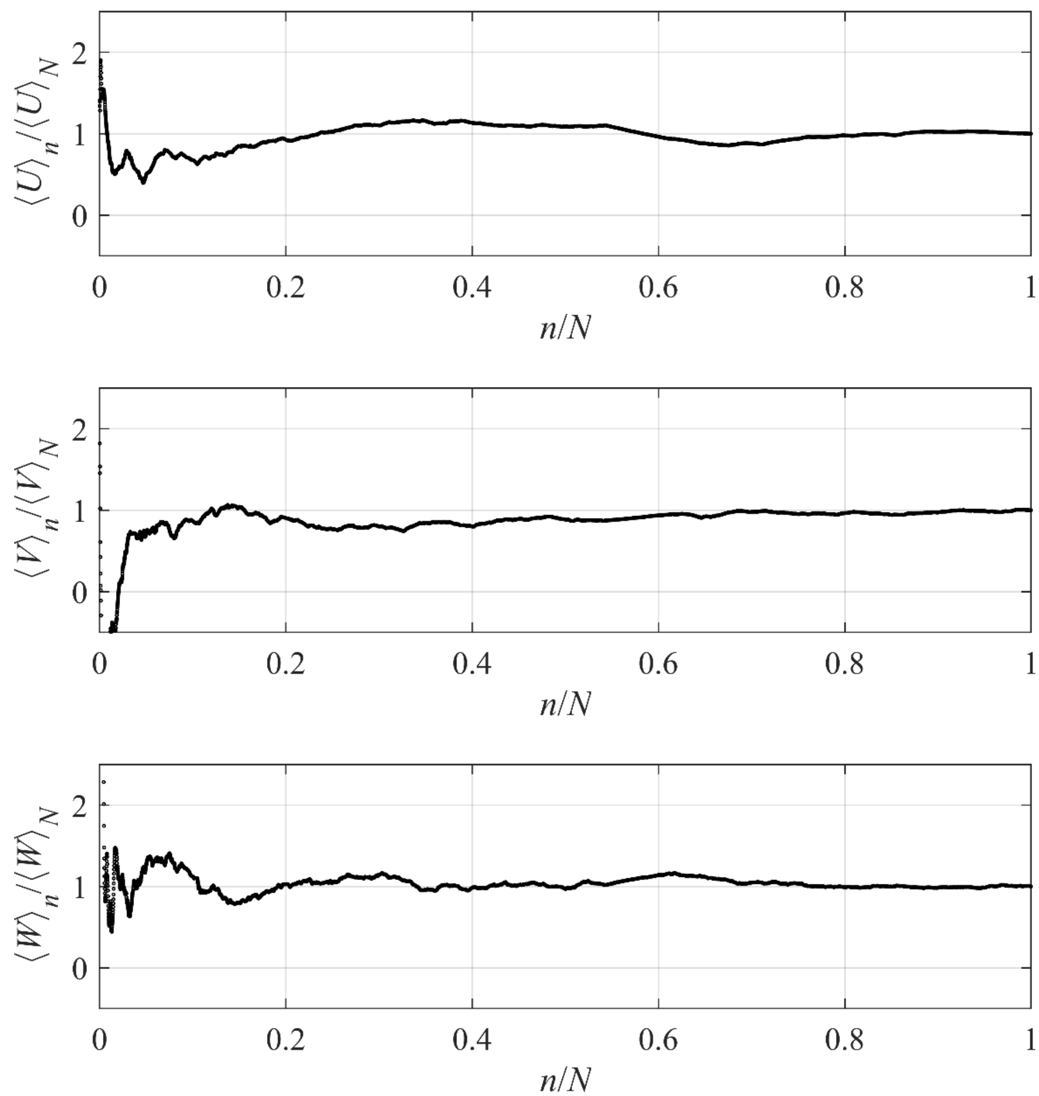

Figure A.2. Statistical convergence plots for (a) *U* (b) *V*, and (b) *W* at $\alpha = 9.7°$, near $x/c \approx -0.15$, $y/c \approx 4\times 10^{-3}$ and $z/c \approx 0.02$.

A.3. Uncertainty analysis for Chapter 5

Using the previously introduced approach, the uncertainties in velocity vectors from the *x*-*y* plane planar PIV measurements are estimated to be 0.086 m/s ($8\times10^{-3}U_\infty$), using the digital resolution (0.19 mm/pix) and time delay between the adjacent laser pulses (222 μs). The convergence plots for U and V are presented in Figure A.3a and b, respectively. The results reveal that U and V quickly converged at $n/N > 0.4$. From $n/N = 0.8$ to 1, the std of $\langle U\rangle_n$ and $\langle V\rangle_n$ are 0.3% and 0.3%, respectively. Note that, the velocity vectors are extracted from $x/c \approx -0.20$ and $y/c \approx 0.01$, which is near-wall and slightly upstream from the mean detachment point.

(a)

(b)

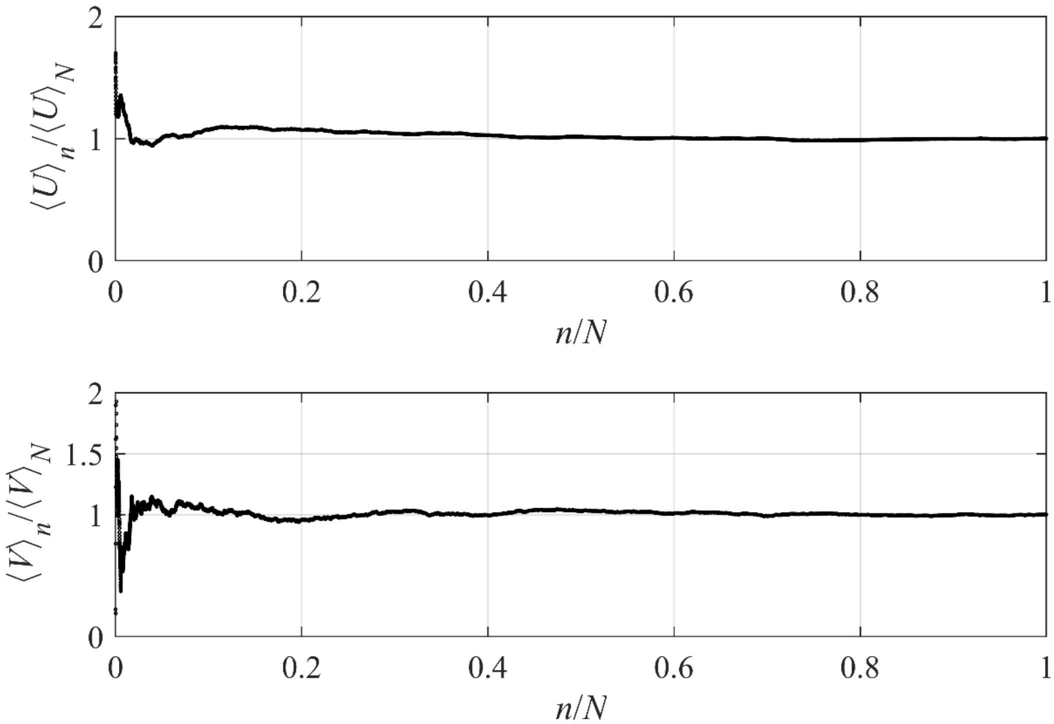

Figure A.3. Statistical convergence plots for (a) U and (b) V, near $x/c \approx -0.20$ and $y/c \approx 0.01$.

Based on the digital resolution (0.28 mm/pixel) and time delay between the laser pulses (250 μs), the uncertainty in the velocity vectors from the *x*-*z* plane is determined as 0.112 m/s ($10\times10^{-3}U_\infty$). The convergence plots for U and W are shown in Figure A.4, in which the velocity vectors are extracted from the $x/c \approx -0.20$ and $z/c = 0$. The std of $\langle U\rangle_n$ and $\langle W\rangle_n$ within the last 20% of realizations are determined to be 2.1% and 5.5%, respectively.

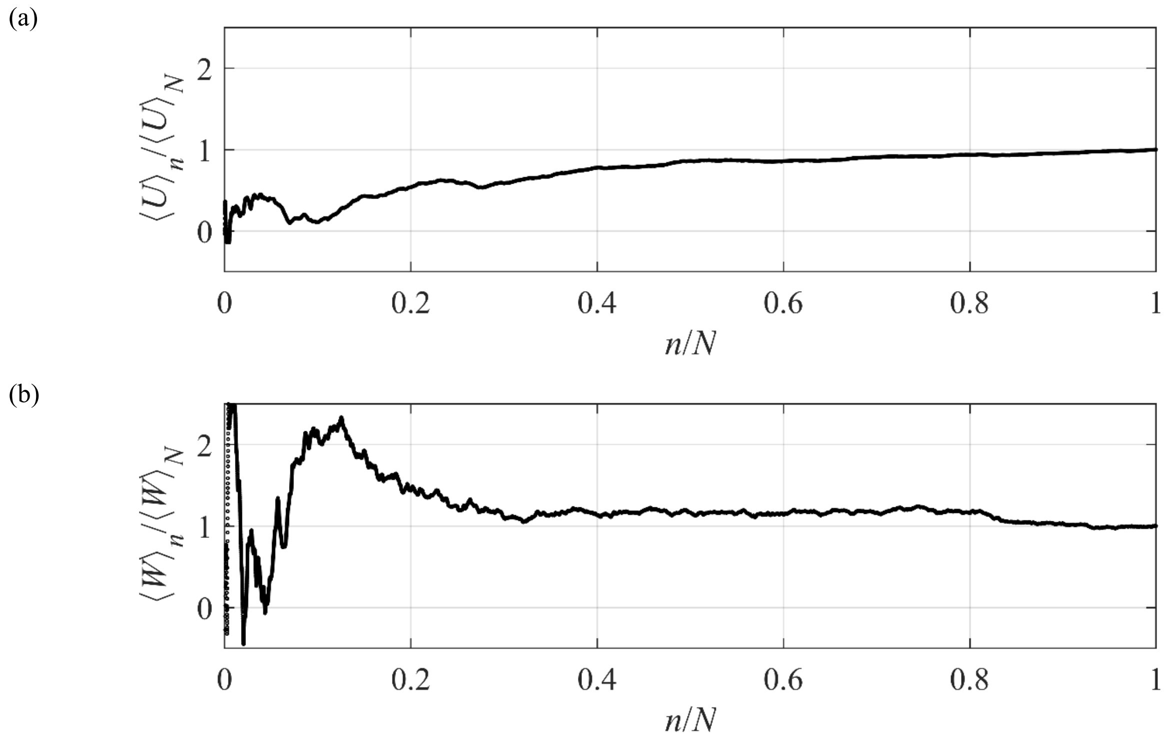

Figure A.4. Statistical convergence plots for (a) U and (b) W, near $x/c \approx -0.20$ and $z/c \approx 0$.

The uncertainty in wall-pressure measurements is specified by the manufacture, which is ±0.25% of the maximum range (62 Pa). The convergence plots for 11 differential pressure dP measurements are plotted in Figure A.5. The results show that all 11 measurements converge well at $n/N > 0.6$. The maximum std for the last 20% realizations is found to be 0.4%.

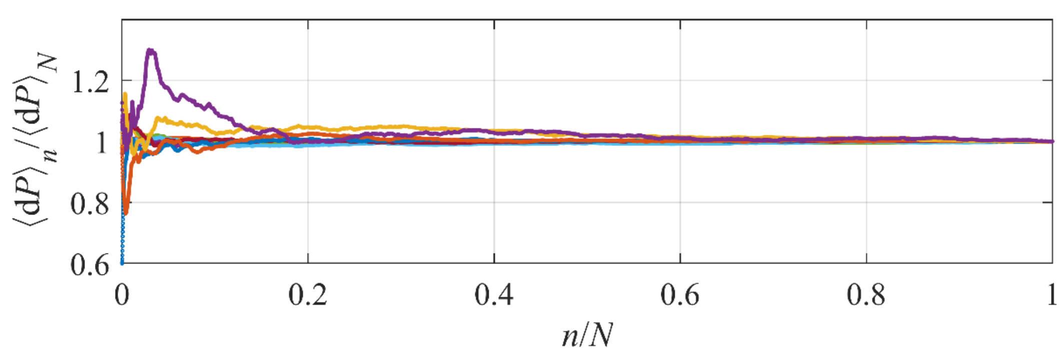

Figure A.5. Statistical convergence plots for differential pressure dP measurements.

A.4. Uncertainty analysis for Chapter 6

The uncertainty in vectors of planar PIV measurements is approximated using the aforementioned approach. Based on the digital resolution (0.20 mm/pix) and time delay between the adjacent laser pulses (500 μs), the uncertainty in velocity vectors is determined to be 0.04 m/s ($4\times10^{-3}U_\infty$). The convergence plots for U and V, extracted from $x/c \approx -0.20$ and $y/c \approx 0.01$, are presented in Figure A.6. At approximately, $n/N = 0.3$, both U and V are observed as converged. The std of $\langle U\rangle_n$ and $\langle V\rangle_n$ within the last 20% realizations are determined as 0.6% and 0.8%, respectively.

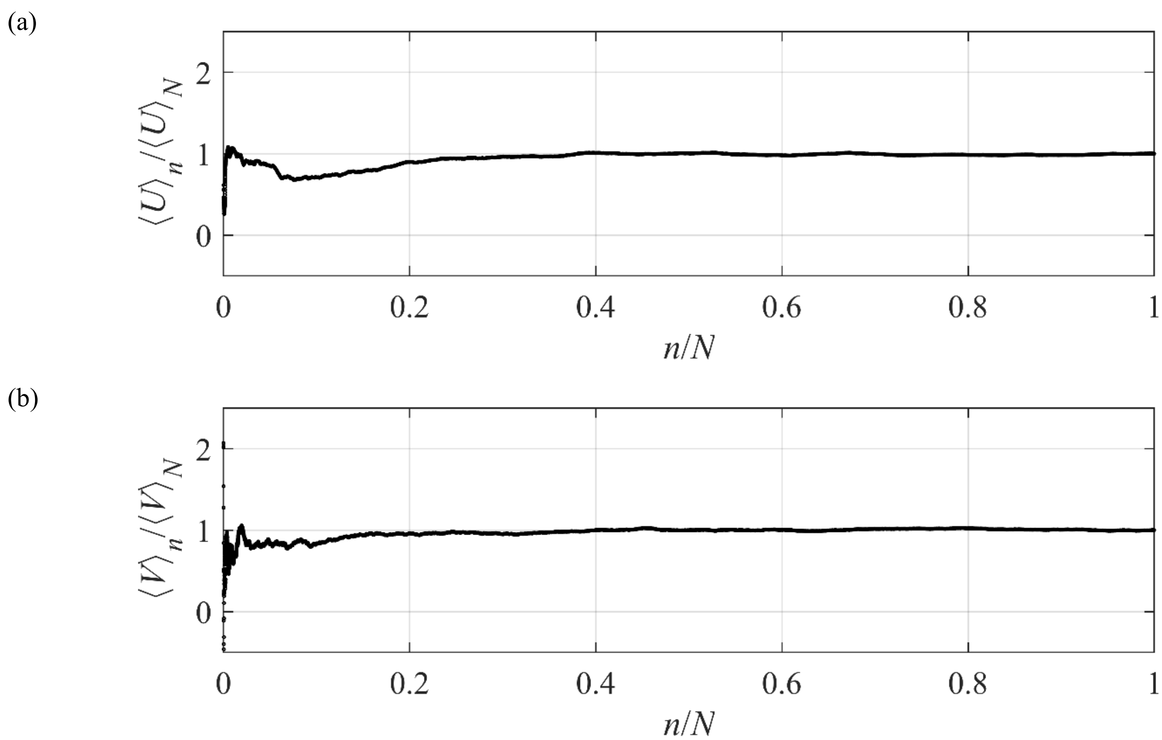

Figure A.6. Statistical convergence plots for (a) U and (b) V, near $x/c \approx -0.20$ and $y/c \approx 0.01$.

For the wall-pressure fluctuation measurements, the manufacturer indicates that the microphone calibrator has an uncertainty of ±0.2 dB for a nominal pressure of 94 dB. Therefore, the uncertainty in instantaneous wall-pressure fluctuation measurement is approximately ±2.1%.

B. MATLAB code

In this section, MATLAB codes for correcting Helmholtz Resonance and estimating the polluted signal due to wind tunnel background noise (Wiener filter) are presented. The codes presented in this section were developed by Bradley Gibeau (Gibeau & Ghaemi, 2021).

B.1. Helmholtz resonance correction

The code presented in this section was used to correct Helmholtz resonance.

```
% Helmholtz Resonance Correction
%
% Function that corrects Helmholtz resonance using a second-order model
%
% resonantFrequency: resonant frequency of the second-order model
%      dampingRatio: damping ratio of the second-order model
%      acqFrequency: signal acquisition frequency
%                 P: input pressure signal
%
%                Pc: corrected pressure signal
function [Pc] = correctHelmholtz(P,acqFrequency,dampingRatio,resonantFrequency)
L = length(P);
% Applying a fast Fourier transform and extracting one side
FFT     = fft(P,L);                         % applied to signal to be corrected
halfFFT = FFT(1:L/2+1);                     % extracting one side
f       = 0:acqFrequency/L:acqFrequency/2; % creating frequency vector
% Calculating magnitudes and phases of second-order system
secondMags   = 1./sqrt((1 - (f/resonantFrequency).^2).^2 +
(2*dampingRatio*f/resonantFrequency).^2);
secondPhases = -1.0*atan2(2*dampingRatio*(f/resonantFrequency),(1 -
(f/resonantFrequency).^2));
% Correcting magnitudes and phases in the frequency domain
for i = 1:length(f)
    z            = halfFFT(i,1);
    mag          = abs(z);
    phase        = angle(z);
    newMag       = mag/secondMags(1,i);
    newPhase     = phase - secondPhases(1,i);
    [a,b]        = pol2cart(newPhase,newMag);
    halfFFT(i,1) = complex(a,b);
end
% Re-assembling full Fourier results for inversing
FFTleft    = halfFFT;                             % left-hand complex
realsLeft  = real(halfFFT);                       % left-hand reals
imagsLeft  = imag(halfFFT);                       % left-hand imaginary
FFTright   = complex(realsLeft,-1.0*imagsLeft);   % right-hand complex
corrFFT    = [FFTleft; flipud(FFTright(2:end-1))]; % corrected FFT
Pc         = real(ifft(corrFFT,L));               % corrected signal
end
```

Published with MATLAB® R2020b

B.2. Wiener noise estimation

The function presented in this section estimates the contents in a signal of interest that are polluted by the wind tunnel background noise. The estimation is based on the pressure measurements conducted in the freestream.

```
% Wiener noise cancelling
%
% Fuction that estimates the noise in a signal of interest, based on a
% measurement of background noise measurement.
%
% signal_1: measurement to have noise reduced
% signal_2: measurement of noise field
%    order: filter order
%
%    noise: correlated noise between two signals
%
% This function finds the correlated noise that is common between two
% signals that have been recorded simultaneously.
function [noise] = wienerNoiseCancel(signal_1, signal_2, order)
N     = length(signal_1);           % signal length
X     = xcorr(signal_2)/N;          % autocorrelation of signal 2
Rv2   = toeplitz(X(N:N+order));     % Toeplitz matrix of autocorrelations
X     = xcorr(signal_1,signal_2)/N; % cross-correlation betweens signals
rxv2  = X(N:N+order);               % cropped cross-correlation vector
w     = Rv2\rxv2;                   % filter coefficients
noise = conv(w,signal_2);           % applying filter to signal 2
noise = noise(1:end-order);         % isolating the useful part
end
```

Published with MATLAB® R2020b

C. SOLIDWORKS drawings

This section provides the SOLIDWORKS drawings of the wing with a modified NACA 4418 profile and the assembly and parts employed in wall-pressure measurements.

C.1. Modified NACA4418 wing

The general dimension of the wing is provided in sheet 1, while the comparison between modified and original TE is presented in sheet 2. The assembly of the wing with a swappable rear plate is demonstrated in sheet 3. The rear plate is painted in black to reduce the glares on the wing surface caused by laser. Replacing the plate facilitates the wall-pressure measurements.

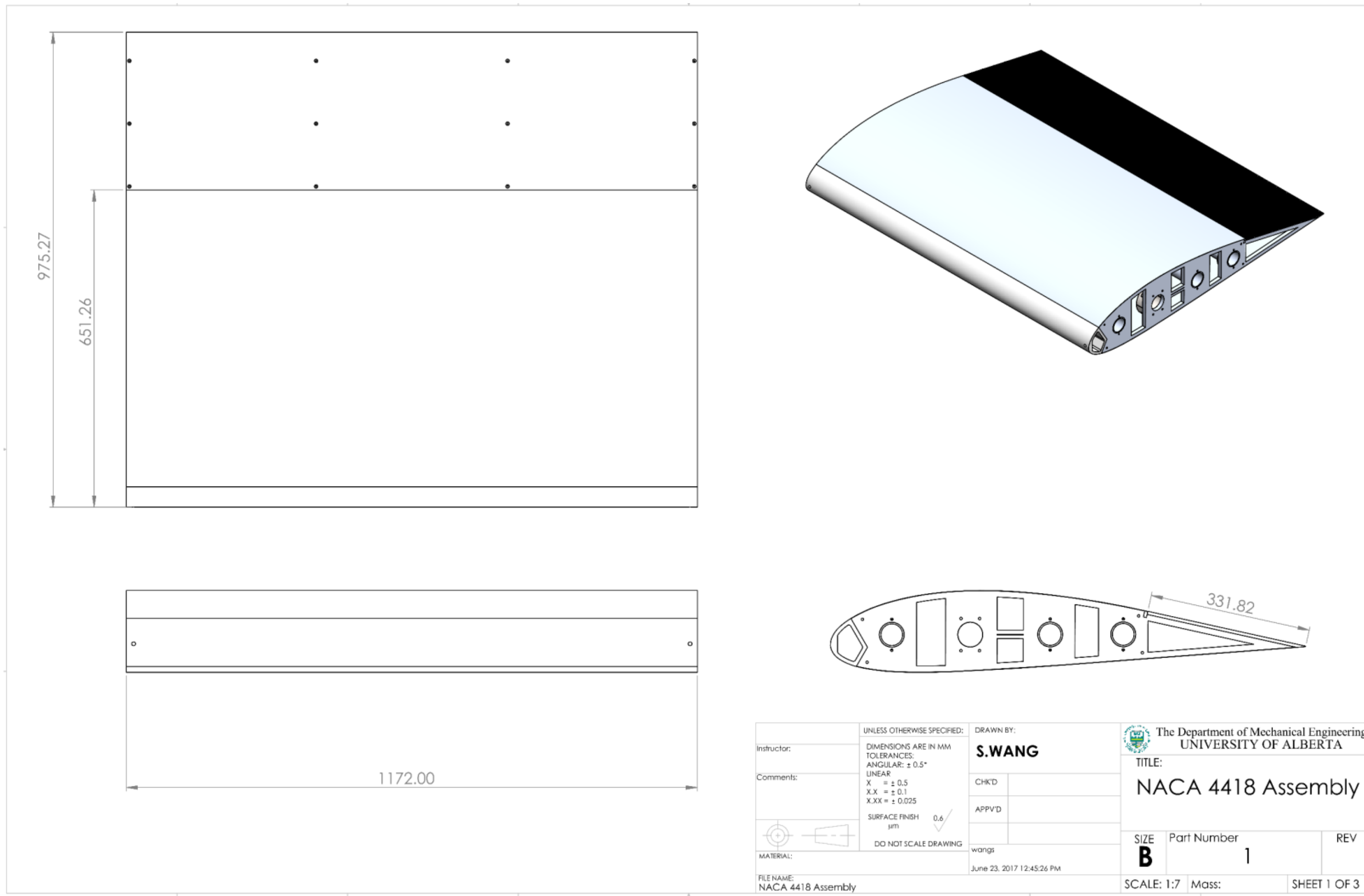
975.27
651.26
1172.00
331.82
UNLESS OTHERWISE SPECIFIED:
DIMENSIONS ARE IN MM
TOLERANCES:
ANGULAR: ± 0.5°
LINEAR
X = ± 0.5
X.X = ± 0.1
X.XX = ± 0.025
SURFACE FINISH 0.6 μm
DO NOT SCALE DRAWING
Instructor:
Comments:
MATERIAL:
FILE NAME:
NACA 4418 Assembly
DRAWN BY:
S.WANG
CHK'D
APPV'D
wangs
June 23, 2017 12:45:26 PM
The Department of Mechanical Engineering
UNIVERSITY OF ALBERTA
TITLE:
NACA 4418 Assembly
SIZE
B
Part Number
1
REV
SCALE: 1:7
Mass:
SHEET 1 OF 3

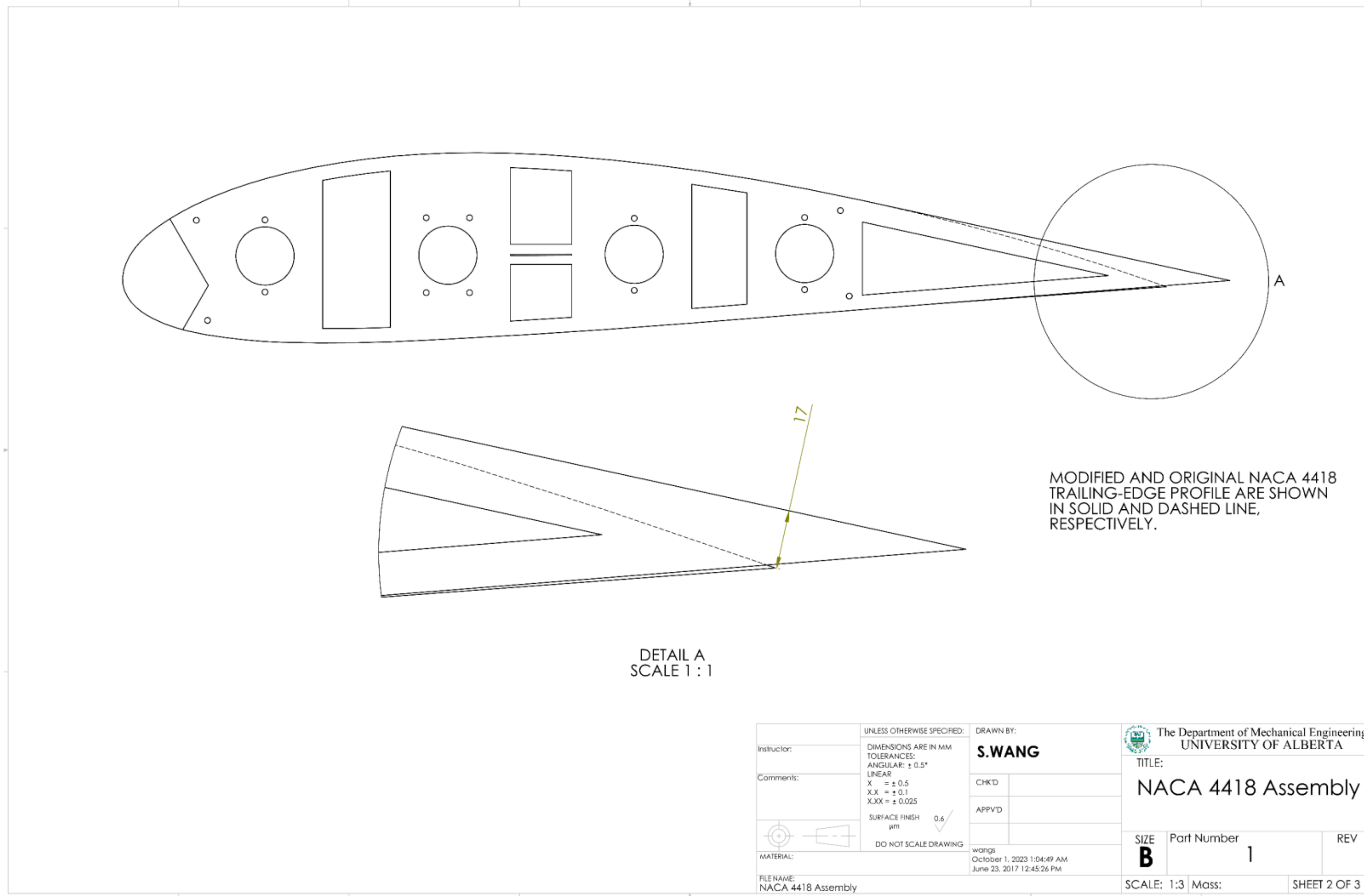
A
17
MODIFIED AND ORIGINAL NACA 4418 TRAILING-EDGE PROFILE ARE SHOWN IN SOLID AND DASHED LINE, RESPECTIVELY.
DETAIL A
SCALE 1 : 1
Instructor:
Comments:
UNLESS OTHERWISE SPECIFIED:
DIMENSIONS ARE IN MM
TOLERANCES:
ANGULAR: ± 0.5°
LINEAR
X = ± 0.5
X.X = ± 0.1
X.XX = ± 0.025
SURFACE FINISH µm 0.6
DO NOT SCALE DRAWING
MATERIAL:
DRAWN BY:
S.WANG
CHK'D
APPV'D
wangs
October 1, 2023 1:04:49 AM
June 23, 2017 12:45:26 PM
The Department of Mechanical Engineering
UNIVERSITY OF ALBERTA
TITLE:
NACA 4418 Assembly
SIZE
B
Part Number
1
REV
FILE NAME:
NACA 4418 Assembly
SCALE: 1:3
Mass:
SHEET 2 OF 3

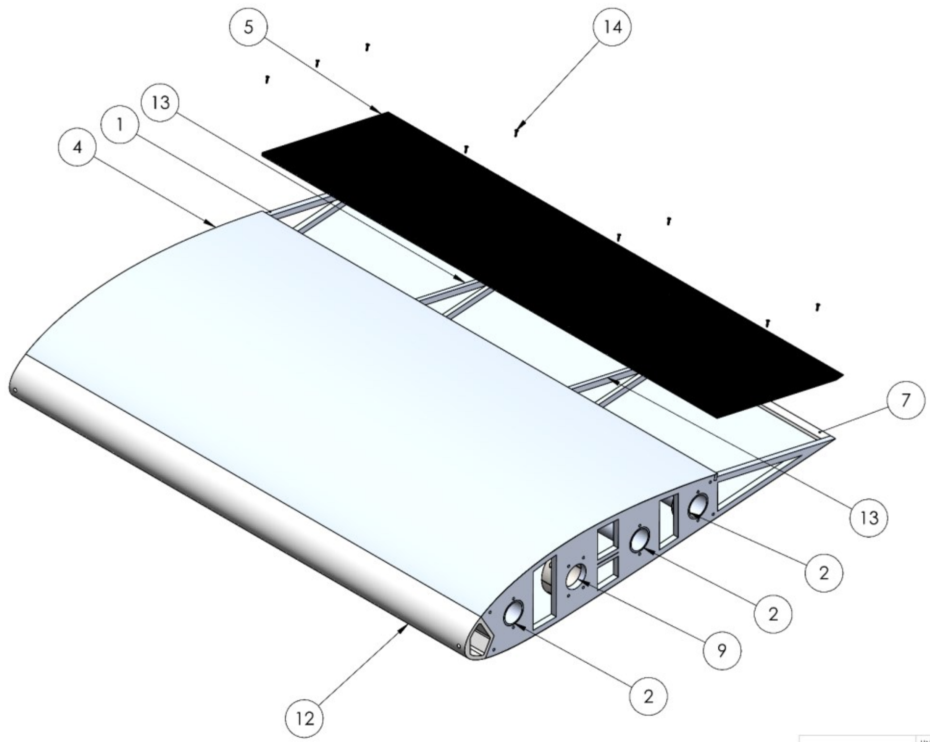

ITEM NO.	PART NUMBER	DESCRIPTION	QTY.
1	NACA 4418 Ribs - End	Spanwise ends ribs	2
2	Side Spar	Supporting spars	3
3	Bottom Skin	Pressure surface skin	1
4	Top Skin	Suction surface skin	1
5	Rear Plate	Modified trailing-edge section	1
6	Small Bonding Spar	Top skin bounding spar	1
7	Backplate Support	Trailing edge rear plate support	2
8	Backplate Support - Center	Trailing edge rear plate support	1
9	Main Spar End Collar	Collar clamp on main spar	2
10	5631T23	Collar clamp on spar	6
11	6435K27	Collar clamp on spar	12
12	NACA 4418 Split Nose	3D printed wing nose	1
13	NACA 4418 Ribs - Center	Internal ribs	2
14	90729A615	Passivated 316 Stainless Steel Hex Drive Flat Head Screw	12

Instructor:	UNLESS OTHERWISE SPECIFIED: DIMENSIONS ARE IN MM TOLERANCES: ANGULAR: ± 0.5° LINEAR X = ± 0.5 X.X = ± 0.1 X.XX = ± 0.025 SURFACE FINISH µm 0.6 DO NOT SCALE DRAWING	DRAWN BY: S.WANG	The Department of Mechanical Engineering UNIVERSITY OF ALBERTA
Comments:		CHK'D	TITLE: NACA 4418 Assembly
		APPV'D	SIZE B — Part Number 1 — REV
MATERIAL: 6061 ALLOY		wangs October 1, 2023 1:04:49 AM June 23, 2017 12:45:26 PM	
FILE NAME: NACA 4418 Assembly			SCALE: 1:7 — Mass: — SHEET 3 OF 3

C.2. The assembly for wall-pressure measurements

A rear plate with a center cutout was designed to accommodate various wall-pressure measurement setup. The drawing illustrated an insert plate positioned underneath the rear plate, serving to house different wall-pressure measurement devices.

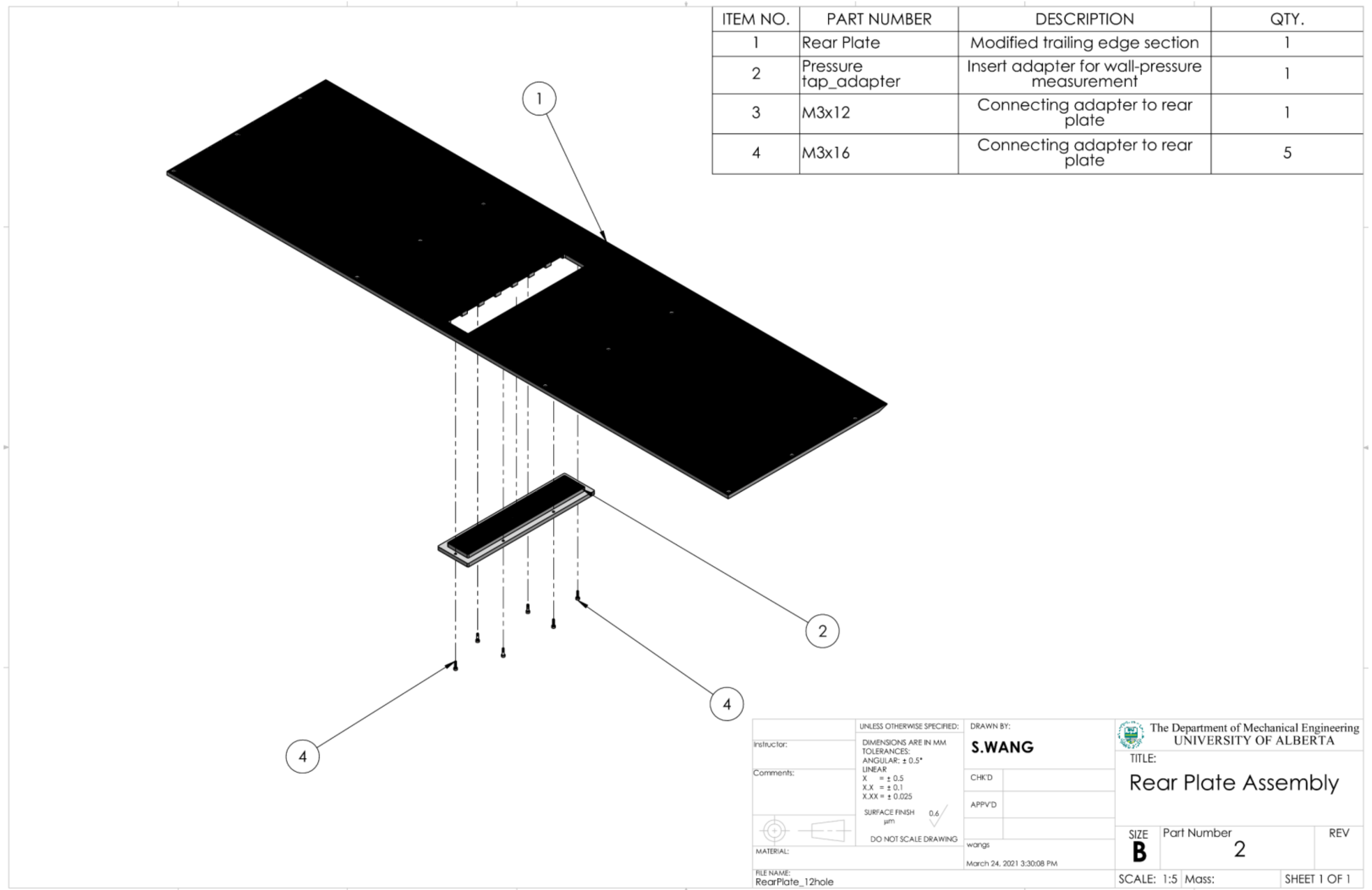

C.3. Wall-pressure measurements insert plate (Chapter 5)

The drawing of the insert plate used in the experiments detailed in Chapter 5 is illustrated in this section. The plate features 12 pinholes, with the foremost pinhole serving as the reference point for differential wall-pressure measurements.

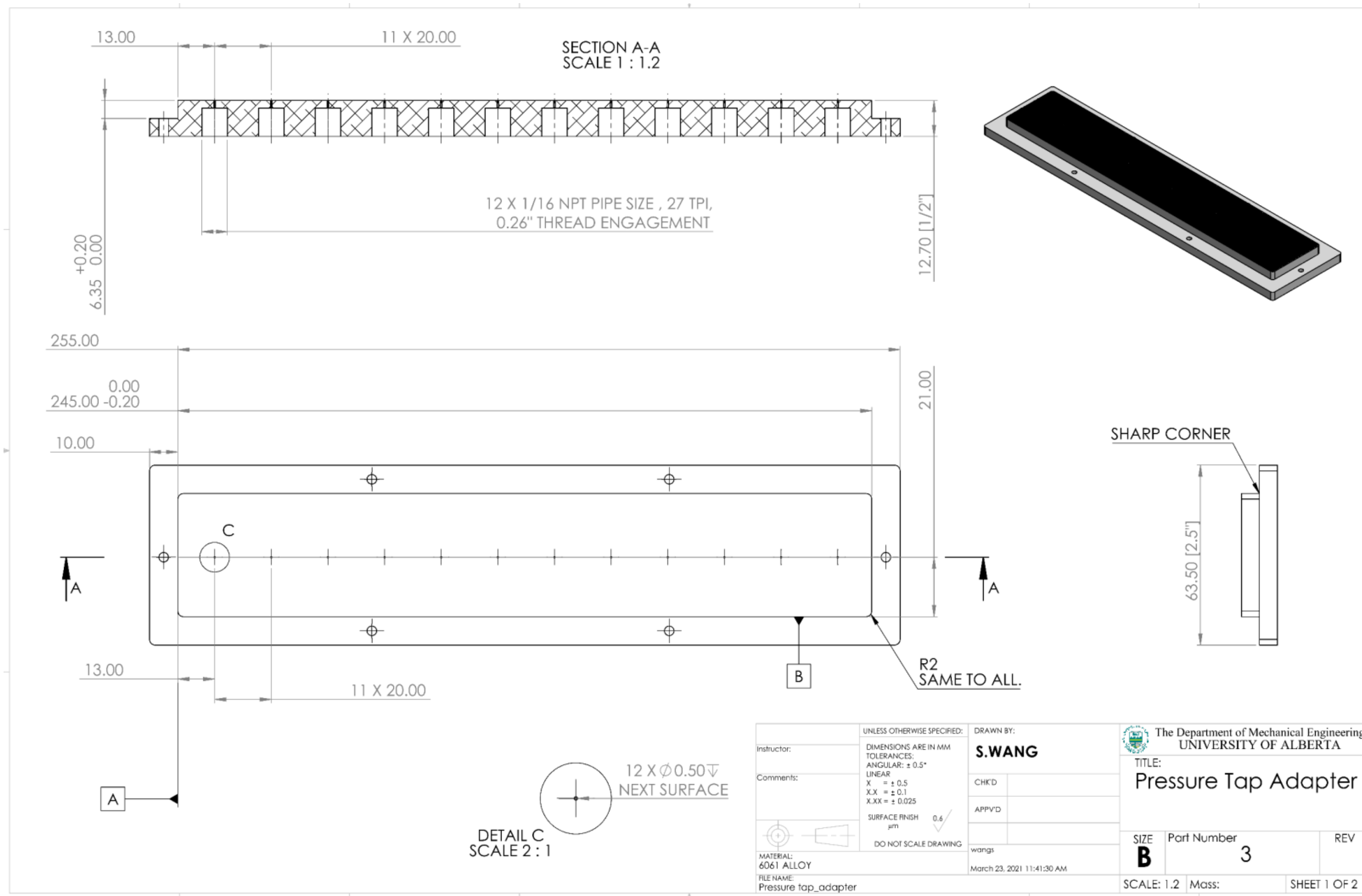

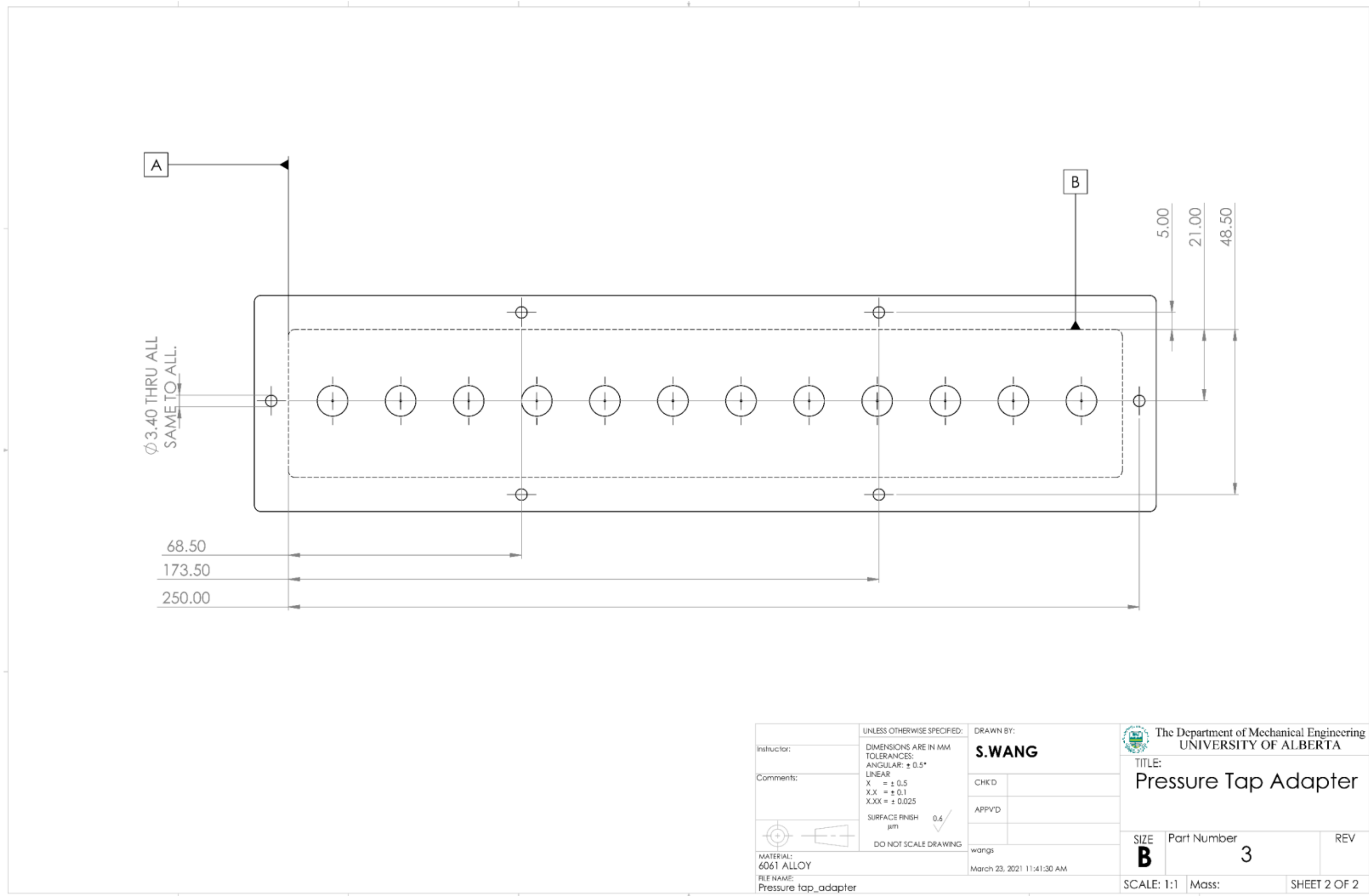
A
B
5.00
21.00
48.50
⌀3.40 THRU ALL
SAME TO ALL.
68.50
173.50
250.00
UNLESS OTHERWISE SPECIFIED:
Instructor:
Comments:
DIMENSIONS ARE IN MM
TOLERANCES:
ANGULAR: ± 0.5°
LINEAR
X = ± 0.5
X.X = ± 0.1
X.XX = ± 0.025
SURFACE FINISH µm
0.6
DO NOT SCALE DRAWING
DRAWN BY:
S.WANG
CHK'D
APPV'D
wangs
March 23, 2021 11:41:30 AM
MATERIAL:
6061 ALLOY
FILE NAME:
Pressure tap_adapter
The Department of Mechanical Engineering
UNIVERSITY OF ALBERTA
TITLE:
Pressure Tap Adapter
SIZE
B
Part Number
3
REV
SCALE: 1:1
Mass:
SHEET 2 OF 2

C.4. Wall-pressure measurements insert plate (Chapter 6)

The drawing of the insert plate employed in the experiments detailed in Chapter 6 is presented in this section. The plate consists of 7 pinholes, and was designed to house microphones for wall-pressure fluctuation measurements.

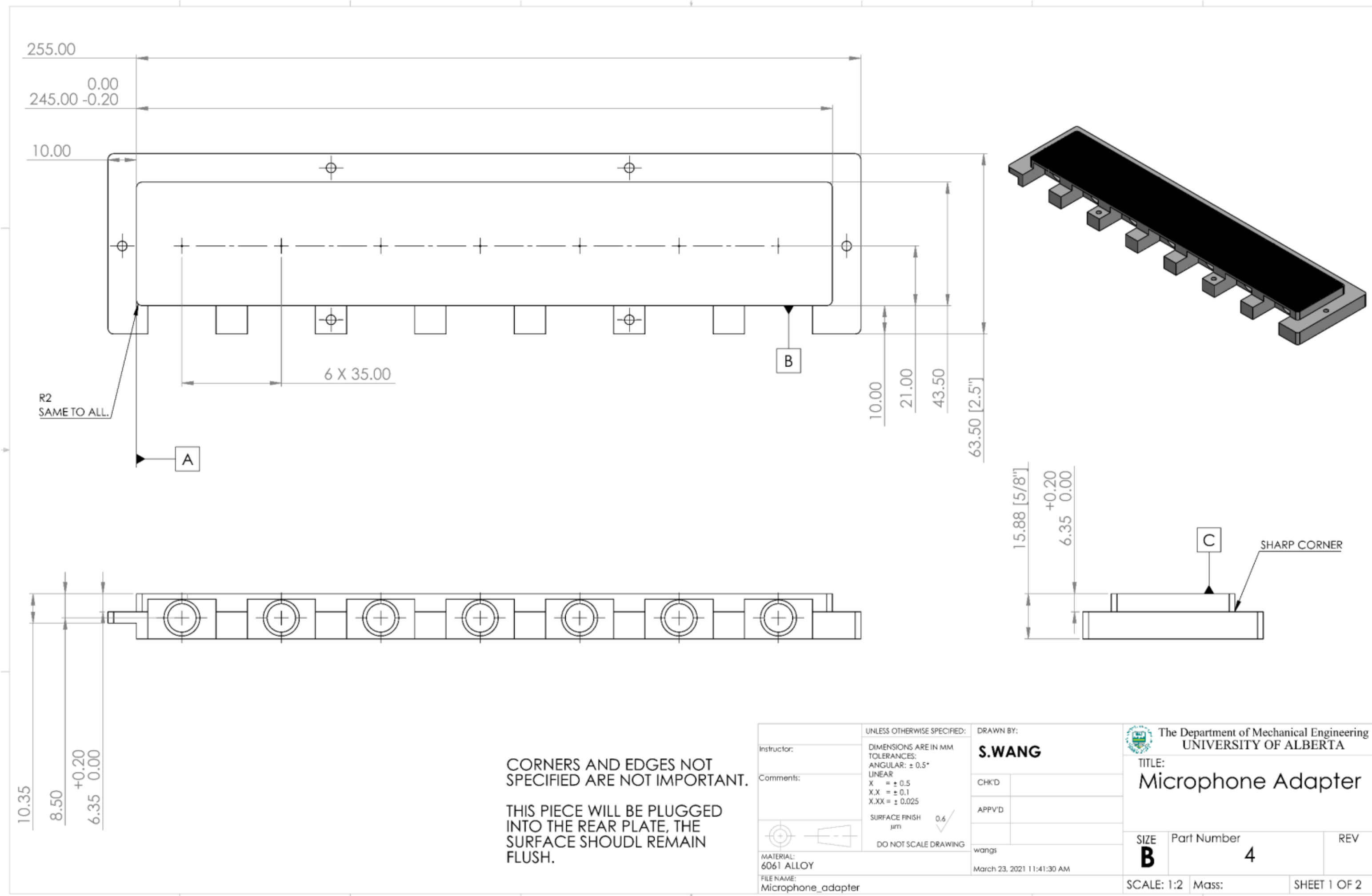

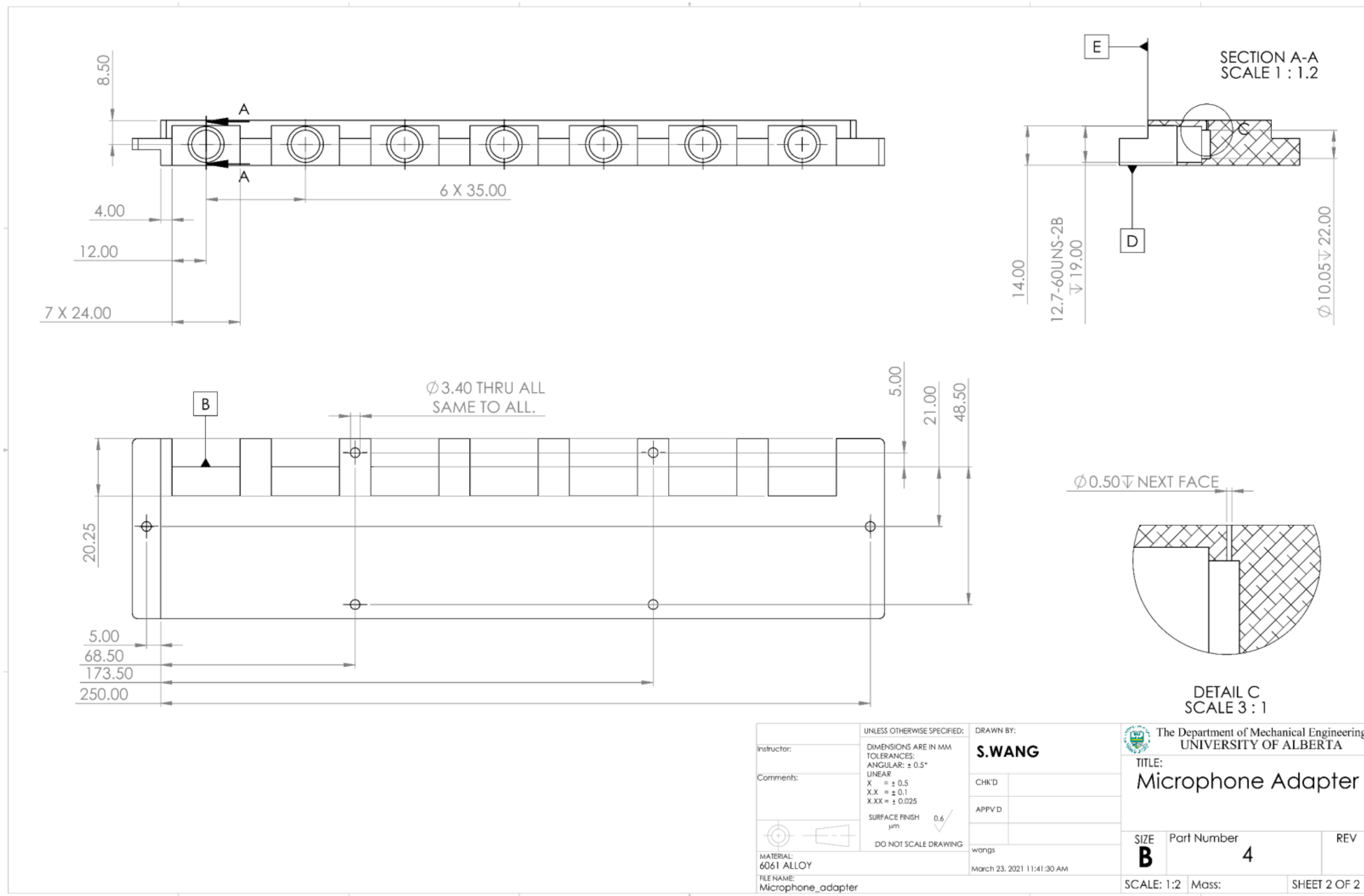

8.50
A
A
6 X 35.00
4.00
12.00
7 X 24.00
E
SECTION A-A
SCALE 1 : 1.2
C
D
14.00
12.7-60UNS-2B
↧ 19.00
∅ 10.05 ↧ 22.00
B
∅ 3.40 THRU ALL
SAME TO ALL.
5.00
21.00
48.50
20.25
5.00
68.50
173.50
250.00
∅ 0.50 ↧ NEXT FACE
DETAIL C
SCALE 3 : 1
Instructor:
Comments:
UNLESS OTHERWISE SPECIFIED:
DIMENSIONS ARE IN MM
TOLERANCES:
ANGULAR: ± 0.5°
LINEAR
X = ± 0.5
X.X = ± 0.1
X.XX = ± 0.025
SURFACE FINISH μm 0.6
DO NOT SCALE DRAWING
MATERIAL:
6061 ALLOY
FILE NAME:
Microphone_adapter
DRAWN BY:
S.WANG
CHK'D
APPV'D
wangs
March 23, 2021 11:41:30 AM
The Department of Mechanical Engineering
UNIVERSITY OF ALBERTA
TITLE:
Microphone Adapter
SIZE
B
Part Number
4
REV
SCALE: 1:2
Mass:
SHEET 2 OF 2